JYU DISSERTATIONS 453

Andrea Coronetti

Relevance and Guidelines of Radiation Effect Testing Beyond the Standards for Electronic Devices and Systems Used in Space and at Accelerators

UNIVERSITY OF JYVÄSKYLÄ
FACULTY OF MATHEMATICS
AND SCIENCE

JYU DISSERTATIONS 453

Andrea Coronetti

Relevance and Guidelines of Radiation Effect Testing Beyond the Standards for Electronic Devices and Systems Used in Space and at Accelerators

Esitetään Jyväskylän yliopiston matemaattis-luonnontieteellisen tiedekunnan suostumuksella
julkisesti tarkastettavaksi marraskuun 17. päivänä 2021 kello 12.

Academic dissertation to be publicly discussed, by permission of
the Faculty of Mathematics and Science of the University of Jyväskylä,
on November 17, 2021 at 12 o'clock noon.

JYVÄSKYLÄN YLIOPISTO
UNIVERSITY OF JYVÄSKYLÄ

JYVÄSKYLÄ 2021

Editors
Ilari Maasilta
Department of Physics, University of Jyväskylä
Timo Hautala
Open Science Centre, University of Jyväskylä

Copyright © 2021, by University of Jyväskylä

ISBN 978-951-39-8915-6 (PDF)
URN:ISBN:978-951-39-8915-6
ISSN 2489-9003

Permanent link to the online version of this publication: http://urn.fi/URN:ISBN:978-951-39-8915-6

Abstract

Coronetti, Andrea
Relevance and guidelines of radiation effect testing beyond the standards for electronic devices and systems used in space and at accelerators
Jyväskylä: University of Jyväskylä, 2021, 147 p. (+ included articles)
(JYU Dissertations
ISSN 2489-9003; 453)
ISBN 978-951-39-8915-6 (PDF)

Radiation effect testing is a key element of the radiation hardness assurance process needed to ensure the compliance with respect to the reliability and availability requirements of both space and accelerator electronic equipment. Existing standard for radiation testing were mainly tailored for radiation-hardened devices, which have less performance than commercial and industrial counterparts and makes them both less attractive and less feasible when it comes to deal with low-budgets, tight schedules and distributed systems. In this work emerging challenges and opportunities in terms of radiation effects criticality and testing methodologies are explored to assess their relevance and to provide the required radiation-matter interaction background required to tailor future guidelines and standards for the verification of the radiation performance of commercial devices to be used in harsh radiation environments. The main topics under analysis are: the sensitivity of deep sub-micron technologies to upsets caused by direct ionization from protons and their relevance for space and accelerator applications; the challenges brought by the physical interaction mechanisms specific of charged pions when it comes to characterize the mixed-field accelerator environment and the suitability of using mixed-field facilities for testing beyond accelerator needs; the possibility to use deep penetrating high-energy hadron beams as a proxy to standard heavy ion testing which can be exploited for fast component screening and system-level testing that are both of interest when it comes to answer the new demanding needs in terms of budget and schedule of the new space industry and of the distributed systems required to reliably operate the Large Hadron Collider. Experimental data and numerical analysis aimed at modelling and understanding the physical processes behind the interactions of the various particles are used to explore the potential threats brought to standard approaches by low-energy protons and high-energy pions as well as to assess the suitability of high-energy hadrons in representing the space environment. Firstly, the work achieved in this thesis reinforces even more the fact that direct ionization from proton is expected to be a severe concern for the upset rate and that a more methodological characterization of devices against these effects would be needed. Secondly, it is shown that the specific interaction mechanisms of pions are not a big concern for the high-energy hadron equivalence approximation and that little is lost if pions are treated just like they were protons. Finally, the high-energy hadron testing is expected to provide some valuable insight when it comes to verify devices or systems against the threats posed by the space environment, though within certain boundaries.

Keywords: pions, protons, neutrons, heavy ions, high-energy hadrons, accelerator, space, single-event effect, cross-section, radiation hardness assurance, FLUKA, Geant4, nuclear interactions, proton direct ionization, upset rate, prediction methodologies, Monte-Carlo simulations, system-level testing, risk acceptance, facilities, test methodology, small satellites, COTS.

Tiivistelmä (Finnish Abstract)

Coronetti, Andrea
Avaruudessa ja kiihdyttimillä käytettävien elektroniikkakomponenttien ja -järjestelmien säteilynkestotestauksen merkitys ja ohjeistukset nykyisten standardien ulkopuolella
Jyväskylä: University of Jyväskylä, 2021, 147 p.
(JYU Dissertations
ISSN 2489-9003; 453)
ISBN 978-951-39-8915-6 (PDF)

Säteilynkestotestaus on avainasemassa huolehdittaessa avaruus- sekä kiihdytinsovelluksissa käytettävien elektroniikkajärjestelmien luotettavuudesta ja saatavuudesta. Olemassa olevat testausstandardit ovat pääasiassa kehitetty säteilynkestävien komponenttien näkökulmasta. Nämä komponentit ovat lähtökohtaisesti yleisesti suoritusteholtaan heikompia ja kalliimpia kuin vastaavat kaupalliset ja teolliset komponentit, mikä tekee niistä epäkäytännöllisiä käyttää matalan budjetin, tiukkojen aikataulujen sekä hajautettujen järjestelmien sovelluksissa. Tämä työ tarkastelee säteilyilmiöiden kriittisyyden ja testausmetodien luomia haasteita ja mahdollisuuksia, jotta saadaa paremmin selville niiden merkitys tulevaisuuden testistandardeja ja ohjeistuksia määritettäessä. Pääasiassa tarkastelun kohteena ovat (1) korkean integraatioasteen teknologioissa havaittavat, matalaenergisten protonien suorasta ionisaatiosta johtuvat, virheet ja niiden merkitys avaruus- ja kiihdytinsovelluksissa, (2) varattujen pionien vuorovaikutusmekanismit ja niiden luomat haasteet luonnehdittaessa kiihdyttimillä vallitsevia säteily-ympäristöjä ja niiden käyttöä muissa kuin kiihdytinsovelluksissa, (3) korkean läpäisykyvyn hadronisuihkujen käyttömahdollisuudet raskasionitestien rinnalla nopeaan komponenttien valinnassa ja järjestelmätason testaamisessa, mitkä molemmat ovat kiinnostavia otettaessa huomioon rajoitetun budjetin ja aikataulujen projektit, esim. New Space teollisuudessa ja LHC kiihdyttimen hajautetuissa järjestelmissä. Kokeelliset tulokset ja numeeriset analyysit, joiden avulla säteilyilmiöiden takana olevia fysikaalisia prosesseja pyritään mallintamaan ja ymmärtämään, on käytetty selvittämään perinteisten testauskäytäntöjen mahdollisia vajaavaisuuksia. Pääasiallinen työssä tehdyt havainnot vahvistavat jo olemassa olevaa arviota siitä, että protonien primäärisestä ionisaatiosta aiheutuvat virheet tulevat kasvavissa määrin olemaan ongelma tulevaisuuden teknologioissa, ja että näiden ilmiöiden tutkimusta tulee jatkaa. Toisaalta myös havaittiin ettei pionien tietyt vuorovaikutusmekanismit eivät ole huolenaihe arvioitaessa korkeaenergisten hadronien aiheuttamien säteilyilmiöiden vastaavuutta pionien kanssa. Toisin sanoen, isoa virhettä ei tehdä jos pioneja käsitellään analyyseissä protonien kaltaisina hiukkasina. Ja lopuksi korkeaenergisillä hadroneilla tehtävällä testauksella uskotaan, tietyissä rajoissa, saavutettavan merkittävää tietoa tutkittaessa komponenttien ja/tai järjestelmien kohtaamia uhkia säteilyympäristöissä.

Avainsanat: pionit, protonit, neutronit, raskaat hiukkaset, korkeaenergiset hadronit, kiihdytin, avaruus, yksittäisten hiukkasten aiheuttamat vauriot, vaikutusala, säteilynkestotestaus, FLUKA, Geant4, ydinreaktiot, protonien ionisaation, virhetiheys, ennustusmetodit, Monte-

Carlo simulaatiot, järjestelmätestaus, riskinsieto, testausmetodit, piensatelliitit, kaupalliset komponentit.

Suomentanut alkuperäisestä englanninkielisestä tekstistä: Arto Javanainen

Author
Andrea CORONETTI
Department of Physics
University of Jyväskylä
Finland
SY-STI-BMI
CERN
Geneva, Switzerland

Supervisors
Dr. Arto JAVANAINEN
Department of Physics
University of Jyväskylä
Finland
Electrical and Computer
Engineering Department
Vanderbilt University
Nashville, TN, USA

Dr. Rubén GARCÍA ALÍA
SY-STI-BMI
CERN
Geneva, Switzerland

Prof. Frédéric SAIGNÉ
Institute d'Électronique
et des Systèmes
University of Montpellier
France

Reviewers
Dr. Christian POIVEY
ESA/ESTEC TEC-QEC
European Space Agency
Noordwijk, The Netherlands

Dr. Ray LADBURY
Goddard Space Flight Center
National Aeronautics and Space
Administration
Greenbelt, MD, USA

Opponent
Prof. Jean-Luc AUTRAN
Aix-Marseille University
Centre National de la Recherche
Scientifique
Institut Matériaux Microélectronique
Nanosciences de Provence
Marseille, France

Preface

This thesis was made possible thanks to the European Union's Horizon 2020 program under the Marie Sklodowska Curie grant agreement no. 721624, namely the RADSAGA project.

The work in this thesis was supervised by Rubén García Alía who followed me in each and every step from test preparation, throughout simulations and then publications. Ruben has all the markings of a great group leader and was an important mentor for my career development.

Arto Javanainen and Frédéric Saigné have been my co-supervisors. They took the time to read and correct whatever I wrote down on paper for my thesis and their critical analysis was always highly appreciated.

My secondment experience at CNES in 2018 at the very early stage of this thesis was very instructive and it allowed me getting in touch with several expert professional in the field of radiation to electronics, in particular: Julien Mekki, François Bezerra, Florent Manni, Jerome Carron and Cedric Virmontois.

Among my many colleagues, an honorable mention goes to Vanessa Wyrwoll, who shared the office with me at CERN for a couple of years and, together, we stood up to the day-by-day challenge of PhD studentships. #LifeIsTooShortToDoAPhD

Several fellow colleagues are worth mentioning from my research groups at CERN and at JYU for their kindness and support. In particular, Matteo Cecchetto, Pablo Fernandez Martinez, Maria Kastriotou, Maris Tali and Nourdine Kerboub from the CERN R2E project, who helped me out when I first started and who also contributed to part of the success of this thesis. On the JYU side, I enjoyed working alongside my colleagues Daniel Söderström, Sascha Lüdeke, Corinna Martinella and Kimmo Niskanen. A few other people from the RADSAGA working group are also worth mentioning, such as Jan Budroweit and Tomasz Rajkowski for having shared the system-level testing experience and whose input helped me in the write-up of the related guideline (yes, I also wrote a guideline in parallel to the thesis!).

Throughout the RADSAGA project I also got in touch with so many researchers, professionals and professors that I will not mention by name, as they are too many, but who gave a contribution to make the RADSAGA project a success.

Time flies and, even if it took four years to complete this thesis, I never felt it as much of a burden on my shoulders, probably thanks to Ruben careful supervision. There have been several significant moments all along the process of becoming a doctor featuring night shifts to collect data, countless technical problems at the accelerators as well as the enjoyable time spent at conferences, where I could present my work and myself.

This chapter closes, but a few other activities are already set into motion for my future in the field, including RADNEXT, CHIMERA, co-supervising interns and PhD students. I can look ahead with confidence, and that is definitely something that this PhD process helped out building.

List of Included Publications

I A. Coronetti, R. García Alía, M. Cecchetto, W. Hajdas, D. Söderström, A. Javanainen, and F. Saigné, "The pion single event effect resonance and its impact in an accelerator environment," *IEEE Trans. Nucl. Sci.*, vol. 67, no. 7, pp. 1606-1613, July 2020.

II A. Coronetti, R. García Alía, J. Wang, M. Tali, M. Cecchetto, C. Cazzaniga, A. Javanainen, F. Saigné, and P. Leroux, "Assessment of proton direct ionization for the radiation hardness assurance of deep sub-micron SRAMs used in space applications," *IEEE Trans. Nucl. Sci.*, vol. 68, no. 5, pp. 937-948, May 2021.

III A. Coronetti, R. García Alía, J. Budroweit, T. Rajkowski, I. da Costa Lopes, K. Niskanen, D. Söderström, C. Cazzaniga, R. Ferraro, S. Danzeca, J. Mekki, F. Manni, D. Dangla, C. Virmontois, N. Kerboub, A. Koelpin, F. Saigné, P. Wang, V. Pouget, A. Touboul, A. Javanainen, H. Kettunen, and R. Coq Germanicus, "Radiation hardness assurance through system-level testing: risk acceptance, facility requirements, test methodology and data exploitation," *IEEE Trans. Nucl. Sci.*, vol. 68, no. 5, pp. 958-969, May 2021.

IV A. Coronetti, R. García Alía, F. Cerutti, W. Hajdas, D. Söderström, A. Javanainen, and F. Saigné, "The pion single-event latch-up cross-section enhancement: mechanisms and consequences for accelerator hardness assurance," *IEEE Trans. Nucl. Sci.*, vol. 68, no. 8, pp. 1613-1622, August 2021.

This thesis is mainly based on the listed articles, which are also appended at the end of this document. All experiments in these articles were conducted by the author of the thesis. All written text, simulations and plots were done by the author of the thesis.

List of Other Publications

I A. Coronetti, F. Manni, J. Mekki, D. Dangla, C. Virmontois, N. Kerboub, and R. García Alía, "Mixed-field radiation qualification of a COTS space on-board computer along with its CMOS camera payload," *Proc. 2019 RADECS Conf.*, September 2019.

II A. Coronetti, M. Cecchetto, J. Wang, M. Tali, P. Fernandez-Martinez, M. Kastriotou, A. Papadopoulou, K. Bilko, F. Castellani, M. Sacristan, R. García Alía, C. Cazzaniga, Y. Morilla, P. Martín-Holgado, M.-J. van Goethem, H. Kiewiet, E. van der Graaf, S. Brandenburg, W. Hajdas, L. Sinkunaite, M. Marszalek, H. Kettunen, M. Rossi, J. Jaatinen, A. Javanainen, M.-H. Moscatello, A. Dubois, S. Fiore, G. Bazzano, C. Frost, M. Letiche, W. Farabolini, A. Gilardi, R. Corsini, and H. Puchner, "SEU characterization of commercial and custom-designed SRAMs based on 90-nm technology and below," *IEEE Radiation Effects Data Workshop*, pp. 56-63, January 2021.

III A. Coronetti, R. García Alía, M. Letiche, C. Cazzaniga, M. Kastriotou, M. Cecchetto, K. Bilko, and P. Martín-Holgado, "Thermal-to-high-energy neutron SEU characterization of commercial SRAMs," *IEEE Radiation Effects Data Workshop*, 2021.

IV A. Coronetti, R. García Alía, A. Javanainen, F. Saigné, "High-energy hadron testing and in-orbit single-event latchup predictions and boundaries,"*Proc. 2021 RADECS Conf.*, September 2021.

These publications are not peer-reviewed papers appearing in journals, but conference proceedings and data workshops, written in their entirety by the first author. They include some of the data that were used for developing this thesis. Chapter 7 of this thesis is also based on publication IV. All written text and plots in these papers were done by the author of this thesis.

V J. Budroweit, S. Mueller, M. Jaksch, R. García Alía, A. Coronetti, and A. Koelpin, "In-situ testing of a multi-band software-defined radio platform in a mixed-field irradiation environment," *MDPI Aerospace*, vol. 6, no. 10, art. 106, September 2019.

VI M. Kastriotou, P. Fernandez-Martinez, R. García-Alía, C. Cazzaniga, M. Cecchetto, A. Coronetti, G. Lerner, M. Tali, N. Kerboub, V. Wyrwoll, J. Bernhard, S. Danzeca, V. Ferlet-Cavrois, A. Gerbershagen, and H. Wilkens, "Single Event Effect Testing with Ultrahigh Energy Heavy Ion Beams," *IEEE Trans. Nucl. Sci.*, vol. 67, no. 1, pp. 63-70, January 2020.

VII R. García Alía, M. Tali, M. Brugger, M. Cecchetto, F. Cerutti, A. Coronetti, S. Danzeca, L. Esposito, P. Fernandez-Martinez, S. Gilardoni, A. Infantino, M. Kastriotou, N. Kerboub, G. Lerner, V. Wyrwoll, V. Ferlet-Cavrois, C. Boatella, A. Javanainen, H. Kettunen, Y. Morilla, P. Martin-Holgado, R. Gaillard, F. Wrobel, C. Cazzaniga, D. Alexandrescu, M. Glorieux, and H. Puchner, "Direct ionization impact on accelerator mixed-field soft error rate," *IEEE Trans. Nucl. Sci.*, vol. 67, no. 1, pp. 345-352, January 2020.

VIII J. Budroweit, M. Jaksch, R. García Alía, A. Coronetti, and A. Koelpin, ”Heavy Ion Induced Single Event Effects Characterization on an RF-Agile Transceiver for Flexible Multi-Band Radio Systems in NewSpace Avionics,” *MDPI Aerospace*, vol. 7, no. 2, art. 14, February 2020.

IX V. Wyrwoll, R. García Alía, K. Roed, C. Cazzaniga, M. Kastriotou, P. Fernandez-Martinez, A. Coronetti, and F. Cerutti, ”Longitudinal Direct Ionization Impact of Heavy Ions on See Testing for Ultrahigh Energies,” *IEEE Trans. Nucl. Sci.*, vol. 67, no. 7, pp. 1530-1539, July 2020.

X M. Cecchetto, R. García Alía, F. Wrobel, A. Coronetti, K. Bilko, D. Lucsanyi, S. Fiore, G. Bazzano, E. Pirovano, R. Nolte, ”0.1-10 MeV Neutron Soft Error Rate in Accelerator and Atmospheric Environments,” *IEEE Trans. Nucl. Sci.*, vol. 68, no. 5, pp. 873-883, May 2021.

XI C. Martinella, R. García-Alía, R. Stark, A. Coronetti, C. Cazzaniga, M. Kastriotou, Y. Kadi, R. Gaillard, U. Grossner, and A. Javanainen, ”Impact of Terrestrial Neutrons on the Reliability of SiC VD-MOSFET Technologies”, *IEEE Trans. Nucl. Sci.*, vol. 68, no. 5, pp. 634-641, May 2021.

XII D. Söderström, L. Matana-Luza, H. Kettunen, A. Javanainen, W. Farabolini, A. Gilardi, A. Coronetti, C. Poivey, and L. Dilillo, ”Electron-Induced Upsets and Stuck Bits in SDRAMs in the Jovian Environment,” *IEEE Trans. Nucl. Sci.*, vol. 68, no. 5, pp. 716-723, May 2021.

XIII J. Wang, J. Prinzie, A. Coronetti, S. Thys, R. García-Alía and P. Leroux, ”Study of the SEU sensitivity of an SRAM-Based Radiation Monitor in a 65-nm CMOS Technology,” *IEEE Trans. Nucl. Sci.*, vol. 68, no. 5, pp. 913-920, May 2021.

XIV C. Cazzaniga, R. García-Alía, A. Coronetti, K. Bilko, Y. Morilla, P. Martìn-Holgado, M. Kastriotou, and C. D. Frost, ”Measurements of low-energy protons using a silicon detector for application to SEE testing,” *accepted for publication in IEEE Trans. Nucl. Sci.*.

XV V. Wyrwoll, K. Roed, R. García-Alía, B. Delfs, A. Coronetti, W. Farabolini, A. Gilardi, and R. Corsini, ”Highly pulsed electron beam induced SEU effects in a SRAM memory,” *Proc. 2021 RADECS Conf.*, September 2021.

XVI G. Lerner, A. Coronetti, J. Kempf, R. García-Alía, F. Cerutti, A. Gilardi, W. Farabolini, and R. Corsini, ”Analysis of the photoneutron field near the THz dump of the CLEAR accelerator at CERN with SEU measurements and simulations,” *Proc. 2021 RADECS Conf.*, September 2021.

XVII K. Bilko, R. García-Alía, M. Sacristan-Barbero, D. Prelipcean, C. Cazzaniga, A. Coronetti, G. Lerner, and W. Hajdas, ”Silicon solid-state detectors for monitoring high-energy accelerator mixed-field radiation environment,” *Proc. 2021 RADECS Conf.*, September 2021.

Concerning these additional publications, the author provided either part of the text or the material included in the paper, or collected the data during the test campaign, or helped preparing the test campaign, or performed some of the data analysis, or was consulted for dealing with certain specific topics. The papers are reported in chronological order and the thesis is not based on them.

Contents

Acronyms

BEOL	Back-End-Of-Line
CCD	Coupled-Charge Devices
CERN	European Organization for Nuclear Research
CHARM	CERN Highly-AcceleRared Mixed-field facility
CMOS	Complementary Metal-Oxide Semiconductors
CNES	Centre National d'Études Spatiales
COTS	Commercial-Off-The-Shelf
CPU	Central Processing Unit
CREME	Cosmic Ray Environment and Effects Model
CUPID	Calcul d'Upsets par Protons en Ionisation Directe
DD	Displacement Damage
DRAM	Dynamic Random Access Memory
DSEE	Destructive Single-Event Effect
DUT	Device Under Test
ECC	Error Correction Code
EEE	Electrical, Electronic and Electromechanical
FLUKA	FLUktuierende KAskade
FPGA	Field-Programmable Gate Array
FWHM	Full Width at Half Maximum
G4SEE	Geant 4 Single Event Effect toolkit
GCR	Galactic Cosmic Ray
GEO	Geostationary Orbit
HEH	High-Energy Hadron (E > 20 MeV)
HEHI	High-Energy Heavy Ions (E > 100 MeV/n)
HEP	High-Energy Proton (E > 20 MeV)
HEπ	High-Energy Pion (E > 20 MeV)
HI	Heavy Ion
IC	Integrated Circuit
IEN	Intermediate-Energy Neutrons (E = 0.1-20 MeV)
IEP	Intermediate-Energy Protons (E = 3-20 MeV)
IRPP	Integral Rectangular Parallelepiped
ISS	International Space Station
ISSI	Integrated Silicon Solutions Inc.
LEO	Low-Earth Orbit
LEP	Low-Energy Proton (E = 0-3 MeV)
LET	Linear Energy Transfer
LET$_0$	Linear Energy Transfer Threshold
LHC	Large Hadron Collider
LINAC	Linear Accelerator
LIRMM	Laboratoire d'Informatique, de Robotique et de Microelectronique de Montpellier

MBU	Multiple-Bit Upset
MCU	Multiple-Cell Upset
MEAL	Mission, Environment, Application and Lifetime
MEO	Medium-Earth Orbit
NASA	National Aeronautic and Space Agency
NIEL	Non-Ionizing Energy Loss
PCB	Printed Circuit Board
PEANUT	Pre-Equilibrium Approach to NUclear Thermalization
PKA	Primary Knocked-on Atom
POT	Protons On Target
RADSAGA	RADiation and reliability challenges for electronics to be used in Space, Avionics, Ground and Accelerator
RC	Resistor-Capacitance
RHA	Radiation Hardness Assurance
RPP	Rectangular Parallelepiped
RTS	Random Telegraph Signal
SEB	Single-Event Burnout
SEE	Single-Event Effect
SEFI	Single-Event Functional Interrupt
SEGR	Single-Event Gate Rupture
SEL	Single-Event Latchup
SEM	Scanning Electron Microscope
SER	Soft Error Rate
SET	Single-Event Transient
SEU	Single-Event Upset
SOI	Silicon-On-Insulator
SPE	Solar Particle Event
SRAM	Static Random Access Memory
SRIM	Stopping and Range of Ions in Matter
SUT	System Under Test
SV	Sensitive Volume
TCAD	Transistor Computer Aided Design
TID	Total-Ionizing Dose
TNID	Total-Non-Ionizing Dose
UR	Upset Rate
VELA	Volume Equivalent LET Approach
μP	Micro-Processor

Chapter 1

Introduction

1.1 Motivation

Effects of radiation on electronics are nowadays among the main concerns to the reliability of electronic systems and equipment, no matter whether they are conceived for, designed for and operating in harsh (i.e., space and accelerator) or mild radiation environments (i.e., avionics and ground). Studies about effects of radiation in electronics have been conducted for several decades now. However, the never stopping innovation in manufacturing techniques bring continuous challenges to electronic system designers when it comes to ensure that their systems will work in compliance with the reliability and availability requirements in the radiation environment of operation.

In order to cope with the issues represented by radiation effects in electronics, several entities in charge of mission quality assurance have developed test standards for radiation effects. These test standards have been conceived with the idea of providing a work-flow process to implement for the radiation qualification of any EEE device used within the system.

While the existing standards cover for most of the traditional needs, the innovations introduced in state-of-the-art electronic devices often challenge the established work frame, inasmuch as radiation engineers often need to be flexible and distance themselves from some of these guidelines. Most of the challenges of new devices are intimately due to the use of advanced manufacturing processes that enable the possibility of having multiple functionalities embedded on the same area of silicon or to the integration of several chips within the same package. This is in particular the case of the state-of-the-art commercial devices, which provide performance that largely outscores those of radiation-tolerant devices (which are typically lagging two or three generations behind).

In addition, most of the previous generation devices, for which the standards were conceived, displayed an intrinsic resilience to certain stochastic radiation effects from weakly ionizing particles. However, due to the miniaturization of the devices, this device intrinsic resilience has started to fade, inasmuch as EEE devices manufactured in deep sub-micron technology (< 100 nm) can suffer from SEEs due to weakly ionizing particles such as low-energy protons, electrons and muons, whereas older devices suffered from SEEs only from heavy ions or hadrons (protons or neutrons).

Finally, the standards provide a rigorous procedure for qualification of EEE parts. However, radiation qualification for industrial needs is a very expensive and time-consuming activity if one has to comply with the standardized procedures, inasmuch as the full radiation characterization of a complex IC may cost up to several hundreds of thousands of dollars. This level of qualification is not well suited for emerging industries, such as New Space, which are constrained by strong limitations in budget and stringent time schedules. In order to answer these emerging needs it is necessary to develop alternative verification strategies typically based on the testing of large ensembles of devices or even entire systems simultaneously. These techniques often require looking into new facilities specifically designed for these new purposes. Characterizing unusual radiation fields available in these new facilities is a first cornerstone that must be laid in order to ensure the suitability for the final application.

The motivation behind this work is, therefore, that of exploring what stands beyond the boundaries defined by the existing standards in order to assess the relevance of radiation testing of electronics for radiation fields that are traditionally disregarded. This has the purposes of establishing (i) whether uncommon radiation testing means shall be used in a more systematic way for the qualification of state-of-the-art EEE devices, (ii) whether the common assumptions defined in previous standards still hold, (iii) whether novel verification schemes could supplement the existing standards in order to answer to the needs of new actors entering the field of radiation effect testing.

In spite of its high-level motivation and conclusions concerning the radiation hardness assurance of electronic systems, the relevance of each of the investigated issues and testing schemes is assessed by exploring the response of EEE devices down to the individual nuclear reactions that stand at the very basis of any effect of radiation in matter.

1.2 Thesis outline

The thesis is structured as follows:

- Chapter 1 provides the motivation behind this work;
- Chapter 2 reports on the standards of radiation effect testing and on the radiation environments of interest for this work;
- Chapter 3 deals with the physics on particle-matter interaction relevant for radiation effects on electronics and provides an insight on the nuclear reaction models used in the numerical analysis;
- Chapter 4 describes the irradiation facilities, the experimental apparatus used for the tests, and the experimental data retrieved during the various test campaigns;
- Chapter 5 discusses sensitive volume modelling aspects and assesses the impact of proton direct ionization on the upset rate of deep sub-micron technologies as well as other secondary proton effects;
- Chapter 6 addresses the verification of the high-energy hadron equivalence against two peculiar pion interaction mechanisms and the possibility of using mixed-field facilities for the verification of electronics to be used beyond the accelerator;
- Chapter 7 presents the comparison between high-energy hadron and high-energy ion experiments and expectations in terms of exposed sensitivity and provides the means necessary to correlate the experimental data obtained in mixed-field with the space environment rates;
- Chapter 8 draws radiation hardness assurance conclusions and gives recommendations for future work.

Chapter 2

Background on radiation effects and testing

This chapter provides the required background concerning radiation effects on electronics that are considered within this thesis. It is not meant to provide a detailed coverage of all radiation environment features, radiation effects or test standards.

2.1 Radiation environments

No matter whether radiation is of natural or artificial origin or whether particle fluxes are mild or harsh, electronic designers and developers are nowadays faced with the threat posed by radiation to the reliability (or even the operational safety) of their electronic equipment.

This work deals with the criticalities related to the use of EEE commercial devices in harsh radiation environments, such as accelerator and space. Some direct implications for milder environments, such as avionics and ground, can also be drawn.

2.1.1 Accelerator

This is an example of a radiative environment which is created as a by-product as a way to enable high energy physics experiments. Other artificial sources of radiation are found in nuclear power plants and in medical therapy centers.

The case of accelerators is, in the following, further specialized to the case of CERN because this accelerator complex has been thoroughly studied in the last decade from the point of view of beam-machine interaction and the resulting radiation environment.

Fig. 2.1 depicts a schematic of the LHC and its injector chain and experimental lines. The LHC machine is used to accelerate two counter-rotating beams of protons (ions sometimes) to very high-energies (7 TeV) and then focus the beams in such a way that protons can be collided by yielding very high levels of integrated luminosity. The integrated luminosity, measured in inverse femtobarns (fm^{-1}), is the main index of efficiency for the LHC operation and provides a measurement about the amount of proton-proton collisions achieved over the operational time.

Radiation levels (dose, high-energy hadron fluence, etc.) in the accelerator scale with the integrated luminosity. This happens at the interaction points, where protons collide with each other, but it is also true for the rest of the accelerator, even at several hundreds of meters from the interaction point. CERN is currently undergoing an upgrade towards the High-Luminosity LHC (HL-LHC) that will bring the integrated luminosity up to 3000 fm^{-1} over 10 years [1].

Radiation levels at the interaction points are so harsh (about 10 kGy(Si)/year) that all the electronic equipment has to be custom designed based on radiation harderning by design rules.

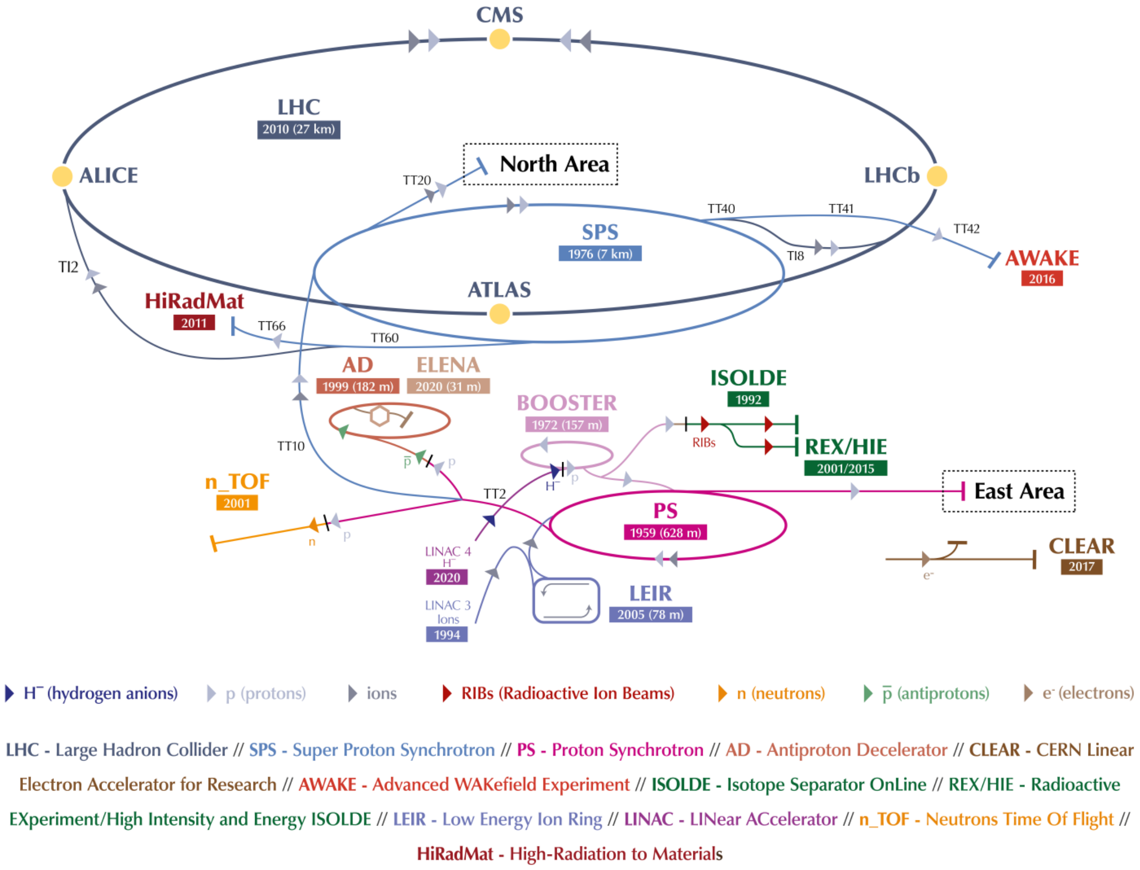

Figure 2.1: Schematics of the CERN LHC and its injector chain (https://home.cern/science/accelerators/accelerator-complex). Image from the public domain.

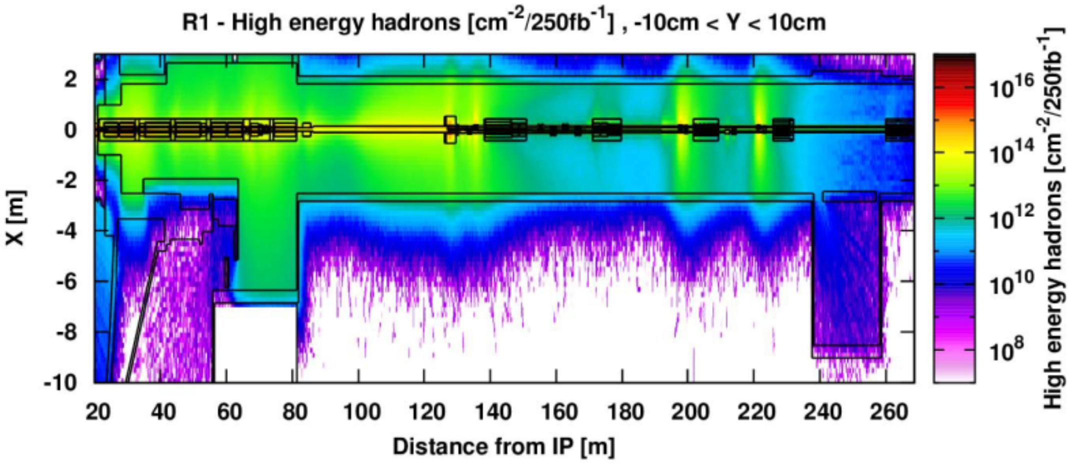

Figure 2.2: High-energy hadron equivalent fluence in the LHC tunnel as a function of the distance from the interaction point and considering all the material in the beamline. Calculated with FLUKA. Reprinted with permission from [1]. © 2017, IEEE.

However, for a proper operation of the LHC, there is still plenty of electronic equipment which is deployed all along the accelerator in order to control and monitor the beam parameters (e.g., power converters to control the bending and focusing magnets, quench protection systems, cryogenics, vacuum, interlocks, etc.).

The radiation fields generated at the interaction points have only minor impact on electronics employed along the LHC tunnel. Indeed, the radiation field along the tunnel is mainly a result of (i) protons interacting with the residual gas in the vacuum pipes and (ii) protons interacting with the beam intercepting devices (e.g., collimators). An example of the LHC tunnel radiation environment is depicted in Fig. 2.2. This shows the high-energy hadron equivalent fluence as a function of the distance with respect to the interaction point and considering the actual geometry of the tunnel and of the actual equipment (magnets, vacuum, etc.) installed along the beamline. The data were obtained by FLUKA [2, 3] Monte-Carlo simulations.

While there are tunnel areas in which the cumulative radiation levels allow employing commercial electronics (< 10 Gy/year), the high-energy hadron fluence often poses very important issues in terms of SEEs [4]. Some of these issues can be mitigated by relocating the electronic racks within shielded alcoves built in the surroundings of the tunnel. For instance, in the case of Fig. 2.3, the electronic racks have been moved to RR57 in order to reduce the radiation levels by few orders of magnitude.

Relocation of electronic equipment was extensively employed at the beginning of the R2E project at CERN. However, it often involves expensive and time-consuming civil engineering interventions. In addition, with the coming of the HL-LHC the radiation levels at the alcoves are expected to increase and pose a renewed threat to the electronic equipment there installed. For these reasons, the R2E project strategy has turned towards preventing radiation-induced failure by means of radiation tolerant designs of the electronic equipment.

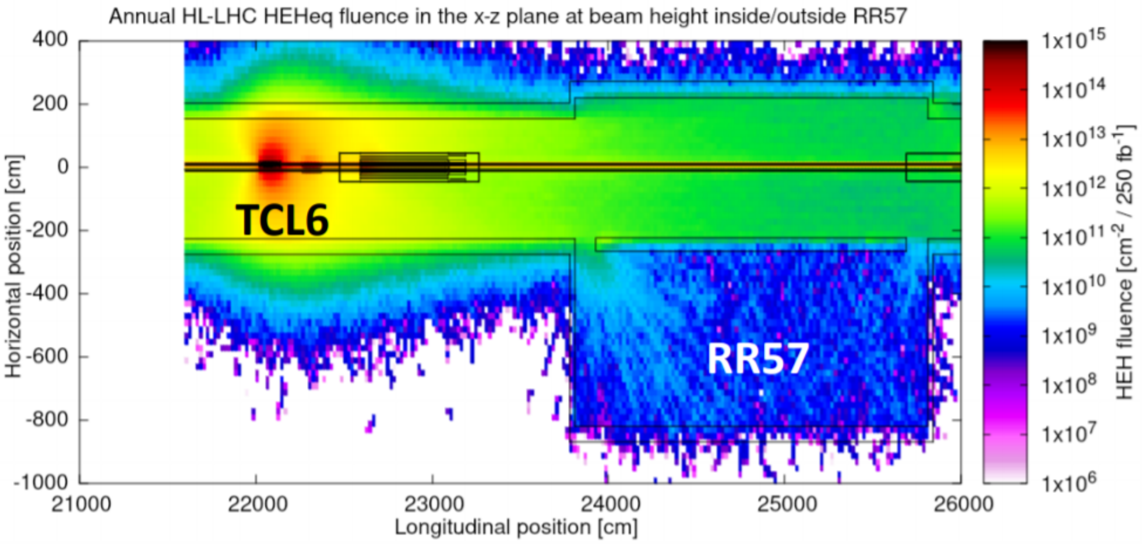

Figure 2.3: High-energy hadron equivalent fluence in one of the LHC shielded alcoves [5]. Calculated with FLUKA. Image from the public domain.

High-energy hadron equivalence

The high-energy hadron equivalent fluence is a major metric in the determination of the radiation environment severity at CERN. It is defined as follows [6]:

$$\Phi_{HEHeq} = \sum_{i=1}^{N_H} \left(\int_{20MeV}^{\infty} \Phi_i(E)dE \right) + \int_{0.2MeV}^{20MeV} \overline{\sigma_n(E)} \Phi_n(E)dE \tag{2.1}$$

As the equation shows, it is given by the integral of the fluxes of all hadrons with energy

> 20 MeV plus a weighted contribution of neutrons with energy < 20 MeV (note that $\overline{\sigma_n(E)}$ is the SEU cross-section of a worst-case SRAM in this energy range [7]).

High-energy hadrons comprise neutrons, protons, pions and kaons released by the interaction of the beam protons with matter (for pion production, see [8, 9]). It is not straightforward to separately measure the fluxes of each particle. Therefore, FLUKA simulations have to be used to resolve for the spectra of each single particle. Hence, eq. (2.1) is an approximation that works under the assumption that all hadrons have the same identical SEE cross-section at energy > 20 MeV. Note that for all SEEs, but SEUs, the intermediate-energy neutron part is suppressed.

The accuracy of this approximation is actually put into question in this work mainly due to the experimental observation that pion SEE cross-sections differ from those of protons and neutrons. Undesirable consequences can be envisaged in case the approximation will be found not to hold. On the one hand, for the equipment [10], one can envisage either an underestimation or an overestimation of the expected SEE rate. On the other hand, for radiation monitoring instruments [11], which determine the HEHeq fluence based on this equation, one may measure either lower or higher fluxes. Both issues may prevent electronic systems from complying with the reliability requirements because either the measured radiation environment or the measured cross-sections are incorrect.

The hadronic abundance of each hadron varies depending on the position where the electronics is installed in the accelerator. Typically, neutrons are the most abundant, given that in shielded areas they can reach about 70% of the overall fluxes. However, in the tunnel, neutron, proton and pion fluxes are comparable. Kaons are typically less than 1% no matter the area.

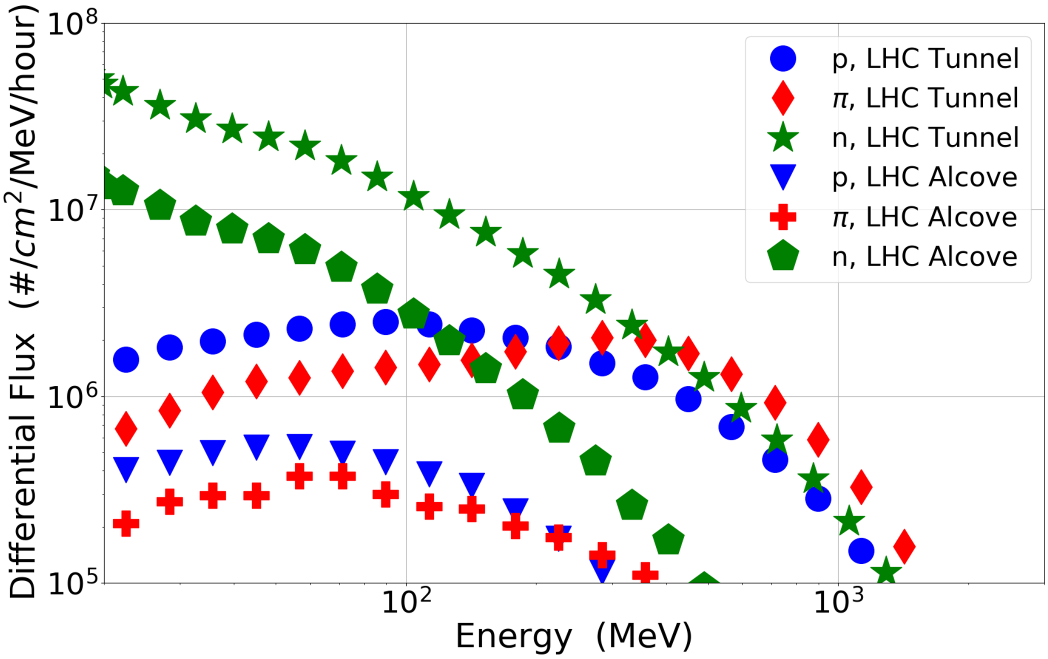

Figure 2.4: Neutron, proton and pion spectra in CHARM [12] positions representative of the LHC tunnel and alcoves as a function of the hadron energy [13]. Reprinted from [14]. © 2020, Coronetti et al., licensed under CC BY 4.0.

Other than the integral abundance, the energy of the hadrons may play a role. Fig. 2.4 depicts the spectra of neutrons, protons and pions for CHARM [12] positions representative of the LHC tunnel and LHC alcoves. Note that neutrons are the most abundant hadron for any energy for the alcoves. However, for the tunnel, they are the most abundant only below 500 MeV. From this energy upwards, pions become more abundant. The actual spectrum of each particle can play an important role when assessing the reliability of the high-energy hadron approximation given that the SEE cross-sections of hadrons are not typically constant at any energy above 20 MeV and, in some cases, they were seen to increase with increasing hadron energy [15–17].

2.1.2 Space

The space radiation environment, even if restricted to the Earth, is quite various and it is subject to both periodical and stochastic variations related to the activity of the Sun (space weather). Space particles of concern for the operation of space systems are typically classified in three categories:

- Trapped radiation: consisting of protons and electrons whose fluxes vary with the solar cycle and which suffer intensification due to strong Sun activity;
- Galactic cosmic rays: consisting of protons, alphas and heavier ions whose fluxes are inversely dependent on the solar activity;
- Solar particle events: consisting of electrons, protons and ions released by Sun flares (or a coronal mass ejection) that occur stochastically during and after the maximum of the solar activity.

Heavy ions from galactic cosmic rays are highly energetic nuclei that, due to their high charge state, are strongly ionizing, i.e., they can generate plenty of electron-hole pairs within a semiconductor material all along their trajectory. Due to their high-energies, most of them are unaffected by the presence of the Earth's magnetosphere and can easily reach the upper side of the atmosphere. Hence, they are typically a threat to the reliability of any terrestrial space mission and they are usually the dominant contributor to the SEE rate for GEO and deep space missions (in particular for DSEEs). LEO and MEO missions can be less affected, in relative terms, by ions because of the very high fluxes of trapped protons with energies up to 500 MeV and also because the Earth's magnetic field shields part of them.

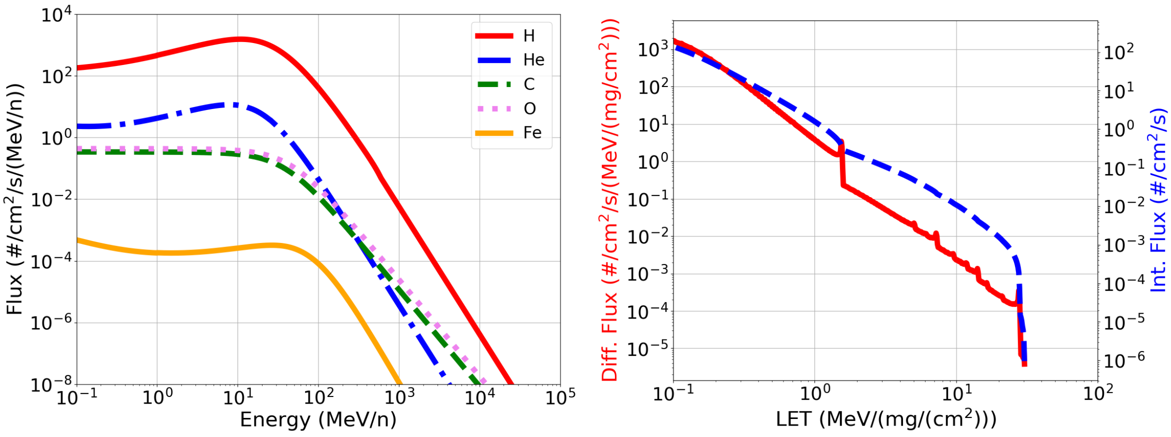

(a)

(b)

Figure 2.5: (a) Differential fluxes of a few selected galactic cosmic ray particles as a function of the energy per nucleon; (b) differential and integral fluxes of all ions having Z = 2-28 as a function of LET. Data in both figures are for GEO, solar minimum conditions, after 100 mils of aluminum shielding and were obtained from the CREME96 model [18, 19].

Fig. 2.5 (a) depicts the differential fluxes of a few selected galactic cosmic ray particles as a function of the energy per nucleon for the GEO environment. Note that the fluxes have already been transported through 100 mils of aluminum shielding. The GCR model used

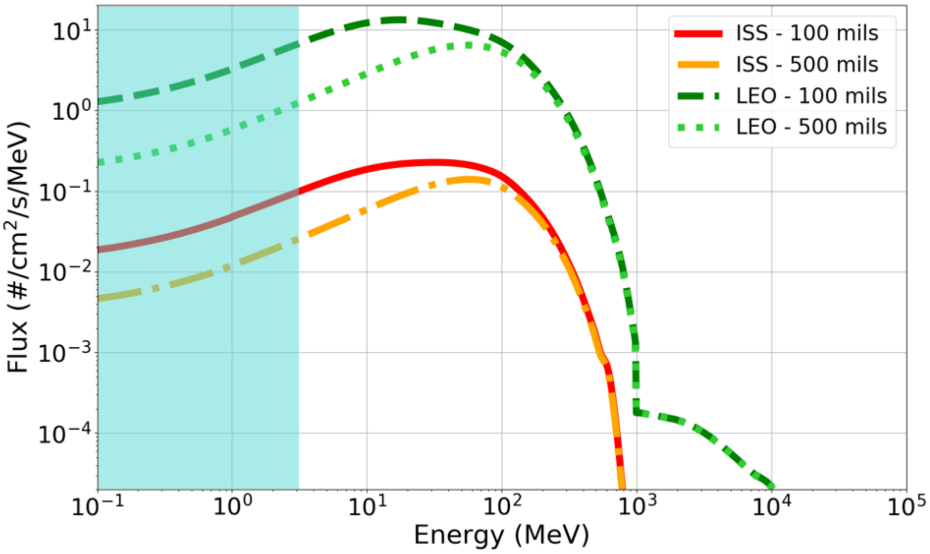

Figure 2.6: Differential fluxes of GCR protons and trapped protons as a function of the energy for the ISS orbit and a LEO (1400 km, 52°), solar minimum conditions, after 100 and 500 mils of aluminum shielding. Data from CREME (AP8 model) [18]. The light blue background is meant to highlight the low-energy proton part of the spectra.

was CREME96 [18]. In order to compute expected SEE rates in space, it is preferred to actually define the fluxes of ions as a function of their LET. This is shown in Fig. 2.5 (b). In this case, the actual atomic numbers of the ions are disregarded and all ion fluxes are summed up together under the hypothesis that their LET will be the sole metric affecting the determination of the on-orbit rates.

Note that the integral ion flux drops at around 30 MeV/(mg/cm^2) (also known as the iron knee). This is quite an important observation for the comparison of space environment energy deposition event distributions and those obtained at high-energy hadron facilities. This is of interest for devices suffering from SEL (e.g., CMOS), given that, statistically 50% of the commercial devices do not latch. Out of the remaining 50% most do latch only at LETs above the iron knee and only half of them latch in a destructive manner. Anyhow, these considerations are strongly device technology and topology dependent and it is not so easy to generalize (e.g., for ADCs and DACs the percentage of devices suffering from SEL is much higher) [20].

GCR protons typically provide negligible contribution to the SEE rate. Trapped protons, on the other hand, while having lower energies (but still in the order of few hundreds MeV), come with fluxes which can be several orders of magnitude higher than those of GCRs. Therefore, upset rates in LEO missions are typically dominated by high-energy protons with a minor contribution from GCR ions.

Fig. 2.6 depicts the proton fluxes for a couple of LEOs, the ISS orbit and another with altitude of 1400 km, inclination of 52°, both obtained in solar minimum condition through the AP8 model. The fluxes were transported through 100 and 500 mils of aluminum. Note that the high-energy tail visible for the LEO is due to GCR protons, whereas basically all protons below 1 GeV are trapped radiation in the Van Allen proton belt. The magnitude of the proton fluxes increases as the orbit gets deeper and deeper within the proton radiation belt. An increase in shielding from 100 mils to 500 mils affects only the proton fluxes below 100 MeV.

Low-energy proton fluxes (with energy < 3 MeV as per [21]) are also highlighted in the figure. For deep sub-μm technologies they can provide potential hazards given that their SEU cross-sections can be of the same order of magnitude of those of light ions, while remaining significantly abundant when compared to high-energy protons.

While for LEO, LEPs can be of concern even in quiet solar conditions, for higher orbits (e.g., GEO), the GCR LEPs are also negligible with respect to the heavy ions when it comes to calculating SEE rates. However, during stormy conditions, higher proton fluxes over the full energy spectrum are expected. Models for SPEs are based on actual measurements performed on board flying satellites and refer to few worst case conditions encountered during the space era. For SPE protons as well, the data are collected from the CREME online tool [18] and based on the October 1989 worst day on-orbit measurements.

Even if SEEs from electrons have been observed for both direct [22] and indirect ionization [23], electron-induced SEEs are negligible for space systems operated around the Earth due to the overwhelming contribution from ions and protons.

2.1.3 Avionics and ground

Avionics and ground radiation environments are only covered marginally in this thesis. This is because both environments are dominated by neutrons, which are not a subject of this thesis. However, some of the conclusions of this work may still be of direct application to the terrestrial cases. For instance, pions are generated upon collision of GCRs with the atmospheric molecules. However, since pions have quite a short lifetime (order of tens of nanoseconds), they soon decay into muons. Therefore, pion fluxes are negligible at ground level and are rather small at high altitude [24] with weak influence on the overall neutron-dominated SER.

2.2 Radiation effects in matter and electronics

Radiation effects in electronics are caused by the interaction of a highly energetic particle (projectile) with atoms (target) belonging to the lattice of the semiconductor, as well as to dielectrics and metal overlayers and plugs. When a high-energetic particle collides with an atom it can interact with both/either its electron cloud (most likely) and/or with its nucleus (less likely).

The first mechanism is called direct ionization and consists in the generation of electron-hole pairs (in silicon an energy of 3.6 eV is sufficient to generate one electron-hole pair), which give rise to charge/energy deposition along the trajectory of the projectile.

The second mechanism can give rise to several different processes that include (i) momentum exchange, (ii) excitation and ionization of both/either the projectile and/or the target nucleus following inelastic reaction or projectile capture, (iii) fission or fusion reactions.

All high-energetic charged particles generated by the interaction of the projectile with the nucleus will deposit energy/charge while interacting with the electron clouds of other atoms. Since the ionization is mainly due to secondary particles, this process is called indirect ionization.

Both direct and indirect ionization contribute to the cumulative Total Ionizing Dose and can contribute to the triggering of SEEs. This effect is typically quantified through the linear energy transfer:

$$LET(E) = -\frac{1}{\rho}\frac{dE}{dx}(E) \tag{2.2}$$

that is the energy absorbed by a material (note that ρ is the density of the material) per unit length. dE/dx is the energy lost by the particle and it can be estimated by the Bethe-Bloch equation [25]:

$$-\frac{dE}{dx} = \frac{4\pi}{m_e c^2}\frac{nZ^2}{\beta^2}\left(\frac{e^2}{4\pi\epsilon_0}\right)^2\left[ln\left(\frac{2m_e c^2\beta^2}{I(1-\beta^2)}\right) - \beta^2\right] \tag{2.3}$$

One of the main features of this equation is that the energy lost from a projectile is proportional to the square of its charge Z. Consequently, fully stripped ions are strongly-ionizing, whereas protons are weakly ionizing and neutrons are non-ionizing.

Relevant information on ionization mechanisms and nuclear interactions is detailed in Chapter 3.

Nuclear recoils knocked off of their original position in the crystalline structure can have a certain probability of interacting with other nuclei and give rise to cascade effects. All interactions causing the displacement of a nucleus from the lattice contribute to the cumulative Total Non-Ionizing Dose.

2.2.1 Single-event effects

Single-event effects are caused by interaction of the semiconductor material with a single projectile. Such events are stochastic, i.e., there is a certain probability that the energy deposited by a single particle at a sensitive node of the device will be sufficient to trigger an SEE.

Categorization

The produced macroscopic effect on the device may vary depending on the semiconductor technology, topology and function. This give rise to several types of SEEs. The most common are named and described as follows:

- single-event upset: change of the logic state of a device;
- single-event transient: transient current/voltage spike at the output of a device (although all SETs are analog, digital SETs are those that propagate to a logic element and would force a change of its logic state);
- single-event functional interrupt: caused by either an SEU or a digital SET that brings the device into a 'stuck-at' logic state from which autonomous recovery is not possible (it can also be associated with high-current states);
- single-event latchup: generation of a self-sustained double parasitic bipolar junction (thyristor) buried in the device that draws a high-current which, if not removed, can lead to the loss of the device;
- single-event burnout: in silicon devices it is caused by a parasitic bipolar junction structure and a subsequent regenerative avalanche breakdown effect that draws high-current and cause the local sublimation of the lattice or the metalization by thermal heating;
- single-event gate rupture: following a particle strike, the strong electric field can cause the accumulated charges at the silicon/oxide interface to open a conductive path through the plasma created in the oxide separating the gate from the semiconductor body. As a result, the gate is shorted to the source and/or the drain and it is no longer possible to drive the device by applying a gate bias.

All SEEs can be considered as quite disruptive for the correct functioning of a device employed in a system. SEUs and SETs are non-destructive effects for the device. However, as mentioned, they can lead other sub-parts of the same complex device, or other devices to which they feed information (or signals), to a more significant malfunction that may affect the whole system (SEFI).

The likelihood of an SEE (except for non-circumventable DSEE) is generally assessed by means of a cross-section, that is the probability of triggering an SEE given a certain fluence Φ of particles having a certain energy (or LET):

$$\sigma = \frac{N}{\Phi} \tag{2.4}$$

N is the number of SEEs observed during the experiment. SEL, SEB and SEGR are either potentially or totally destructive for the device. Therefore, while the failure is localized, the loss of a single device can cause the loss of the whole system. Given their criticality, SEB and SEGR are typically avoided by application of derating rules [26].

Depending on the criticality of the function, a device suffering from SEL can either be rejected or tolerated (devices suffering destructive SELs will have to be rejected). For both SEL and SEFI an external supervisory element is required to detect, isolate and terminate them and then restore the device functionality.

SETs can similarly be filtered by means of RC circuitry or redundant voting algorithms. SEUs, on the other hand, can be corrected by means of error detection and correction codes.

All the previously described techniques go under the name of radiation effect mitigations. Sometimes it is possible to render devices more resilient to some of these SEEs by applying radiation-hardening-by-process techniques (e.g., for SEL [27]), which are implemented at the level of manufacturing of the device.

Particles triggering SEEs

It is important to distinguish particles in the following categories:

- strongly-ionizing particles: ions;
- weakly-ionizing particles: protons, pions, all other charged hadrons, muons, electrons, etc.;
- non-ionizing particles: neutrons.

Strongly-ionizing particles can trigger SEEs by direct ionization. Nuclear interactions are also possible and their contribution can more or less impact the response [28–30]. However, note that not all ions can trigger SEEs. The LET is used to determine how strongly ionizing an ion can be. In this respect, high-LET ions are considered the most reliable particles to determine whether a device is susceptible to a certain SEE or not.

Weakly-ionizing particles (or singly-charged particles) are very different from one another. Particles with high-energy have insufficient LET to trigger SEEs in devices having even a quite low critical charge. However, upsets due to direct ionization of protons (see Section 2.4.1), electrons [22] and muons [31, 32] have been observed under many circumstances.

High-energy weakly-ionizing particles can nonetheless trigger SEEs by indirect ionization. This kind of SEEs are generated by the secondary ions released upon interaction of the primary weakly-ionizing particle with the nucleus. The LET of these secondary ions is limited, making high-energy charged hadrons quite inefficient at reproducing SEEs caused by primary high-LET ions.

Non-ionizing particles are also capable of causing SEEs, but only from indirect ionization (recall eq. (2.3)), making them as inefficient as charged hadrons in triggering SEEs.

2.2.2 Total-ionizing dose

TID results in a cumulative damage to an electronic device. In this case there is not a probability for a charged particle to deposit a sufficient amount of energy to trigger a macroscopic effect because all particles will create a certain amount of electron-hole pairs depending on their LET and contribute to the total dose (in Gy(Si)) according to:

$$TID = 1.602 \times 10^{-7} \times \sum_{i=1}^{n} \int LET_i(E)\Phi_i(E)dE \tag{2.5}$$

Where the LET is expressed in MeV/(mg/cm^2) and the fluence in cm^{-2}. The TID mainly affects the gate oxide and other dielectrics (e.g., field oxides, spacers, etc.) of a device. The generation of electron-hole pairs coupled with the application of an electric field across the oxide promotes the trapping of charges at metal-oxide interfaces. This mechanism creates a build-up of charges of opposite signs that yield a secondary electric field which is superposed to that applied across the gate oxide upon gate bias. Consequently, the threshold voltage of the transistor (that controls the opening of the channel) shifts, inasmuch as an n-type MOSFET may remain 'on' even when the bias applied to the gate terminal is null, whereas a p-type MOSFET will require applying an increasingly higher negative bias at the gate terminal to turn the transistor 'on'.

The macroscopic consequences of the transistor switching characteristic shifts are an increase in the power consumption and ultimately the failure of the device (for instance, in a memory element, the shift would correspond to the inability of the memory cell to retain the stored information).

In terms of TID, the technological scaling of transistors has enhanced the resilience of EEE devices to radiation (use of thinner oxide), though some issues still remain [33]. As opposed to CMOS, bipolar technologies are also sensitive to the dose rate [34, 35], inasmuch as the cumulative damage received is more important in the typical low dose-rates of applications than in the dose-rates applied during the tests. This effect is taken into account in the radiation testing standards [36].

There are no big new needs in terms of TID testing for state-of-the-art electronics and standards for components are of straightforward application to systems, except for some specific reliability analysis (e.g., worst case analysis) [37].

2.2.3 Displacement damage

Displacement damage [38, 39] mechanisms differ from those of TID because the projectile interacts with the semiconductor material nuclei rather than with the electron clouds. Therefore, any massive primary particle (whether charged or uncharged) can yield displacement damage.

The mechanism is initiated when the projectile collides with a nucleus. The exchange of momentum is enough to displace the nucleus from its initial position in the lattice to a new position which does not respect the regular lattice structure. As a consequence a pair of vacancy-interstitial is created, the vacancy being the empty place in the regular lattice structure and the interstitial the misplaced nucleus in the lattice.

What was previously described is known as point defect and it is typical of low projectile energies. At higher energy, when the momentum transferred from the projectile to the primary knocked-on atom is high, the PKA can further interact with other nuclei in the surrounding lattice and displace many more of them, which, in turn, can further displace others in a cascade effect.

Note that not all radiation particles crossing a semiconductor material will cause displacement damage given that the probability of colliding with a nucleus is lower than that of interacting with the electron cloud.

In order to account for all these variables, the concept of non-ionizing energy loss is introduced:

$$NIEL(E) = \frac{N_A}{A} \int_{\theta_{min}}^{\pi} L(T(\theta))T(\theta)\frac{d\sigma}{d\Omega}d\Omega \tag{2.6}$$

N_A/A (Avogadro's number over atomic mass number) expresses the dependency on the target material, whereas $T(\theta)$ is the energy that the projectile transfers to the target nucleus. $L(T(\theta))$ is the Linhard's partition factor that is used to determine how much of this energy is non-ionizing. σ is the nuclear cross-section of the projectile, which may depend on the angle of arrival Ω. The TNID is then given by convolving the NIEL(E) with the particle fluence Φ(E).

The main advantage of using the NIEL is that it is possible to determine relative damage scaling factors among different particles and energies. These are called hardness factors and they are calculated as the ratios between the NIEL of a certain particle at a certain energy with respect to the NIEL of 1 MeV neutrons.

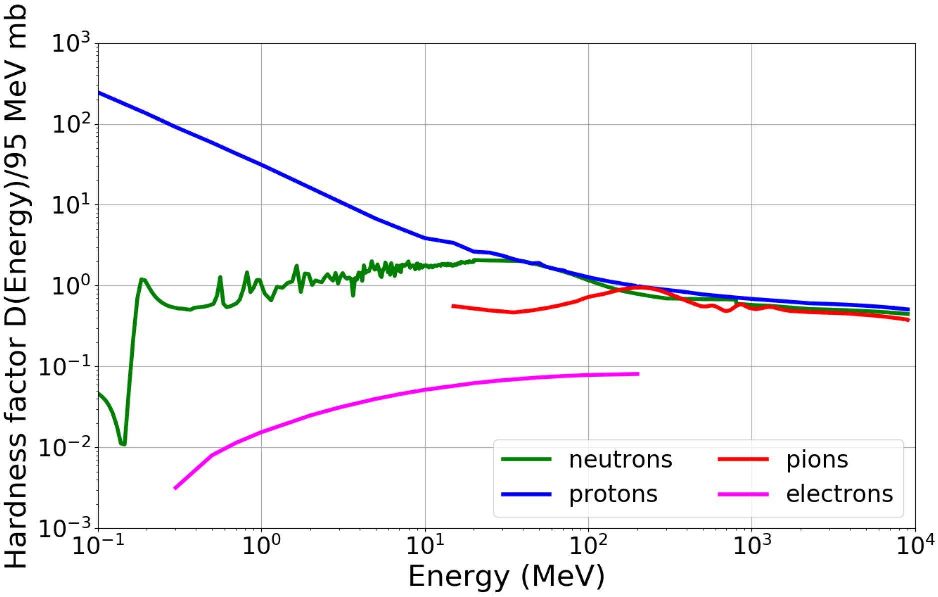

Figure 2.7: NIEL hardness factor for silicon as a function of the particle type and energy [40–44].

Fig. 2.7 depicts the hardness factors of several particles from 100 keV to 10 GeV as experimentally measured. The hardness factors for hadrons tend to overlap above 100 MeV. Below this energy, the proton NIEL grows, while the neutron NIEL is strongly impacted by the resonances in the nuclear cross-section.

Typically, protons are used for DD testing of space electronics. In accelerator protons, neutrons and mixed-fields are used, although it is worth noting that while the NIEL scaling works very well for silicon, it does not work that well for other materials, such as GaAs [45].

Displacement damage becomes important at rather high fluences. One big drawback coming from the use of protons and neutrons for testing purposes is that they cause strong activation of the material. This raises potential issues related to radiation exposure safety that typically do not allow accessing the irradiated material upon testing.

Note that electrons can also cause displacement damage. At 200 MeV they are about 12 times less damaging than 1 MeV neutrons. Differently from protons and neutrons, electron-induced activation is very low and does not pose a hazard to human beings. Therefore, provided a facility capable of delivering very high high-energy electron fluxes is available, it would be possible to perform displacement damage testing with electrons. The main drawback with the use of electrons for DD testing is that, despite depositing 12 times less TNID, they deposit as much TID as protons. Therefore, TID effects may prevent from accomplishing a DD test. Charging of device/package can also be a significant issue for some parts.

Naming	Body	Title
ECSS-E-ST-10-12C	European Cooperation for Space Standardization (ECSS)	Space engineering: method for the calculation of radiation received and its effects, and a policy for design margins
ECSS-E-HB-10-12A	European Cooperation for Space Standardization (ECSS)	Space engineering: calculation of radiation received and its effects and margin policy handbook
ECSS-Q-ST-60-15C	European Cooperation for Space Standardization (ECSS)	Radiation hardness assurance - EEE components
MIL-HDBK-814	US Department of Defence	Ionising dose and neutron hardness assurance guidelines for microcircuits and semiconductor devices
IEC 62396	International Electromechanical Commission (IEC)	Process management for avionics - atmospheric radiation effects
ISO 26262	International Organization for Standardization (ISO)	Road Vehicles - Functional Safety

Table 2.1: Summary of standards for radiation hardness assurance of electronics to be used in space, avionics and ground.

In terms of macroscopic effects on electronics, DD is responsible for the generation of defects in the conduction band of the semiconductor that can enhance the occupation (acceptor defects) or the release (donor defects) of electrons. As a consequence, the electronic device may suffer leakage current (called dark current in image sensors) or even give rise to intermittent effects (such as the random telegraph signal or intermittent stuck bits).

2.3 Standards for radiation testing and hardness assurance

Radiation testing standards for the qualification of electronic components are typically provided by certification institutions, military or space agencies and sometimes even by manufacturers consortia. Performing radiation characterization following the standards provides the system designer/developer with the means to demonstrate that the final system has been qualified following rigorous quality assurance procedures. These procedures can be more generally referred to as radiation hardness assurance. Table 2.1 reports a few documents relevant for space, avionics and ground, which reports the best practices required to accomplish RHA of an electronic equipment.

While these standards have to be used in order to tailor an RHA process relevant for the final application (such as radiation design margins or worst case analysis), radiation effect testing is described in other standards. At the time of the writing of this thesis, only component-level standards are available. It is indeed objectively complicated to develop quality assurance standards for systems with respect to radiation verification without relying on a bottom-up approach. Nevertheless, there have been some efforts within the radiation community to provide some first guidelines about board- and system-level radiation verification schemes. A guideline for system-level testing of space systems was tailored and published by the author of this thesis [46, 47].

2.3.1 Component-level test standards

These test standards have the purpose of providing a traceable procedure concerning the screening and qualification of components for various environment (most typically space and avionics), although they are also directly used for other applications (e.g., accelerator, nuclear power plants, etc.).

Table 2.2 presents some of these standards with a subdivision based on the type of radiation effect. There are currently several test standards for SEE testing. This is mainly due to the fact that the requirements and the guidelines to perform SEE tests vary depending on

Naming	**Body**	**Title**
Single-event effects		
ESCC 25100	European Space Component Coordination (ESCC)	Single event effects test methods and guidelines
MIL-STD-750 Method 1080	US Department of Defence	Single event burnout and single event gate rupture tests
EIA-JESD57	Electronic Industries Alliance (EIA) JEDEC	Test procedures for the measurement of single-event effects in semiconductor devices from heavy ion irradiation
EIA-JESD89A	Electronic Industries Alliance (EIA) JEDEC	Measurement and reporting of alpha particle and terrestrial cosmic ray-induced soft errors in semiconductor devices
EIA-JESD234	Electronic Industries Alliance (EIA) JEDEC	Test standard for the measurement of proton radiation single event effects in electronic devices
Total-ionizing dose		
ESCC 22900	European Space Component Coordination (ESCC)	Total dose steady-state irradiation test method
MIL-STD-883 Method 1019.10	US Department of Defence	Steady-state total dose irradiation procedure
Displacement damage		
ESCC 22500	European Space Component Coordination (ESCC)	Guidelines for displacement damage irradiation testing

Table 2.2: Summary of standards for radiation effects testing of components.

the radiation particles that are used. Fewer test standards are available for TID and TNID damage. A first reason is that these effects are only pertinent in harsh radiation environments. In addition, displacement damage is very application specific and concerns a smaller set of devices.

2.3.2 Most common shortcomings

Standards for TID are typically applicable to highly-integrated and advanced packaging technologies. This is because they typically rely on the use of deep penetrating radiation fields (e.g., γ-rays from ^{60}Co sources). Nevertheless, some very integrated solutions require preparing dedicated test benches in order to perform parametric drift measurements that can cover all of the device features. Similarly, TNID testing can follow on the standard also for these highly integrated devices.

More important shortcomings appear in SEE testing with heavy ions. The main issues with ions are related to their short range in matter. In order to cope with that there is need to use vacuum chambers (when the ion energy is below 10 MeV/n) and the removal of the package of the device so that the ion has direct access to the die. The package removal is performed with expensive and intrusive techniques (either by a chemical or a mechanical processes) that may actually end up damaging the device (typical acids used to remove the package will destroy copper bonding wires). Moreover, advanced packaging solutions often rely on the stacking of several dies one on top of the other, or even on the integration of several discrete devices within the same package (in 2D or 3D layouts). In such conditions, it becomes almost impossible to render all the sensitive areas of the component accessible to a standard energy heavy ion beam.

It is still possible sometimes to overcome these issues by testing with high-energy heavy ions. Fig. 2.8 depicts the properties of several ions available in facilities worldwide as a function of their energy. Typically, SEE testing with heavy ions for RHA is achieved by means of high LET ions. These ions often have insufficient range in matter to penetrate through the package and/or through various layers of sensitive material without suffering from fragmentation and beam intensity degradation.

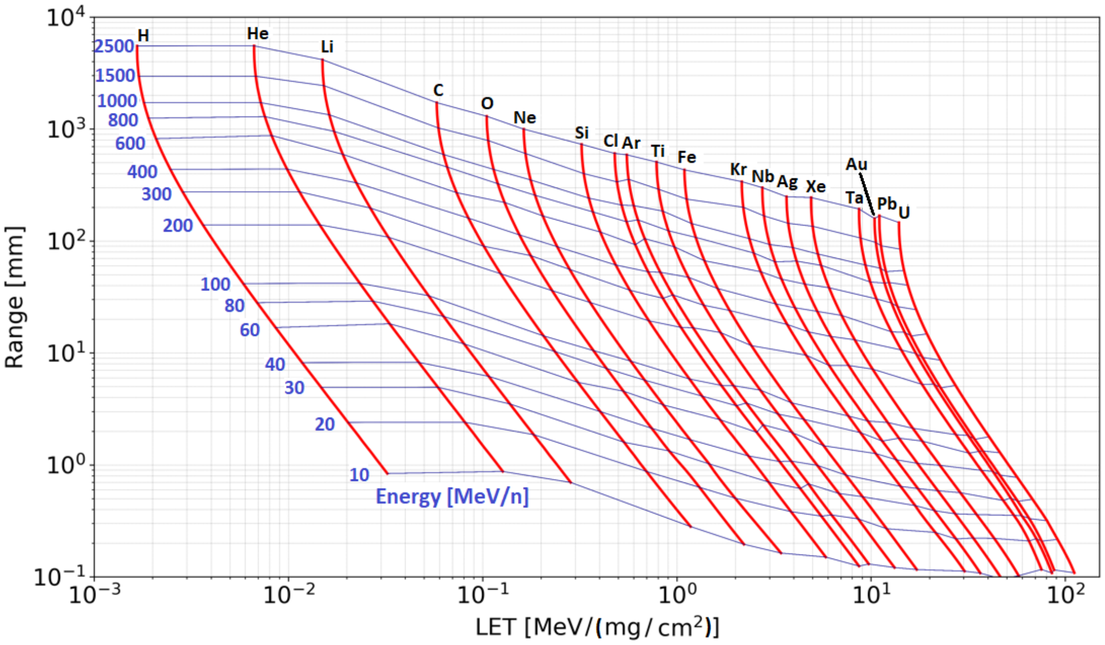

Figure 2.8: LET and range in silicon of ions as a function of the primary energy as obtained from SRIM [48]. Most radiation facilities only cover a fraction of the state-space. Reprinted from [47]. © 2021, Coronetti et al., licensed under CC BY 4.0.

There are only a few ions with range of 1 mm and LET $\geq$ 10 MeV/(mg/cm^2). Most of these ions are available at the NSRL facility [49]. Ions of similar or even higher energy are also available at CERN [50–52]. The use of these ions can overcome most of the limitations related to beam penetration.

Nevertheless, high-energy ion facilities are characterized by other drawbacks. For instance, NSRL has an access cost which is almost 10 times higher than that of standard energy ion facilities. Other facilities, such as CERN and GSI are currently available only for short periods of time and can only provide access for scientific purposes (although CERN will soon move to industrial access). Hence, the main drawback of high-energy heavy ions is that they are quite unusual.

The other big hindrance of an RHA process based on extensive component-level testing is the related costs associated with the test bench developments and beam time access costs, which can span in the 25-600 k\$/device range depending on the device complexity [53]. In addition, performing the whole range of test required by the RHA standards may take a lot of time due not only to the test bench development and verification, but also to the rather saturated beam time availability at the various facilities, which can spread over several months the accomplishment of all the necessary tests to qualify the part.

Both the cost and time constraints may be incompatible with the typical product life-cycles of certain space systems (low-budgeted and with time pressure due to the requirement of meeting launch opportunities). That is why, in many cases, both private manufacturers and public agencies rely on leaner verification schemes that are not aimed at verifying the resilience of a single device to radiation, but of a wider set of components all within the same radiation test. This kind of test scheme is already largely (if not systematically) employed by system developers for ground and accelerator applications.

Finally, testing highly integrated devices embedding several different functionalities (e.g., FPGAs, μPs, etc.) comes with several additional challenges [54, 55].

2.3.3 Guidelines for board- and system-level testing

Although this may look as a recent subject for space applications, board- and system-level radiation testing and connected RHA methodologies (such as the MEAL approach [56] provided by NASA) have been investigated for more than two decades [57, 58]. Most of these efforts relied on the use of protons for irradiating commercial electronic boards, with very limited insight either in heavy ion induced SEEs or in the impact of cumulative effects. The lessons learnt have been summarized in a guideline for proton board-level testing [59, 60] whose main application are the non-critical systems of the ISS.

Nevertheless, board- and system-level testing remain quite immature practices and more work will be needed before a standard would be distilled. These schemes are often lacking enough requirements traceability and environment representativeness to be considered as qualification schemes, inasmuch as that the term qualification can hardly find rigorous usage and terms like verification or screening are preferred.

One of the key points developed in the system-level radiation testing guideline [47] is indeed that these test schemes are not meant at replacing more standard approaches based on component-level radiation testing. Rather, they are targeted towards space missions for which no degree of radiation verification is implemented, although there would be a benefit from accomplishing such kind of verification.

Currently, there have been some efforts in that respect, mainly enabled by the CHARM mixed-field facility [12] (designed with system-level testing needs in mind), from several entities [61–64]. However, system-level testing employing high-energy heavy ions has also been studied [65].

Sometimes, both the concept of system and system-level testing are evanescent. For instance, one can also consider system-level testing the irradiation of a single device that is operating within a system rather than the irradiation of the whole assembly of devices. This opens the door to also heavy ion testing at standard energy as well as laser testing [66].

System-level radiation testing is a more consolidated practice for other radiation environments. In the accelerator environment it has a dual use. It is either used in complement to component-level characterization for the validation and approval of installation of equipment within the LHC and its injection chain or it is used as a stand-alone for the qualification of fully commercial systems used in less critical radiation areas.

Even at the level of the accelerator there is not a standard for preparation and execution of system-level testing, but rather system-level testing is considered only for its role in the general RHA process [67, 68].

This is also true for system-level testing applied in avionics and ground applications, for which this test methodology is widely applied, but, due to competitive advantages, the actual system-level testing practices are kept confidential.

The reason why system-level testing will not be extensively covered in this thesis is because the physics of failures of systems, in terms of particle-matter interaction, is actually the physics of failure of its single devices placed in the wider system operating context.

The related work in this thesis will thus be focused on the representativeness of using HEHs as a proxy to HIs for SEE coverage.

2.4 Literature review

This section provides literature background concerning the main subjects developed throughout this thesis.

2.4.1 Upsets from low-energy protons

SEUs from LEPs and their impact in the space environment, for which the LEP fluxes are considerable, have been a matter of investigation for about 15 years. 65 nm SOI SRAMs [69, 70] were first observed to be highly sensitive to direct ionization from LEPs. The main characteristic of LEP cross-sections is that they are 3-4 orders of magnitude higher than those of high-energy protons (actually the highest measured enhancement was of 6 orders of magnitude for a 90 nm SRAM [71]). The main mechanism involved at these low energies is direct ionization (as opposed to indirect ionization). Therefore, LEP cross-sections are expected to be in the same ballpark as those from light ions having LET < 0.55 MeV/(mg/cm^2). First findings [72] suggested that modelling the LEP response upon the light ion response was a viable worst case approach.

The data collection approach by which LEP cross-section data are collected has often been put into question as well. The data in the first papers were typically obtained by degrading a high-energy beam down to very low energies in air [73] (high-energy protons do not need vacuum, so HEP facilities are typically not equipped with the required apparatus to operate the DUT in vacuum). However, this procedure introduces several uncertainties on the actual energy of the protons reaching the device and, to be even more precise, its SV. Protons obtained from degradation would have quite an energy spread and would suffer from straggling [74] (i.e., at very low energy the trajectory of protons in matter can be more easily deviated, affecting their chance of penetrating down to the SV). When digital-to-physical maps of the device were available, the use of a variable thickness degrader was also considered [75], though this approach may introduce some further uncertainties on the amount of bits involved.

Two main techniques were developed in order to standardize the collection of LEP cross-sections. One is based on pure proton acceleration and the other is based on a more controlled HEP degradation.

In the first case, the accelerator (typically a LINAC or a cyclotron) is set to accelerate the protons to a well resolved energy (although obtaining mono-energetic protons remains quite a challenge given that, for a normally distributed proton beam, the 2σ energy deviation can rarely be reduced below 100 keV and this can have much more influence on the data collected at energies ≤ 1 MeV than it can at 10 MeV or higher energy). The upset rate due to LEPs is then determined by convolving the LEP cross-sections collected at various energies with the space proton flux of the orbit of interest. Using the energy convolution can provide more reliable upset rate predictions whenever the device critical charge is rather low (not so sharp fall-down of the cross-section at $E > 1$ MeV) as opposed to the simple multiplication of the peak cross-section for the LEP fluxes [76].

In the second case, a careful study [21] of the HEP degradation from quite high-energy (≈ 70 MeV) has shown that the proton spectrum obtained after degradation (and accounting for straggling) is very similar in the 0-3 MeV energy range to that found in the space environment after transportation through spacecraft shielding (see Fig. 2.9 (a)).

Therefore, a method to determine the expected LEP upset rate in space that exploits this strong beam degradation was developed. The method requires measuring SEU cross-sections from an increasingly degraded beam (which is described by the average proton energy of the so-obtained proton spectrum) until no more events are observed (no protons reaching the DUT SV anymore) and to repeat this procedure for several angles of incidence. A peak cross-section (see Fig. 2.9 (b)) can be identified from these measurements for each angle of incidence. It is then assumed that all the upsets measured by these degraded beams are fully due to the 0-3 MeV energy component of the beam. This part of the resulting proton spectrum typically represents only 13% of the total beam at the LEP cross-section peak average energy. Therefore, this value can be used to correct the proton fluence measured by the facility instrumentation and the peak SEU cross-section can be recalculated to account

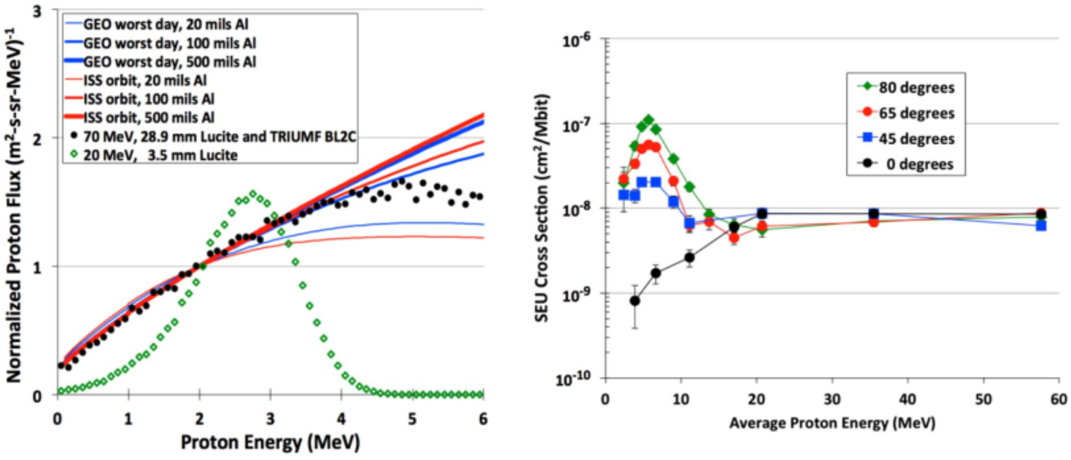

(a)

(b)

Figure 2.9: (a) Comparison of the energy spectrum of degraded 20 and 70 MeV proton beams with the proton spectra obtained for a few space orbits after shielding. (b) Example of the type of measurements obtained by means of this method for a 65 nm SOI SRAM. Reprinted with permission from [21]. © 2014, IEEE.

for the actual 0-3 MeV proton fluence. Finally, an isotropic SEU cross-section is determined (given that the space proton fluxes are isotropic). This is obtained by summing up the contributions of each SEU cross-section measured at different angles of incidence by accouning for the covered solid angle associated with each angle of incidence. Once the isotropic cross-section is obtained it suffices to multiply it by the integral of the 0-3 MeV proton fluxes in space to obtain the predicted upset rate.

This study was later complemented by widening the range of technologies under analysis, including 20-90 nm logic and memory devices (with also some core voltage dependency) [77]. The main findings of this study revealed that LEPs are expected to be an important contributor to the upset rate in space (they can be expected to contribute for up to 70% to the total upset rate, including also HEP and HI contributions). Hence, it is concluded that if no LEP tests were accomplished (either through mono-energetic or degraded beams), a safety margin of 5 on the upset rate calculated after the HEP and HI upset rates could be applied to account for the untested LEP response.

The good agreement between the two methods was further demonstrated [78] and both are considered equally valuable in the space standard for SEE testing [79].

An analytical method [80] has been proposed for the modelling of the LEP cross-section and the calculation of the upset rate having as a starting point the data retrieved in experiments. The model aims at determining the size of the RPP based on the critical energy E_c required to trigger an SEU and it takes into account the possible angular variation of the LEP sensitivity.

Similarly to the LET for ions, the analytical model implies that only protons with an initial energy $E > E_c$ can trigger an SEU, which is reasonable and equivalent to the standard RPP model. This reasoning is also at the basis of the CUPID model [paper not yet published]. CUPID makes use of the LEP experimental data to further calculate RPP size, thickness and critical charge. The assumption that protons will deposit their entire primary energy in the SV remains a bit questionable. This process typically yields very deep SV (> 5 μm thickness) which are much thicker than what it is typically assumed for SEUs in highly-integrated devices and quite high critical charges (≈ 10 fC) that are incompatible with those of memory devices with technological node below 90 nm (< 1 fC) [81].

Other than direct ionization, some other complementary studies have been performed to study the effect of elastic scattering in low- (0-3 MeV) and intermediate-energy (3-20 MeV) proton cross-sections. These kinds of studies rely on numerical simulations which is the only tool allowing separation of the contributions to the total SEU cross-section of the various physical processes that are present in experiments. The most complete studies [82, 83] showed that the peak LEP cross-section is fully established by direct ionization. Nuclear elastic scattering is typically as important as nuclear inelastic scattering at 6-10 MeV and it can still provide a minor contribution up to 20 MeV. The importance of recoil ions from elastic and inelastic scattering for both SBUs and MCUs was later further strengthened [84].

The literature also provides challenges to the assumption that the LEP response can be assumed to be equal to that of light low-LET ions. The total upset LEP cross-section may indeed be higher than that of ions [85]. This is mainly due to the fact that while LEPs and light ions induce SBUs in similar numbers, LEPs are capable of triggering many more MCUs (double-bit upsets and higher multiplicity) than light ions. Given the longer range, at the same time, low-LET ions may also cause SEUs by indirect ionization and this may also be a cause of divergence.

Process variation down to intra-die variations among the single SRAM cells was shown to affect the device cross-section response due to low-LET particles (e.g., low-energy protons, alphas and low-LET light ions) [86, 87]. This can come into play when there is need to calculate the upset of the whole SRAM. It is observed that typically SRAM cells may exhibit non-uniform retention voltage distributions either Gaussian [88, 89] or skewed towards lower retention voltage than the average of the whole SRAM [90]. The cell retention voltage V_{DR} connects to the individual sensitivity of the SRAM cells given that it can be directly linked to the critical charge Q_c and, hence, to the LET_0 of the cell:

$$Q_c = aC(V_{DD} - V_{DR}) \tag{2.7}$$

As a result, experimental data of LEP cross-sections (and similarly low-LET ions) are affected by the fact that some cells (those with lower Q_c) are more likely to upset than others, inasmuch as that, in the same die, there may be cells which are not sensitive to LEP-induced upsets. Standard upset rate calculation methods do consider that the memory cells are all identical and that the measured cross-section can be taken as the response of each cell. Hence, the experimentally measured cross-section is applied indiscriminately to all cells.

For upset rate predictions one shall also consider that spacecraft shielding [91, 92] can have a very strong impact on LEP fluxes and, consequently, on the upset rate itself. The typical approach is to use isotropic fluxes with a fixed spherical shielding of aluminum. However, the LEP upset rate can be severely affected by the actual geometry of a satellite, hence ray tracing techniques are recommended as a way to determine the actual anisotropic fluxes at the device location in the spacecraft. While this would be useful for a known satellite, it is not possible to generalize as much when the spacecraft layout data are not available. So, the standard approach based on spherical shielding is retained for the analyses in this thesis.

It is noted that LEPs are not of concern only for the space environment, but also for the accelerator environment [93]. Upset rates in memories very sensitive to LEPs are expected to play an important role in spite of the quite dominating contributions of upsets from neutrons of thermal, intermediate- and high-energy.

2.4.2 Pion single-event effects

A very rich literature exists for high-energy proton and neutron single-event effects in electronics. High-energy pions, on the other hand, have, for a long time, been the forgotten little brother (pion mass is much lower than that of the other more common hadrons, ≈ 139 MeV/c^2 vs. ≈ 938 MeV/c^2) of the HEH family. Consequently, the literature on mono-energetic pion experiments and consequences for the SEE rates in state-of-the-art electronics was very limited prior to the papers produced for this thesis.

The only two works available in the literature from the last two decades are dedicated two SEUs in SRAMs and DRAMs [94, 95]. The experimental data from these two works are also rather contrasting. In one of the works [94], the pion SEU cross-section is seen to be even three times higher than that of proton, whereas, in the other work [95], no enhancement or even lower pion SEU cross-sections are found. As a result, it is not so evident to understand whether the pion SEE cross-section would be different from that of protons in more integrated devices and if that would have consequences on the HEH equivalence approximation [6].

2.4.3 High-energy hadron testing for space systems

Use of HEH testing for space devices may be applicable to high risk acceptance mission categories Q1 and Q2 based on COTS devices (see ESA COTS initiative review [96]).

Monte-Carlo simulations have often been used to either confirm or disprove the possibility of using high-energy hadrons (protons, neutrons, mixed-fields) for bounding the space SEE rate. On the one hand, this experimental approach is typically successful for SEUs [47, 97–100]. This is mainly due to the very low collected charge that is needed to cause an SEU in highly integrated electronics. On the other hand, this approach usually fails for destructive SEEs [101, 102] due to the fact that the collected charge needed to trigger such mechanisms are much higher and usually not attained from secondary ions of HEH elastic and inelastic reactions with silicon nuclei.

Moreover, HEHs are very ineffective at producing ions (low nuclear cross-sections, only one in a few 10^5 HEHs may interact with a nucleus), but, at the same time, each single proton will deposit ionizing dose into the device. A good balance between these two characteristics of the physics of particle-matter interaction is often hard to find. However, neutrons have lower TID yield than charged hadrons when considering the same amount of secondary ions released.

The HEH equivalence approximation that is valid in the accelerator mixed-field environment can also enable the use of high-energy neutrons (mono-energetic or spallation) or mixed-field themselves as a proxy to mono-energetic protons. Good agreement between mono-energetic protons, spallation neutrons, the CHARM mixed-field and the space in-orbit measurements was demonstrated through experimental analysis [17, 103].

Chapter 3

Physics of radiation effects and modelling

3.1 Particle-matter interaction mechanisms

As initially mentioned in Section 2.2, radiation effects in electronics originate from the interaction of at least one particle with the semiconductor material. These effects are either stochastic or they appear gradually after a significant fluence of particles has been delivered to the device. In this chapter the main focus is on particle-matter interactions responsible for SEEs.

All interactions occur through ionization of the semiconductor material, i.e., generation of electron-hole pairs (that may in part recombine soon after they are generated). The ionization source can either be the primary particle itself (direct ionization) or a secondary particle (indirect ionization) generated by interaction of the primary particle with the nucleus of an atom in the semiconductor lattice.

3.1.1 Direct ionization

Every charged particle can deposit energy by direct ionization. While any tiny amount of deposited energy contributes to the global damage for cumulative effects of radiation, not all charged particles can deposit enough energy to trigger SEE mechanisms. This is because there is a threshold energy/charge (called critical energy/charge) that it is necessary to deposit to trigger an SEE. This is the reason why, for older technologies, weakly ionizing particles could not trigger any SEE by direct ionization. However, this is no longer the case in very deep sub-micron technologies.

The LET (eq. 2.2) is a metric of the energy deposition mechanism from direct ionization that accounts for the average number of electron-hole pairs generated by a particle per unit length of its trajectory. The LET is typically a suitable metric for particles having a long range, but not as much for particles stopping in the SV or in its proximity. This is due to the fact that the LET varies while the particles is slowing down. Therefore, there may be some uncertainties related to the actual amount of energy deposited along the particle trajectory.

3.1.2 Indirect ionization

In indirect ionization, the energy deposition due to the secondary particles proceeds in the same fashion as for direct ionization. However, the generation of these secondary particles can happen through many different interaction mechanisms. These mechanisms are:

- Coulomb elastic scattering
- Nuclear elastic scattering

- Nuclear inelastic scattering
- Nuclear absorption/capture
- Fission
- Electro-nuclear scattering
- Photo-nuclear scattering
- Compton scattering

Not all the mechanisms are applicable to all the particles. For the matter of this thesis, the only relevant interaction channels are those of hadrons with light nuclei, i.e., elastic and inelastic scattering and nuclear absorption and fission.

All the particle-nuclear interaction mechanisms are stochastic, i.e., there is a certain probability that a particle will interact with a nucleus through one of these processes. This probability is called cross-section (most commonly expressed in mb) and can strongly change with the primary particle type and energy as well as the target material.

For nuclear reaction mechanisms (nuclear inelastic scattering and absorption) the release of secondary ions follows a complex process. The final secondary particles (or nuclear recoils) are released after certain additional nuclear process steps are completed, such as intra-nuclear cascade, exciton pre-equilibrium, coalescence and evaporation. Note that all these processes occur within a very small fraction of a second. The superposition of all these mechanisms can lead to the generation of a whole bunch of secondary particles that may differ in atomic mass and number, kinetic energy, angle of deflection/emission.

Elastic scattering

Whether through electro-magnetic or nuclear interaction, elastic scattering results in a pure momentum exchange between the primary particle and the nucleus. In the case of Coulomb scattering (for charged particles only) this occurs because the primary particle and the nucleus exchange momentum through the Coulomb force. In the case of nuclear scattering (for all hadrons) the primary particle and the nucleus exchange momentum by collision. After having acquired a certain kinetic energy the nucleus of the atom is set in motion and can deposit small amounts of energy in the surrounding semiconductor atoms. Such energy deposition events can yield SEUs, but are typically insufficient to trigger other SEEs.

Elastic scattering cross-sections in common semiconductor materials, i.e., silicon, vary with respect to the type and energy of the primary particle. Ions produced from elastic scattering are typically not as ionizing as ions produced by inelastic scattering and nuclear absorption.

The effect on a device SEU cross-section is typically significant for intermediate energy protons (2-20 MeV, see Fig. 3.1) and low- and intermediate-energy neutrons (0.1-20 MeV), i.e., whenever the other mechanisms of nuclear interactions have a very low cross-section and direct ionization is negligible.

Inelastic scattering

Inelastic scattering is a much more complicated mechanism that, as said, involves several more physical processes, which can give rise to a wide variety of secondary particles. In contrast to elastic scattering, the number of reaction products following inelastic scattering can vary a lot depending on the level of fragmentation attained. For instance, the interaction of a high-energy proton/neutron with silicon can result in the release of a combination of protons, neutrons, pions, alpha particles and light ions of very variable kinetic energy and scattering deflections.

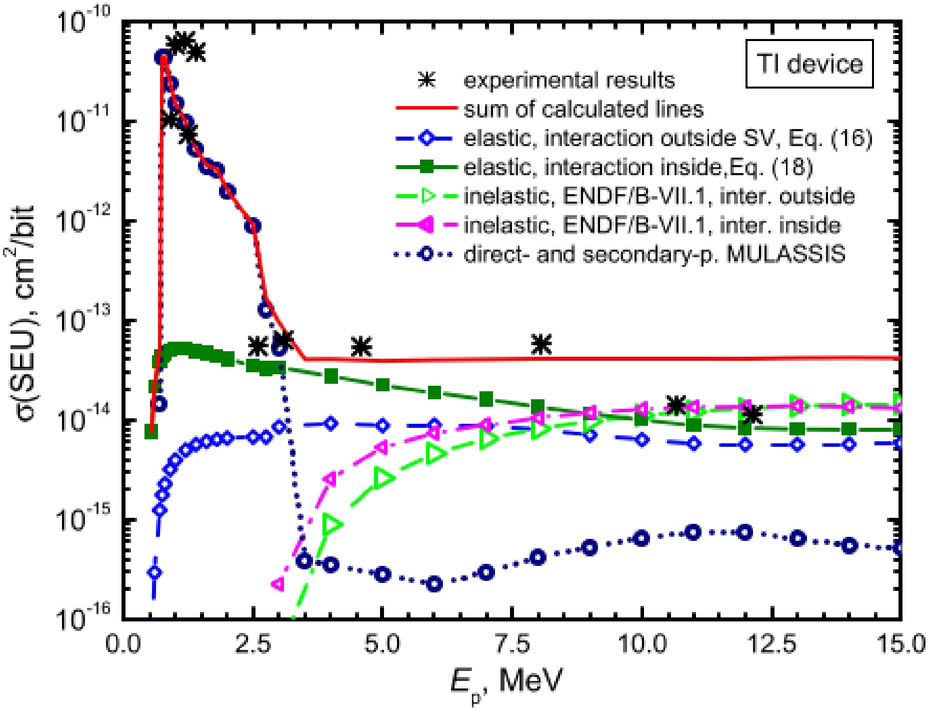

Figure 3.1: Contributions of various energy deposition mechanisms to the total proton cross-section when varying the energy of the primary proton. Reprinted with permission from [82]. © 2017, IEEE.

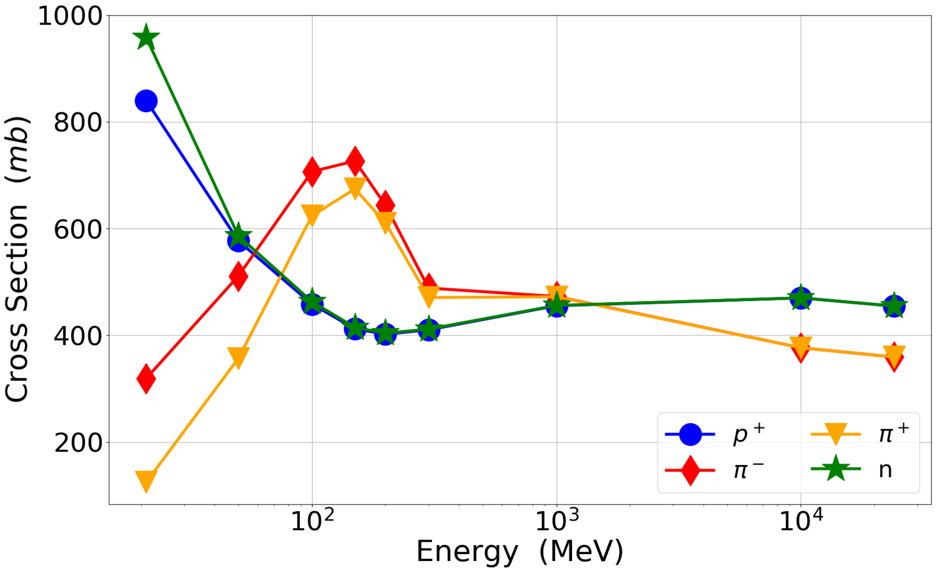

Figure 3.2: Total nuclear reaction (inelastic scattering + nuclear absorption) cross-section of protons, neutrons, positive and negative pions as a function of energy. Extracted from the FLUKA output [2, 3]. Reprinted from [14]. © 2020, Coronetti et al., licensed under CC BY 4.0.

The inelastic scattering cross-section can also vary a lot with the particle type and energy. Fig. 3.2 depicts this variability in protons, neutrons and charged pions. Note that for pions it is better to talk about total nuclear reaction cross-section (given that it is given by the sum of the inelastic scattering and nuclear absorption cross-sections). The two mechanisms are typically not separated because they trigger similar physical processes when it comes to the formation of nuclear recoils.

It is noted that protons and neutrons have nearly identical total nuclear cross-sections for the whole energy range, with just a slight divergence at about 20 MeV. This is one of the reason why protons and neutrons have nearly identical SEE cross-sections above 20 MeV.

On the other hand, pions are assumed to yield a similar SEE cross-section than protons and neutrons. However, their total nuclear reaction cross-sections differ quite some from those of protons and neutrons. The 75-250 MeV energy region for which the pion nuclear cross-section is nearly a factor of 2 higher is due to the $\Delta(1232)$ resonance [104], which is generated through the primary reaction channel of pions with nuclei.

It is also noted that the pion nuclear reaction cross-section falls off very sharply below 50 MeV, so that it can be a factor of 3 lower than that of protons for negative pions and a factor of 7 lower for positive pions at 20 MeV. The difference between positive and negative pions, which appears below 200 MeV, and becomes more and more evident down to 20 MeV is fully due to the different nuclear absorption cross-section. Due to their negative charge, negative pions stands a higher chance of being absorbed in the nucleus than positive pions.

Nuclear absorption

Nuclear absorption is a nuclear reaction mechanism that differ from inelastic scattering. It occurs for light hadrons (and sometimes for leptons), such as pions, and it is more likely for negatively charged hadrons. As a consequence of absorption, the pion gives up its rest mass (139 MeV/c^2) which contributes to the excitation of the nucleus. The strong de-excitation that follows can cause the fragmentation of the nucleus in several secondary reaction products. From that moment on, the reaction proceeds as for an inelastic scattering reaction. However, since the pion rest mass is converted into kinetic energy available to the secondary particles, these can have higher kinetic energy than those released by the simple hadron-nucleus inelastic scattering.

Given the similarities in the follow-up reaction product emission, the nuclear absorption cross-section is often assimilated within the inelastic scattering cross-section, as shown in Fig. 3.2. Measurements of true pion absorption cross-sections are available in the literature [105]. These data show that absorption can contribute to the total nuclear reaction cross-section for up to 50% and 70% for positive and negative pions, respectively.

3.2 Full transport Monte-Carlo

Primary and secondary particles have to be transported within a medium (the semiconductor and its surroundings) until either their kinetic energy is fully spent into the generation of electron-hole pairs or they leave the medium.

The radiation transport problem can be expressed analytically as the variation of the density of particles in terms of their type and their kinetic energy. However, the radiation transport equation is a multi-dimensional integral equation that does not have a closed solution, if not for very simple cases (e.g., simple geometry with a reduced list of interaction models). Numerical methods have been developed to solve it.

The full transport Monte-Carlo is one of these methods. It has several advantages over analytical and numerical solution methods. It can indeed treat very arbitrary radiation fields in basically any geometry, while remaining efficient in terms of CPU time.

Similarly to the physical processes at play, the Monte-Carlo method is stochastic, i.e., it simulates particle histories defined by known interaction cross-sections, while keeping track of their influence by means of statistical estimators. These particle histories are sampled randomly by pseudo-number generators. Each history is advanced and each interaction with a material releasing a secondary particle is tracked. Secondary particles are then added to the stack of particles whose histories will be explored. In most of the cases, these secondary particles are electrons generated by direct ionization, however, based on the cross-sections, a certain number of nuclear recoils can also be generated.

The convergence of the Monte-Carlo method is ensured by the central limit theorem, in that, if there is a sufficiently large number of contributors to the statistical estimator, then the distribution will tend to have a gaussian shape centred at the expected value.

This convergence is achieved by both simulating a sufficiently large amount of primary particles and by repeating the simulations N times. Note that even when the number of particles is large enough, the statistical uncertainty of the simulation will be 100% if N is set to 1. Systematic uncertainties are strictly correlated to the physical models and the transport algorithm. Note that the uncertainty on the physical process cross-sections may have an impact on the result as well as an inaccurate knowledge of the material and geometry. The latter is the typical issue with commercial electronic devices for which geometrical and construction properties can only be retrieved by SEM analysis or destructive inspection.

Several codes exist for full transport Monte-Carlo and for some of them some specific applications for SEE testing in electronic devices have been developed. Among them there are FLUKA [2,3] and G4SEE [106] (Geant4 based [107]), which have been developed at CERN and were used in this thesis, and CREME MC [18,108], which was used during the work, but whose results are not included in the thesis. At the time of the writing of this thesis, one of the advantages of CREME is that nested sensitive volumes are directly handled, whereas for FLUKA and G4SEE this feature is not directly implemented.

3.2.1 Application to micro-electronics and SEE

Monte-Carlo codes are very reliable when it comes to simulate the small structures associated to state-of-the-art electronic devices. However, other than the geometry, there are other aspects that are important in order to build an efficient MC simulation with all the trimmings.

One of the main problems when it comes to finding the balance between efficiency and representativeness arises by the fact that generating and transporting all secondary particles, no matter their energy, will require a huge amount of computational time with little gain in terms of accuracy. This is particularly the case of photons, electrons and positrons which have a very low energy and whose contribution to the total deposited energy may be, in most of the cases, nearly negligible. To make the MC solver more efficient it is necessary to set thresholds for secondary particle generation and transport in terms of kinetic energy underneath which they will either not be generated or not be transported. The trade-off problem is more important for delta rays (secondary electrons), which are very important contributors to the energy deposition and whose thresholds should not be set too high. This can typically be verified by trial and error. Typical thresholds for generation and transport are in the order of 1-10 keV.

As earlier introduced, there are several physical mechanisms at play that can contribute to the energy deposition in the semiconductor material. Hence, it is necessary to ensure that all the physical processes are included through the relevant libraries. For indirect ionization, however, one has to deal with the fact that electromagnetic and nuclear cross-sections are quite low, inasmuch as only one primary particle in several hundreds of thousand will interact through one of these processes.

The SEE response of electronic devices to HEHs is, however, dominated by indirect ionization processes due to the fact that HEHs are very weakly-ionizing particles (and neutrons are not ionizing) that cannot yield energy deposition events comparable to those from the very few secondary ions that they can generate through nuclear interactions. Obtaining a statistically meaningful amount of these nuclear interactions for representativeness would require simulating an exponentially growing amount of primaries (of which most of them will remain of no use to indirect ionization processes). This problem is more efficiently handled by means of biasing.

The kind of biasing that is used in this case consists in forcing a fictitious increase of the elastic and inelastic scattering cross-sections by a factor of a few orders of magnitude so that given the same number of primaries 100-1000 times more particle histories than normal will yield to a Coulomb or nuclear interaction. Note that, while more of these histories are simulated, their global weight on the overall energy deposition distribution is accounted for by reducing the probability for that energy deposition event to happen.

3.2.2 FLUKA

FLUKA is the baseline Monte-Carlo code used for this thesis. It has been used for all the various studies. The FLUKA 'Precision' physics option already include all the physical processes of interest. So, if one wishes to isolate a single physical process (e.g., nuclear elastic or inelastic scattering), it is necessary to remove them by setting very high kinetic energy thresholds (typically 1 GeV is enough in most of the cases) for the generation energy of secondaries.

Nuclear interactions are treated with PEANUT, which embeds the intra-nuclear cascade models and the exciton pre-equilibrium. Coalescence and evaporation have to be explicitly requested, on the other hand. For the generation of secondary ions evaporation is a key process that, for light ions (A $<$ 18) (typical of silicon reaction product), is handled by the Fermi break-up model.

It is to be noted that energy deposition event scoring is handled by external routines. However, it was noted during the work performed for this thesis that the existent scoring routine do not work for Coulomb elastic scattering, i.e., the processes is simulated, but the resulting energy deposition events are not scored. This was compared against G4SEE and it is important in explaining the differences in the intermediate-energy proton response for the ISSI memory (see [109] at the end of this thesis).

Apart from this mishap (which has very marginal effects for the matter of this thesis), the current FLUKA SEE tool can be proficiently used for scoring energy deposition events related to SEU and SEL. It is possible to run both mono-energetic beams as well as spectra, such as those available at certain facilities (e.g., CHARM or ChipIr) or the space environment trapped protons, SPEs and GCRs. In addition, it is possible to simulate mono-directional (beams at facilities) or isotropic (space environment) fluxes. These features were fully exploited to predict the low-energy proton impact in space.

One additional potentiality of FLUKA is the possibility of running other simulations than full transport MC that are of specific interest for the simulation of nuclear interactions. This is achieved by the preex tool. Preex allows simulating nuclear interactions resulting from inelastic scattering and nuclear absorption again based on PEANUT, coalescence and evaporation models to extract reaction-by-reaction secondary product characteristics such as kinetic energy and scattering angle, that can be used to deduce also LET and range. The advantage of preex is that every primary is forced to interact with a silicon nucleus to generate secondaries. So, it provides a better overview on the generated secondaries. What preex does not do, is the transport of the particles, so it is not possible to obtain energy deposition. However, while this is not the purpose behind the use of preex, it was demonstrated that energy deposition can be partly recovered (see [110] at the end of this thesis).

3.2.3 G4SEE

The use of G4SEE [106] is not reflected in any of the papers at the end of this thesis, but will be nonetheless employed throughout this thesis. At the moment it has some limitations with respect to the FLUKA SEE tool, but it also provides coverage of some of the gray-black areas of FLUKA that were previously mentioned.

G4SEE requires explicit inclusion of the physics library of interest for each physical process and it actually has a larger set of libraries (elastic and inelastic scattering of different particles can be better handled by one or the other).

Intra-nuclear processes are handled by the Liege intra-nuclear cascade, whereas all other follow-up models are identical to those of FLUKA. Concerning photon and electron generation and transport thresholds, these are not expressed in terms of kinetic energy, but of range (which depends on the material, but whose link to the kinetic energy can be extracted from Geant4 itself).

The advantage of G4SEE over FLUKA, at the moment, is that it scores also energy deposition events from Coulomb elastic scattering. Finally, G4SEE can also be run with detailed scoring. This feature allows covering the same functionalities of preex, but, in addition, it enables the transport of secondary particles on an event-by-event basis and provides the related energy deposition in the selected SV.

3.3 Single-event effect modelling

Energy/charge deposition due to a primary particle interaction with the semiconductor material (by either direct or indirect ionization) is the first stage of an SEE. In order to trigger an SEE this deposited energy has to be collected into the transistor layout at a circuit level. This is the reason why electronic devices performing the same identical function can have very different SEE cross-sections. Indeed the transistor construction and local circuit characteristics (e.g., resistivity and capacitance) provide a strong discriminator on whether the energy/charge deposited will be sufficient to trigger the SEE. For some SEEs, this transition from energy/charge deposition to end effect requires in-depth knowledge of the characteristics of the transistor (which for commercial devices it is typically not possible to gather by means of any complementary analysis and may, thus, just rely on the use of standard values defined for similar technologies for which the process and construction of the transistors are known).

This level of analysis typically involves the use of TCAD solvers (used to determine the charge deposition spatial distribution and its time evolution) or circuit layout definition and simulation (e.g., SPICE) for which the collected charge is a transient acting within the circuit and propagating.

3.3.1 The single RPP model

For certain SEEs (such as SEU and SEL) this level of abstraction can be avoided in favour of a much simpler approach solely based on the energy deposition within a representative sensitive volume, the RPP, whose characteristics have to be determined. Single RPPs as those used in this work would look like volumes V2, V3 or V4 in Fig. 3.6, with charge collection efficiency of 100%.

Application to SEU

The circuital response is reduced to the definition of a single critical charge/energy that will reflect whether the transient injected in the circuit will have sufficient amplitude to propagate or to change the logic state of the transistor. For SEUs the critical charge can be determined by measurements of the retention voltage (see eq. (2.7)) or by determining the SEU LET threshold from ion irradiation:

$$Q_{crit} = \frac{E_{crit}}{22.5} = \frac{LET_0 \cdot \rho \cdot t}{22.5} \tag{3.1}$$

In this equation, 22.5 MeV/pC is the conversion factor between the energy deposited and the number of electron-hole pairs generated in silicon (3.6 eV will correspond to one electron-hole pair and one electron has a charge of 1.602 x 10^{-19} C). The concept of critical charge marks a sharp boundary between energy deposition events that will trigger an SEU and those that will not. This concept is explained through Fig. 3.3.

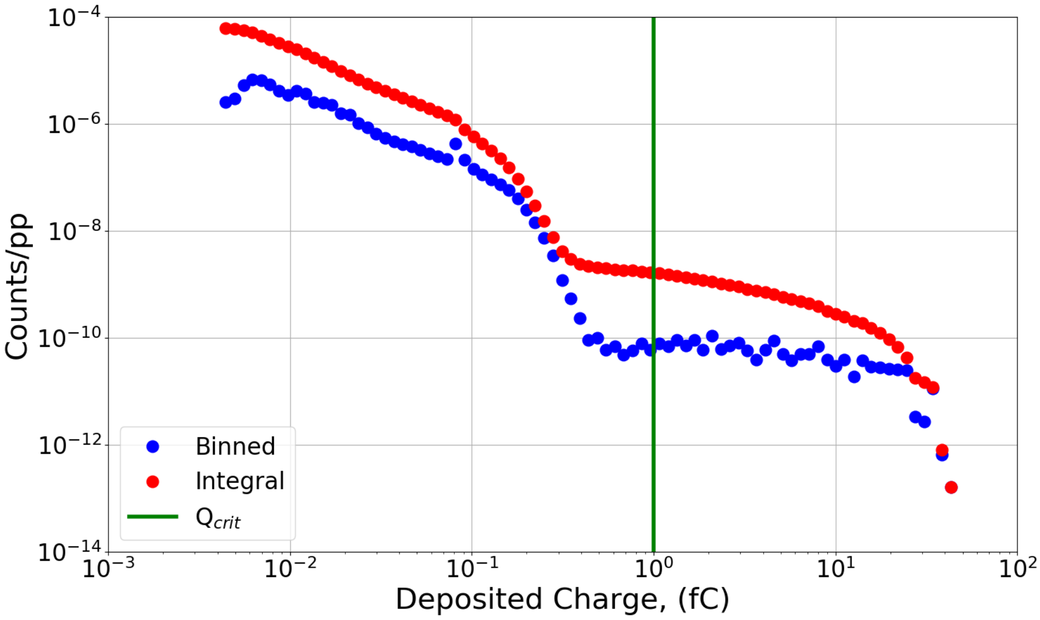

Figure 3.3: Binned and integral charge deposition distribution as a function of deposited charge for primary protons with energy of 200 MeV. Obtained with FLUKA for the ISSI SRAM model described in Chapter 5.

The figure shows the energy/charge deposition distribution for a mono-energetic 200 MeV proton beam. On the y-axis there is the number of energy deposition events of a certain energy/charge per primary proton (therefore, a probability). As it is clear from the figure, one of the strengths of the Monte-Carlo approach is that it allows assessing what would be the SEU cross-section depending on the selected critical charge.

In the figure, 1 fC is taken as reference Q_{crit}. This means that all charge deposition events for which the collected charge exceeds 1 fC will lead to an upset, whereas all events for which the collected charge will be below 1 fC will not be enough to trigger an SEU. This is why it is very convenient to perform the reverse integral of the probability in order to extract the cumulative SEU cross-section (which is obtained by normalizing the integral counts per primary particle with respect to the beam size in the simulation).

Note that the charge deposition distribution depends on the SV geometry as well and, hence, it is necessary to perform various simulations to retrieve the variability with respect to these parameters. On the other hand, once the SV geometry is established, a single simulation allows assessing how the SEE cross-section changes when the critical charge is varied.

The shape of the charge deposition distribution is also noteworthy. As earlier said, for HEHs (of which 200 MeV protons are an example) the SEU response is dominated by indirect ionization effects. This is quite obviously distinguishable in the figure given that it is easy to identify two regions. One below $\approx$ 0.3 fC and one above. Indirect ionization effects dominate the response above this critical charge and give rise to a sort of plateau for which the sensitivity of the cross-section with respect to the critical charge is very weak for a quite wide range.

Below $\approx$ 0.3 fC the counts sharply rise, and so will the cross-section. This is the region where direct ionization takes over and become the most dominant mechanism for the SEU cross-section. Even the most sensitive devices available nowadays do not have such a low critical charge for direct ionization effects from HEHs to affect the SEU cross-section. It is also noted that, for neutrons, the direct ionization mechanism does not exist. Thus, the indirect ionization component is the only contributor to the SEU cross-section, which does not increase much with respect to 1 fC no matter how low the critical charge is.

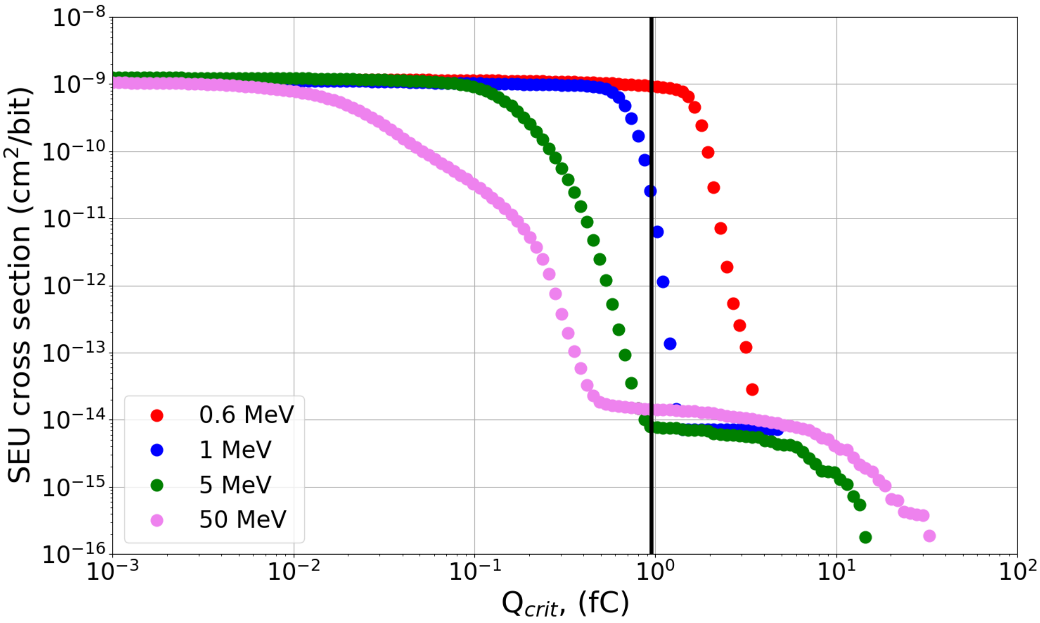

Figure 3.4: SEU cross-sections as a function of critical charge for primary protons of various energies. Obtained with G4SEE for the ISSI SRAM model described in Chapter 5.

Fig. 3.4 also shows how the situation changes when the energy of the primary protons is varied. A unique critical charge has to be chosen to describe the whole SEU response at any energy. The resulting SEU cross-section at 50 MeV is thus very similar to that for 200 MeV protons. However, when the proton energy is reduced (5 MeV) the inelastic scattering cross-section becomes lower and other processes, such as the elastic scattering, can become comparable and are also responsible for the energy deposition events at high Q_{crit}.

Note that all the curves at low critical charge tend asymptotically to the same maximum SEU cross-section. This corresponds to the physical size of the SV used in the simulation. Cross-sections can typically not be larger than the physical size of the SV of the cell (exceptions occur when particles, e.g., delta rays, outside the cell contribute to the charge collection inside the cell). Heavy ion cross-sections measured for memory devices cannot be larger than the physical size as well. However, experimentally measured cross-sections at high LET are typically larger. This is because those measurements are affected by MCUs (events that involve more than one cell, but that, in the absence of a logical-to-physical mapping, may end up being treated as individual single upsets).

However, what most notably changes with the decreasing proton energy is that the critical charge for which the direct ionization takes over increases. Hence, a device having the critical charge shown in the plot will be sensitive to direct ionization from protons at an energy of 1 MeV. If, on the other hand, the device had a Q_{crit} of 10 fC, the low-energy proton cross-section would be null and the device would suffer only from SEUs due to indirect ionization and only from primary proton energy $>$ 20 MeV. In the past, that proton SEU cross-sections of now outdated devices could indeed be expressed with a Weibull function [111] with a threshold energy for SEU (similarly to that of ions and which is still applicable to neutrons).

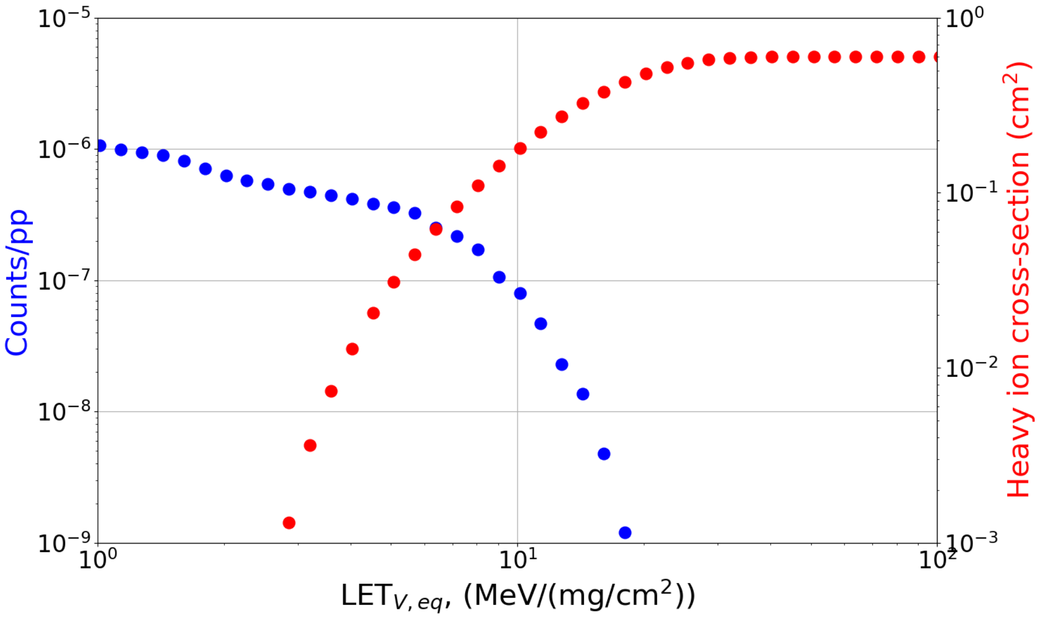

Figure 3.5: LET$_{V,eq}$ deposition distribution and Weibull heavy ion cross-section as a function of the LET$_{V,eq}$ threshold. Obtained from FLUKA. Weibull data from [15].

Application to SEL

The approach used for SEUs can also be seen as the convolution of the integral energy deposition distribution and a unitary step function which is 0 below the set critical charge and 1 above. This method is less effective when describing other SEEs, such as SEL. A device that is characterized by only the LET$_0$ and the heavy ion saturation cross-section can similarly be described with a step function when it comes to convolving the cross-section as a function of LET with the space ion fluxes. However, this provides very conservative estimations, as, in practice, the SEL cross-section above the LET$_0$ does not increase so sharply.

Concerning SEL predictions through MC, the knowledge of these two parameters may also yield overestimations in the HEH response. Getting a wider set of experimental data in order to fit a 4-parameter Weibull curve [111] can, on the other hand, provide more representative figures [112] (that are also at the basis of methods like PROFIT [113] or SIMPA [114], which are used to determine the proton cross-section from the heavy ion cross-section).

The energy deposition for the SEL mechanism can be obtained in a similar fashion (that relies almost entirely on MC simulations) as that for the SEU mechanism. For SELs it is definitely more practical to talk about LET threshold (or even volume equivalent LET threshold) than of critical charge. As shown in eq. (3.1), there is an almost immediate conversion between the two quantities, which requires the knowledge of the SV thickness. The latter can be determined experimentally by testing at various angles of incidence [115] or through laser testing.

Fig. 3.5 better depicts the situation. As said, the x-axis has been converted to LET$_{eq}$ from Q$_{crit}$ accounting for the thickness. The probability function was also normalized with respect to the beam size and the SV size in order to obtain an adimensional cross-section that is brought to the correct units of cm^2 when convolved with the heavy ion Weibull distribution. The LET threshold for the case under exam was 2.4 MeV/(mg/cm^2) and it should be rather straightforward to understand which would be the difference in the convolution if a step function starting at this LET$_0$ would be used instead.

Such an approach is useful to obtain the cross-section from MC simulations of every particle, i.e., both HEHs and HIs.

The other important difference between the SEU and the SEL treatment in MC simulations is the RPP geometry. Highly integrated devices are characterized by smaller and smaller transistor structures, which are reflected in smaller and smaller RPPs (smaller critical charge are also achieved, but they are more linked to the reduction in the core voltage). Therefore, it is common to see nanometric RPP structures for SEUs.

On the other hand, SEL is a mechanism that is specific of CMOS structures and it is triggered by the generation of a parasitic PNPN junction, whose contacts are the source contacts of PMOS and NMOS and the internal contacts of the p-well and n-well. So, it develops over a larger volume than SEUs and the resistance of the PNPN junction is higher when the distance between the contacts is higher, making the SEL easier to trigger. In the MC simulations with single RPP it is assumed that the whole volume has the same susceptibility with respect to SEL. However, in reality, the place where the energy is deposited matters as well. The resistance is higher (SEL more likely) if the energy deposition occurs far from the well contacts. So, in principle, the cross-section is affected by the location where the particle (primary or secondary) deposits the energy. However, this is somewhat lost in the single RPP model, but recovered when convolving the energy deposition with the heavy ion response.

Highly integrated technologies tend to be less sensitive to SEL, not only because of the reduced size, but also because of the lower core voltage. Anyway, for the memories under study (180 nm technology), the RPP side is still several micrometers large and wide and a few micrometers thick. In order to get these dimensions one can, for instance, rely on the use of laser probing [116–121], which consists in depositing energy by means of photons in highly localized areas. This allows retrieving information such as the RPP size and thickness, the LET_0 (by estimating the energy deposited by the photons to the corresponding ion LET) and the number of sensitive cells.

3.3.2 The nested RPP model

It is also possible to overcome some of the simplifications introduced by the single RPP by means of multiple nested RPPs [72]. This technique is meant to define several regions of various dimensions that can contribute to the SEE response and that are contained one inside the other. Other than size and thickness, each RPP has the further degree of freedom of having a different charge collection efficiency. Typically, the charge collection efficiency of the innermost volume is taken to be 100% and the charge collection efficiencies of all other surrounding volumes are defined in relative terms with respect to that of the innermost RPP.

Fig. 3.6 reports a schematic of the nested RPP, where $\hat{\alpha}_i$ is the charge collection efficiency of each ith region. The figure shows that the innermost volume is actually not nested within the larger volumes, which are placed just below. Several other implementations are nonetheless possible, that have all the volumes nested one inside the other and that may employ variable or constant thickness.

The nested sensitive volume can be particularly useful when it comes to account for those effects associated with long range secondary ions (indirect ionization processes). Typically, direct ionization processes are fully resolved by the innermost RPP with unitary $\hat{\alpha}$ and the presence of the outermost RPPs does not have any effect on the SEU cross-section from direct ionization of protons and ions. Therefore, the nested RPP is used to better fit HEH data after the innermost SV size has been determined from low-LET ions or low-energy proton experimental data.

Experimental ion cross-section measurements at medium and high LET can be used to define the characteristics of each outer RPP. Keeping for simplicity the surface of the RPP a square, the ith RPP side can be determined as the root square of the ion cross-section ($\sqrt{\sigma_i}$).

The charge collection efficiency is related to the thickness of each RPP by [72]:

$$\hat{\alpha}_i = \frac{Q_{crit}}{LET_i \cdot t_i} \tag{3.2}$$

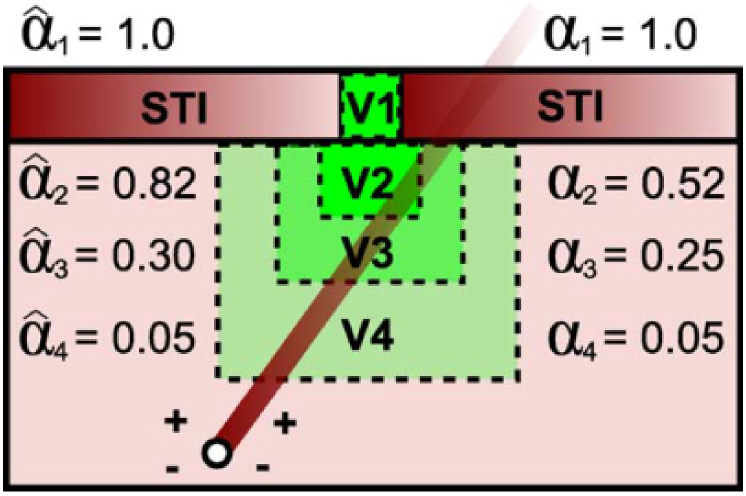

Figure 3.6: Example schematic of a nested RPP used for SEU MC simulations. Reprinted with permission from [72]. © 2009, IEEE.

In this equation it is noted that the Q_{crit} is common to all RPPs, on the other hand LET_i is the LET of the primary ion to which the i^{th} RPP surface is connected to. Keeping constant the critical charge while allowing the thickness to change would mean that each RPP has a different LET_0. Therefore, keeping a constant thickness, equal to that of the innermost volume can ensure having both common Q_{crit} and common LET_0 among the RPPs.

The relative charge collection coefficients (with respect to the innermost sensitive volumes) are given as $\hat{\alpha}_i/\hat{\alpha}_1$. In the case of common critical charge and thickness, this fraction actually reduces to a ratio of LETs (LET_1/LET_i). LET_1 is quite easy to resolve for high-energy low-LET ions, but it is more hard to determine for low-energy protons (see LET determination of low-energy protons in 4.3.2). However, if the LET_i of the heavy ion data-points is high enough, the slight variability of LET_1 will be of lesser importance.

The charge collection coefficients do not have to rigorously adhere to the earlier reported equations and relationships. In [72], this is presented as an iterative method, so that the various free-parameters can be tweaked in order to get the most suited combination that provides the most representative agreement with HI, LEP and HEP experimental cross-sections.

The method was shown to be very helpful for SEUs [28, 32, 72], but also for SELs [122], given that it allows building nested volumes with variable collected charge that can be correlated to the sensitivity obtained from laser testing.

The nested RPP is fully implemented in CREME. However, at the moment, a direct implementation is not available for both FLUKA and G4SEE. Nevertheless, it is possible to rebuild an approximated nested RPP by simulating the individual RPPs and then adding up the various contributions weighted by the relative charge collection efficiency coefficients. The so-obtained FLUKA nested RPP data, used in this thesis, were compared with those of CREME in order to confirm that this approximation did not introduce any error.

Chapter 4

Experimental measurements

This chapter contains a description of the irradiation facilities as well as of the tested devices used for the experimental work of this thesis. Finally, all the experimental data collected during the Ph.D work and used in this thesis are provided.

4.1 Radiation facilities overview

Thanks to the RADSAGA project it was possible to access various facilities for irradiation of electronics in Europe. The used facilities enabled testing with very diverse particles under various ranges of energies. Facilities are listed in alphabetic order.

4.1.1 CHARM

The CHARM facility [12] is built at the end of the East Area T8 beamline of the Proton Synchrotron. The radiation field is obtained by extracting high-intensity (5 x 10^{11} p/spill) proton bunches at an energy of 24 GeV from the PS and by colliding them with a metal target (8 cm diameter, 50 cm length). The resulting radiation field is called mixed-field because it consists of several particles with very wide energy spectra. Such a complex radiation field is characterized by means of radiation monitoring in conjunction with detailed FLUKA simulations [13] of the facility.

The CHARM facility is a one-of-a-kind facility, inasmuch as it has potentialities and constraints that differ from those of standard facilities for radiation testing of devices. The CHARM facility is mainly designed for the qualification of CERN electronic equipment. Hence, its two main characteristics are (i) the representativeness of the radiation field with respect to that of the accelerator and (ii) the strong beam homogeneity that can be achieved over very large surfaces as well as in terms of penetration.

A floorplan of the irradiation area of CHARM is available in Fig. 4.1. Note that the electronics under test is placed in the same room as the target from which the radiation field is generated. This has the advantage of yielding wide uncollimated radiation fields for the irradiation of large systems. In addition, hardness, composition and flux vary inside the room, inasmuch as it is possible to achieve diverse test conditions by repositioning of the setup. Rackable positions (R-) are marked in the figure along with some additional special positions. The radiation field at certain specific rackable position resembles that of certain LHC environments. For instance, the hardness and spectra in position R10 can be used to qualify equipment to be stored in the LHC shielded alcoves, whereas position R13 can be used for the qualification of electronics that will be installed directly in the LHC tunnel. Some lateral positions (with respect to the primary beam trajectory) have a HEH spectrum that resembles that of the space proton radiation belt (but without ions).

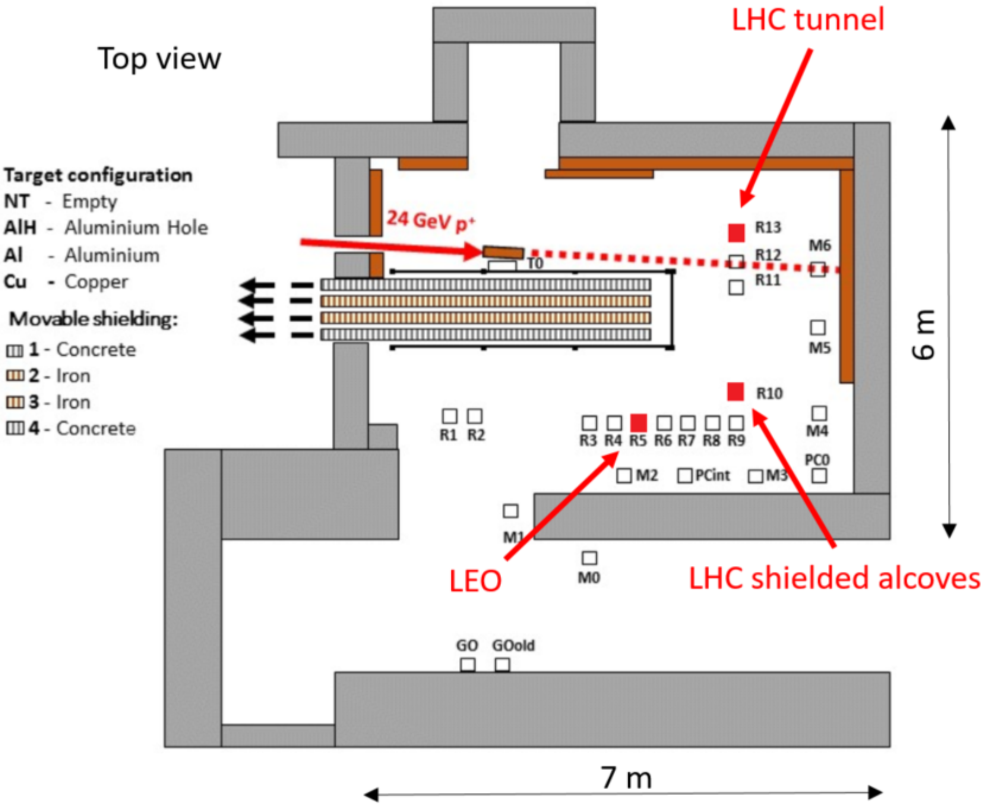

Figure 4.1: Floorplan of the CHARM irradiation area.

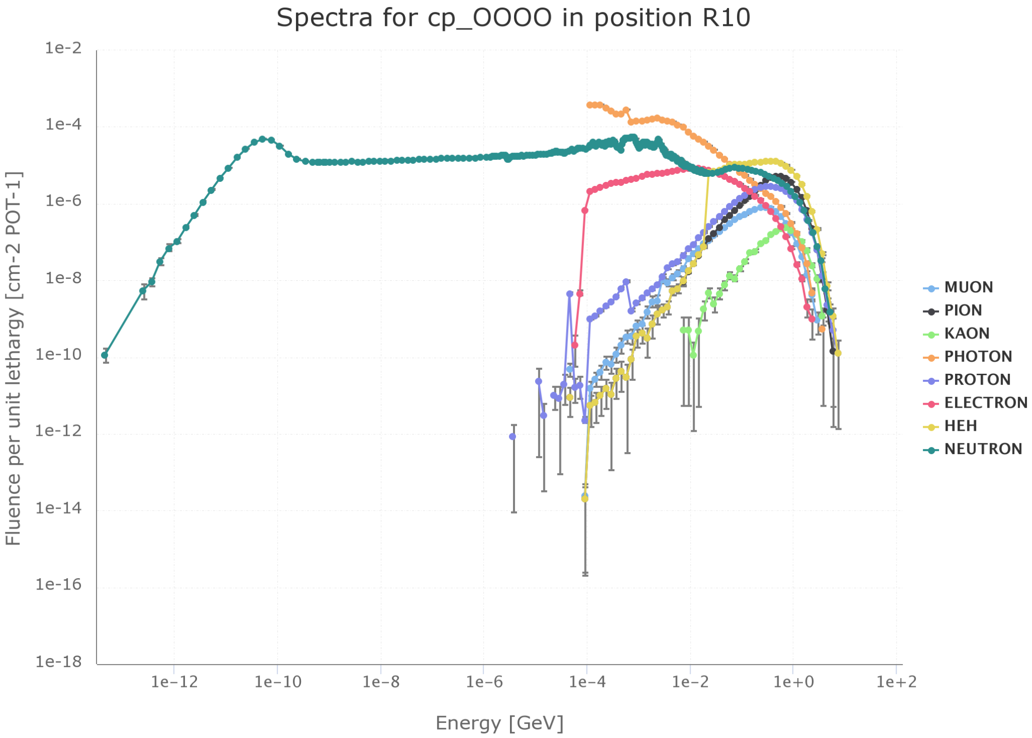

Figure 4.2: Mixed-field spectra of the CHARM facility for the configuration with copper target, no shielding and the rackable position R10 [123]. Obtained with FLUKA.

Other than by the positioning of the system, the hardness, the spectra and the HEH flux can be changed by swapping the target material (standard is copper, but two aluminum versions are available) and by inserting up to four 20 cm shields made of concrete and iron, although the shields can vary the field only for the lateral positions.

The radiation field is present within the irradiation area only when a proton bunch is extracted from the PS. The spill has a duration of 350 ms, yielding high instantaneous fluxes ($> 10^7$ HEH/cm^2/s) for all the rackable positions. Typically, 5-6 bunches are extracted from the PS every minute and the irradiation, which cannot be interrupted (unless the primary user requests so), lasts for nearly 120 consecutive hours. This allows the tested equipment to sustain integral radiation levels equivalent to 20 years of operation in the accelerator during a single week of testing at CHARM.

4.1.2 CNA

The Centro Nacional de Aceleradores [124] holds both a LINAC (linear accelerator) and a cyclotron that can be used to accelerate protons to 0.5-5.9 MeV and 9-18 MeV, respectively. Only the LINAC was used for the purpose of the low-energy proton studies in this thesis.

The LINAC is a Pelletron 3 MV Tandem based on the van-de-Graff linear acceleration principle. The energy at which protons are accelerated depends on the magnetic field and the voltage. The energy resolution is typically of the order of 50 keV. Protons are accelerated and delivered to the DUT in vacuum (10^{-7} mbar).

The proton flux provided by the LINAC can be tuned over a 10 orders of magnitude scale (10^2-10^{12} p/cm^2/s). This is very useful given that the proton cross-sections of the DUTs in the 0.5-5.9 MeV energy range can change by 4-5 orders of magnitude (flexible flux tunability enables testing around an optimum flux at each energy that would allow fast data collection, would not overload the acquisition system and would reduce the probability of double bit-flips in the same bit to a negligible level). Note that the mentioned fluxes are average fluxes. In order to reduce the average flux, the beam (instantaneous size of 1x1 cm^2) was swept over a surface of 18x18 cm^2.

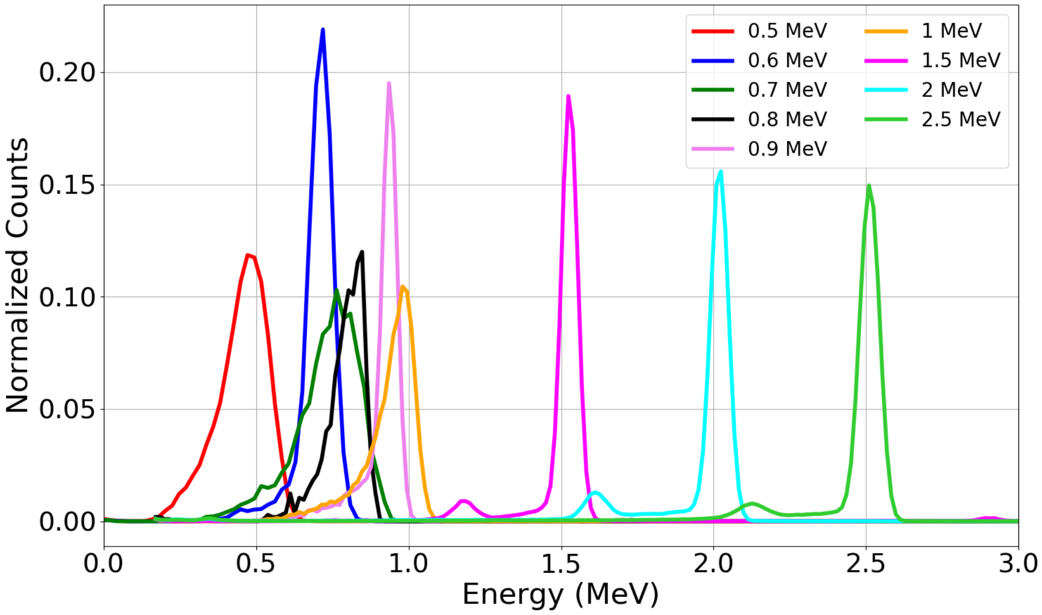

Figure 4.3: Measured proton energy spectrum at CNA with a silicon diode [125, 126] for protons fully stopping within the 140 μm thick silicon. The energy indicated in the legend is the supposed mono-energetic energy set with the accelerator.

While the accelerating structure was capable of delivering such variable fluxes, at the time of the test, the facility was equipped only with a proton current integrator capable of measuring only beam currents above 50 pA (corresponding to about 10^6 p/cm^2/s over an 18x18 cm^2 surface). In order to measure the flux in the lower range, the same dosimetry system currently employed at the ChipIr facility [125, 126] was set-up. This system is based on a silicon diode and works as a pulse counter. Due to the limited bandwidth, the system can be employed only for a proton flux below 10^6 p/cm^2/s, which was anyway sufficient to cover the full range of interest for these tests. Since this system is based on energy deposition measurements in silicon (and it is rather thick with respect to the range of low-energy protons in silicon) it was also used to determine the actual energy of the protons in the beam.

Fig. 4.3 depicts the proton spectra in terms of normalized counts for each mono-energetic irradiation from 0.5 to 3 MeV. When it comes to energy resolution, it is shown that the mono-energetic beams actually have a gaussian shape centred at the selected energy. While the measurement and acquisition chain can partly contribute to widening the measured FWHM, this is thought to contribute for less than 10%. Nevertheless, it is noted that the FWHM can be in the order of 100-120 keV. A few of the spectra are also slightly skewed towards lower energy and those at high energy also exhibit a secondary mode with a magnitude which is of less than 5% that of the main mode.

4.1.3 KVI-CART

The Kernfysisch Versneller Institute (KVI) [127] hosts the Center for Advanced Radiation Technology (CART) which operates the AGOR cyclotron. This cyclotron can be used to accelerate protons, light and heavy ions in energy range and with penetration capabilities compatible with the space standard for SEE testing [79].

Proton testing

The cyclotron can be tuned to extract protons with a primary energy of 120-190 MeV or 30-90 MeV. However, it is more convenient (in terms of time to prepare and calibrate the beam) to tune the cyclotron at the highest energy and to obtain intermediate lower energies by degradation. Therefore, during the tests, the cyclotron was tuned to 190 MeV (note that due to the double scattering foil the protons actually have a maximum energy of 184 MeV at the DUT position) and degraded energies of 164, 124, 80 MeV were used. Concerning the low energy range, the cyclotron was tuned to 66.5 MeV and degraded energies of 50 and 40 MeV were used.

Energy degradation is obtained by combining different sets of aluminum slabs with variable thickness. Note that upon degradation the beam is no longer mono-energetic, so the indicated energies are to be intended as peak energy of the resulting proton spectra. In addition, the degradation shrinks the surface over which beam homogeneity can be attained.

While the dies of the targeted DUTs are small (typically less than 1 cm^2), in order to save on irradiation time for other experiments, the SRAMs that were tested at KVI-CART were irradiated in parallel. They were placed so that they were all falling within a square with 10 cm side (see Fig. 4.4). The same beam size was used for both SEU and SEL testing.

The flux is tunable over several orders of magnitude (3 x 10^2 - 10^9 p/cm^2/s). For the purposes of the experiments in this thesis, a flux of 10^7 p/cm^2/s was used for SEU testing and fluxes of 10^6 - 10^7 p/cm^2/s were used for SEL testing.

In terms of dosimetry, beam field size and homogeneity are measured with a lanex screen scintillator and a CCD camera. These are used only during the beam calibration. The flux is instead monitored with an ionization chamber that is permanently in the beam.

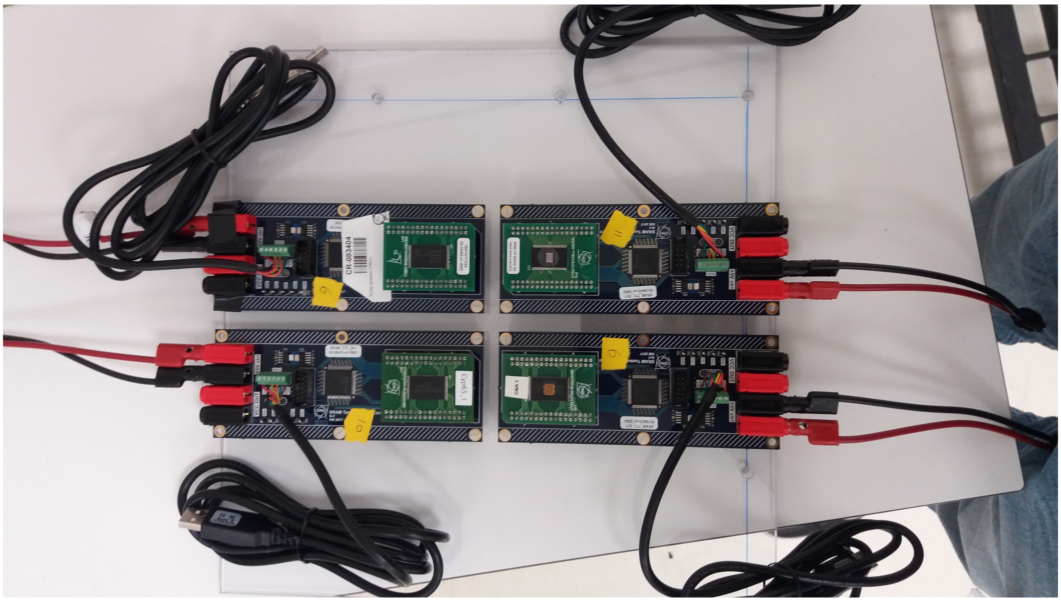

Figure 4.4: Configuration of commercial SRAMs for SEU proton testing at KVI-CART [128].

Ion	Energy [MeV/n]	LET [MeV/(mg/cm^2)]	Range(Si) [μm]	Degrader
Xe	20.8	43.1	220	No
Ar	26.3	5.2	546	No
Ar	13.9	8.0	203	300 μm Al
C	88.6	0.23	11400	No
C	60.5	0.31	5820	5 mm Al
C	31.8	0.50	1850	8.5 mm Al

Table 4.1: Properties of the ions used during the KVI test campaign. The data are calculated using SRIM [48].

Light and heavy ion testing

Light and heavy ions can also be accelerated by means of the same cyclotron used for protons. The heaviest elements (Xe, Kr, Ar, and Ne) can be accelerated up to a primary energy of 30 MeV/n. The lightest elements (Ne, O, C, and He) can be accelerated up to a primary energy of 90 MeV/n. The extraction beamline and the test area are also common to those used for proton testing. However, a vacuum pipe is installed in order to deliver the ions at the DUT position at the correct primary energy.

Nevertheless, the final step of the irradiation is performed in air (no vacuum chamber). So, the primary energy is that at the vacuum pipe exit window, but it cannot be maintained up to the DUT surface, which, in these experiments, was located 80 mm away. Degrading plates can be inserted between the beam exit window and the DUT to further degrade the ion energy (in order to boost the LET, while lowering the range). Both the in-air irradiation and the degrading can affect the ion energy distribution. Expected mean energies were calculated by means of SRIM [48] considering the degrading material and the air distance. The used configurations are reported in Table 4.1.

Similar to protons, the beam field homogeneity is impacted by using degraders (see Fig. 4.5). However, for ion irradiations the attained homogeneity was more than enough since only a single DUT was irradiated per run and it was placed in the center of the beam. The size of the beam for the tests was 3x3 cm^2. Note that the pencil ion beam is scanning this

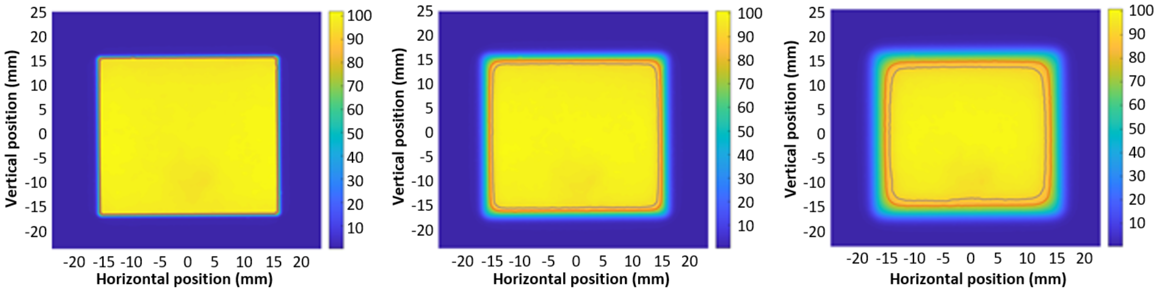

Figure 4.5: Beam field homogeneity for a 3x3 cm^2 Carbon beam undegraded (left) and degraded with increasing aluminum thickness (center and right) [128].

area at a 200 Hz frequency. Device tilting is also possible, but it was not exploited for these measurements.

The beam intensity can change dramatically whether light or heavy ions are used. In the heavy ion configuration the average flux can be in the 10^2 - 3 x 10^4 ions/cm^2/s range. In the light ion configuration the average flux can be further increased up to 5 x 10^6 ions/cm^2/s.

Flux monitoring is achieved by means of four pulse counters that are located on the four edges surrounding the collimator and the counts are calibrated to the flux at the center of the field based on the ionization chamber measurements. Other beam characteristics are assessed in the same way and with the same instruments as for protons.

4.1.4 PSI

The Paul Scherrer Institute (PSI) is a research center which is provided with several accelerating structures. Two of them are considered here since they can provide beams suitable for irradiation of electronics. Both accelerating structures are cyclotrons. On the one hand, pure proton beams from the PROSCAN accelerator are delivered at the Proton Irradiation Facility (PIF). On the other hand, the protons accelerated by the High Intensity Proton Accelerator (HIPA) are collided with fixed targets to generate spallation products. Only the secondary beamlines surrounding targets M and E can be used for irradiation of electronics. From these secondary beamlines beams of pions, electrons and muons can be extracted.

Pion testing

Mono-energetic pion testing was achieved at the πM1 facility [129]. Pions are generated by colliding 590 MeV protons with a fixed target. The πM1 beamline is built to extract secondary particles emitted in the spallation process and makes use of a double bending magnet system as depicted in Fig. 4.6.

Note that several particles are emitted from the target at the extraction angle of 22°. In addition, despite the double bending magnet structure all charged particles sharing the same momentum and charge can reach the πM1 irradiation hall, no matter their nature. Therefore, the composition of the beam may change according to the momentum of the particles extracted. Typically, the beam will be mainly composed of pions and electrons, with a small component of muons. Due to the length of the beamline, pions will decay into electrons before they reach the DUT if the magnets are set to extract the beam with a momentum of 100 MeV/c or below. Therefore, pion testing can be achieved only for momentum > 100 MeV/c. The pion contribution to the beam grows quasi-linearly with increasing momentum, so that more than 95% of the beam at 350 MeV/c (the maximum momentum at which the beam can be extracted) is composed of pions and only the remaining 5% of electrons (see Fig. 4.7). All tests were performed with negative pions. Positive pion

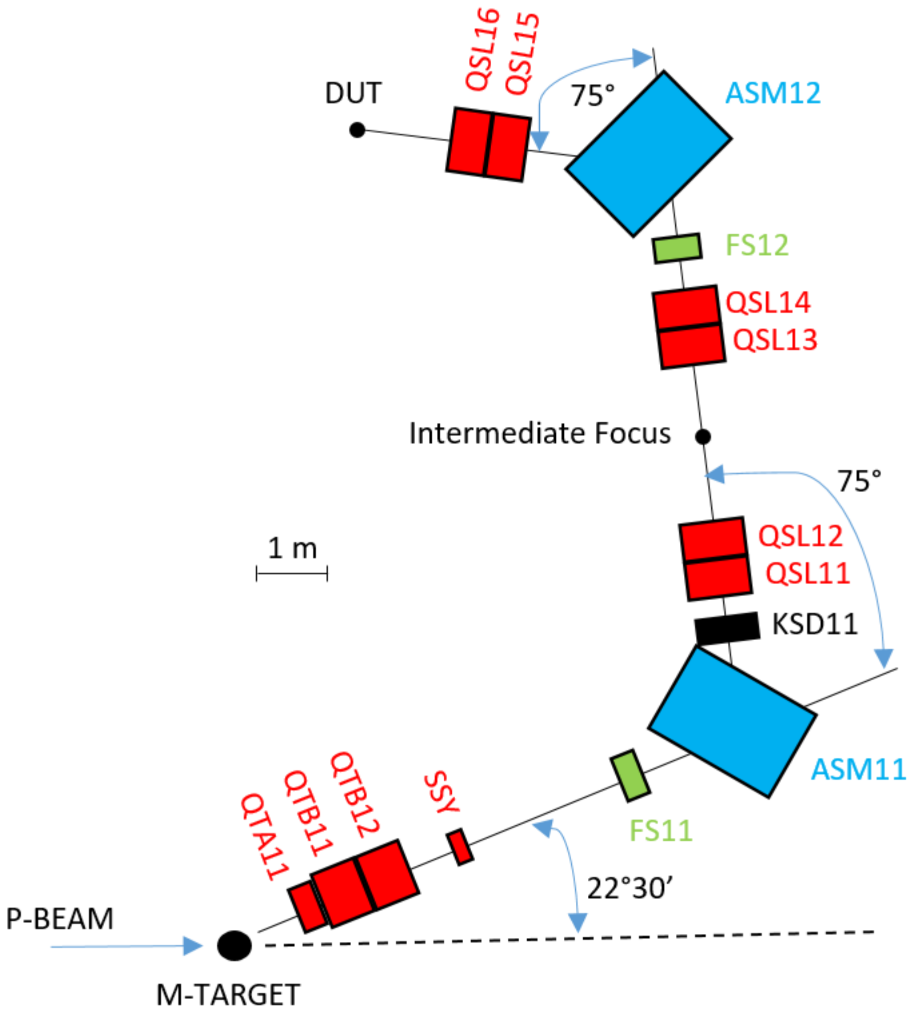

Figure 4.6: The piM1 beamline used to extract mono-energetic pion beams [130].

beams would be similarly contaminated by positrons, although a complete set of time of flight measurements is not available.

The tests were performed by setting the magnets to extract beams with momentum of 130, 200, 270 and 345 MeV/c. Under such conditions, the resulting pions have energies of 51, 104, 164 and 233 MeV.

The beam is typically homogeneous over a surface with a 1 cm diameter, which is enough to irradiate all the tested components (except the ESA Monitor for which only one die was irradiated). The beam size is calibrated prior of the tests by means of a pixelated ionization chamber.

The composition of the beam has to be taken into account because the dosimetry system currently in place at the facility cannot discriminate between pions and electrons when it comes to the online monitoring of the flux during irradiation. The used dosimetry instruments were found to be compatible with providing a one-to-one correspondence between pions and electrons, so that it is possible to multiply straight away by the particle concentration (obtained through time of flight measurements) to separate the flux of pions from that of electrons. For instance, since about only 5% of the beam is composed of residual pions at 130 MeV/c, the actual pion flux will be just 5% of that logged by the facility instruments.

A maximum flux of 3 x 10^6 $\pi^-/\text{cm}^2/\text{s}$ was attained at 345 MeV/c. However, the flux progressively reduces to the point that at 130 MeV/c it is as low as 5 x 10^4 $\pi^-/\text{cm}^2/\text{s}$. The variable flux provided several challenges as (i) the lower end is quite low for getting an

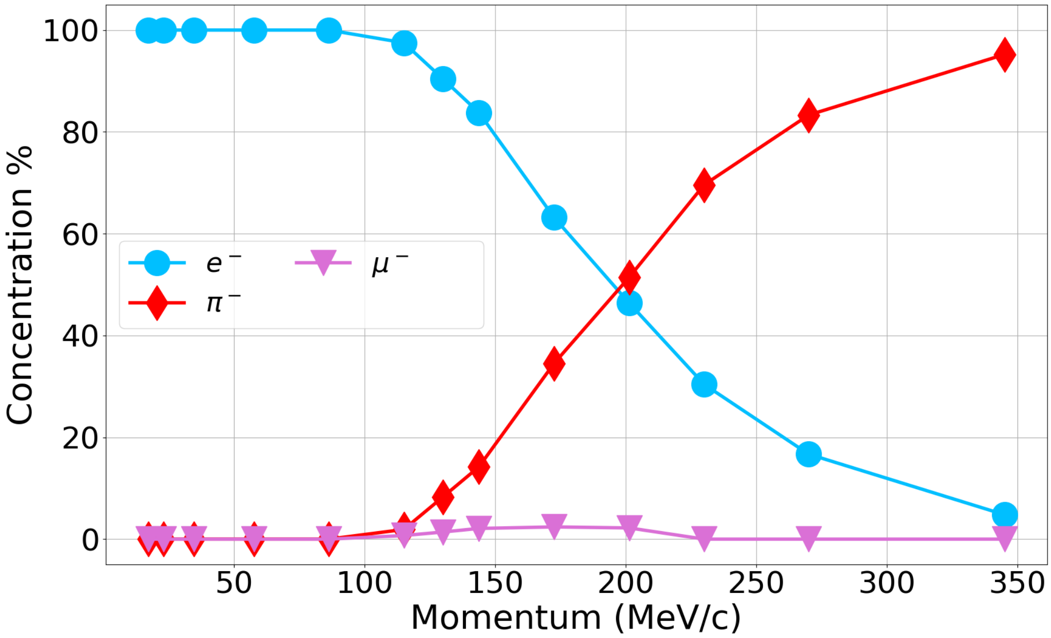

Figure 4.7: Beam composition at the πM1 for negative polarities as a function of the momentum based on time of flight measurements performed by the facility [129]. Reprinted from [14]. © 2020, Coronetti et al., licensed under CC BY 4.0.

appropriate amount of SEEs, thus requiring very long irradiations and (ii) the standard instrumentation available at the facility could not measure the pion flux over the full energy scale.

Three different sets of instrumentation were used for the online monitoring of the flux. For high momentum (> 200 MeV/c) and high flux (> 5 x 10^5 $\pi^-/\text{cm}^2/\text{s}$) the flux was obtained by converting the current produced in an ionization chamber placed between the DUT and the beam exit window. Whenever the flux was reduced below 5 x 10^5 $\pi^-/\text{cm}^2/\text{s}$ it had to be monitored by converting the signal of a scintillator placed just behind the DUT and previously calibrated by putting it in place of the DUT in order to assess the beam attenuation when passing through the PCBs. Finally, for the measurements at the lowest momentum (130 MeV/c), the scintillator was again used in conjunction with the measurements of the proton beam current before the target to extrapolate the pion flux.

In spite of all the complications introduced by the diverse instrumentation used the measured pion fluences provided quite compatible results when it came to use them for cross-section measurements. Some SEU measurements were also repeated in a successive test campaign and returned results compatible with a standard uncertainty on fluence of ±10%. Nevertheless, an uncertainty of ±20% is used for calculation of the error bars later on.

Proton testing

Proton irradiation was carried out at PIF [131], which is a standard test facility for irradiation of industrial electronics whose quality is assured by ESA. Currently, the PROSCAN accelerator can be set to provide protons with primary energies of about 72 and 200 MeV. Several intermediate and lower energies can be obtained by means of metal degraders. As a result of degradation the beam becomes quasi-monoenergetic around the energy given by the facility. Typically, the beam can be considered to be quasi-monoergetic down to 17 MeV. Further degradation is possible, but at that point the beam is composed of a broad spectrum of protons. This configuration can actually be used to perform low-energy proton measurements according to the method described by Dodds et al. [21], although it is necessary to measure the actual proton spectrum.

Standard degradation can be obatined by inserting in the beam before the DUT different combinations of copper slabs of variable thickness (see Fig. 4.8). In order to further reduce the energy thin aluminum slabs can also be used. These were placed after the collimator and the ionization chamber and immediately before the DUT.

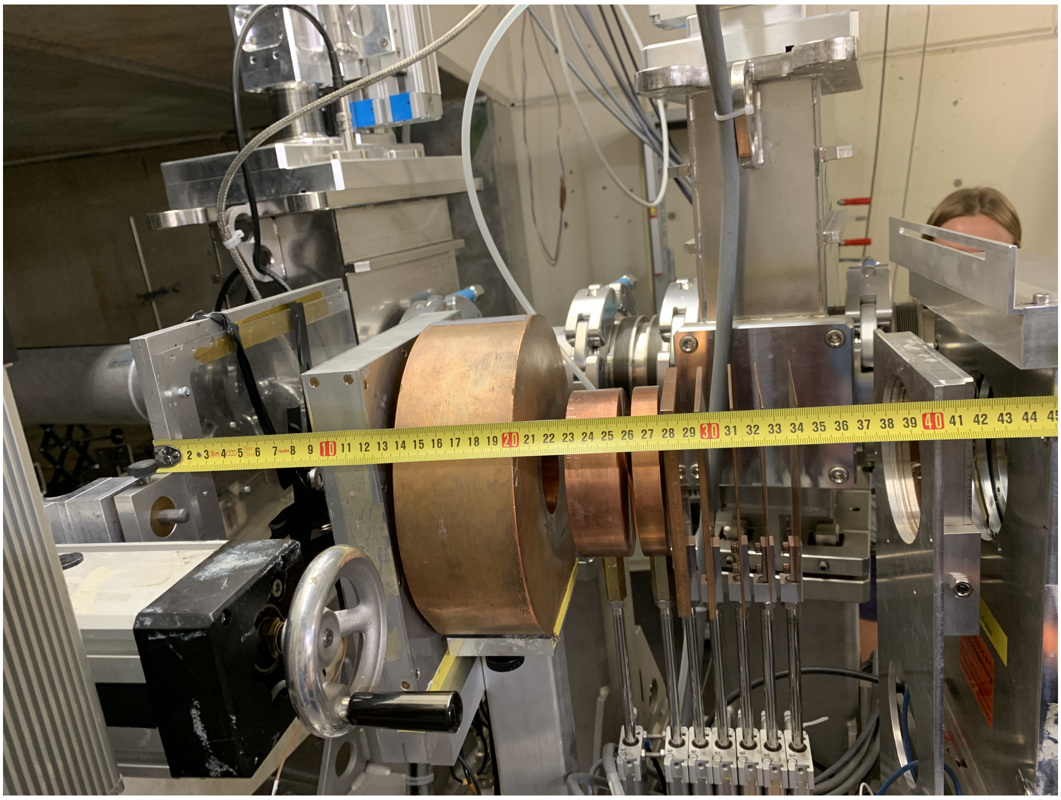

Figure 4.8: Test position at the PIF facility showing the degraders, the collimator and the ionization chamber.

The standard collimator of 5 cm diameter was used for the irradiations of single devices. The flux can be tuned over several orders of magnitude. However, it is noted that fluxes as high as 5 x 10^8 p/cm^2/s can be attained only when the accelerator is set to a primary energy of 200 MeV. On the other hand, when setting the accelerator to 72 MeV primary energy the maximum flux is below 2 x 10^7 p/cm^2/s. Degrading the 200 MeV beam to 100 MeV resulted in a flux reduction of a factor of 2. Degrading the 72 MeV beam down to 17 MeV resulted in a flux reduction of a factor of 7. Given that the further aluminum slabs were placed downstream the ionization chamber used to monitor the flux, it cannot be guaranteed that the flux measured by the ionization chamber was that actually reaching the DUT.

4.1.5 RADEF

The RADiation Effect Facility (RADEF) [132, 133] makes use of the K-130 cyclotron at the University of Jyväskylä to accelerate heavy ion and proton beams. The facility also belongs to the ESA consortium of facilities for irradiation of industrial electronics. No data from the heavy ion beams were collected for the work of this thesis, so the ion cocktail is not described. On the other hand, low-energy proton data were collected for one of the tested devices and are used in this thesis.

Protons can be provided by the cyclotron in the 6-55 MeV energy range.Lower energies are obtained by aluminum foil degradation of the primary beam and energy selection is achieved by means of magnetic bending. An energy resolution lower than 200 keV can be

Ion	Energy [MeV]	LET [MeV/(mg/cm^2)]	Range(Si) [μm]
Ar	379	10	121
Cr	513	16	108
Kr	769	32.4	94
Rh	972	45.8	89
Xe	995	62.5	73

Table 4.2: Properties of the ions used during the UCL test campaign.

achieved for low-energy protons. The beam is scattered before the last 90° bending magnet, which is used to select the most appropriate energy. A vacuum chamber is installed at the end of the beamline to enable low-energy proton testing and the vacuum is typically set for irradiations below 10 MeV. The flux varies according to the energy of the beam in the 10^4 - 3 x 10^8 p/cm^2/s range. Beam homogeneity over a surface of 5 cm diameter can be guaranteed for any test energy.

In contrast to CNA, data on the proton spectrum were not collected at the time of the tests and it is not possible to verify which is the actual FWHM of the mono-energetic beams.

4.1.6 UCL

The Université Catholique de Louvain-la-neuve (UCL) operates the CYCLONE cyclotron to accelerate heavy ion and proton beams. The facility also belongs to the ESA consortium of facilities for irradiation of industrial electronics. Some heavy ion SEL data of COTS ICs were collected for this thesis thanks to the collaboration with CNES. The data of the heavy ions used during this test campaign are reported in Table 4.2.

All irradiations were performed in vacuum on delidded samples. Each device was irradiated singularly making use of the beam spot of 2.5 cm diameter. The flux can be tuned over a quite wide range (10^1-10^4 ions/cm^2/s). All ions in the cocktail are accelerated to an energy of $\approx$ 9 MeV/n.

4.1.7 Other facilities

Several other measurements were performed in other facilities here not explicitly mentioned because the data are not used for the thesis. A summary of all the data that were collected along with a description of the concerned facilities is available from a dedicated radiation effects data workshop publication [134].

4.2 Description of the experimental setups

4.2.1 Targeted devices

This thesis deals primarily with hadron interaction with matter and consequences for electronic devices. Device technology can significantly impact the radiation susceptibility. While several devices from different families can be sensitive to SEEs from heavy ions, the number of devices sensitive to SEEs from hadrons (mainly through indirect ionization) is more limited, especially in the case of destructive SEEs.

SRAMs are quite common devices in both space [135] and accelerator applications [10, 11]. These devices are quite sensitive to SEEs. SRAMs manufactured with older technologies ($>$ 100 nm) are typically more prone to latchup, whereas newer technologies can also manifest upsets from weakly ionizing particles. Thus, SRAMs are quite useful when it comes to

Reference	Manufacturer	Technology [nm]	Array size [Mbits]	Datecode
AT86166H-YM20-E	Atmel	250	16	1817
BS62LV1600EIP55	Brilliance	180	16	9254
LY62W20488ML	Lyontek	180	16	1529
CY62157EV30LL-45ZSXI	Cypress	90	8	1437, 1843
CY62167EV30LL-45ZXA	Cypress	90	16	1525, 1843
CY62167GE30-45ZXI	Cypress	65	16	1731
RADSAGA 65 nm SRAM	KU Leuven	65	32 kbits	N/A
IS61WV204816BLL-10TLI	ISSI	40	32	1650

Table 4.3: Main characteristics of tested SRAMs. The background color indicates the purpose of the tests: blue: SEU, white: SEL.

assessing general reliability trends in electronics used in accelerator equipment thanks to the high sensitivity and wide application.

Given these features, SRAMs are used in both space and accelerator application as memory devices for digital processing as well as radiation monitors to determine the particle fluxes. An in-depth characterization of the devices is needed for both contexts. For the former, measuring the sensitivity to the various particles and energies can help determining an event rate for the application. For the latter, measuring the sensitivity to various particles can help deconvolving the flux of the various particles in an unknown or not well characterized radiation environment as well as to monitor the radiation levels relevant for the reliability of other electronics (e.g., this is typically performed to separate the contribution to SEUs of HEHs and thermal neutrons to determine the respective fluxes).

For all these reasons, several SRAMs manufactured in a wide range of technologies (250 nm to 40 nm) were irradiated. Following CERN necessities for the development of distributed systems and the new trends in space, most of the tested devices are COTS (i.e., devices which have not undergone any process to make them more resistant to radiation or any harsh environment, e.g., vacuum, thermal, etc.). The complete list of memories considered in this study is reported in Table 4.3 in descending order of technology node size.

A few exceptions are present. While sensitive to SEUs, the Atmel SRAM (also known as ESA Monitor) is radiation hardened to TID and does not suffer from SEL. The RADSAGA 65 nm SRAM is a custom-designed SRAM manufactured in 65 nm TSMC technology, currently available as a test chip with a limited array size (the second version embeds 786 kbits).

The datecode can be used to determine to which lot of production a device belongs and the radiation response may change from lot to lot. For the two Cypress 90 nm SRAMs, in some cases, memories with different datecodes were tested, given that it was not possible to procure again devices with the older datecode.

4.2.2 Test configuration

Other than the devices, the setup and the conditions under which the SEE cross sections were measured are important. For instance, the applied core voltage has a significant impact on both the SEU and SEL susceptibilities and, similarly, the temperature can strongly affect the SEL response.

SEU testing

Three test setups are used for SEU testing. The ESA Monitor and the RADSAGA SRAM have their respective testing setup. On the other hand, the commercial SRAMs share the same test setup. The ESA Monitor test setup is the one commercially available. That of the

RADSAGA SRAM was developed at KU Leuven and that of the commercial SRAMs was developed at CERN.

SRAM SEU testing consists in writing the whole array of the memory, irradiating it in standby mode and reading up the whole array in search for discrepancies with respect to the original pattern that was written. The reading operation was typically performed at a fixed frequency during irradiation. In a few cases, the SRAM was read only after the beam was removed. The former was generally preferred in order to assess the progress of the measurements and to adjust the particle flux. The latter was used more rarely, for instance, in the second version of the RADSAGA SRAM this was basically a need given the very long readout time of the readout interface (22 seconds). The ESA Monitor readout also takes up to 5-10 seconds, typically. On the other hand, the readout of the commercial SRAMs can be completed in just 1.5 seconds. No thorough investigation was conducted on whether the two approaches would lead to different cross-sections for the targeted SRAMs, but the few cases in which this was assessed did not hint at any difference in this respect.

The ESA Monitor and the commercial SRAMs were written with a checkerboard pattern (alternation of 0's and 1's in physically or logically adjacent addresses), whereas the RADSAGA SRAM was written with all 1's. While there are some SRAMs showing asymmetric behavior with respect to the information stored in the memory cell (in particular for multiple bit/cell upsets [136]), this was not a topic of investigation here. The checkerboard pattern can anyway be considered as a valuable tool to assess the average response of the cells. The RADSAGA SRAM [137] was designed so that this asymmetry would not be possible.

For all the tests, the commercial SRAMs were powered at a nominal I/O voltage of 3.3 V. Following Dennard scaling this may result in a core voltage of 1.0-1.2 V [138]. The ATMEL SRAM of the ESA Monitor is biased at 3.3 V (I/O), which according to the same scaling would result in a 2.0-2.5 V core voltage. Finally, the core voltage tuning is the main characteristics of the RADSAGA SRAM. It can be varied continuously in the 0.3-1.2 V range from a 1.8 V (I/O voltage). In order to characterize the device and assess the variable SEU sensitivity, measurements were typically taken at 0.3, 0.6, 0.9 and 1.2 V core voltages.

Apart from the ESA Monitor and the RADSAGA SRAM, which are manufactured without any packaging on top of the die, the commercial SRAMs are enclosed in a thin package made of epoxy. While the package can have a thickness below 500 μm, this is enough to alter significantly the energy at the sensitive volume of the chip or to even stop certain particles before they can reach the sensitive volume. This is the case of short range particles such as ions and low-energy protons. Data collected with these particles were thus attained on delidded samples (on which the package was removed chemically or mechanically to expose the die). For high-energy hadron testing the package has a negligible effect above 50 MeV. For these irradiations, samples with or without package were used promiscuously.

For almost all of the memories it was not possible to perform MCU analysis. This requires access to the logical-to-physical mapping (which is proprietary information in case of the commercial SRAMs). While the ESA Monitor embeds that kind of mapping, this is not resolved down to the single addresses, but just to chunks of 32 kbits. Therefore, it cannot be used to determine MCUs. Thanks to a collaboration with LIRMM (which has obtained the logical-to-physical mapping of the Cypress 65 nm SRAM) it was possible to extract some information on MCUs for the Cypress 65 nm SRAM, that is reported in section 4.3.3.

SEL testing

Brilliance and Lyontek SRAMs are tested with the same setup. No programming on the SRAM is performed for this kind of test and only the V_{CC} and ground pins are connected to the power supply. For all the measurements that were accomplished, the I/O bias was set to 3.3 V.

SEL data for these SRAMs were collected only with high-energy hadrons. Hence, all devices were irradiated with the original lid. Heavy ion data for the Brilliance SRAM are available from previous studies [15]. All experiments were performed at room temperature (maximum junction temperature is worst case for SEL [135], however the scope was not device qualification in this case).

A Keysight E3648A was used to monitor the input current to the SRAM. Note that the maximum current was set to 0.5 A in order to protect the SRAM from permanent damage. While the nominal current of these memory is below 1 mA, both memories can suffer from high-state currents of several hundreds of mA. Latchups were detected under the following conditions:

- the input current increased above 10 mA;
- the high-current state was maintained for at least 600 ms (hold time).

The power supply was set to cut the bias to the SRAM after the hold time had elapsed. The reset time was set to 900 ms. After the reset time the bias to the SRAM was restored and the test continued. Note that the flux for SEL testing had to be adjusted so that, on average, the mean time between two SELs was at least 10 × (hold time + reset time). This criterion is applied in order to ensure the correct removal of the SEL. Whenever the current passed the 10 mA threshold for shorter times than 600 ms, this was considered a micro-latchup (it can also be bus contention) and not accounted for the cross-section calculation.

SEL data were collected on a single device and the test was stopped whenever 100 SELs were detected for each tested particle and energy. No a posteriori device characterization was executed on the tested devices to check whether they were still programmable. However, no power consumption variations were identified on the irradiated samples.

4.3 Experimental data

In this section the whole data collection from the devices listed in Table 4.3 and for the targeted facilities described in Section 4.1 is reported. Note that not all targeted devices were tested with all the beams. This is because either the devices were not sensitive to that particular beam (e.g., ESA Monitor not sensitive to low-energy protons) or the device was not yet available at the time of the test (e.g., RADSAGA SRAM not yet taped out at the time of the pion tests).

The data are reported graphically for direct comparison. More complete information can be found in the indicated test reports and publications.

The datasets are subdivided in such a way that the information on experimental data are easily accessible for the two studies on SEEs from singly-charged particles in Chapters 5 and 6. For this reason, some of the high-energy proton data are reported in both of the next subsections.

All the data are presented with error bars calculated at 95% confidence level. The error bars for the cross-section σ were computed considering the relative uncertainties on the fluence given by the facility and on the number of events according to the following formula:

$$\delta\sigma = 2\sigma\sqrt{\left(\frac{\delta\phi}{\phi}\right)^2 + \left(\frac{\delta N}{N}\right)^2} \tag{4.1}$$

$\frac{\delta\phi}{\phi}$ is typically provided by the facility to account for the dosimetry measurement uncertainties. Well calibrated facilities typically report an uncertainty of ±10%. For facilities such as πM1, whose beams are more rarely employed, a larger uncertainty was assumed (i.e., ±20%).

$\frac{\delta N}{N}$ is the uncertainty on the number of events, which decreases with an increasing number of observed SEEs (N) according to the following formula, where the 2 is given by the 95%

confidence level:

$$\frac{\delta N}{N} = \frac{2}{\sqrt{N}} \tag{4.2}$$

Given the large number of events collected, for SEUs the error bar is typically dominated by $\delta\phi$. For SELs the number of events is lower (i.e., in the order of 100), so δN is not negligible with respect to $\delta\phi$.

Although it is rarely the case for the data here reported, whenever the number of SEEs was quite low, upper bounds to the cross-section were calculated according to a Poisson distribution at 95% confidence level [139].

Note that error bars are always plotted in each of the following figures. However, for those plots in which the cross-sections can vary by 3-5 orders of magnitude, the error bars are always too small to appear in the plot.

4.3.1 Comparison between high-energy pions and protons

In order to assess whether high-energy pion and proton cross-sections would differ, several irradiations were performed at PSI and at KVI-CART for both SEU and SEL sensitivities.

SEU data

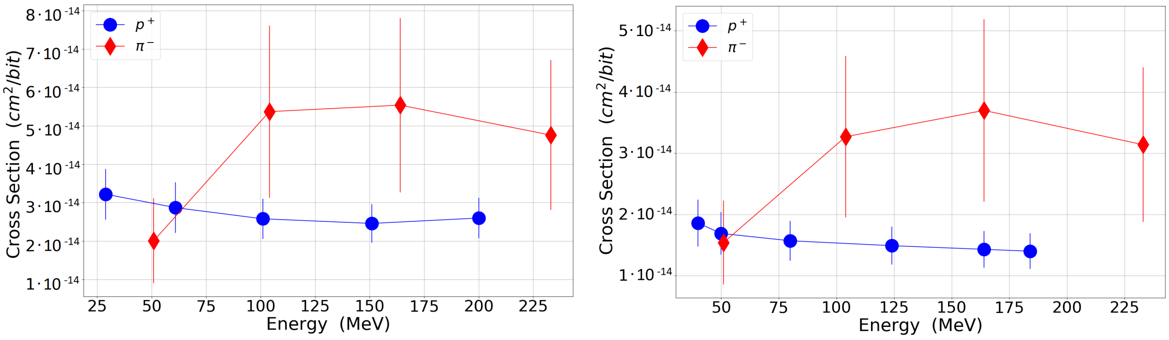

Figure 4.9: SEU cross-sections of high-energy pions and protons for the ESA Monitor (left) and the ISSI SRAM (right). Reprinted from [14]. © 2020, Coronetti et al., licensed under CC BY 4.0.

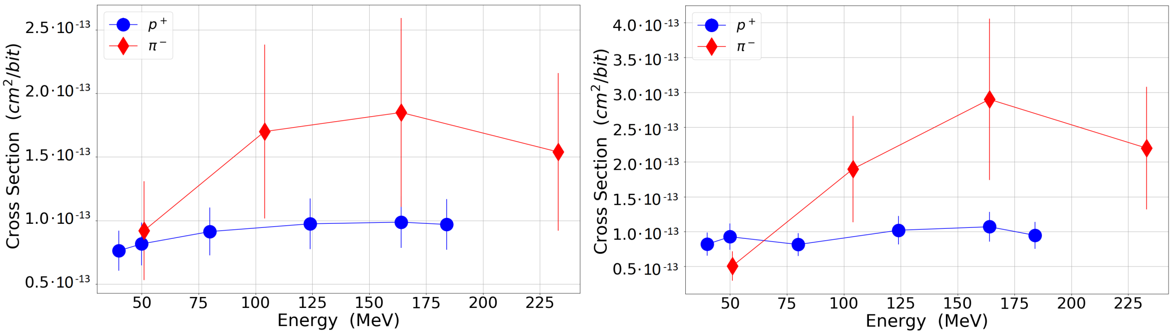

Figure 4.10: SEU cross-sections of high-energy pions and protons for the two versions of the Cypress 90 nm SRAM, (left) 8 Mbits, (right) 16 Mbits. Reprinted from [14]. © 2020, Coronetti et al., licensed under CC BY 4.0.

Fig. 4.9 (left) depicts the SEU cross-sections of high-energy pions and protons as a function of energy for the ESA Monitor. The pion data were collected at the πM1 facility at PSI and the proton data at the PIF facility at PSI. For all the tested energies the proton cross-section is rather stable with a slight increase at lower energies. The pion cross-section, on the other hand, increases of a factor of 2.5 from 50 to 100 MeV and remains quite high up to 233 MeV.

Fig. 4.9 (right) depicts the SEU cross-sections of high-energy pions and protons as a function of energy for the ISSI SRAM. In this case the proton data were collected at KVI-CART. The ISSI cross-sections for both protons and pions are of the same order of magnitude as those of the ESA Monitor. Observations are also similar, though in this case the 50 MeV pion cross-section is closer to that of protons. Again, an increase of a factor of 2.5 is visible for all data-points above 100 MeV.

Fig. 4.10 depicts the SEU cross-sections of high-energy pions and protons as a function of energy for the two Cypress SRAMs, which do not have the same exact cross-section. Proton data were collected at KVI-CART. For both protons and pions the cross-sections are about one order of magnitude higher than those of the ISSI and the ESA Monitor. Again, the proton cross-sections are rather stable for all the tested energy range, although they slightly decrease at lower energy. For the pions, the cross-sections increase by factors of 2 and 5 for the two SRAMs, respectively, at energies > 100 MeV.

Tabulated SEU cross-sections can be found in the test reports [128, 130] and the data workshop paper [134].

SEL data

To the best of the author's knowledge, no other pion SEL cross-sections are available in the literature than those performed for this work. For both Brilliance and Lyontek SRAMs the pion data were collected at πM1 at PSI.

Fig. 4.11 (left) depicts the SEL cross-section for high-energy pions and protons as a function of energy for the Brilliance SRAM. Proton data were collected at both PSI (30 and 230 MeV) and KVI-CART (all other energies). There are some important differences among SEU and SEL data for both proton and pions. For both particles, the cross-sections are seen to decrease towards lower energy. For protons, the SEL cross-section is over one order of magnitude lower at 30 MeV and a factor of 2 lower at 50 MeV with respect to 200 MeV. Similarly, the pion cross-section is a factor of 2 lower at 50 MeV than at 200 MeV. In contrast to SEUs, however, at 50 MeV, the pion SEL cross-section is still more than a factor of 2 higher than that of protons.

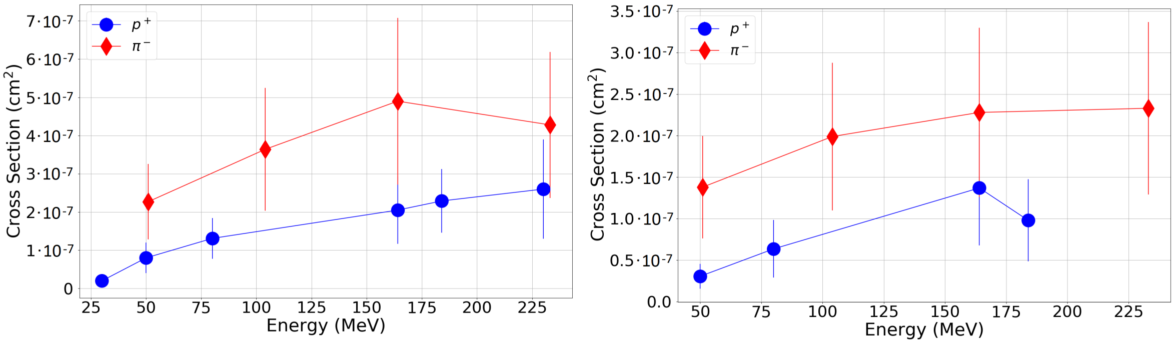

Figure 4.11: SEL cross-sections of high-energy pions and protons for the Brilliance SRAM (left) and the Lyontek SRAM (right). Reprinted from [110]. © 2021, Coronetti et al., licensed under CC BY 4.0.

Fig. 4.11 (right) depicts the SEL cross-section for high-energy pions and protons as a function of energy for the Lyontek SRAM. Proton data were fully collected at KVI-CART. The behavior of the Lyontek SRAM is similar to that of the Brilliance SRAM. However, the pion SEL cross-section at 50 MeV is even a factor of 4 higher than that of protons.

Therefore, while for SEUs the measured pion cross-section was higher only for data-points at energies $\geq$ 100 MeV, for SEL the pion cross-section was found to be higher for all the tested energies.

Tabulated SEL cross-sections can be found in the test reports [128, 130].

Other than the cross-sections, another interesting phenomenon differentiates pion and proton SEL responses. This is the intensity of the high-current states. Note, however, that the analysis of the available data is limited by the fact that, during the data acquisition, the power supply was set to deliver a maximum of 0.5 A. Therefore, events provoking higher current states than this limit are still logged as if the current was only 0.5 A.

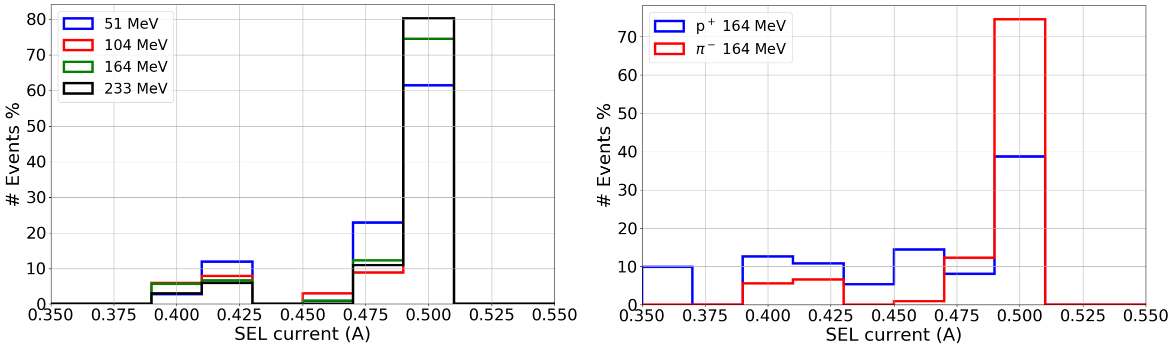

Figure 4.12: (Left) Histogram of the high-current states for the Brilliance SRAM for all the tested pion energies. Note that the red line for the 0.5 A bin is behind the green line. (Right) Histogram of the high-current states of the Brilliance SRAM for pions and protons at 164 MeV. Reprinted from [110]. © 2021, Coronetti et al., licensed under CC BY 4.0.

Fig. 4.12 (left) is a histogram of the high-current states from pion SELs at all the tested energies. Note that, irrespectively of the energy, most of the high-current states (i.e., 60-80%) are associated to currents as high as 0.5 A and that the severity of the SEL slightly increases with energy.

Fig. 4.12 (right) is a histogram of the high-current states from pion and proton SELs at the common energy of 164 MeV (comparisons for other exact energies are not possible, however, comparisons for similar energies show very similar histograms as the one in this figure). It is interesting to note that less than 40% of the SELs from protons yield currents of at least 0.5 A, whereas for pion, more than 70% of the SELs are above this limit.

The differences in the distributions of high-current states are somewhat unexpected. While it is known [119] that the point at which the energy is deposited is important to establish both the probability of a SEL and its magnitude, it is unlikely that, given the quite good level of statistics, pion strikes for all tested energies could occur more often at the most sensitive area(s). In addition, pion and proton SELs are both triggered by similar indirect ionization mechanisms and, as it will be shown later, at energies above 100 MeV their nuclear reactions release particles with similar LET distributions. Therefore, it would be expected that, letting aside the statistical uncertainty, their high-current state distributions would match, unless of course different parts of the circuit are diversely impacted by one particle than the other.

4.3.2 Comparison among low- and high-energy protons and ions

The primary goal is to assess the contribution of low-energy protons to the total upset rate in space and accelerators of deep sub-μm SRAMs. In order to do that the SRAMs were experimentally characterized for their low- and high-energy proton cross-sections as a function of the proton energy. Note that, as explained in Chapter 3, the mechanisms behind low- and high-energy proton induced upsets are different. For this reason, and to determine the complete dataset needed to calculate space upset rates, ion cross-sections as a function of LET were also measured. Low-energy proton data can also be expressed as a function of LET given that their upsets are triggered by direct ionization and can be, in first approximation (the LET of protons will vary much more in the SV than for high-energy ions), compared with ions.

Low- and high-energy protons

When considering low-energy protons, the cross-section can vary of several orders of magnitude within a few MeVs or, sometimes, even a few hundreds of keVs. On the other hand, high-energy proton cross-sections do not vary as much. For this reason, the data are presented with logarithmic scale energy units in order to magnify on the low-energy region.

Energy resolution is a big deal when performing low-energy proton testing. Even if the devices are delidded, the few microns of the BEOL still contributes to (i) slow down the protons and (ii) to scatter them in such a way that their trajectories may be deviated of a certain angle. Therefore, it is actually a spectrum of protons that reach the SV of the device. For the sake of data presentation in this section, the low-energy proton data are presented considering the energy as given by the accelerator before interaction with the BEOL. The presence of the BEOL is the primary reason why the low-energy proton peak is shifted in energy between one device and the other.

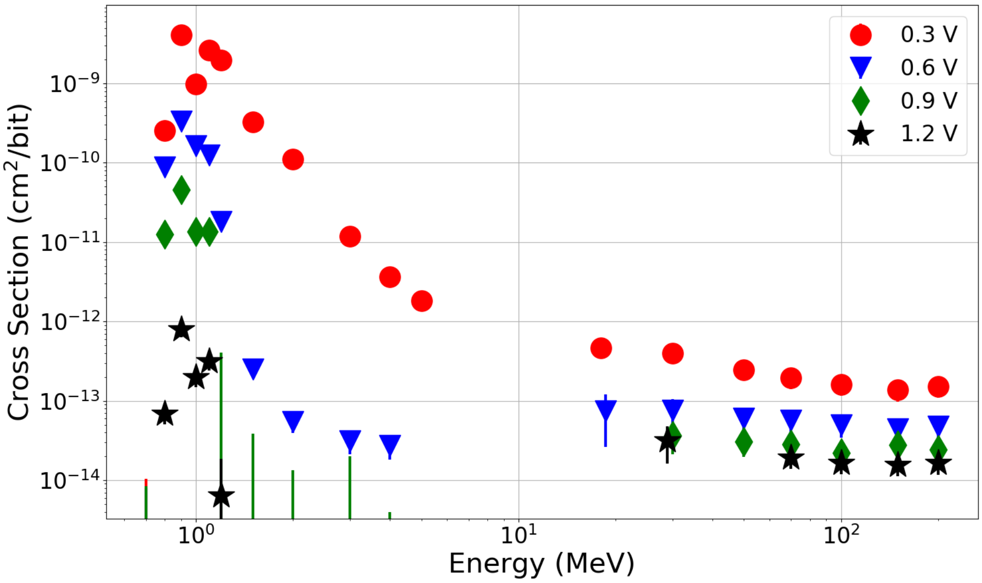

Figure 4.13: Low- and high-energy proton experimental cross-sections as a function of proton energy for the RADSAGA 65 nm SRAM at various core voltages. Lines appearing from below are upper bounds. Reprinted with permission from [134]. © 2020, IEEE.

Fig. 4.13 presents the experimental proton cross-sections for the RADSAGA 65 nm SRAM as a function of the primary proton energy for four different core voltages covering the full range available. Low-energy proton data were measured at CNA and high-energy proton data at PSI.

As the plot shows the sensitivity of the memory can be tuned effectively when varying the applied core voltage for the whole energy interval. The core voltage (on which the critical charge depends) impacts more the low-energy part of the curve than the high-energy part. For instance, if one takes the ratio between the low-energy peak cross-section and the high-energy saturation cross-section this decreases from about 10^4 to 10^2 when switching from 0.3 to 1.2 V. In addition, the higher core voltage (and thus the higher critical charge) also plays a role towards intermediate energies (2-10 MeV). At 0.3 V the cross-section decreases less sharply than at higher core voltages. Indeed, for all voltages but the lowest, the intermediate-energy cross-section is either similar or lower than the high-energy cross-section.

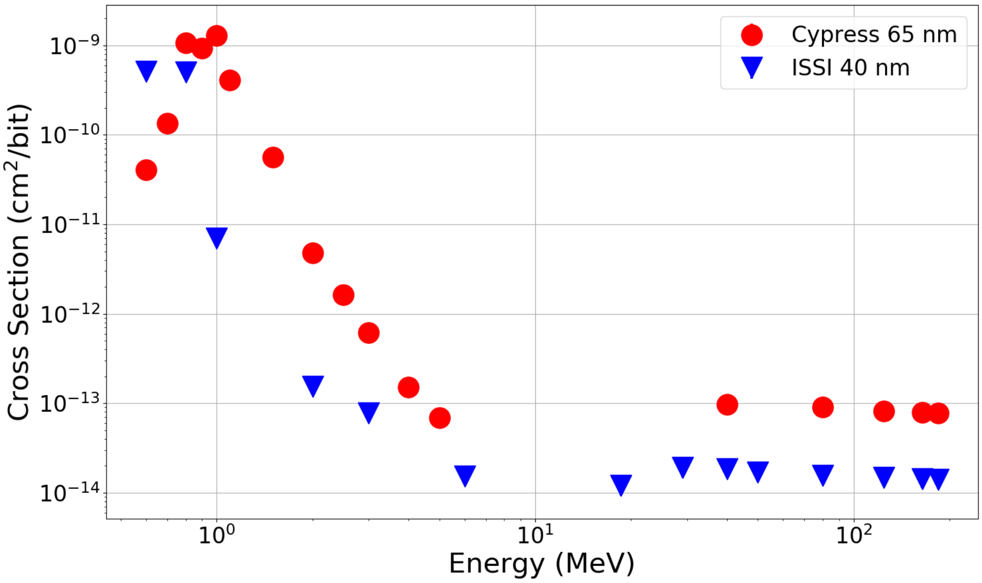

Figure 4.14: Low- and high-energy proton experimental cross-sections as a function of proton energy for the ISSI 40 nm and Cypress 65 nm SRAM [134].

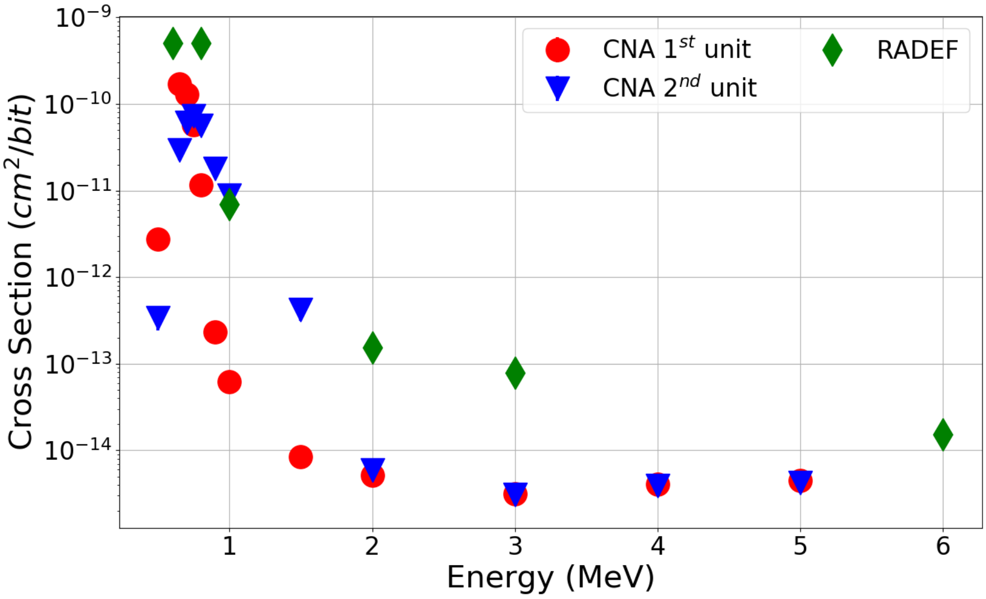

Figure 4.15: Low-energy proton experimental cross-sections as a function of proton energy for three different units of ISSI 40 nm SRAM measured at RADEF and CNA. Reprinted with permission from [134]. © 2020, IEEE.

Fig. 4.14 presents the experimental proton cross-sections for the ISSI 40 nm and the Cypress 65 nm SRAMs as a function of proton energy. Both memories were tested only at the standard core voltage given by supplying the SRAMs with a 3.3 V I/O voltage. For the ISSI SRAM the low-energy proton data are those measured at RADEF, whereas for the Cypress SRAM they are those measured at CNA. High-energy proton cross-sections were measured in both cases at KVI-CART.

In spite of their higher core voltage, these memories display low-energy proton cross-sections almost as high as those of the RADSAGA SRAM at 0.3 V. Indeed, the ratios between the low-energy peak cross-section and the high-energy saturation is also in the order of 10^4 for both SRAMs. Concerning intermediate-energy, the cross-section is seen to decrease faster in both cases, but the high-energy value is reached only at around 3 MeV, making them an intermediate case between the RADSAGA SRAM at 0.3 and 0.6 V.

Considering the RADEF dataset, the ISSI SRAM is the one for which the low-energy peak cross-section and the high-energy saturation cross-section is higher (3.3 x 10^4). ISSI SRAMs were also tested at CNA. Fig. 4.15 depicts the comparison between the RADEF data and those of two different units tested at CNA. Note that the memory tested at RADEF was not tested at CNA, so the data in the figure belong to three different units. Therefore, while the RADEF data are typically higher than those at CNA, it is not possible to conclude whether these differences are a matter of precision in the dosimetry or if these are indeed intrinsic differences among the various units. It is worth mentioning that all the SRAM belong, nonetheless, to the same fabrication lot.

There are many features of interest from this comparison. Even if the peaks of the three cross-sections do not match (up to a non-negligible factor of 10 difference), they are seen to occur at the same energy (between 600 and 800 keV). So, it is possible to assume that the material in the way (BEOL thickness and average composition) between the beam and the SV was the same, otherwise the peak would have been shifted. Other differences are less easy to explain, even when considering only the two units tested at CNA (to remove the dosimetry aspect). The first unit shows a higher peak cross-section, but, at the same time, its cross-section falls off much faster with energy than for the second unit. This seems to be quite in contradiction because one would normally assume that a lower critical charge would be responsible for both the higher peak at low-energy and the higher cross-section at intermediate-energy, but here it is not the case.

The observed differences among different units may be related to the fact that for weakly ionizing particles (such as low-energy protons), the fact that not all the cells are identical (i.e., that there is a distribution of retention voltages, or critical charges, within the memory array) may play a role in differentiating one memory from another while leaving the high-energy response rather unaffected.

Low-energy protons and ions

Both low-energy protons and ions can deposit enough energy to trigger an SEU by direct ionization. For ions having a sufficient range (40 μm [79]) it is possible to assume that the LET is constant along the ion track (or at least within the depth of the SV, which for SEU it is typically much shorter).

The LET of low-energy protons, on the other hand, is not as simple to determine. Fig. 4.16 shows the simulated proton spectra of several mono-energetic and gaussian (FWHM = 120 keV) proton beams after transport through the BEOL of the ISSI memory (whose composition is known from SEM analysis). Sticking to mono-energetic protons, the protons after the BEOL are no longer mono-energetic after passing through the BEOL. They also display quite wide peaks (as observed also in [140]). In order to account for not fully mono-energetic beams at the facility, Gaussian beams with a FWHM of 120 keV have also been considered. The main difference with respect to mono-energetic cases is that the peaks are even more spread towards both higher and lower energies.

For the mono-energetic 0.6 MeV case, only 80% of the primary protons made it through the BEOL, while the remaining 20% have stopped within the BEOL. For the gaussian case the difference is not so high in this respect, considering that 75% of the primary protons went through the BEOL. These data are indicative because, in principle, one would need to

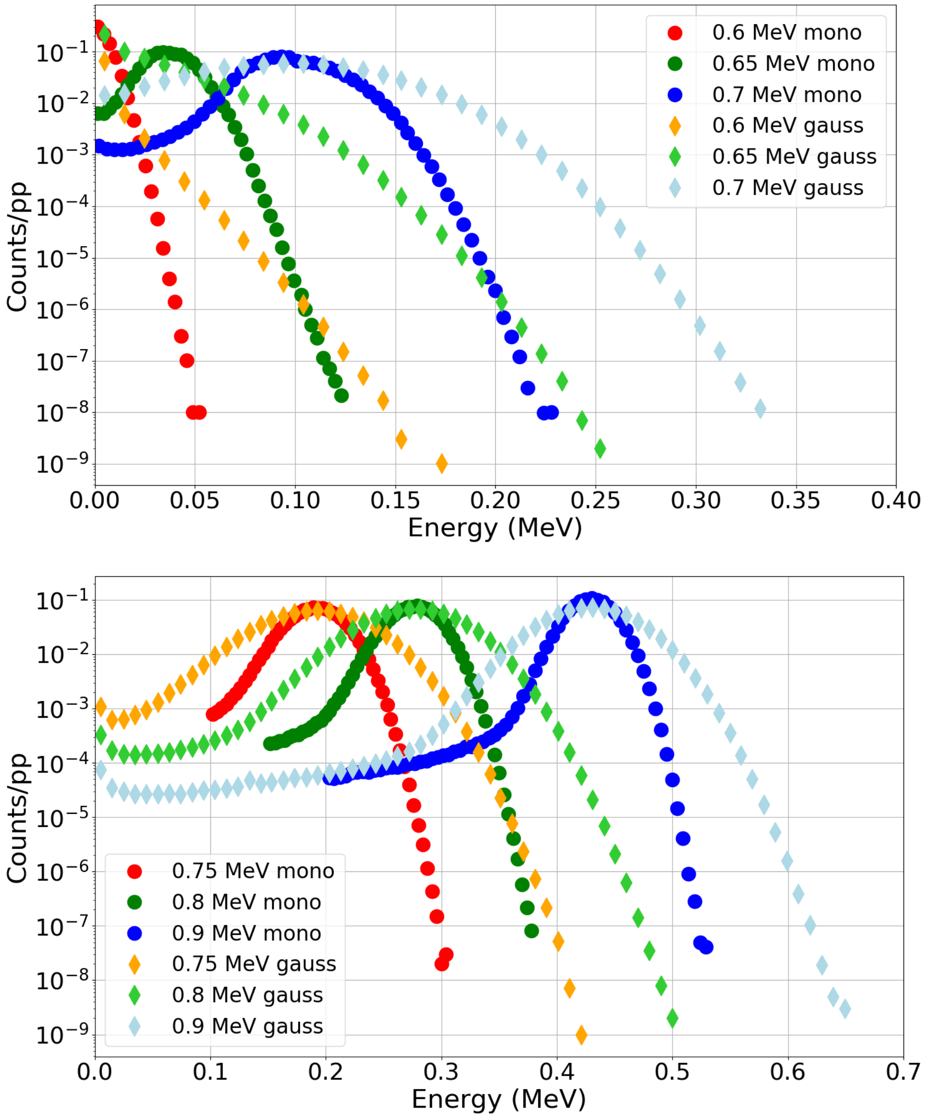

Figure 4.16: Simulated low-energy proton spectra of mono-energetic and gaussian (FWHM = 120 keV) proton beams after transportation through the BEOL of the ISSI memory.

correct the measured cross-sections according to the lower fluence at the SV.

LET distributions of these proton spectra can be computed by means of softwares like SRIM [48], for instance. However, SRIM returns the 'initial' LET of the particle and, although providing also the range (according to a continuous slow down approximation), it does not account for the fact that protons of such low-energy will lose all their energy within fractions of a micron or a few microns.

Therefore, other than the initial LET computed by SRIM, an approximated calculation of the average LET based on the residual proton kinetic energy E_k and the range R in silicon is calculated as follows:

$$LET(E_k, R) = \frac{E_k}{\rho R} \tag{4.3}$$

The main justification for this formula stands in assuming that the protons will lose all their energy within their range in silicon rather than an energy given by the product of their initial LET and the range.

Up to this point, no assumptions on the thickness of the SV have been made. If the proton has a range much longer than the SV thickness, then it can be assumed that the proton LET through the SV will indeed correspond to the initial LET. For cases in which the range is shorter than the SV depth, eq. (4.3) would be a better approximation.

For readability, the LET spectra calculated for the two methods are reported only for the case of primary mono-energetic protons.

Fig. 4.17 provides a comparison of the LET spectra of protons from mono-energetic beams based on either the initial LET from SRIM or the LET calculated with eq. (4.3) and indicated with E_k. It is noted that the LET distribution calculated upon eq. (4.3) are generally narrower than those obtained with the initial LET. However, the spread for 0.6 MeV is in both cases quite large. Therefore, whichever LET value is chosen to plot the data for comparison with ion cross-sections, it will be associated with a large error bar. It is also noted that the maximum LET that can be achieved through eq. (4.3) is lower than the maximum tabulated value for protons (around 0.55 MeV/(mg/cm^2) [141]). Actually, looking into the data for 0.7 MeV, an asymptote at 0.5 MeV/(mg/cm^2) can be recognized for the calculation based on eq. (4.3). At the same time, for all energies $\geq$ 0.75 MeV, the LET distribution from eq. (4.3) provides typically higher peak LETs.

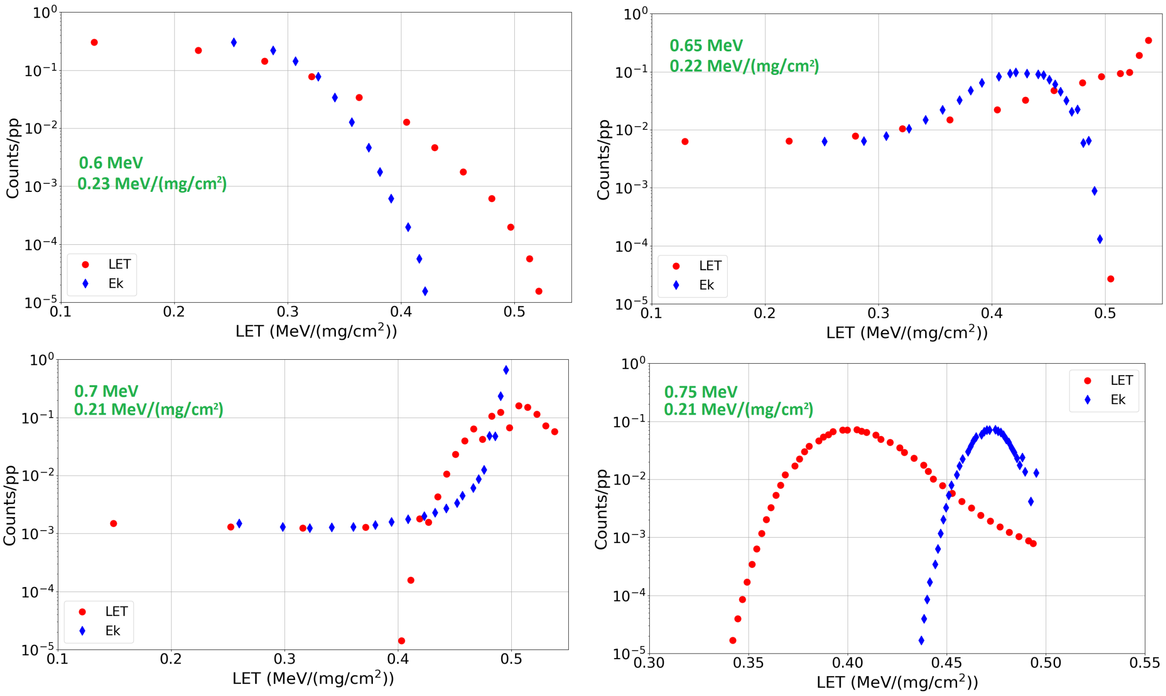

Figure 4.17: Low-energy proton LET spectra of mono-energetic proton beams after transportation through the BEOL of the ISSI memory. Data in red are those extracted from SRIM [48], data in blue are those calculated with eq. (4.3).

The LEP data will be plotted in the following figure along with the ions by placing each data-point at the peak LET calculated following eq. (4.3). Using a single LET (no matter which method is followed) is associated with an uncertainty due to the fact that there is not a unique LET, but rather a spectrum. Data will therefore be presented with the horizontal error bars to account for the uncertainty on the LET.

One of the main assumptions behind both the initial LET extraction and the LET calculation in eq. (4.3) is related to the actual composition and thickness of the BEOL through which it is necessary to transport the mono-energetic protons. This information vary from one device to another and they are not always available for commercial devices. Using an equivalent thickness of SiO_2 may be helpful for these cases. One can deduce this equivalent thickness from the experimental data themselves. These data show a minimum primary energy at which the cross-section is not null before the peak. This information can be used to deduce that protons below the peak energy will likely (mostly) stop within the BEOL and not reach the SV. Based on this, one can estimate the thickness of SiO_2 required to completely stop the proton transport.

Therefore, a SiO_2 BEOL of 6 μm will stop protons with energy below 0.6 MeV before the BEOL, whereas 10 μm will stop protons with energy of roughly 0.8 MeV.

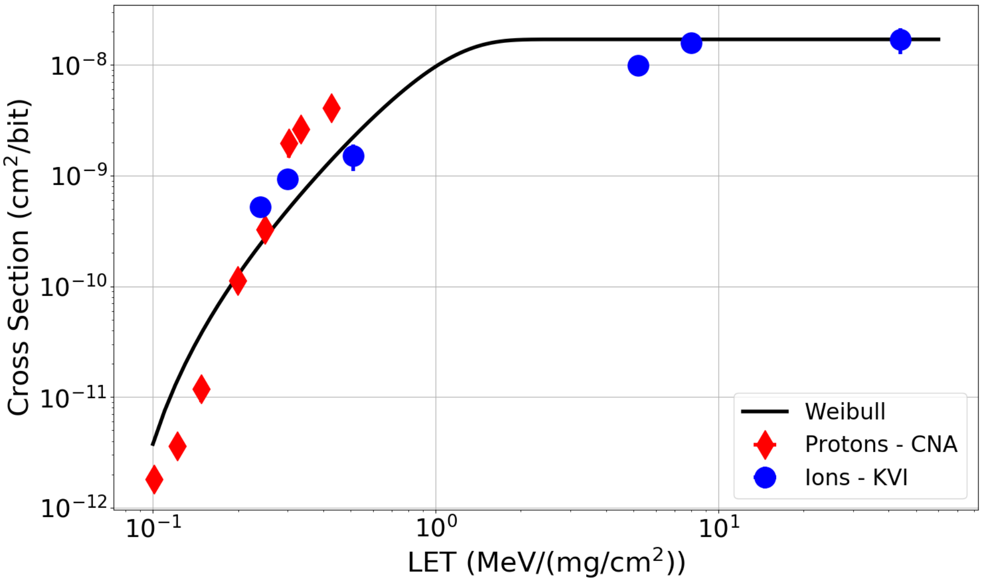

Figure 4.18: Low-energy proton and heavy ion cross-sections as a function of LET for the RADSAGA 65 nm SRAM when tuned at 0.3 V. Weibull parameters: σ_{sat} = 1.7 x 10^{-8} cm^2/bit, LET_0 = 0.07 MeV/(mg/cm^2), W = 1 MeV/(mg/cm^2), s = 2.4. Reprinted from [109]. © 2021, Coronetti et al., licensed under CC BY 4.0.

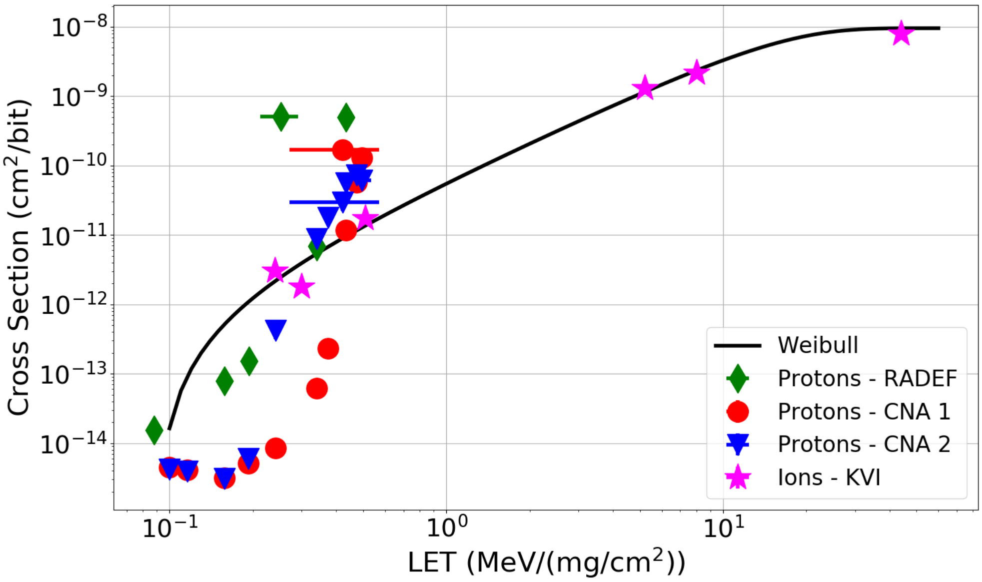

Figure 4.19: Low-energy proton and heavy ion cross-sections as a function of LET for the ISSI 40 nm SRAM. Weibull parameters: $\sigma_{sat} = 9.56$ x 10^{-9} cm^2/bit, $LET_0 = 0.09$ MeV/(mg/cm^2), W = 16 MeV/(mg/cm^2), s = 1.8.

Fig. 4.18 presents the low-energy proton and ion cross-sections for the RADSAGA SRAM as a function of LET. A Weibull fit is also shown and its parameters are reported in the caption

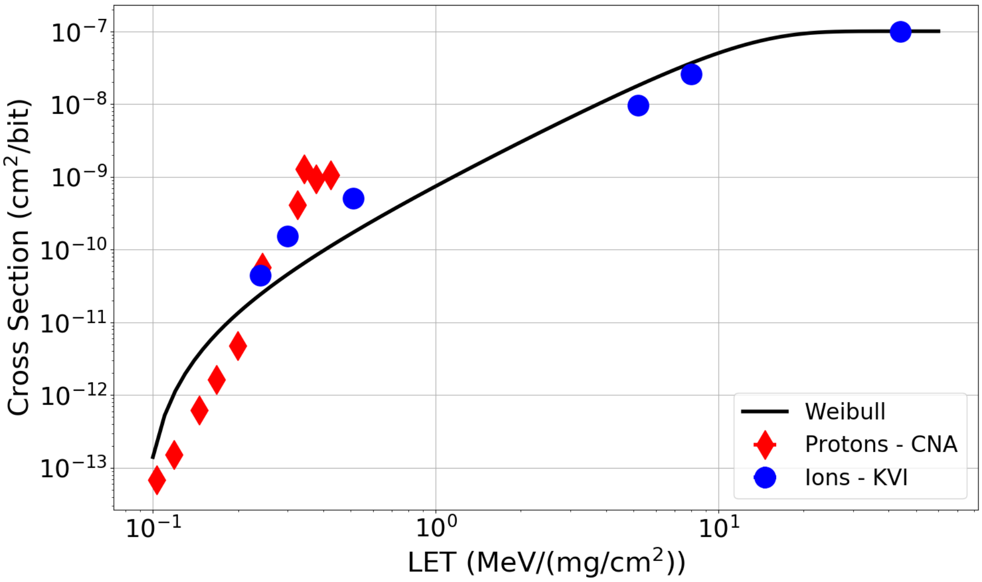

Figure 4.20: Low-energy proton and heavy ion cross-sections as a function of LET for the Cypress 65 nm SRAM. Weibull parameters: σ_{sat} = 1 x 10^{-7} cm^2/bit, LET$_0$ = 0.09 MeV/(mg/cm^2), W = 12 MeV/(mg/cm^2), s = 1.9. Reprinted from [109]. © 2021, Coronetti et al., licensed under CC BY 4.0.

of the figure. Note that the Weibull parameters were obtained by fitting ion and low-energy proton data by hand rather than with a fitting algorithm. The reason is that low-energy proton and ion cross-sections at similar LET did not agree very well with each other. So, the fitting algorithm would rather be very imprecise or not converge at all. Indeed, when differences were quite remarkable, the Weibull was calculated to fit the ion data preferably.

The RADSAGA SRAM is actually the memory for which the differences between low-energy and ion cross-sections of similar LET are smaller. It is reminded that ion data-points were obtained with carbon ions with much longer range.

Fig. 4.19 shows data in the same fashion, but for the ISSI SRAM. This is the SRAM for which the situation differs the most. The plot shows not only the RADEF data, but also the CNA data of the other two units. The peak low-energy proton RADEF data are a factor of 50-100 higher than the respective carbon data at the same LET. The CNA datasets are still a factor of 10 and 5 higher than the ion data.

At lower LET, the proton data for RADEF still seem to belong to the same curve as the ions, whereas the CNA data clearly points towards a much higher LET threshold.

The ISSI is also the only case for which visible error bars for the LET can be seen (compare Fig. 4.17) for the quite wide LET distributions at 0.6 and 0.65 MeV. However, these two LET distributions are very different and it is quite unlikely that the first would return a higher cross-section than the second.

Fig. 4.20 shows data for the Cypress SRAM. The situation is more similar to the RADSAGA SRAM, inasmuch as the discrepancy between low-energy proton and ion data is just of a factor of 3 maximum.

It is hard to conclude the reason behind the observed discrepancies. The introduced approximation does not play a role for the proton LET because the proton LET cannot be higher than 0.55 MeV/(mg/cm^2). However, the proton data for the ISSI SRAM are more compatible with LETs of 4 MeV/(mg/cm^2) for the RADEF data and of 1-2 MeV/(mg/cm^2) for the CNA data. One possible explanation that was proposed for SOI SRAMs [85] is that LEP yields a much higher count of MCUs than light ions of same LET. However, though this cannot be verified for the ISSI SRAM, it will be verified for the Cypress 65 nm SRAM.

4.3.3 MCU analysis

In highly integrated devices, MCUs are nowadays expected to contribute for a very significant portion of the total soft error rate. Furthermore, they can more easily defy error correction schemes when their multiplicity increases. Nowadays, MCUs were seen to contribute for even 20-50% to the total SER from HEHs depending on the cell technology [142]. MCUs are events that, although still related to a single particle strike, can cause logic state changes in more than one cell within the memory device. One can then define several types of upsets based on the cell multiplicity: 1CU (1-cell upset), 2CU (2-cell upset), etc., and determine the cross-section of each of them and their respective contribution to the total SEU cross-section.

Whenever available, the logical-to-physical mapping of the memory can be used to convert the logical address into a physical position within the memory array. Such information is not always available. Thanks to the collaboration with LIRMM (and their collaboration with Cypress) it was possible to retrieve some MCU information that could provide additional insight on the previous points.

Other than the logical-to-physical mapping, in order to retrieve MCUs, it is necessary to perform the readout of the memory with quite high frequency (i.e., the memory has to be read several times while under irradiation). This makes negligible the probability that two upsets close-by were caused by two different particles and not by the same one.

The algorithm that is used to determine if an upset is a 1CU or if it belongs to a cluster requires some time and space resolution triggering. Following the LIRMM approach [143, 144], for every upsets the algorithm search for other upsets occurring in the surrounding ±3 cells in both x and y (resulting in a square composed of 7x7 cells). If another upset is found within the considered cell span, the operation is repeated recursively until there are no more close-by upsets to the most external flipped bits in the cluster.

In terms of time resolution, the search is done over ±1 second with respect to the timestamp at which the upset under consideration occurred. Considering that the typical readout frequency for the Cypress SRAM was 5 seconds, this further reduces the search to the single readout entry in the raw data log.

With respect to the work done by LIRMM [143, 144], the very first result is that, although the algorithm is now powerful enough to resolve for various types of MCUs, the data did show only MCUs type A (those previously described) and no MCUs type B, C or D (which are typically due to readout artefacts). This confirms that the data used to calculate SEU cross-sections in the previous paragraph are real SEUs occurring during the standard operation of the memory.

Similarly to what has been done before, the idea is to compare MCU data among particle types and energies.

Fig. 4.21 presents the MCU event cross-sections for 1CU and MCUs with multiplicity of 2-10 for various proton primary energies. Sticking to this plot it appears that MCUs of high-multiplicity are not happening due to direct ionization from low-energy protons, given that only 1CUs and 2CUs are observed at around 1 MeV. Also, the event cross-section of 2CUs is two orders of magnitude lower than that of 1CUs, so even the real 2CU cross-section (multiplicity times the event cross-section) contributes for only 2% or less to the total SEU cross-section.

On the other hand, from 2.5 MeV a few event with higher multiplicity appear. At even higher energy both the multiplicity and the event cross-section of each MCU increase. That is, the 2CU event cross-section is less than one order of magnitude lower than the 1CU event cross-section.

The real MCU cross-section there shown is defined as follows:

$$\sigma_{MCU,real} = \sum_{m=2}^{20} m \times \sigma_{mCU,event} \tag{4.4}$$

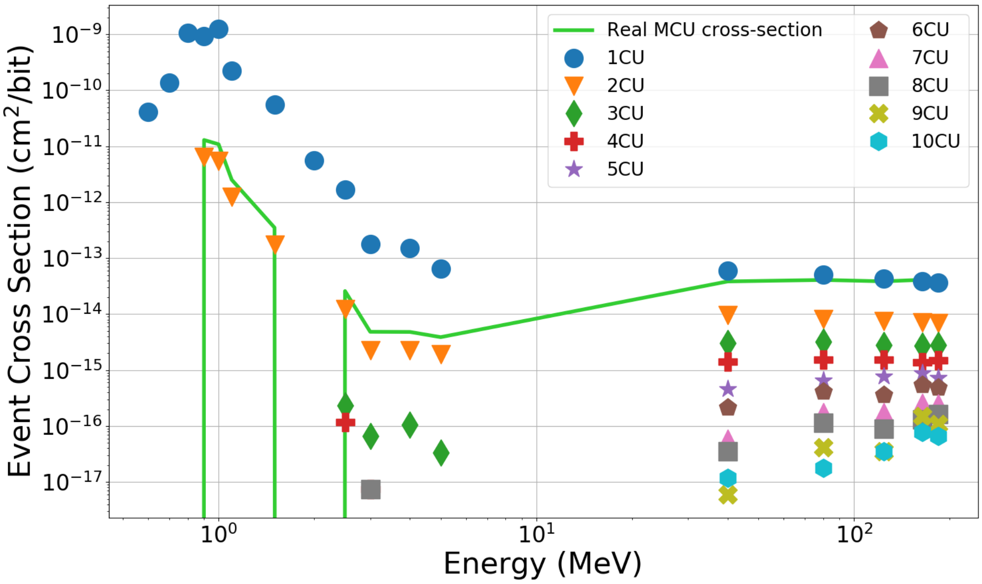

Figure 4.21: MCU event cross-sections for 1-10CUs for the Cypress 65 nm SRAM as a function of the proton energy. The real MCU cross-section is also plotted.

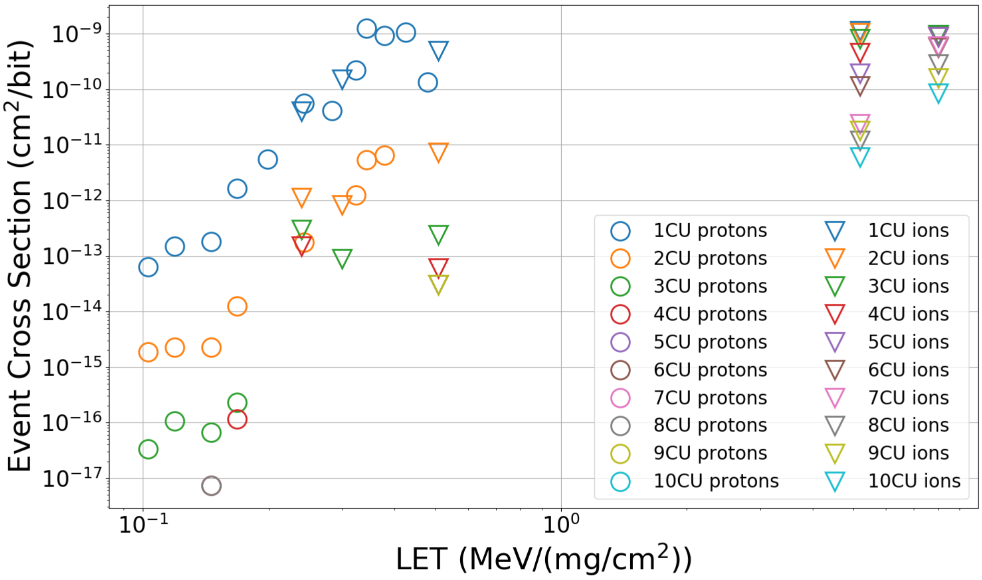

Figure 4.22: MCU event cross-sections for 1-10CUs for the Cypress 65 nm SRAM as a function of LET for low-energy protons (circles) and low-LET ions (triangles).

In the equation, m is the multiplicity (going from 2 to 20) and $\sigma_{mCU,event}$ is the event cross-section of multiplicity m. Therefore, $\sigma_{MCU,real}$ is obtained by the sum of all the bits in error no matter the multiplicity of the MCU.

As shown in Fig. 4.21, the real MCU cross-section can equate the 1CU cross-section for HEPs. Therefore, it can contribute to about 50% of the total HEP SEU cross-section, which in accordance with the literature findings for 65 nm technology [142] may indicate that the memory cells have a triple well structure (this technique consists in adding a N+ or P+ layer underneath the p- or n-doped substrate and has the advantage of reducing noise and SEL sensitivity [145]).

The non-negligible amount of MCUs is likely the reason why a single RPP model may fail to describe the HEP cross-section and why, under the assumption that all SEUs were individual, one has to employ a nested RPP to recover the experimental cross-section. Indeed, large MCU multiplicity and event cross-sections are typical of heavy ions (where $> 99\%$ of the upsets can be MCUs).

Fig. 4.22 depicts the MCU event cross-sections for 1CU and MCUs with multiplicity of 2-10 for low-energy protons and low-LET ions. Higher LET ions are also plotted for comparison. Similarly to what was observed before, it is noted that also for light ions the 2CU event cross-section is a couple of orders of magnitude lower than the 1CU event cross-section. Therefore, it is possible to conclude that the discrepancies experimentally observed between the cross-sections of LEPs and ions of similar LET are probably not due to MCUs, at least for this bulk silicon SRAM.

On the opposite, towards 0.5 MeV/(mg/cm^2) ions can also have MCUs with higher multiplicity than 2, although their cross-section is also typically very small if compared to that of 1CUs.

The other interesting thing is that the 1CU event cross-section seems to reach a saturation for 0.5 MeV/(mg/cm^2) at 10^{-9} cm^2/bit. Actually, this is not at all a saturation, given that the 1CU event cross-section further reduce to 10^{-10} cm^2/bit at LET above 10 MeV/(mg/cm^2) (whereas the total SEU cross-section is as high as 10^{-7} cm^2/bit). This means that, at high LET, 1CUs contribute for only 0.1% to the total SEU cross-section.

4.3.4 Heavy ion SEL data on COTS devices for the CNES Strateole2 atmospheric balloon

A few additional COTS devices were tested in collaboration with CNES for the Strateole2 atmospheric balloon mission. Information on the experimental setup to measure SELs is not provided because it is CNES proprietary information. The data are used in the context of the thesis in Chapter 7 for the analysis of HI SEL predictions and upper bounds based on the HEH test results. Differently from the other data taken from the literature, these data have never been published. Heavy ion Weibull parameters were collected following SEL cross-section measurements at UCL and are reported in Table 4.4. Only normal incidence irradiations at room temperature were performed.

Reference	**Type**	**LET$_0$ [MeV/(mg/cm^2)]**	σ_{sat} **[cm^2]**	**W [MeV/(mg/cm^2)]**	s
74LVC3G17DC	Schmitt trigger	20	2.0 x 10^{-6}	26	3.1
ADUM1100BRZ	Isolator	10	4.0 x 10^{-5}	25	3.7
CD74HC4068M	Multiplexer	40	1.3 x 10^{-5}	15	4.8
MAX6301ESA+	Supply supervisor	5	1.6 x 10^{-5}	20	1.3
MCP23018E/MJ	Expander	12	2.5 x 10^{-4}	38	1.7
MCP6292E/MS	Op-amp	28	2.5 x 10^{-5}	38	3.8

Table 4.4: Heavy ion SEL Weibull parameters for the CNES Strateole2 atmospheric balloon COTS devices tested at UCL.

Chapter 5

Direct ionization from protons

The topic of soft errors induced by direct ionization from protons in highly integrated ICs can already benefit from a substantial amount of literature. However, given the absence of standardized practices on how to determine the PDI upset impact in space missions, determining the expected proton upset rate in orbit from the experimental data remains mostly an open question. Therefore, several prediction methods are investigated and compared.

PDI may also be relevant for accelerators, though neutrons of various energy scales are supposed to be the dominant contributors.

The experimental data for the targeted devices demonstrate a very high LEP cross-sections if compared to HEP and HI cross-sections. A main focus of this chapter will be devoted to the building of representative SV models based on these experimental data. These can later be used to determine the upset rate in space by means of full transport MC.

Experimental data also showed small-to-large differences when comparing the upset cross-sections of LEPs and ions of similar LET. However, the underlying physics does not seem to provide an answer for that. It cannot be excluded that the observed divergence among the cross-sections was actually due to collateral aspects, such as differences in dosimetry among LEPs and ion facilities, differences in manufacturing processes on a part-to-part basis or even different contribution of MCUs to the total SEU cross-section (although the latter was excluded at least for the Cypress 65 nm SRAM).

Upsets from protons with energy < 20 MeV are not caused only by direct ionization, but also by other mechanisms related to indirect ionization. This topic is covered by comparing the MC simulation results of FLUKA and G4SEE.

While MC simulations are supposed to provide a representative picture of what happens in the SV of a device, there are always some uncertainties at play that can affect both the modelling and the prediction of the upset rate due to PDI. For instance, as it will be mentioned later, the models built in the paper [109] were based on the assumptions that both the RADEF and CNA data were fully mono-energetic, although it was shown that they were not. In addition, in the paper, the BEOL itself was built upon assumptions and assuming a generalized SiO_2 equivalent thickness. Finally, the critical charge is typically not identical among different cells of the SRAM, but this was not taken into account initially. The effect of all these approximations on the upset rate is also evaluated.

5.1 Modelling of sensitive volumes

5.1.1 Modelling rules applied in this work

Building representative sensitive volume models is an iterative task that can be achieved through MC simulations. However, the modelling of the SV of the three SRAMs under consideration (RADSAGA, ISSI and Cypress 65 nm) into RPPs enabled establishing some easy-to-use rules that can be extended to the modelling of the SV of any SRAM, provided the SRAM is sensitive to PDI and a sufficient amount of experimental data is available. As will be shown later, there are two options on the table: the single RPP and the nested RPP. The first step of this iterative method stands in understanding whether a single RPP model would be suited to represent the experimental data. Only when this is not the case, a nested RPP is used to fix the HEP cross-section.

The experimental data needed to build a representative RPP model of the SV are the LEP, HEP and HI cross-sections with a sufficient amount of data-points with respect to energy and LET. Although this is a very empirical approach, it should be reminded that the RPP model shall still bear some physical link with the SV size and the actual critical charge. Having as many experimental data-points as possible can help fine tuning the SV model. For all the three targeted devices (RADSAGA, ISSI and Cypress 65 nm) the data-set was rich enough to build quite reliable models that were returning very faithful numerical MC cross-sections.

The single RPP is mainly characterized by the geometrical sizes of the RPP volume. The simplest version is that of a cubic RPP. In this case only the side of the volume is necessary. More complicated cases can rely on RPPs based on three different sides. In this work it was always assumed that the face of the RPP normal to the beam at the facility was square with side d_{RPP} and, in first approximation, that the thickness, t_{RPP}, of the RPP was also identical to d_{RPP}. However, this first tentative RPP was found not to allow a correct representation for all the targeted devices, so the thickness was also, in the case of the RADSAGA SRAM, used as a free parameter.

The second important parameter of the sensitive volume is the critical charge (or the critical energy or the LET threshold). It is possible to determine the critical charge by measuring the retention voltage (according to eq. 2.7), but this also requires the knowledge of some construction parameters of the SRAM, which are not available for the targeted devices. As an alternative, the critical charge can also be determined by experimental measurements of the LET threshold. However, this is a quite complicated task when considering devices that are sensitive to LEPs because the LET threshold will be very low. As earlier mentioned, using low-energy protons may be inadequate because of the energy spread in the BEOL (which may also be uncertain in thickness and composition) that yields an LET spectrum at the SV. Long range low-LET ions can be more useful in this sense, although one should take care not to mistake indirect ionization SEUs for direct ionization SEUs.

One can solve the problem related to the determination of an appropriate critical charge by profiting from the fact that the MC simulation returns how the cross-section of a certain RPP varies with this parameter. Therefore, through an iterative process, one can find a combination of RPP geometrical sizes and critical charge that returns numerical LEP, HEP and HI cross-sections that match those measured experimentally.

The final parameter to tune in the RPP model is the BEOL. Unless known (as it is for the RADSAGA SRAM, because manufacturing rules were known, and for the ISSI SRAM, by SEM analysis), some hypotheses can be made by simplifying its composition to a single material (e.g., SiO_2) of an equivalent thickness.

Fig. 5.1 is meant to explain some easy-to-use rules to define a first single RPP out of the experimental LEP, HEP and HI cross-section data. The figure shows the proton cross-section as a function of energy and the heavy ion cross-section as a function of LET. The arrows highlight some of the peculiarities of the two responses that can be used to model the single or nested RPP.

The green arrow points at the peak of the LEP cross-section. The geometric size of the single cubic RPP can be determined, in first approximation, as:

$$d_{RPP} = t_{RPP} = \sqrt{\sigma_{LEP,peak}} \tag{5.1}$$

In most of the cases assuming $t_{RPP} = d_{RPP}$ may be enough. However, it is noted that, for

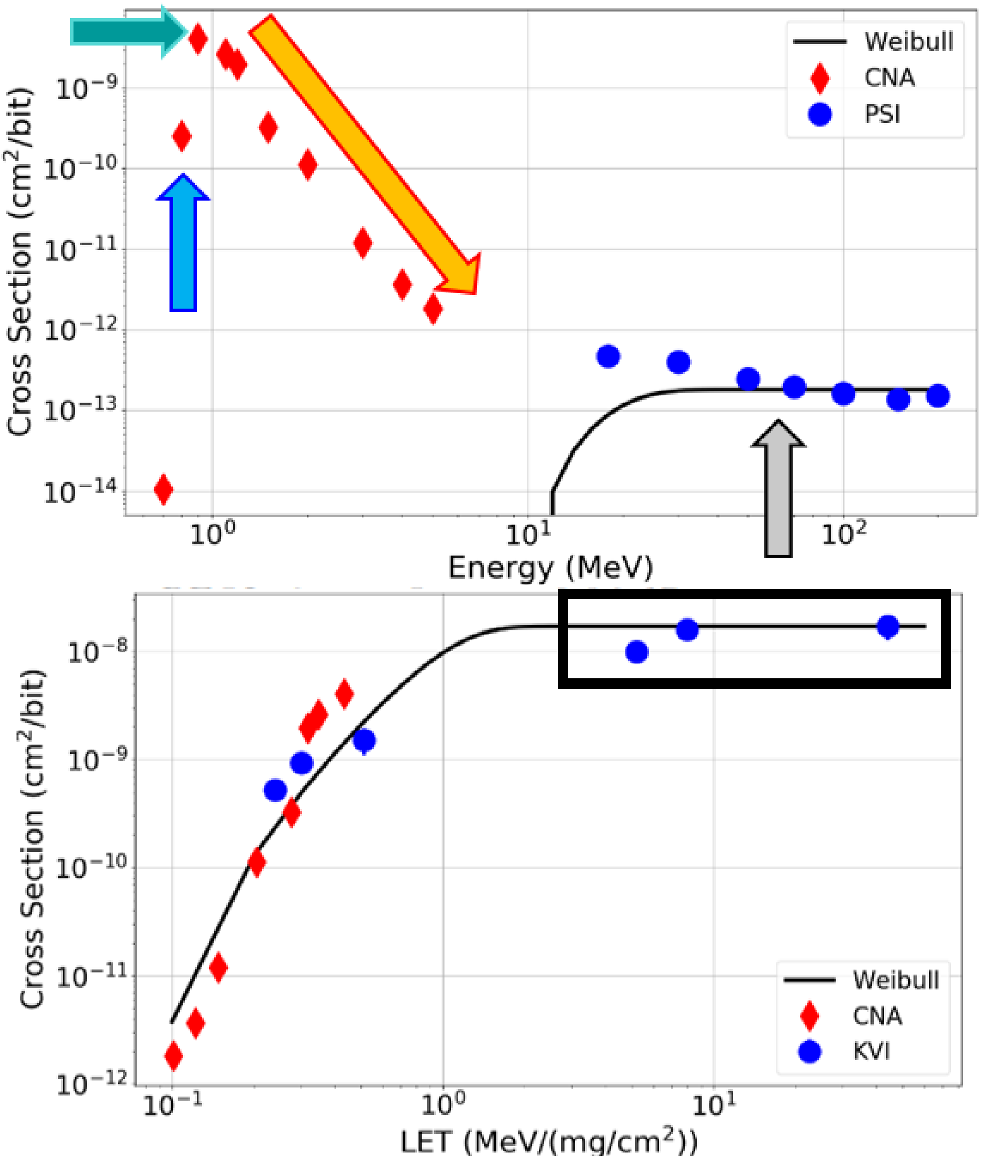

Figure 5.1: Modelling of single and nested RPP characteristics from the experimental LEP, HEP and HI cross-section data. The blue arrow indicates the reference energy to determine the BEOL thickness, the green arrow indicates the LEP peak to determine the SV size, the yellow arrow the slope needed to determine the SV thickness and the boxed HI data are used to generate the outer SVs in order to match the HEP data.

some SRAMs, a better representation of the response between the LEP peak and 10 MeV can be achieved by varying the thickness of the RPP. The example reported in the figure is that of the RADSAGA SRAM at 0.3 V. This is the case in which there is a clear benefit from varying the thickness of the SV (orange arrow). Typically, lower thickness at same critical charge will result in higher proton cross-sections.

As said, for commercial SRAMs BEOL thickness and composition are typically unknown. However, one can use the experimental LEP data and devise an equivalent SiO_2 thickness. Indeed, the cross-section at energies less than the LEP peak is not lower because the device is less sensitive to protons of these energies, but because there are less protons than those used to determine the cross-section (through the fluence as measured by the facility) that can reach the SV. Indeed, if there was no BEOL, the full low-energy curve would be shifted towards the proton Bragg peak ($\approx$ 50 keV). In the case in the figure (blue arrow) between 700 and 800 keV fewer and fewer protons can reach the SV. The BEOL can thus be built so that the cross-section out of MC simulations would be null in this energy range (or nearly null). As a result, for instance, it is determined that to have a null cross-section just below 800 keV for the RADSAGA SRAM one would need a BEOL with an equivalent SiO_2 thickness of around 12 μm.

Even if not shown directly in the graph, the experimental cross-sections have to be matched by using the same critical charge. Therefore, the critical charge is determined as the one that provides the best fitting to the whole experimental data-set for that RPP.

Building a single RPP upon the aforementioned design rules can allow a fair representativeness of the low- and intermediate-energy proton experimental cross-sections. However, in spite of any attempt at iteratively varying the parameters, it may not be possible to simultaneously match the LEP, IEP and HEP cross-sections by means of the single RPP. Typically, when the LEP (and IEP) cross-sections are matched, the HEP cross-sections are lower by a factor of 2 or more with respect to the experimental measurements. One of the reason behind this is that there is an impact from MCUs in the total HEP SEU cross-section (as there is in even larger abundance in the HI SEU cross-section).

The problem here is that often it is not possible to separate 1CUs from MCUs because the logical-to-physical mapping of the SRAM is not available. Nevertheless, it is noted that the heavy ion cross-section may exceed the size of the single physical cell (typically a 65 nm 6T SRAM has a cell surface of 0.5-0.7 μm^2 [146], which corresponds to d_{RPP} = 700-850 nm). Therefore, what it is retrieved is a single cell response that is no longer representative of the single cell, but that it is describing phenomena involving a larger set of cells, i.e., the MCUs.

The original idea behind the nested RPP model is not that of building a cell that could account for the impact of MCUs, though. Rather, it is that of considering an enhanced sensitivity to secondary ions produced by HEPs outside of the SV and depositing energy in its vicinity. This energy/charge is then collected to the SV by diffusion processes.

Anyhow, the main justification for using a nested RPP that can either take into account the energy deposition of these additional secondary ions or the MCU contribution is that, whether caused by one or the other, the upset rate in space will in principle follow the total HEP SEU cross-section. Therefore, building a model that can account for the total HEP SEU cross-section would provide more representative upset rates.

In order to achieve a higher HEP cross-section while leaving unaffected the LEP cross-section, the nested RPP technique, described in section 3.3.2, can be implemented on top of the single RPP. This makes use of the HI cross-sections (grey arrow and black box in Fig. 5.1) at high-enough LET with respect to that of LEPs to build secondary RPP volumes surrounding the single innermost RPP. Several recipes are available for this fitting technique that can allow to match the HEP cross-section. For the cases in this thesis, the various RPP sides have been built so that:

$$d_{RPP_i} = \sqrt{\sigma_{HI_i}} \tag{5.2}$$

On the other hand, the thickness of each SV is kept constant and equal to that of the initial single RPP ($t_{RPP_i} = t_{RPP_1}$).

Once integrated together the responses of each simulated RPP will provide a single energy deposition distribution that can be used to extract the cross-section and make sure that all the RPPs are set to the same critical charge (after application of the charge collection efficiency).

5.1.2 Sensitivity to the various parameters

In order to show how the various RPP parameters impact the proton SEU cross-section, with a particular focus on LEPs and IEPs, single RPPs with variable parameters can be compared by varying one of the parameters while keeping the others constant.

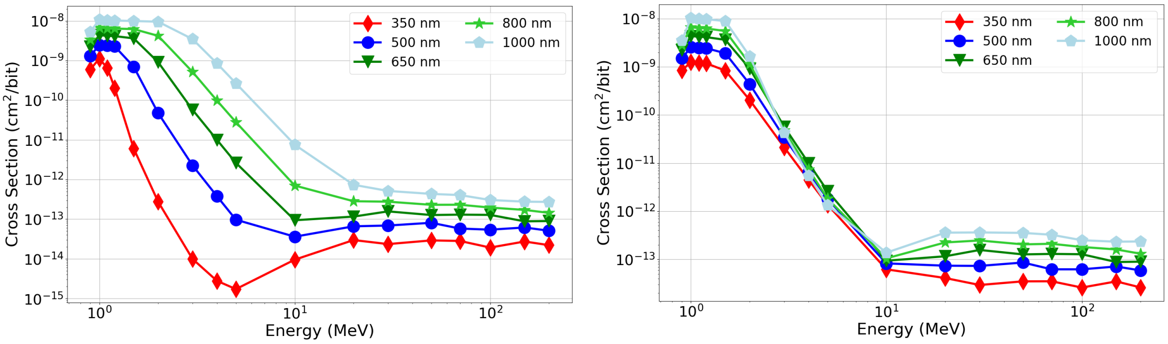

Figure 5.2: Variability of the proton cross-section with respect to the size of the cubic RPP: (left) critical charge is kept constant (0.96 fC), (right) LET threshold is kept constant (0.16 MeV/(mg/cm^2)). Obtained with FLUKA.

However, it is noted that while the RPP side d$_{RPP}$ is quite independent from the other parameters, the thickness of the RPP t$_{RPP}$ is intertwined to the relationship between the critical charge and the LET$_0$ of the device. Since in the first parametric analysis, cubic RPPs (hence d$_{RPP}$ = t$_{RPP}$) of various sizes are considered, the comparison is performed both at constant critical charge and at constant LET$_0$.

Fig. 5.2 depicts the proton SEU cross-sections of RPPs of various size (typical of deep sub-μm technologies). In the left side plot the critical charge is kept constant among the various RPPs, letting the LET$_0$ rescale according to the RPP thickness.

As earlier mentioned, the LEP peak cross-section will vary so that it tends to the size of the RPP surface (d$^2_{RPP}$). At the same time a larger RPP is also associated with a larger HEP cross-section. All these variations can be reconducted to the fact that having a larger surface will increase the probability that a proton will pass through the SV and either deposit enough energy to trigger a direct ionization upset or interact with a silicon nuclei and trigger an indirect ionization upset.

It is also noted that, when the critical charge is kept fixed among different volumes the largest variations in the cross-section are observed in the IEP region. This is due to the fact that with a thicker volume a larger amount of energy can be deposited in the SV also from protons with higher energy, i.e., the Bragg peak of IEPs is closer to the SV than for a thinner volume.

The right plot in Fig. 5.2 shows that this is no longer the case when the LET threshold is kept constant. All RPPs tend to have the same exact slope and IEP cross-sections due to the fact that it is always the same portion of the proton spectrum that can cause upsets by direct ionization.

The variations with respect to the RPP size, for constant LET$_0$ (Fig. 5.2, right), for LEPs and HEPs are notably very similar to those on the left plot (though, for HEPs the fixed Q$_{crit}$ brings wider spread than the fixed LET$_0$), which indicates that the cross-section here is not that sensitive with respect to the LET of the LEPs or to the LET of the secondary ions produced by HEP-silicon interactions.

As a second case, d$_{RPP}$ is kept constant, but t$_{RPP}$ is taken as free parameter in order to assess how the proton cross-section varies in thinner or thicker SVs.

Fig. 5.3 portrays the sensitivity of the proton cross-section for a SV with d$_{RPP}$ = 650 nm, whose thickness is varied from 250 to 1050 nm. In the left plot, the critical charge is again kept constant, while the LET$_0$ is allowed to vary according to the thickness of the RPP.

It is noted that the LEP peak cross-section is typically identical among all geometries of the RPP. Only for the very thin RPP the maximum is not reached due to the increase in the LET$_0$ that would, in that case, exclude a large part of the proton spectrum from causing

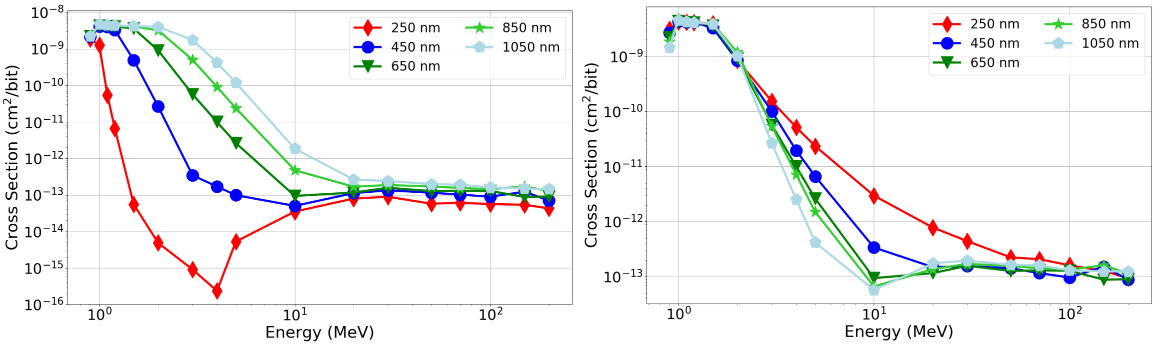

Figure 5.3: Variability of the proton cross-section with respect to the thickness of the RPP (with constant d_{RPP} = 650 nm): (left) critical charge is kept constant (0.96 fC), (right) LET threshold is kept constant (0.16 MeV/(mg/cm^2)). Obtained with FLUKA.

upsets. Concerning HEPs it is noted that the variability is much smaller than that achieved by varying the RPP side. This is due to the slight variation in LET$_0$ that can allow lower LET secondary ions to contribute to the response when the thickness is increased. Concerning IEPs, the situation is somewhat similar to that of the RPP side.

The right plot in Fig. 5.3 shows that, when the LET threshold is kept constant, the variability with respect to the thickness is almost negligible for LEPs and HEPs. In addition, when the thickness is larger than the side of the cube ($\geq$ 650 nm) the variability with respect to the thickness is also minimal for the IEPs. However, for thinner SVs, a shorter thickness forces the increase of both the IEP cross-section and a part of the HEP cross-sections.

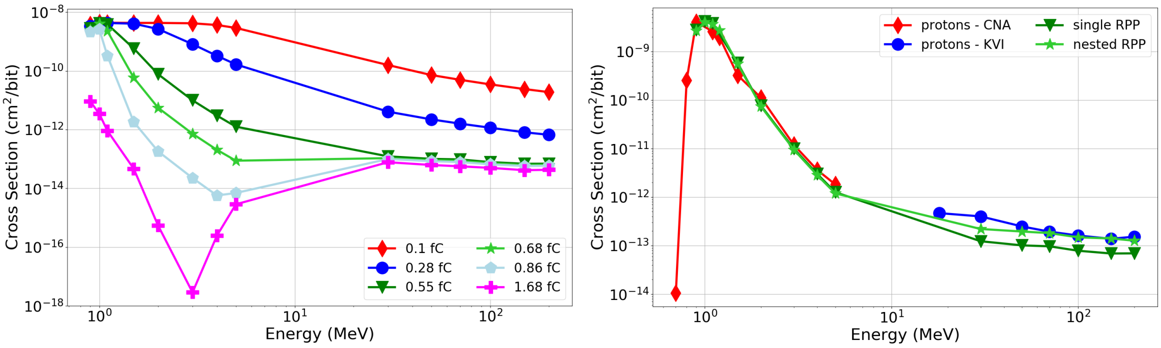

Figure 5.4: (Left) Variability of the proton cross-section with respect to the critical charge. The RPP here considered has d_{RPP} = 650 nm and t_{RPP} = 250 nm. (Right) Improvement of the HEP cross-section attained by means of the nested RPP for the RADSAGA SRAM compared against the single RPP with d_{RPP} = 640 nm and t_{RPP} = 250 nm and the experimental data. Obtained with FLUKA.

Keeping now the RPP geometry fixed, it is possible to assess the variability with respect to the critical charge (and given the fixed thickness, this would correspond also to a variation of the LET$_0$). An RPP with d_{RPP} = 650 nm and t_{RPP} = 250 nm is considered. Fig. 5.4 (left) depicts how the proton cross-section for this RPP would vary for critical charges in the 0.1-1.7 fC range. For information, the model that mostly resembles the RADSAGA SRAM experimental cross-sections for LEPs and IEPs is that with 0.55 fC.

It is evident that even slight variations of the critical charge can already yield very different results. For instance, for a critical charge of 0.28 fC (half of the most faithful one) the direct ionization effects would be important also at IEP and potentially at HEP energies, so that the cross-sections would be 1-2 orders of magnitude higher. On the other hand, increasing the critical charge by roughly 50% (0.86 fC) will even start to affect the LEP peak cross-section, bringing down the 1.1 MeV point and yielding slightly lower values at 0.9 and 1 MeV. The IEP cross-section would be underestimated by 2 orders of magnitude. In contrast, the HEP cross-section is not severely affected.

Going to the extreme case, the LEP peak cross-section is completely lost and so is the IEP behavior, whereas the HEP cross-section is just about a factor of 2 lower. This cross-section starts to be more similar to those of the 90 nm Cypress SRAMs [134].

The improvements provided by the nested RPP with respect to the single RPP for the RADSAGA SRAM in terms of HEP cross-section is depicted in Fig. 5.4 (right). Details of the model are reported in the next section. Thanks to the nested RPP the HEP cross-section is about a factor of 2 higher than with the single RPP, while not affecting neither the LEP or the IEP cross-sections. This improvement is necessary in order to be sure that, when the LEP upset rate will be compared to the HEP upset rate, the two are both reproduced in the best possible way.

Table 5.1: Single and nested RPP model for HEPs compared to the experimental 1CU, MCU and total SEU cross-sections for the Cypress 65 nm SRAM.

Energy (MeV)	σ_{1CU} **(cm^2/bit)**	σ_{MCU} **(cm^2/bit)**	σ_{SEU} **(cm^2/bit)**	$\sigma_{singleRPP}$ **(cm^2/bit)**	$\sigma_{nestedRPP}$ **(cm^2/bit)**
40	5.95 x 10^{-14}	3.83 x 10^{-14}	9.78 x 10^{-14}	3.80 x 10^{-14}	1.01 x 10^{-13}
80	5.06 x 10^{-14}	4.08 x 10^{-14}	9.14 x 10^{-14}	2.83 x 10^{-14}	9.05 x 10^{-14}
186	3.67 x 10^{-14}	4.06 x 10^{-14}	7.73 x 10^{-14}	2.58 x 10^{-14}	6.75 x 10^{-14}

Table 5.1 provides a comparison of the experimental 1CU, MCU (see defintion in eq. (4.4)) and total SEU cross-sections and the simulated single and nested RPP cross-sections for the Cypress 65 nm SRAM. The purpose of this comparison is to check whether the single RPP model, cleansed from the MCU events, is capable of reproducing also the HEP 1CU cross-section (as it does for the LEP 1CU cross-section). It turns out that the single RPP provides an underestimation of the 1CU cross-section in the order of 30-50%. Therefore, a nested RPP would be needed even to recover the 1CU HEP cross-section.

5.1.3 RPP models validation

Three devices were modelled for the LEP study. The information of each model is reported in Table 5.2.

For the ISSI SRAM three LEP data-sets are available and they differ consistently with each other. Given the previous analysis, it is clear that it will not be possible to fit all the experimental data with a single model. This is because both the LEP peak cross-section and the slope of the IEPs are different from one another and will require different RPP dimensions and critical charges. Given that the RADEF experimental data provide a worst case in terms of both the LEP and IEP responses (expected upset rate in space will be the highest) these data were taken for the modelling of the ISSI SRAM.

The single RPP of the ISSI SRAM is based on a cube of 310 nm with a BEOL with 6 μm SiO$_2$. As shown in Fig. 5.5, the proposed single RPP provides already a quite satisfactory match for the LEP and HEP experimental data without need of reiterating on a nested RPP. If the CNA data were to be used, on the other hand, given that the experimental HEP cross-section is common to the various LEP data-sets, a nested RPP would have been needed to fit the HEP data as well (LEP data requiring smaller RPP).

The ISSI experimental data were those affected by the largest discrepancies not only among LEP data-sets, but also among IEP data-sets and even when comparing LEP cross-

Table 5.2: RPP models for the three SRAMs under consideration. Reprinted from [109]. © 2021, Coronetti et al., licensed under CC BY 4.0.

ISSI SRAM		
BEOL 6 μm, $Q_{crit} = 0.96$ fC		
SV side (nm)	**SV thickness (nm)**	α
310	310	1

RADSAGA SRAM		
BEOL 12 μm, $Q_{crit} = 0.55$ fC		
SV side (nm)	**SV thickness (nm)**	α
638	250	1
996	250	0.077
1304	250	0.050

Cypress 65 nm SRAM		
BEOL 10 μm, $Q_{crit} = 0.86$ fC		
SV side (nm)	**SV thickness (nm)**	α
360	360	1
984	360	0.057
1612	360	0.037
3160	360	0.007

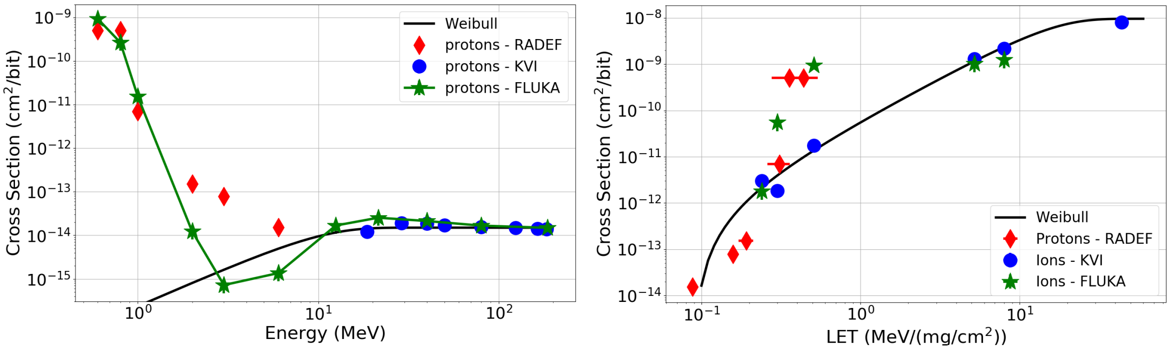

Figure 5.5: Comparison between experimental and numerical cross-sections of mono-energetic LEPs and HEPs (right) and LEPs and HIs (right) for the ISSI SRAM. Concerning simulations in the right plot, note that only ion simulations are reported. Obtained with FLUKA. Reprinted from [109]. © 2021, Coronetti et al., licensed under CC BY 4.0.

section with those of ions with same LET. The figure clearly shows that the IEP part of the proton curve is the one that mostly diverges from the experimental data. In the paper [109] it was shown that this part of the curve is not so important when it comes to convert the cross-section into an upset rate in space. This is because in this energy region the fluxes are comparable to those from LEPs, but the cross-section is already 3-4 orders of magnitude lower. In particular, reducing the thickness of the RPP would have enhanced the cross-section in the IEP area. However, it would have also enhanced that around the LEP peak (for, e.g., 1 MeV), causing a much higher LEP upset rate with little gain on the IEP uspet rate accuracy.

Concerning the ion simulations, it is shown that this single RPP can provide reliable estimations for high-LET ions as well as for the lowest LET carbon data-point. On the other hand, the estimated MC cross-section for the other carbon ions with slightly larger LET progressively diverge from the carbon data-points, while converging to the LEP data-points. This is not so surprising considering that for both proton and ions of similar LET the main mechanism of upset is coming through direct ionization.

Therefore, FLUKA and the physics of direct ionization seem to confirm that the cross-sections of protons and ions in this LET region should coincide. In this case, it is not possible to explain the mismatch by the lack of some physics in FLUKA given that identical results were found with Geant4 based tools like G4SEE and CREME. The most likely explanation is some data mismatch either due to the energy-LET or fluence measurement at the facility. Indeed, it is noted that this energy region is close to the LET threshold of the modelled RPP (the cross-section changes by two orders of magnitude between carbon ions of 0.24 and 0.5 MeV/(mg/cm^2)). Therefore, an even slight uncertainty on these parameters can drastically affect the result.

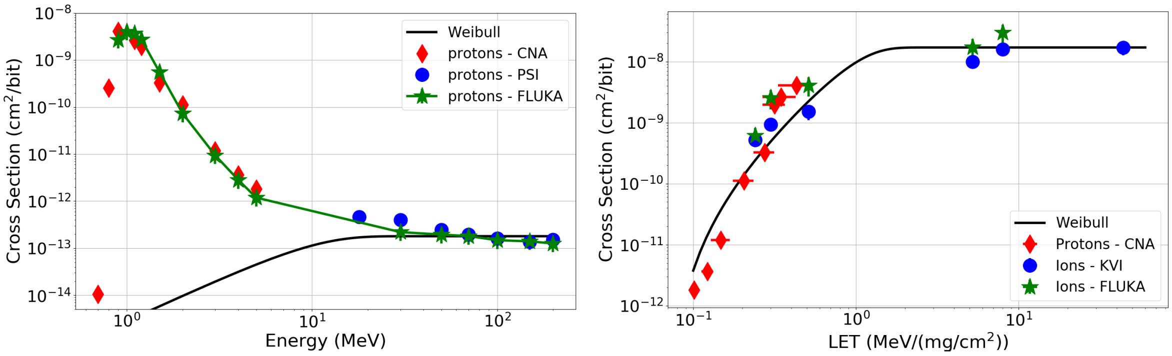

Figure 5.6: Comparison between experimental and numerical cross-sections of mono-energetic LEP and HEP (left) and LEP and HI (right) for the RADSAGA SRAM (0.3 V). Note that in the right plot only ion simulations are reported. Obtained with FLUKA. Reprinted from [109]. © 2021, Coronetti et al., licensed under CC BY 4.0.

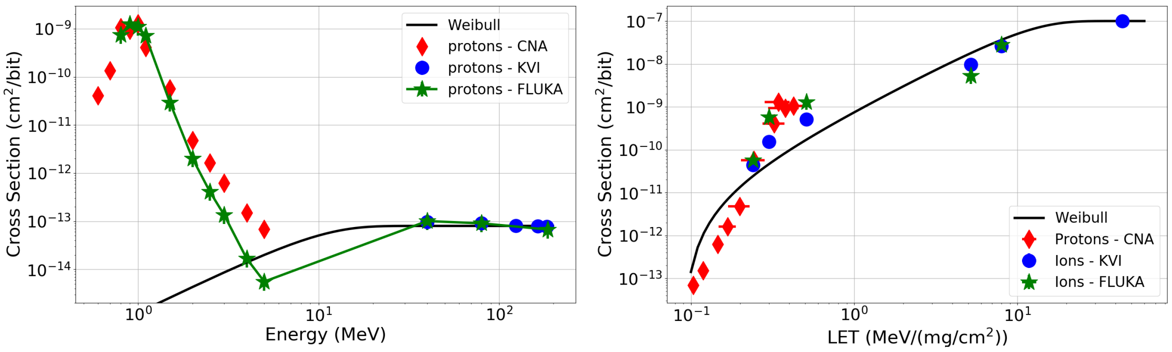

Figure 5.7: Comparison between experimental and numerical cross-sections of mono-energetic LEP and HEP (right) and LEP and HI (right) for the Cypress 65 nm SRAM. Note that in the right plot only ion simulations (for carbon and argon ions used during the KVI-CART experiments) are reported. Obtained with FLUKA. Reprinted from [109]. © 2021, Coronetti et al., licensed under CC BY 4.0.

For the RADSAGA and Cypress 65 nm SRAM it was necessary to rely on the nested RPP due to the insufficient fitting of the HEP data. Some details about the difference between single RPP and nested RPP were provided in section 5.1.2.

Fig. 5.6 presents the comparison between the experimental data and the numerical data of the nested RPP used for the RADSAGA SRAM when the core voltage is set to 0.3 V. Given the LEP peak cross-section, an RPP side of 640 nm was selected. However, the IEP cross-section did not decrease as fast as for the other memories. Therefore, in this case the thickness was progressively reduced from 640 nm to 250 nm to obtain the almost perfect matching depicted in the figure.

The critical charge for this memory was set to 0.55 fC and the BEOL was initially set to 12 μm of SiO_2. In order to fit the HEP data, two outer RPP volumes were added based on the argon ion experimental data. The Xenon data-point was not considered because the cross-section is already in saturation for the higher LET argon point. The data for these additional volumes are reported in Table 5.2 along with the charge collection efficiency (α), which, given the shared thickness among the three SVs, reduces to the ratio between the LEP peak LET (0.4 MeV/(mg/cm^2), it is noted that the results are almost unaffected if the maximum proton LET is used instead) and the ith ion LET.

The RPP model of the RADSAGA SRAM also shows quite good agreement to light and heavy ion data, even though it is still possible to note that the simulated carbon ion data tend to converge more towards the LEP experimental data than the ion experimental data themselves.

The Cypress SRAM followed a similar approach to the RADSAGA SRAM for the modelling. All data for this model are reported in Table 5.2. Fig. 5.7 presents the model validation for this SRAM. It is noted that the model well fits the LEP and HEP data. There is still some discrepancy in the IEP region, which is again negligible for upset rate calculations. Observations for ion data are the same as those for the RADSAGA SRAM.

Coming back to the appropriateness of the nested RPP model for a single cell, the RADSAGA SRAM, despite being manufactured in 65 nm technology, does not respect the construction standards and has SRAM cells with a surface of 1.78 μm^2 (or cell side of 1.33 μm). Interestingly, the largest volume of the nested RPP has a side of 1.30 μm, therefore, the nested RPP can be considered appropriate to describe the bit flip sensitivity of the individual cell.

On the other hand, for the Cypress 65 nm SRAM, though it is not known which is the exact size of the SRAM cell, it is clear that if standards are taken [146], at least the third (1.6 μm side) and fourth (3.1 μm side) largest volumes would be much larger than the size of a single 6T SRAM cell. Therefore, in this case, the nested RPP is forcing the responses of multiple cells on top of that of a single cell. This is confirmed by the earlier reported MCU analysis.

5.1.4 Angular dependency

The models were validated against proton and ion experimental data at normal incidence. Although data at different angle of incidence are not available, it is worthwhile to show what would be the response of the various RPPs to proton beams arriving at the SV with different angles of incidence. This is because later these models are used to calculate the response under 4π sr proton and ion fluxes representative of the actual configuration in space.

Fig. 5.8 reports the simulated proton cross-sections as a function of energy for the RPP models of the RADSAGA, ISSI and Cypress SRAMs, for different angles.

The plots have some characteristics in common. It is noted that the HEP response is not strongly affected by the angle of incidence. This is because indirect ionization is the dominant process.

On the other hand, the LEPs and the IEPs can be more severely affected. It is noted that the peak LEP cross-section is seen to be lower at increasing angle of incidence. This is in good agreement with experimental findings showing that the normal incidence cross-section for bulk silicon SRAM is worst case at normal incidence [77].

It is also noted that the peak LEP cross-section moves towards higher energies with increasing angle of incidence. This is consistent with the longer path of the LEPs through the BEOL that makes higher energy protons more likely to arrive at the SV with very small residual kinetic energy (and higher LET) than in the normal incidence case.

At the same time, it is noted that the cross-section, at lower energies than the LEP peak and at an angle of incidence $> 0°$, is not null, but it is usually around one order of magnitude lower than it was at normal incidence.

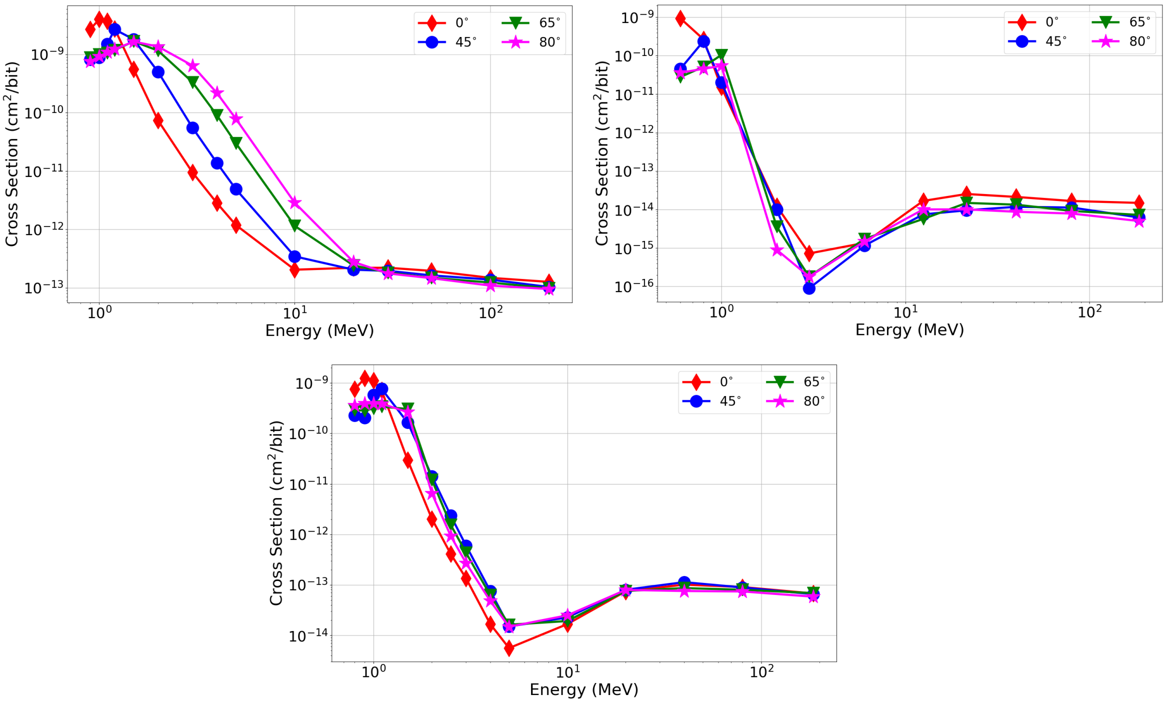

Figure 5.8: Angular response of the RPP models of the RADSAGA (top left), ISSI (top right) and Cypress (bottom) SRAMs. Obtained with FLUKA.

For the IEPs, the data differ from one SRAM to the other. For the RADSAGA SRAM the shift of the LEP peak also involves a much higher cross-section at energies up to 10 MeV. On the other hand, no big effect is seen for the ISSI and Cypress SRAM.

5.2 Proton upset mechanisms with varying energy

5.2.1 A comparison between FLUKA and Geant4

As earlier introduced, in the context of this LEP study it was possible to identify some issues related to the current implementation of the MC SEE tools implemented with FLUKA.

Fig. 5.9 depicts the numerical FLUKA and G4SEE cross-sections with respect to the experimental data. The RPP models used in FLUKA and G4SEE are identical for every parameter. However, while the two models well agree for the LEPs and the HEPs, they diverge in the IEP region. FLUKA returns a much lower cross-section than that of experiments. On the other hand, G4SEE is much more accurate at 2 and 6 MeV and shows just a larger underestimation in between. Therefore, the model developed in FLUKA would be even more accurate than what was portrayed in the previous section if the missing energy deposition events where to be scored.

The reason behind these differences in the IEP region can be attributed to how differently the single physical processes are handled within FLUKA and G4SEE. Fig. 5.10 depicts the SEU cross-section contributions of the nuclear elastic and the nuclear inelastic processes as calculated with FLUKA and G4SEE for the ISSI SRAM in the 3-20 MeV energy range when the critical charge is varied.

The differences between the inelastic processes in FLUKA and G4SEE are minimal (if the 3 MeV case is excluded, though the inelastic process is anyway negligible for G4SEE, too).

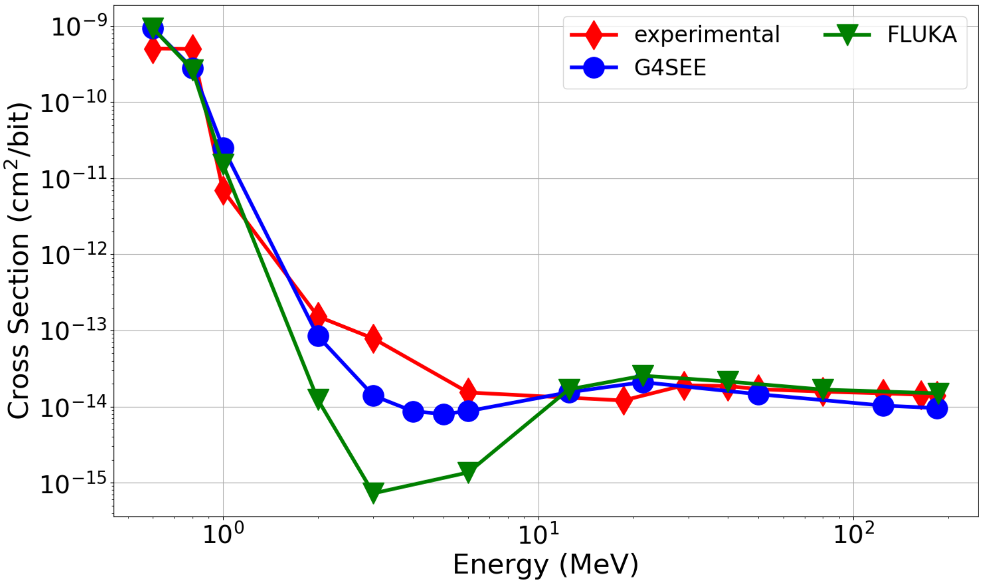

Figure 5.9: Comparison between the numerical cross-sections as determined from FLUKA and G4SEE for the same identical single RPP proposed for the ISSI SRAM. The experimental data are also shown.

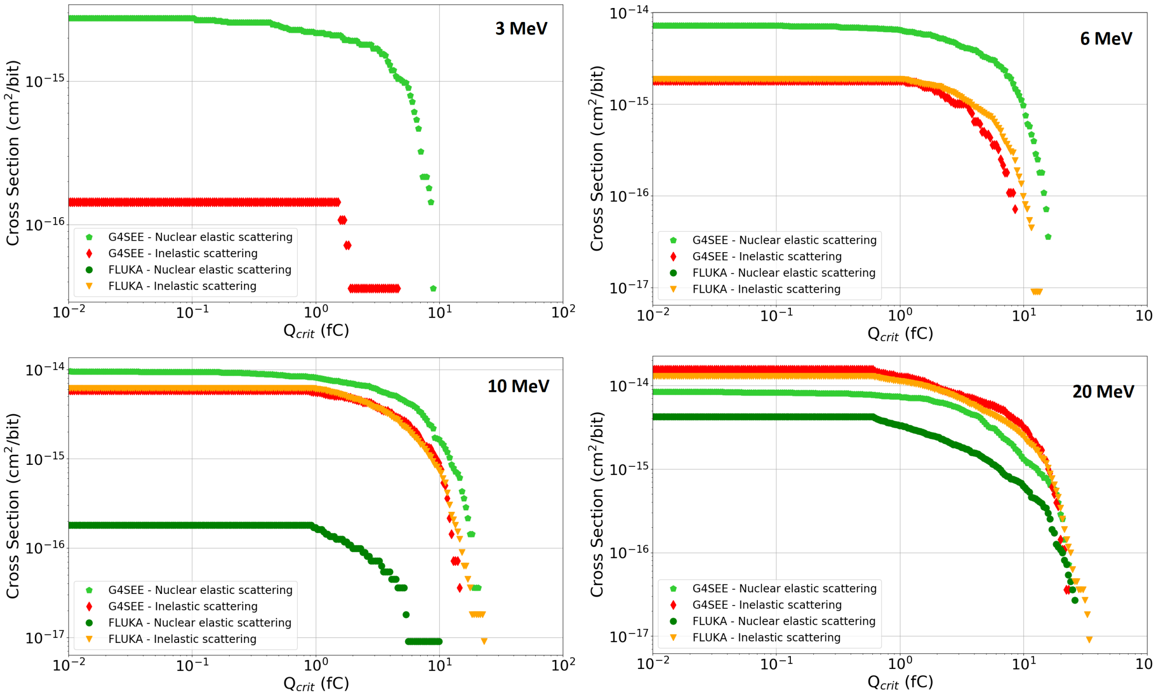

Figure 5.10: Comparison between the numerical nuclear elastic and inelastic contributions to the cross-sections, as determined from FLUKA and G4SEE, for the same identical single RPP proposed for the ISSI SRAM.

The nuclear elastic process in FLUKA is internally enabled only starting at 10 MeV. As it is clear from the plot, the absence of this process has a major impact on the estimation of the total SEU cross-section, given that it is the most important according to G4SEE for the 3-10 MeV interval and is also significant at 20 MeV.

In addition to the energy threshold for the process, one can note that there are quite important differences between the nuclear elastic process of FLUKA and G4SEE for the energies of 10 and 20 MeV that can also impact the total SEU cross-section. Therefore, it seems that there can be other discrepancies on how the models are actually implemented in FLUKA and Geant4.

Although the Coulomb single and multiple elastic scattering are not shown, it is noted that, while the processes are actually simulated in terms of kinematics, energy deposition events from these processes are not scored in FLUKA at the moment. Therefore, their contribution to the SEU cross-section is null at every energy. In G4SEE these processes are present and their impact on the SEU cross-section is discussed in the next section.

5.2.2 Contribution of all the processes to the SEU cross-section

As shown in Fig. 5.9, G4SEE can reproduce with better fidelity the proton cross-section at intermediate energy. However, the potentialities of G4SEE allow having a deeper look into the proton SEU mechanisms at basically any energy and to examine the contribution of various relevant processes.

G4SEE simulations of the ISSI RPP were run to calculate the SEU cross-section resulting from various physical processes. These processes are either electro-magnetic interactions such as the direct ionization and the Coulomb elastic scattering (single and multiple) or nuclear interactions such as nuclear elastic scattering and nuclear inelastic scattering.

As earlier shown, MC simulations enable a prompt assessment of the data with respect to parameters such as the critical charge (or the LET threshold). Data for energies of 1-186 MeV are presented in Fig. 5.11.

The eight plot figure allows assessment of what happens at each energy and how slowly things change as the primary proton energy is increased. The critical charge of the ISSI SRAM can be taken to be around 1 fC.

For 1 MeV (and also lower energies) only electro-magnetic processes are active. Therefore, there are no energy deposition events generated by nuclear interactions of protons and silicon. The direct ionization mechanism is largely dominating over the Coulomb elastic scattering. However, the latter is the reason why, for SRAMs with higher critical charge (not sensitive to direct ionization), one could still see a small amount of events even down to this energy.

At 2 MeV nuclear elastic interaction channels open. The only process available is the nuclear elastic scattering, though. And, as one can see, while the deposited energies are similar to those from Coulomb elastic scattering, the probability of such events is one order of magnitude lower. Considering the global cross-section, at 2 MeV it is still dominated by the direct ionization, though there start to be a small contribution from the Coulomb elastic scattering.

At 3 MeV also the nuclear inelastic scattering channels open, although their contribution is completely negligible. Nuclear elastic scattering, on the other hand, is now as important as Coulomb elastic scattering. Together these two processes contribute in keeping the cross-section around 10^{-14} cm^2/bit. Indeed, at 3 MeV direct ionization for the critical charge of 1 fC becomes less important and contribute for only a small fraction to the total SEU cross-section.

Moving to 6 MeV, the nuclear elastic scattering has further increased so that it becomes the dominant mechanism for the reference critical charge. On the other hand, the probability of Coulomb elastic scattering energy deposition events is starting to decrease and it is very similar to that of inelastic scattering.

At 10 MeV the contribution of the nuclear inelastic scattering process starts to be important and, along with nuclear elastic scattering contributes to the SEU cross-section at the reference critical charge. The main difference is that nuclear elastic scattering still yields events depositing higher energy than inelastic scattering. Both electro-magnetic processes are negligible from this energy upwards.

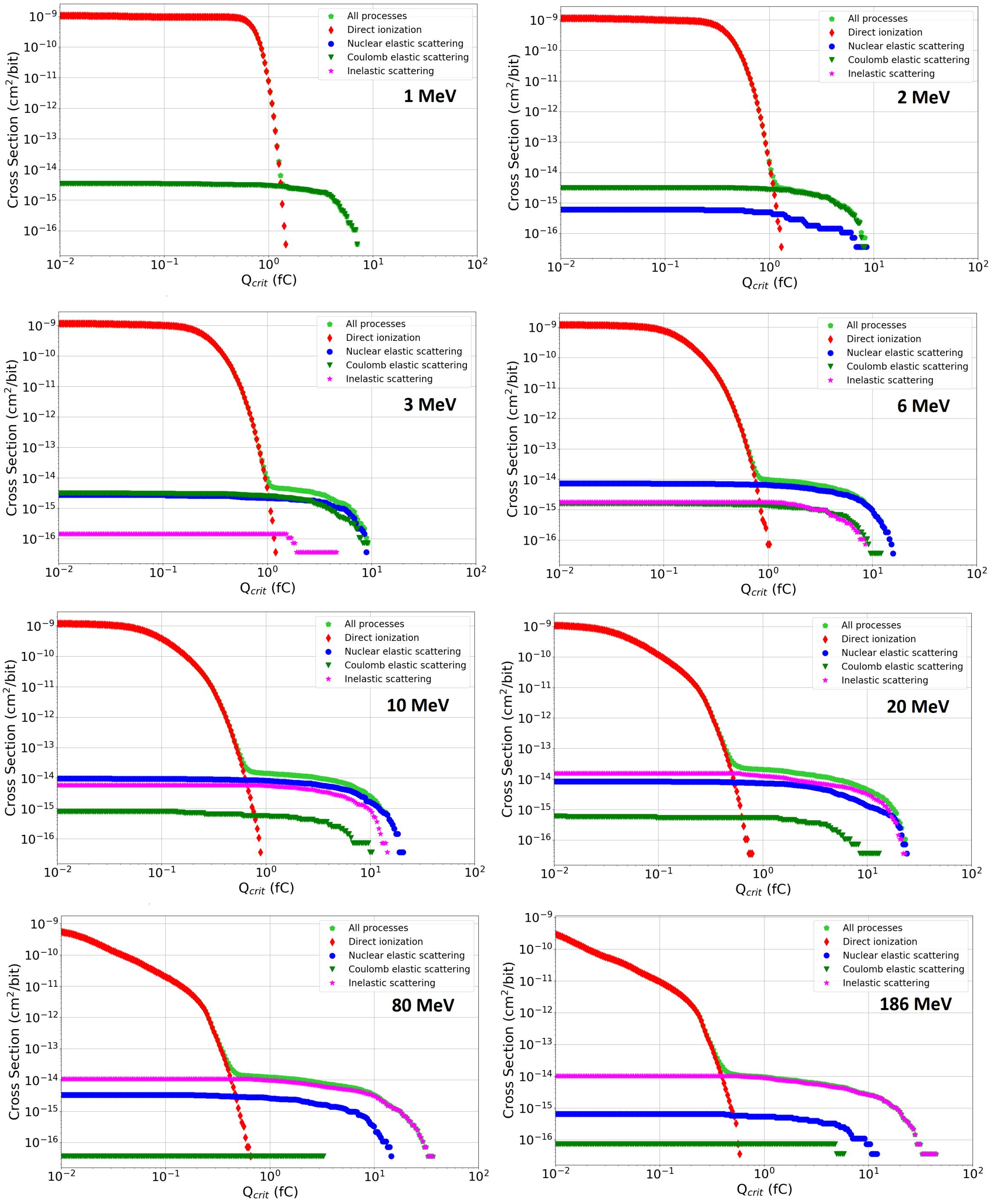

Figure 5.11: Contributions to the proton SEU cross-section of various interaction mechanisms as a function of the proton energy and the critical charge for the ISSI RPP. Obtained with G4SEE.

At 20 MeV inelastic scattering overtakes nuclear elastic scattering, though both contributions are almost equally important and reach the same level of deposited energy.

At increasing energy the differences between nuclear inelastic and elastic scattering keep on growing. At 80 MeV, inelastic scattering is the most important contributor to the cross-section, though nuclear elastic scattering still contribute for a small part. It is also noted that the inelastic scattering now yields energy deposition events with higher energy than nuclear elastic scattering.

At 186 MeV, the difference between the two nuclear processes are much higher. To the point that, nuclear inelastic scattering is dominating the response thanks to the much higher probability and the higher energies involved.

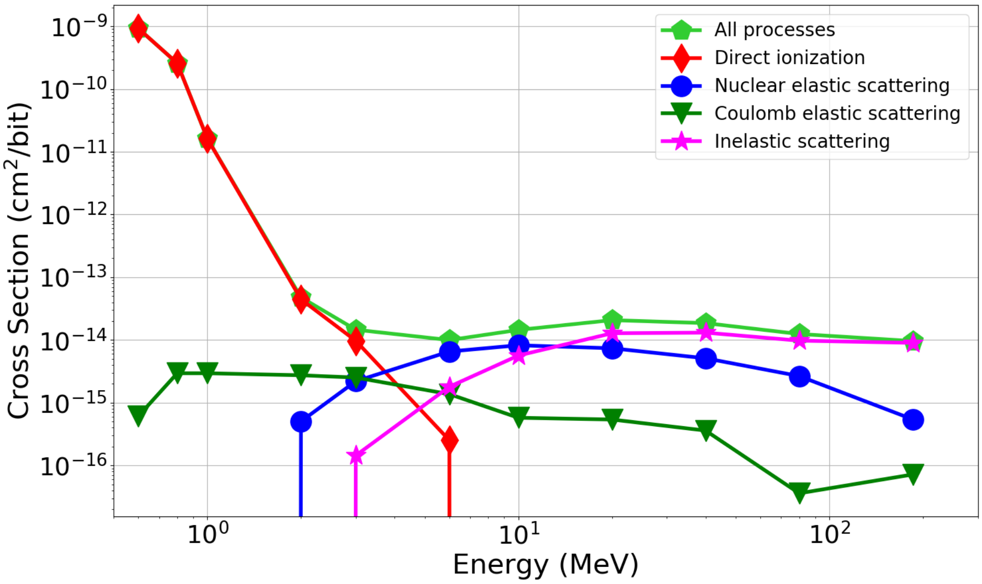

Figure 5.12: Proton SEU cross-section of various interaction mechanisms as a function of the primary proton energy for the ISSI SRAM. Obtained with G4SEE.

The findings from these plots can be also summarized by showing the proton SEU cross-section for each process and how it varies as a function of the proton primary energy. This is shown in Fig. 5.12.

As one can see, things change significantly for each process as the energy is varied. Direct ionization is dominant up to 2 MeV and also still quite important at 3 MeV, though it becomes negligible at 6 MeV. All in all, the direct ionization SEU cross-section sharply decreases with increasing energy.

The Coulomb elastic scattering cross-section is always below 3 x 10^{-15} cm^2/bit. This shows that this process is in most of the cases negligible and, as earlier mentioned, plays a role only in the 3-6 MeV energy region where nuclear processes still have to develop and direct ionization falls rapidly.

Nuclear elastic scattering processes are not relevant below 2 MeV. From there, the related cross-section increases reaching an absolute maximum at around 10 MeV. However, the process remains important for a quite large energy range and starts fading only above 50 MeV. Therefore, it is noted that nuclear elastic scattering seems to be the reason why the proton SEU cross-sections are higher at 20-50 MeV in highly integrated technologies than at energies $>$ 100 MeV. Therefore, the increase in the nuclear inelastic cross-section at these lower energies (recall Fig. 3.2) is not the responsible mechanism.

Finally, the nuclear inelastic scattering seems to have a threshold at around 3 MeV and starts becoming important only at 10 MeV and dominant only above 50 MeV. At even higher energies, nuclear inelastic scattering is expected to remain the only relevant process.

5.3 Prediction methods and the D-factor

5.3.1 Methods for calculating the LEP upset rate

The reason why some stress was put upon the fidelity of the SV models in representing both LEP and HEP cross-sections is that the resulting RPP can be directly submitted to a simulation having as input a radiation environment composed of the proton and/or ion spectra (e.g., any space orbit). This way a MC calculation can directly provide the upset rate from the various components of the spectra (i) without need to rely on any other prediction model and (ii) allowing to determine the relative contribution of LEPs, HEPs and HIs to the total upset rate.

For these kind of simulations the RPP and the surrounding materials are kept identical to the previous beam simulations. However, the particle spectra are transported through a metal shielding given that typically electronics is never exposed directly to the outer space, but it is stored inside electronic boxes meant to ensure, among others, thermal insulation. The most standard approach for space shielding consist in using a spherical aluminum cover of equivalent thickness. Typically, 100 mils of aluminum are assumed for upset rate calculations in space missions. However, sometimes, this is not that realistic and a larger or smaller thickness may have to be employed.

As a result, the transported proton and ion spectra will maintain their isotropic nature before reaching the semiconductor materials. Note that the RPP response to some of the space particles may change according to the angle of incidence of arrival. Nevertheless, the RPP models that were set up were validated only against experimental cross-sections collected with normally incident protons and ions (given that data at a different angle of incidence were not collected at the time of the experiments). Therefore, the isotropic response of the RPP is that derived from the models defined at normal incidence through simulations and it is not possible to say whether the data in section 5.1.4 would fit actual measurements.

No prediction method for the upset rate from LEPs is currently standardized and widely accepted. As introduced in Chapter 2, a few methods have been proposed. The most standard way of calculating the upset rate would be to apply the same techniques that are used for HEPs and HIs. Weibull fitting is one of them and it is based on the convolution of a cross-section function (the 4-parameter Weibull) with the proton or ion spectra in the orbit of interest. The 4-parameter Weibull, however, does not allow describing the low-energy part of the proton SEU response.

In this vein, a technique based on the energy convolution of the experimental data can be set up. A piece-wise linear approximation from one data-point to the next is used for this purpose (a different interpolating function can also be devised).

Given the huge uncertainty on the actual LET of the protons reaching the SV, the LET convolution of the low-energy proton spectra is not considered as a viable calculation method.

Lastly, as suggested by Dodds, experimental measurements from a degraded proton beam were shown to be a promising way of calculating upset rates from LEPs, but such experimental data are not available in the framework of this thesis. Therefore, in the paper [109], an approximated method was used instead.

Concerning HEPs and HIs, on the other hand, the well established Weibull function convolution with proton and ion spectra should provide the most reliable estimation. These are also used in the Dodds' method, for instance.

Table 5.3 reports the upset rate from LEPs, HEPs and HIs calculated according to the earlier introduced methods. The data for the upset rate from LEPs are all quite consistent, i.e., the maximum variations is of a factor of 3. For HEPs the methods to compare are the first three and they provide and agreement better than a factor of 2 for all devices.

For HIs only two methods are available, the MC simulations and the Weibull. Though small discrepancies within a factor of 3 are again present for the RADSAGA and the Cypress, more than one order of magnitude difference was found for the ISSI. The discrepancies are indeed due to the fact that the RPP is built upon the LEP data and, thus, at low-LET the cross-section follows the LEPs even in the case of the light ions, while this is not the case for the Weibull convolution (which is only based on the ions). Indeed, the offset seems to be very in line with the observed experimental differences.

Table 5.3: Comparison of upset rate prediction methods for LEP, HEP and HI for the RADSAGA, ISSI and Cypress SRAMs. The ISS environment is used for all methods (500 km, 51.6°, solar min, 100 mils Aluminium). The upset rate units are events/bit/day. MC refers to FLUKA. Reprinted from [109]. © 2021, Coronetti et al., licensed under CC BY 4.0.

RADSAGA			
Method	$\mathbf{UR}_{HEP}$	$\mathbf{UR}_{LEP}$	$\mathbf{UR}_{HI}$
Energy convolution	5.42×10^{-7}	8.49×10^{-6}	X
Weibull	4.57×10^{-7}	X	2.65×10^{-7}
MC environment	3.04×10^{-7}	1.47×10^{-5}	4.07×10^{-7}
Convolution Dodds	4.57×10^{-7}	1.43×10^{-5}	2.65×10^{-7}
MC Dodds	4.57×10^{-7}	4.85×10^{-6}	2.65×10^{-7}
ISSI			
Energy convolution	4.06×10^{-8}	6.27×10^{-7}	X
Weibull	3.81×10^{-8}	X	3.90×10^{-9}
MC environment	2.33×10^{-8}	5.76×10^{-7}	5.34×10^{-8}
Convolution Dodds	3.81×10^{-8}	1.20×10^{-6}	3.90×10^{-9}
MC Dodds	3.81×10^{-8}	9.12×10^{-7}	3.90×10^{-9}
Cypress			
Energy convolution	2.25×10^{-7}	1.92×10^{-6}	X
Weibull	2.03×10^{-7}	X	4.02×10^{-8}
MC environment	1.58×10^{-7}	1.88×10^{-6}	1.10×10^{-7}
Convolution Dodds	2.03×10^{-7}	3.41×10^{-6}	4.02×10^{-8}
MC Dodds	2.03×10^{-7}	1.32×10^{-6}	4.02×10^{-8}

This is the reason why in [109] the heavy ion MC results were discarded for all devices and the Weibull convolution was used instead in analogy to the Dodds' method.

Finally, note that, for all the targeted SRAMs, the UR_{LEP} is always from a minimum of a factor 10 to a maximum of a factor of 100 larger than the UR_{HEP} and UR_{HI}.

5.3.2 Results for some orbits and shielding

The paper [109] provides an extensive assessment of the reciprocal and absolute variability of the upset rates from LEPs, HEPs and HIs in a few selected orbits that will not be re-listed again here (the data are based on trapped protons and GCRs for LEO and also SPEs for GEO worst day). In general it is observed that LEPs may be of concern for all LEO missions, no matter the altitude and the inclination, due to the high LEP fluxes. On the other hand, for the GEO in quiet conditions, the LEP fluxes are quite low if compared with the HEP fluxes. Therefore, LEPs do not contribute significantly to the total upset rate. However, during stormy conditions, also GEO missions can suffer from LEP events in measure comparable to those of a medium altitude LEO mission.

Overall, the LEP contributions to the upset rate (no matter the calculation method) were found to contribute for 65-99% of the total upset rate. Therefore, for many instances and for these very devices LEPs are expected to be a potentially dominant contributor to the total upset rate.

The paper [109] also provides some analysis about shielding by comparing the 100 mils of equivalent aluminum case to that with 500 mils of aluminum.

5.3.3 D-factor

The D-factor is a good metric to quantify the impact that direct ionization can have on the total upset rate. It can be defined as the ratio between the total upset rate, including also the LEPs, and the upset rate that would result only from HEP and HI sensitivities:

$$D = \frac{UR_{HEP} + UR_{HI} + UR_{LEP}}{UR_{HEP} + UR_{HI}} \tag{5.3}$$

By definition, the D-factor is 1 when the LEP contribution to the UR is negligible with respect to the sum of the other two. On the other hand, when LEPs are no longer negligible the D-factor can be considered as a safety margin that can be applied to the upset rate calculated at the denominator to account for the LEP contribution without performing dedicated testing. For instance, when the D-factor is equal to 2, it means that LEPs alone will contribute to 50% of the total upset rate, while the remaining 50% will be caused by the HEP and HI combined. Above D = 5, LEPs will contribute for more than 90% to the total upset rate (dominant contributor).

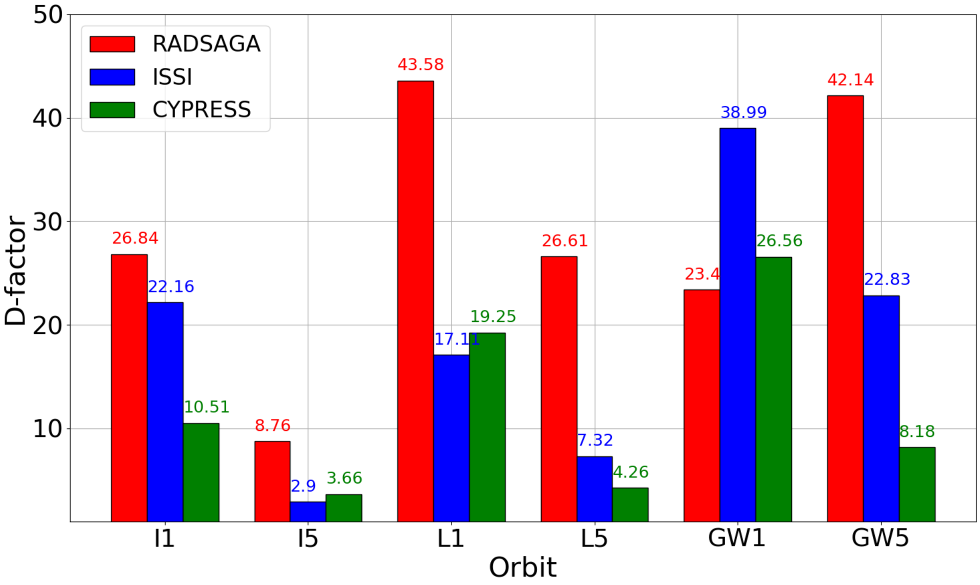

Figure 5.13: D-factors for three space environments (ISS, a medium altitude LEO and the GEO stormy conditions) and two shielding configurations (100 and 500 mils of Al). Data were calculated based on the FLUKA MC simulations of the RPP models of the three devices.

Fig. 5.13 reports the D-factors calculated for three space environments and two shielding configurations for the three targeted SRAMs. The D-factors were calculated following FLUKA MC simulations of the proposed RPPs for HEP and LEP responses and using the Weibull response for HIs. The orbits under consideration are the ISS (I1 and I5), a LEO with 1400 km altitude and 52° inclination (L1 and L5), and the GEO under worst day solar storm conditions (GW1 and GW5).

As the figure shows, for these three devices, the D-factor is typically larger or much larger than 1. This indicates that the LEPs are expected to be an important, or even dominant, contributor to the total upset rate no matter the orbit or the shielding configuration. The RADSAGA SRAM, in particular, can reach D-factors of even 40 for a couple of conditions.

Typically, the targeted LEO, which is deep into the Earth's proton belt, is very impacted by the presence of LEPs. On the other hand, by comparing with the data in the paper [109], it is clear that the LEPs become important for GEO only under solar storm conditions, whereas they have only a minor or negligible contribution in quiet conditions.

Shielding is usually beneficial, although the D-factors do not scale in the same manner for different memories and orbits. This may be concerning considering that the sensitivity with shielding can thus depend both on the actual device response and on the orbit, which makes it harder to generalize.

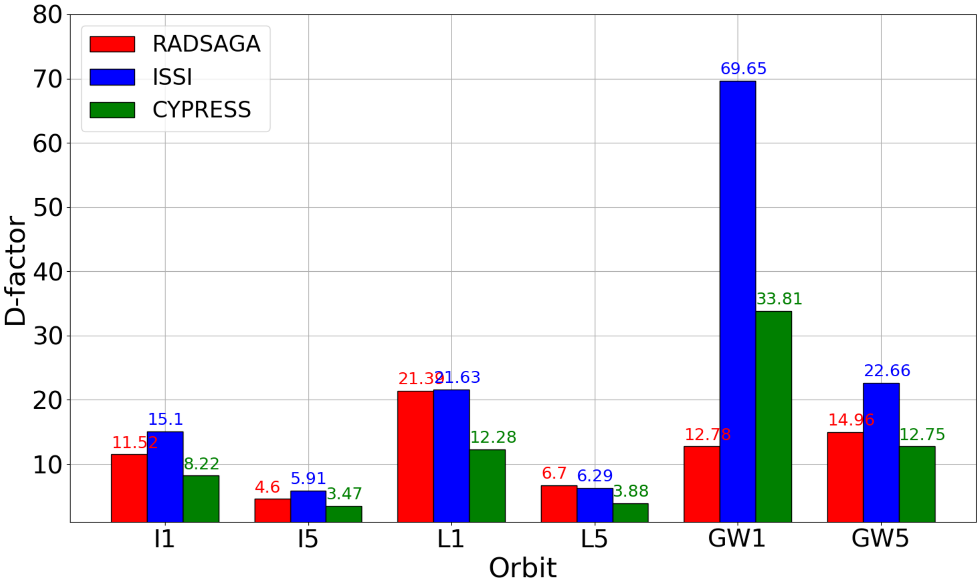

Figure 5.14: D-factors for three space environments (ISS, a medium altitude LEO and the GEO stormy conditions) and two shielding configurations (100 and 500 mils of Al). Data were calculated based on the energy convolution of the experimental cross-sections for the three devices.

Fig. 5.14 shows the D-factor calculated for the same devices and conditions, but by relying on the energy convolution. The HI upset rate is again based on the Weibull interpolation of the ion data only. This upset rate calculation method provides D-factors which can differ by even a factor of 3 with respect to those from MC and are typically lower. The general conclusion, however, is unchanged. Even with the energy convolution method the D-factors are larger, or much larger, than 1. Therefore, the LEPs are still the most significant, and sometimes dominant, contributor to the total upset rate.

It is noted that typically the RADSAGA SRAM is the one for which the D-factors are lower for energy convolution than for MC simulations. One possible explanation is that using this mono-directional response as a proxy to the response to isotropic fluxes for LEPs may lead to stronger underestimations for this SRAM due to its particular high cross-section not only at the LEP peak, but also in the IEP region.

For the ISSI SRAM the situation is less obvious. In some of the cases, the energy convolution can return an even higher upset rate than the MC simulations, e.g., by almost a factor of 2 for GW1, whereas for other cases it is either equal or slightly lower. One possible explanation in this case is that the energy convolution is based on the RADEF data, which are not as numerous around the peak LEP cross-section as those measured at CNA. Therefore, when performing energy convolution the level of resolution is lower than that of RADSAGA and Cypress SRAMs.

The Cypress SRAM is the memory for which the two methods are, overall, in best agreement, given that the D-factors are typically within ±30%.

5.4 Evaluation of some uncertainties

As earlier introduced, the measurement of LEP cross-sections is plagued by strong uncertainties and so are some other assumptions, e.g., the assumption that all cells will have the same response as well as some modelling assumptions concerning the layout of the SRAM cells. The combination of all these uncertainties can have strong impact on the determination of the LEP upset rate. Therefore, in this section, some discussion on a few of these points is provided to assess whether these uncertainties may have a strong or weak influence on the earlier determined D-factors.

5.4.1 D-factors for the three ISSI data-sets

From experimental data it was reported that the LEP cross-sections for the ISSI SRAM differed substantially for the three tested units (one tested at RADEF and two tested at CNA) with differences also for units tested in the same facility. So far the analysis focused on the RADEF data-set given that it is worst case for both the LEP peak cross-section and the IEP cross-section. However, it is worth performing a comparative analysis based on the responses of the three units of the ISSI SRAM.

A simplified analysis is performed in this case and it is based on the energy convolution method. For the three devices it is assumed that the HI and HEP cross-sections and, therefore, the associated upset rates in space will be identical (this was not experimentally verified, but it is a reasonable assumption).

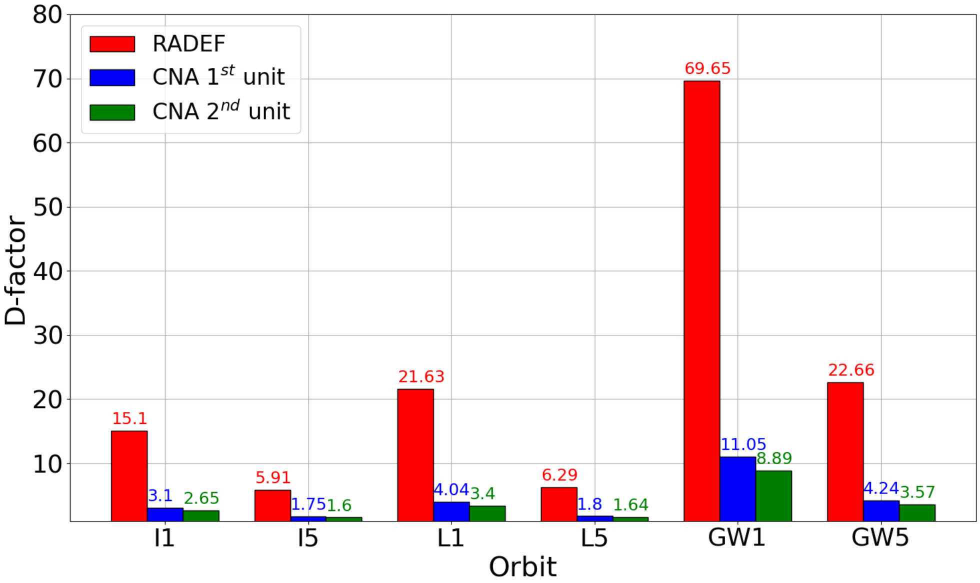

Figure 5.15: Comparison of the D-factors of three ISSI units measured at RADEF and CNA based on the energy convolution method for three orbits and two shielding configurations.

Fig. 5.15 depicts the D-factors of the three tested units for the usual three orbits and two shielding configurations. It is evident that the D-factor of the CNA unit with the highest LEP peak (1^{st} unit) is a factor of 5 lower than that based on the RADEF data, whereas the D-factor of the CNA unit with the lower peak (though wider, 2^{nd} unit) is a factor of 6 lower than that based on the RADEF data, irrespectively of the orbit or shielding configurations.

This differences between the RADEF unit and the CNA units are not negligible when it comes to predicting the impact of LEPs in orbit for SRAMs belonging to the same lot. It is also true that while the two CNA units were measured to have different LEP cross-sections, when it comes to the D-factor, the discrepancy between one and the other would be always below 25%, which is a rather acceptable uncertainty.

Concerning the D-factors in absolute terms, the CNA units still point at an important contribution from LEPs to the total SEU response, although this is usually less the case for a shielding of 500 mils of Al. Under these conditions, in the ISS and LEO cases, the D-factors fall below 2, indicating that the contribution arising from LEPs may not be so high.

At the same time, the D-factors for GW1 are, for both memories, above 5. This would still indicate a dominance of LEPs when SPEs are considered. For comparison with the existing literature, the two ISSI SRAMs tested at CNA seems to be just a factor of 2 worse than the worst case previously identified [77].

5.4.2 Modelling uncertainties

There are two main modelling uncertainties that could have severely affected the design of the RPPs used for the MC simulations:

- the RPPs were built considering that the experimental LEP cross-sections were obtained from fully mono-energetic beams. However, this was shown not to be true for the CNA facility (and likely it won't be true for the RADEF facility). Therefore, the first assessment will consist in verifying whether different RPP models would have emerged as a result of running MC simulations with gaussian spectra with 120 keV FWHM (that measured at CNA) instead of mono-energetic beams.
- the RPPs were built assuming an equivalent SiO_2 thickness for the BEOL. However, the BEOL is much more complex than that and may alternate various metal and oxide layers. The actual composition can have an effect on the actual energy lost by protons through the BEOL. Therefore, the second assessment will concern the analysis of the different responses that would be obtained with different BEOLs. These are meant to mimic at least the two extreme cases, i.e., the most resistant path (full metal, e.g., copper) and the least resistant path (full oxide).

Considering the amount of parameters and their interplay, the analysis was restricted to the ISSI SRAM RPP modelled on the experimental RADEF data (the only model based on single RPP). Here it is therefore assumed that the uncertainty on the beam energy at RADEF was the same from CNA. As said, the analysis consists in running MC simulations with 120 keV FHWM for all proton energies around the peak LEP cross-section (i.e., 0.6-1 MeV). Proton spectra after passing through the real BEOL of the ISSI SRAM for both the mono-energetic and the gaussian case were provided in Fig. 4.16. The numerical cross-sections from a gaussian proton spectrum are then compared against those obtained from a purely mono-energetic beam.

The analysis concerning the BEOL variability is conducted in parallel. In this case, the composition of the BEOL of the ISSI SRAM was studied with SEM analysis. As a result one can obtain a better model of the BEOL tha the one relying merely on SiO_2. The actual BEOL was found to be 5.739 μm thick. It is composed of several layers, as shown in Fig. 5.16 ,with an almost in scale representation of each layer thickness. The actual thickness of each layer is reported in Table 5.4.

Even the BEOL with several layers is, however, an approximation of the average path of a proton across the BEOL because the BEOL has a tri-dimensional structure (i.e., there could be material variations along the thickness). Therefore, in order to account for the all possible variability associated to the path of a proton through the BEOL two extreme cases are also considered. A first one that is very optimistic (full oxide) and a second one which is very conservative (full copper), given that these materials have the lowest and highest densities.

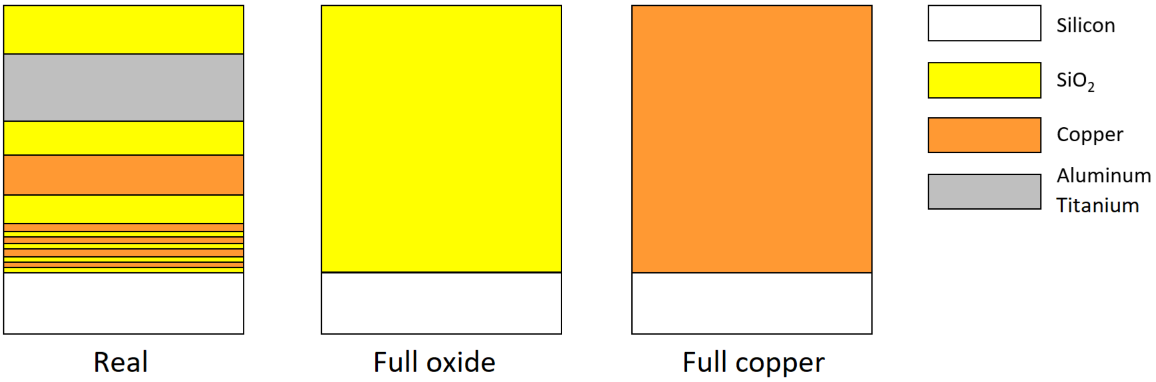

Figure 5.16: BEOLs of the ISSI SRAM. The real one was obtained from SEM analysis. The other two are considered limiting cases for LEPs based on the lightest and heaviest elements in the BEOL.

Table 5.4: BEOL of the ISSI SRAM based on SEM analysis. Layers are reported from top to bottom.

Layer	**Material**	**Thickness [nm]**
Passivation	$SiO_2 + Si_3N_4$	1048
Metal	Al-Ti	1580
Insulator	SiO_2	717
Metal	Cu	877
Insulator	SiO_2	545
Metal	Cu	141
Insulator	SiO_2	92
Metal	Cu	141
Insulator	SiO_2	78
Metal	Cu	141
Insulator	SiO_2	73
Metal	Cu	112
Insulator	SiO_2	194

The data for the analysis on the mono-energetic vs. Gaussian proton spectra and for the BEOL are plotted in Fig. 5.17. The cross-sections were calculated using the single cubic RPP with 310 nm side. In spite of the different proton spectra for the mono-energetic and gaussian cases, it is noted that the difference between the cross-sections in one case and the other are negligible. In fact, there is a quasi-perfect correspondence between the cross-sections no matter whether the beam is mono-energetic or gaussian at all energies around the LEP peak. Therefore, if for the same SV the cross-sections are identical, it is concluded that considering the protons to be fully mono-energetic would not yield any big uncertainty on the design of an RPP model for the SV.

Concerning the BEOL composition, Fig. 5.17 clearly points out that there is some effect. The LEP peak cross-section is moving towards larger proton energies whenever the average density of the BEOL grows. This is expected, given that protons will lose much more energy in a denser material than in a lighter material. Overall, however, the peak LEP cross-section is not really affected by the BEOL composition and also the width of the peak in terms of energy seems weakly affected.

In order to further demonstrate that the BEOL composition does not introduce a large

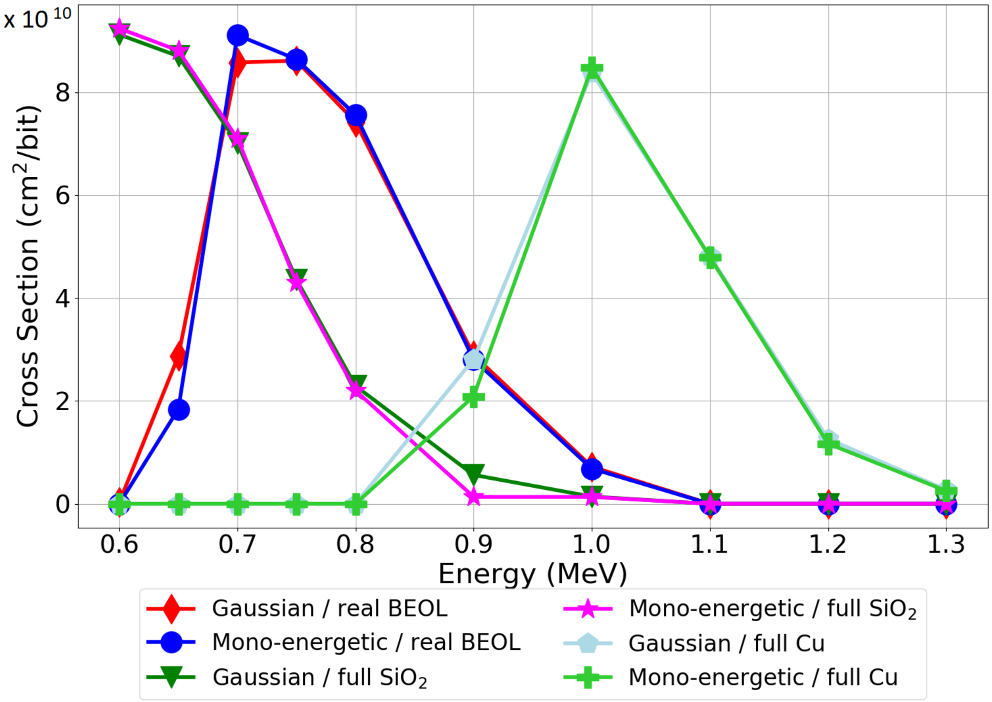

Figure 5.17: LEP cross-sections as a function of the BEOL composition for mono-energetic and gaussian proton beams. Obtained with FLUKA.

Table 5.5: Comparison of LEP upset rates for the ISSI SRAM with three different BEOL compositions. Data calculated for the ISS and 100 mils of Al. The upset rate units are events/bit/day. Obtained with FLUKA.

BEOL	**UR**$_{LEP}$
Real BEOL	4.21 x 10^{-7}
Full SiO_2	4.22 x 10^{-7}
Full Cu	4.37 x 10^{-7}

uncertainty on the upset rate calculated for space, simulations of the RPPs with each of the three BEOLs were run for the space proton spectrum of the ISS with 100 mils of shielding. The LEP UR for each case is reported in Table 5.5. It is evident that having the protons going through a more or less dense BEOL does not drastically affect the upset rate from LEPs. This is mainly due to the fact that the proton fluxes at energies between 0.5 and 2 MeV are more or less the same. Therefore, shifting the LEP peak at lower or higher energies does not yield any visible impact.

It can then be concluded that knowing the actual composition of the BEOL may not be a need when it comes to the calculation of the upset rate expected from LEPs in space. After all, this information was also not used in the other upset rate calculation methods, but the MC, and the other methods returned LEP upset rate compatible with MC simulations.

5.4.3 Variable critical charge distribution

Another uncertainty on the data may arise from the fact that in the simulations it is assumed that all cells have the same identical behaviour, i.e., that each cell has exactly the same critical charge. However, as shown in other works [90], this is typically not the case and, by means of retention voltage measurements and knowing some construction parameters of the SRAM

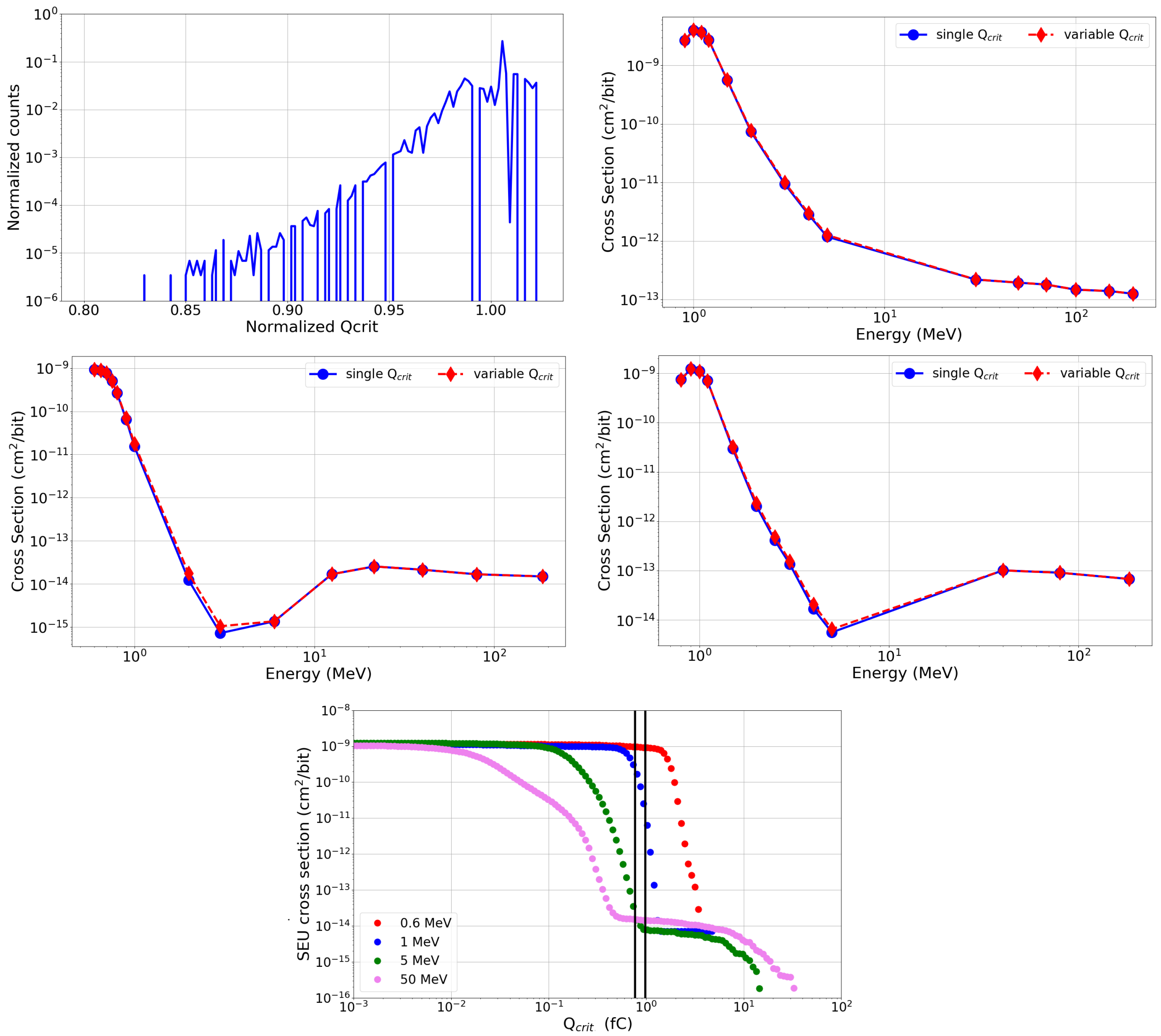

Figure 5.18: Q_{crit} distribution as measured in [90] (top-left) and the comparison between the proton cross-section as a function of energy either calculated based on a single critical charge or with the critical charge distribution for the RADSAGA (top-right), ISSI (center-left) and Cypress (center-right) SRAMs. The interval of concerned critical charges is also shown with respect to the SEU cross-section as a function of critical charge obtained from the FLUKA MC simulations of the ISSI RPP (bottom).

it is possible to determine that a non-uniform distribution of critical charges exists among the SRAM cells.

In the scope of this work it was not possible to neither measure the retention voltage, nor to obtain the required parameters (recall eq. (2.7)) to correlate it to the critical charge. Considering that the data in [90] were collected for an SRAM with similar technological node, using the measurements reported in that paper to obtain a distribution of critical charges is deemed representative for the technologies under analysis here. Such a distribution is also depicted in Fig. 5.18 in the top-left plot. The plot reports the normalized number of bits that belong to a certain critical charge bin. The critical charge is also normalized with respect to the reference one. In the case of this study, the critical charge corresponding to this value is that obtained in the previous modelling steps (i.e., 0.55 fC, 0.96 fC and 0.86 fC for the RADSAGA, ISSI and Cypress SRAMs, respectively).

It is noted that the critical charge distribution is not Gaussian, but skewed towards lower critical charges, i.e., there may be a larger amount of more-than-average sensitive cells in the SRAM and this may have an impact on the SEU cross section. In order to determine this impact, the critical charge distribution is convolved with the cross section distribution as a function of critical charge obtained from the MC simulations. This will provide a cross-section for the whole memory with variable critical charges that can then be compared with that for a single uniform critical charge.

The comparison for the three SRAMs is reported in Fig. 5.18. As one can see for all memories the critical charge variability does not generally lead to a higher cross-section for LEPs and HEPs, while this is possible for IEPs. Indeed, the impact of this variable critical charge is put into the perspective of how the cross-section varies with the critical charge in the bottom plot of Fig. 5.18 for the ISSI RPP. The plot shows that a critical charge variation this small (0.77-0.98 fC for the ISSI SRAM) does not lead to a cross section spread for both the 0.6 MeV and the 50 MeV cases. The only energy region where this spread can partly be felt is for intermediate energies, where the cross section changes by orders of magnitude with small variations of critical charge. However, as shown in the cross section versus energy plots, the effect does not change the IEP SEU cross sections by more than 5%.

Considering that the variations are this small and that the IEP part of the cross section curve does not impact the upset rate significantly, it is possible to conclude that the non-uniformity of the critical charge among different cells is not expected to provide a remarkable uncertainty on the upset rate. Furthermore, the assumption of an average cell to describe the whole memory array does not introduce any strong under/overestimation of cross sections or upset rates.

5.5 Direct ionization from protons in the accelerator

5.5.1 D-factor in the accelerator

Given the potential big impact of direct ionization from LEPs in the space environment, it may be important to determine whether these same devices would suffer from an unexpectedly high upset rate in the accelerator environment. The purpose, as always, is two-fold. On the one hand, it may help determine whether neglecting LEP effects in the accelerator may bring to underestimations of the total upset rate. On the other hand, determining the D-factor at CHARM may help understanding whether a CHARM test can provide also some indications about LEP susceptibility for space applications.

The D-factor in the accelerator would have to be redefined to account for different contributors than those in space. Following the work on thermal and intermediate energy neutrons for the commercial devices under consideration [7, 147] there are at least four contributors to the upset rate to be considered:

$$D = \frac{UR_{HEH} + UR_{n,th} + UR_{n,int} + UR_{LEP}}{UR_{HEH} + UR_{n,th} + UR_{n,int}} \tag{5.4}$$

That is, other than the rather standard HEH contributor, there are also important contributions from thermal (< 0.5 eV) and intermediate-energy neutrons (0.1-20 MeV) that have to be considered outside of the standard HEH equivalence based on outdated memories. Therefore, in this instance, the D-factor provides the additional contribution to the upset rate from LEPs on top of all the other neutron-dominated contributors.

Note that there are other particles which can cause upsets in mixed-field, such as low-energy pions, muons and electrons, all by direct ionization. For the sake of this analysis they are neglected because (i) no experimental data are available and (ii) other considerations may allow neglecting them. Indeed, while one may expect the low-energy pion cross-sections to be similar to those of LEPs, the fluxes of low-energy pions are expected to be lower according to FLUKA simulations of accelerator areas and of the CHARM facility. Concerning muons and electrons, their cross-sections are not expected to be comparable to those of LEPs. Therefore, the particles found in the accelerator mixed-field D-factor are expected to comprise all the most important contributors to the error rate in a mixed-field environment.

Fig. 5.19 (left) depicts the hadron spectra for two very different CHARM test positions. G0 is a position for which the thermal neutron and intermediate energy neutron spectra are substantially higher than the HEH spectrum. On the other hand, R13 is a position in which HEHs have very comparable fluxes to thermal and intermediate energy neutrons. The three regions of pertinence for the three general contributors to the upset rate are indicated (note that for intermediate energy only neutron shall be considered).

Fig. 5.19 (right) depicts the proton spectra for four CHARM positions, including also the space-like R5 and the most used accelerator test position R10. The region of interest for LEP is highlighted in the figure. It is noted that, except for G0, LEP fluxes are very similar among the other rackable positions. It should also be noted that these fluxes were not transported through any shielding (although it may have been worth including the device package).

The reason why the LEPs may have an impact for the accelerator in spite of the rather low fluxes is that the HEH, thermal and intermediate-energy neutron cross-sections are typically 4 to 6 orders of magnitude lower than those of LEPs. Therefore, even if LEPs come with fluxes 3 to 4 orders of magnitude lower, they may end up providing a similar contribution to the total upset rate than the other contributors.

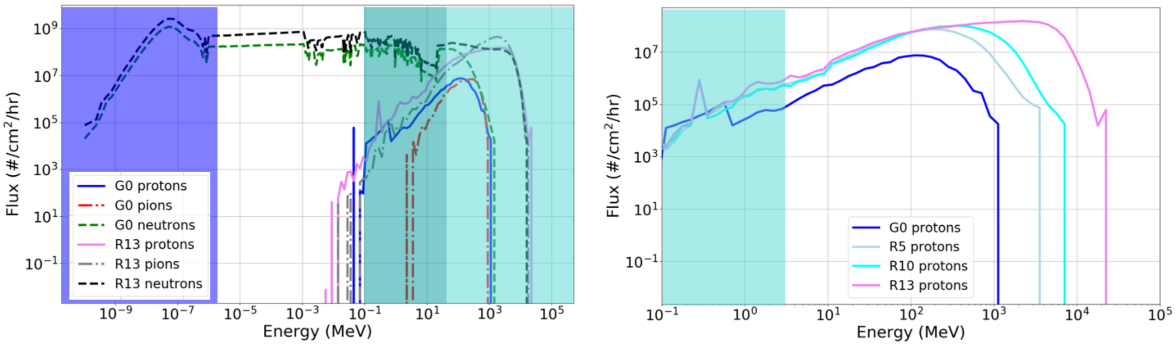

Figure 5.19: (Left) Hadron spectra for two CHARM positions. Highlighted are the HEH, intermediate energy and thermal neutron parts. (Right) Proton spectra for four CHARM positions. Highlighted is the LEP part of the spectra. Spectra from FLUKA simulations.

Upset rates are calculated as follows:

- UR_{HEH} is calculated by multiplying the 200 MeV proton cross-section by the integral of proton, pion and neutron fluxes above 20 MeV, that is, through the HEH equivalence approximation;
- $UR_{n,int}$ is calculated by convolving the neutron fluxes between 0.1 and 20 MeV with the Weibull functions defined in [7];
- $UR_{n,th}$ is calculated by multiplying the thermal neutron cross-section by the thermal neutron flux;
- UR_{LEP} is calculated by means of the energy convolution of the LEP cross-section with the LEP fluxes.

The data analysis is restricted to the ISSI and the Cypress 65 nm SRAM given that for the RADSAGA SRAM the intermediate energy neutron cross-sections are not available.

Table 5.6 reports the upset rate calculated for each contributor and the respective D-factors of the four CHARM positions for the two SRAMs. The D-factors look small if

Table 5.6: Upset rates and D-factor for different CHARM positions.

SRAM	**UR$_{HEH}$ (ev/bit/hr)**	**UR$_{n,th}$ (ev/bit/hr)**	**UR$_{n,int}$ (ev/bit/hr)**	**UR$_{LEP}$ (ev/bit/hr)**	**D-factor**
G0					
ISSI	1.03×10^{-5}	1.75×10^{-5}	1.82×10^{-5}	5.56×10^{-5}	2.21
CY65	5.68×10^{-5}	2.73×10^{-6}	1.19×10^{-4}	4.45×10^{-5}	1.25
R5					
ISSI	2.13×10^{-5}	3.86×10^{-5}	5.81×10^{-5}	1.31×10^{-4}	2.11
CY65	1.18×10^{-4}	6.03×10^{-6}	3.77×10^{-4}	3.15×10^{-4}	1.63
R10					
ISSI	3.62×10^{-5}	4.11×10^{-5}	4.34×10^{-5}	1.21×10^{-4}	2.00
CY65	2.00×10^{-4}	6.42×10^{-6}	2.81×10^{-4}	3.53×10^{-4}	1.72
R13					
ISSI	9.51×10^{-5}	3.93×10^{-5}	4.90×10^{-5}	1.70×10^{-4}	1.93
CY65	5.25×10^{-4}	6.14×10^{-6}	3.18×10^{-4}	5.14×10^{-4}	1.61

compared to those for space, the maximum being just above 2 for the ISSI SRAM. However, a factor of 2 would already indicate a contribution of around 50% to the total upset rate, which is certainly not negligible if one considers that it is not calculated on top of the HEH contribution alone, but also considering thermal and intermediate energy neutrons.

The D-factor also behaves differently for the two SRAMs. It monotonically decreases when moving towards more energetic environment when it comes to the ISSI SRAM. On the other hand, it is very similar for the rackable positions for the Cypress 65 nm SRAM and lower for the G0 position.

5.5.2 Comparison with CHARM measurements

It has to be noted that, in contrast to space, some level of validation for the accelerator is possible because the ISSI SRAM was tested in the G0 position in CHARM [148]. At the time of the test (end of 2018), the high LEP, thermal and intermediate energy neutron sensitivities of the device were not known. In addition, the SRAM had not been tested against HEPs or HIs. Therefore, at the time, the cross-section was calculated as if all SEUs measured in CHARM were due to HEHs (and with an intermediate-energy neutron contribution identical to that of another outdated memory previously considered worst-case) [148].

Another significant issue is related to the fact that in order to calculate the cross-section at CHARM one has to rely on a conversion coefficient between the protons on target and the HEH or HEHeq per cm^2 received at the test position. The issue comes from the fact that FLUKA typically predicts higher yield of HEH/cm^2/POT and HEHeq/cm^2/POT than the RadMon [11] actually measures. For instance, for the period of testing, the HEHeq yield for G0 from FLUKA is 7.67×10^{-6} HEHeq/cm^2/POT, while that of the calibrated RadMon was 3.46×10^{-6} HEHeq/cm^2/POT. This yields a non-negligible difference of about a factor of 2 on the fluence to be used for cross section calculations.

Sticking to the RadMon calibration factor, it is possible to calculate the HEHeq calibration not for the RadMon SRAM, but for the ISSI SRAM directly. This differs from that of the RadMon SRAM itself because the ISSI SRAM is far more sensitive to intermediate energy neutrons. After having replaced the Weibull of the Toshiba SRAM [7] for that of the ISSI in the convolution of the IEN fluxes, the resulting calibration factor for the ISSI SRAM is

5.88 x 10^{-6} HEHeq/cm^2/POT.

The RadMon yield recalibrated to the ISSI SRAM is used to calculate the HEHeq fluence received during the CHARM test starting from the POTs for G0. As a result, the HEHeq cross-section measured at CHARM (based on HEHs and IENs) is 3.34 x 10^{-14} cm^2/bit. This has to be compared with HEH cross-sections measured elsewhere. For instance, the HEH cross-section measured in ChipIr was 9.59 x 10^{-15} cm^2/bit, whereas that measured with 186 MeV protons was 1.40 x 10^{-14} cm^2/bit.

The reason why the HEHeq cross-section in CHARM is much higher is that in CHARM the SRAM is subject to a mixed-field which contains also thermal neutrons and LEPs, which can cause upsets. However, the HEHeq fluence does not take them into account.

According to Table 5.6, the HEHeq in G0 are expected to contribute for about 28% (HEHs + IENs) to the total upset rate, whereas the thermal neutrons and LEPs are expected to yield contributions of 17% and 55%, respectively. If one makes the ratio between the ChipIr HEH cross-section and the CHARM HEHeq cross-section, one finds 0.29. This is in very good agreement with the expected contribution of HEHeq in the CHARM G0 position. On the other hand, if the same ratio is calculated with respect to the 186 MeV proton cross-section, the ratio is 0.42.

Concerning the thermal neutrons, it is predicted that they will yield 17% of the total upsets in G0. During a separate CHARM run, the ISSI cross-section was measured by covering the SRAM with 4 mm of B_4C, which is expected to fully remove the thermal neutron component of the spectrum. When this was done, the HEHeq cross-section that was measured at CHARM was 2.68 x 10^{-14} cm^2/bit, i.e., a reduction of 20%, which is also in good agreement with the expected contribution of 17%.

Therefore, it can be confirmed that there is a significant surplus of upsets when testing at CHARM, i.e., more upsets were measured than the HEH, IEN and thermal neutron sensitivities would yield. This difference can span from 38% to 51% depending on which HEH cross-section is considered for comparison (either 186 MeV protons or ChipIr, respectively). And, at least for the case of Chipir, this is in very good agreement with the predictions and pointing towards a D-factors of 2, which, in first approximation, is certainly of concern.

5.5.3 Conclusions

If once again the D-factors are considered only as safety margins, applying a margin of 2 on top of the upset rate from the other three contributors may be sufficient to account for LEPs in accelerator without dedicated LEP testing.

Concerning the use of CHARM for space it is clear that the attained D-factors are far from those encountered in space despite the similar proton spectra (and mainly due to the intermediate and thermal neutron dominance of the response). Therefore, LEP testing may better be achieved by a separate test. This is because, while the thermal neutron upsets can be suppressed in CHARM by means of B_4C shielding, one still needs to know the IEN Weibull response of the device in order to calculate the contribution of LEPs in CHARM and, then, to rescale it to a space environment.

Chapter 6

Pion SEEs and the HEH equivalence approximation

The experimental data collected in the scope of this thesis for HEPs and HEπs in section 4.3.1 show that the assumption that all HEHs have the same SEE cross-section is violated for a quite wide energy interval and that the results are not identical for SEUs and SELs:

- the SEU and SEL pion cross-sections are higher than those of protons for 100-230 MeV primary energies, in good agreement with the total nuclear reaction cross-sections of pions and protons (recall Fig. 3.2) for this energy interval;
- the SEL pion cross-sections (both positive and negative pions) are higher than that of protons at 50 MeV primary energy in open contrast with the observation that the total nuclear reaction cross-section of pions is lower than that of protons at this energy.

The goal here is to determine whether these differences have an impact on the HEH equivalence approximation for mixed-field environments. On the one hand, this is important for the accelerator context for both qualification and calibration purposes. In terms of qualification because neglecting the presence of pions may result in an underestimation of the failure rate in operation if the devices are qualified with protons (or neutrons). This can be an important threat with respect to the compliance with the availability and reliability requirements of the LHC. In terms of calibration because SRAM-based radiation monitors are used to measure HEH fluxes in the LHC (and its injector chain) and work under the hypothesis that pions have comparable cross-sections to those of protons and neutrons. A higher pion cross-section can yield overestimations of the actual HEH fluxes in the LHC. On the other hand, it may question the representativeness of the CHARM facility for testing electronic devices and systems to be used in other environments (e.g., space, avionics, ground) where pions are not present in any significant proportion.

Nothing more than what was reported in section 4.3.1 can be achieved on an experimental basis given that there are no pion facilities that can cover for the full pion energy range of interest for the accelerator environment. Therefore, in order to determine the impact for accelerator RHA, numerical simulations of the physical processes can be used to extend the knowledge about the pion response beyond what was achieved experimentally. The additional benefit of numerical simulations is that they also allow understanding why the charged pion cross-sections differ from those of protons and neutrons.

Most of the work has been accomplished in two of the papers reported at the end of this thesis [14, 110].

6.1 Simulated HEH cross-sections

Numerical simulations are used to extend the knowledge of the SEU and SEL cross-sections of the various devices at primary energies lower and higher than those that it was possible to test with. The idea is to determine the cross-section of each hadron for a few selected energies between 20 MeV and 20 GeV, which is the typical energy interval of HEH fluxes in accelerator radiation fields. In order to do that, it is first necessary to derive SV models for the SRAMs that would allow reproducing with quite good fidelity the experimental cross-sections.

For this work, the ISSI SRAM for the SEU case and the Brilliance SRAM for the SEL case are considered. The first can be considered representative for current highly integrated bulk silicon technologies. The latter is a forced choice given that heavy ion data needed for the convolution with the energy deposition distribution are available for the Brilliance SRAM, but not for the Lyontek SRAM.

The model for the ISSI SRAM was developed in Chapter 5. The model for the Brilliance SRAM is explained later on.

FLUKA is used for all the MC simulations. The effectiveness of FLUKA in reproducing nuclear hadron-silicon interactions, that are central to HEH SEU and SEL mechanisms, and, in particular, accounting for all the mechanisms related to pion nuclear reactions were demonstrated by the FLUKA developers [149–151].

6.1.1 SEU

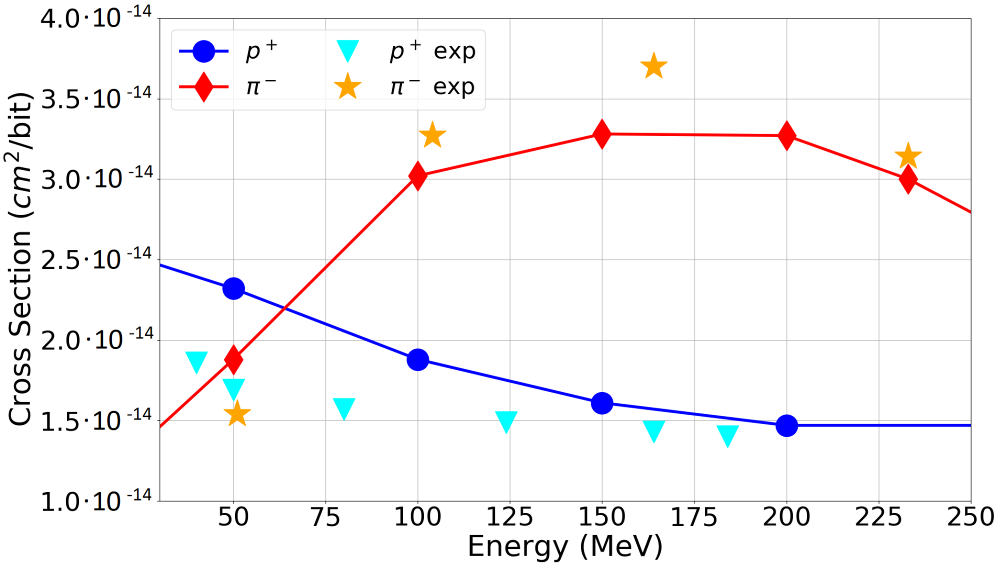

Figure 6.1: SEU cross-sections of protons and negative pions as a function of energy as simulated with FLUKA. The experimental data refer to the ISSI SRAM. Reprinted from [14]. © 2020, Coronetti et al., licensed under CC BY 4.0.

Fig. 6.1 provides a cross-comparison between the proton and negative pion experimental data and the MC simulated data for the ISSI SRAM SV RPP model. The simulated data points are reported with markers and linearly interpolated in between. The agreement all over the range for which experimental data are available is typically better than ± 35% and it is obtained for both protons and negative pions. Therefore, the numerical data correctly reproduce the observed resonance in the 75-250 MeV region.

The same RPP SV model is then used to get the response from mono-energetic hadrons of a wider energy range. The results are plotted in Fig. 6.2 also including positive pions,

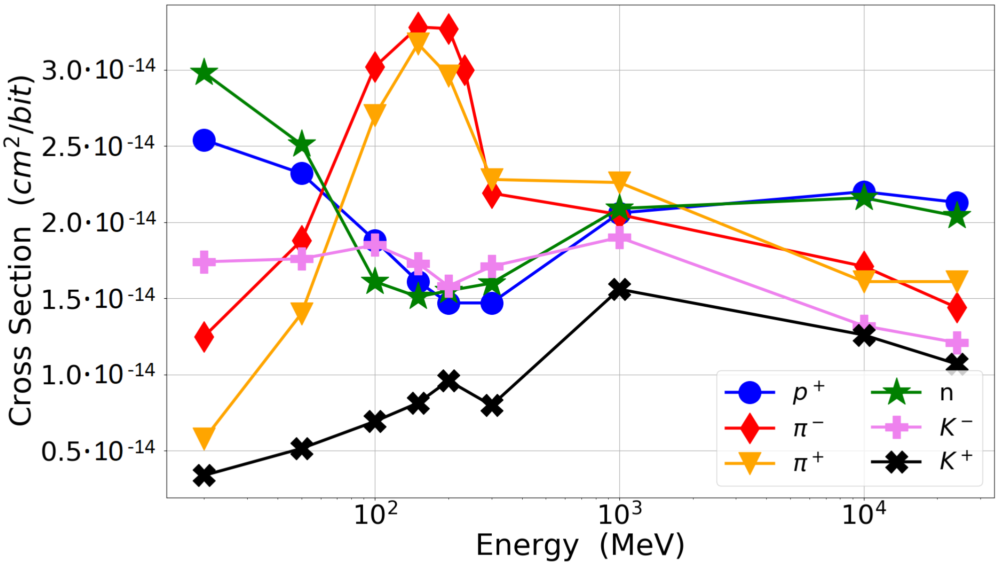

Figure 6.2: SEU cross-sections for the most important hadrons in mixed-field as a function of energy for the model of the ISSI SRAM as simulated with FLUKA. Reprinted from [14]. © 2020, Coronetti et al., licensed under CC BY 4.0.

neutrons and charged kaons (although the latter are expected to provide a negligible contribution due to the very low fluxes). The numerical data provide a better picture overall of the SEU cross-section behaviour for each primary particle.

Protons and neutrons have very similar SEU cross-sections, that have an absolute minimum at a few hundreds of MeV and an absolute maximum at the lowest simulated energy (21 MeV). Charged pions have also very similar cross-sections with some slight discrepancies that are caused by slight variations in the total nuclear reaction cross-section. It is noted that the pion cross-section is actually higher than those of protons and neutrons only for the resonance, which starts to fade out already at 300 MeV. At 1 GeV all hadrons have very similar cross-sections. For even higher energies pion SEU cross-sections are lower than those of protons and neutrons.

6.1.2 SEL

Fig. 6.3 provides the comparison between the experimental proton and negative pion cross-sections with the MC simulated cross-sections for the SEL SV RPP model of the Brilliance SRAM. Two models of the SV were considered here, both having the same surface (20 x 4 μm^2), but different thickness (1.8 vs. 3.0 μm). For both cases the model is completed with a 6 μm SiO_2 BEOL and a 0.4 μm tungsten layer placed within the BEOL 0.2 μm above the SV.

The model with thinner volume returns a higher SEL cross-section for all energies than the thicker one. The thinner model seems to better agree with the data at high-energy, while the thicker at lower energies. However, the difference in absolute cross-section is usually within ±35% at any energy and for every particle whether one model is used or the other. So, any thickness in between 1.8 and 3 μm can adequately reproduce the experimental data.

As already shown on the left edge of Fig. 6.3, the charged pion SEL cross-sections are predicted to diverge more and more from those of protons and neutrons as the energy decreases towards 20 MeV. This is an interesting observation given that the nuclear pion cross-sections are much smaller than those of protons and neutrons at this lower energies (recall Fig. 3.2).

This behaviour is further studied in Fig. 6.4, where the SEL cross-sections of protons,

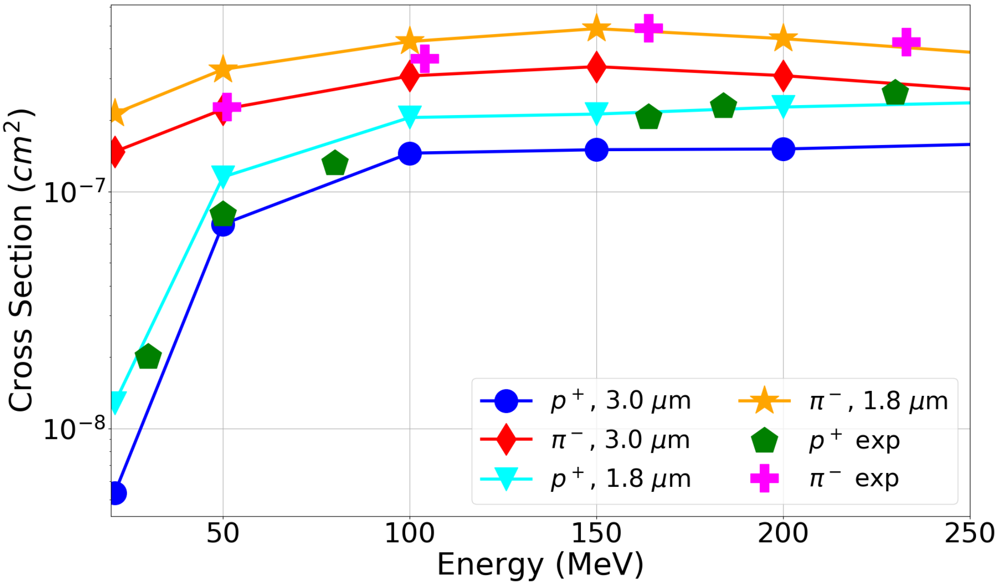

Figure 6.3: SEL cross-sections of protons and negative pions as a function of energy for two SEL SV geometries as simulated with FLUKA. The experimental data refer to the Brilliance SRAM. Reprinted from [110]. © 2021, Coronetti et al., licensed under CC BY 4.0.

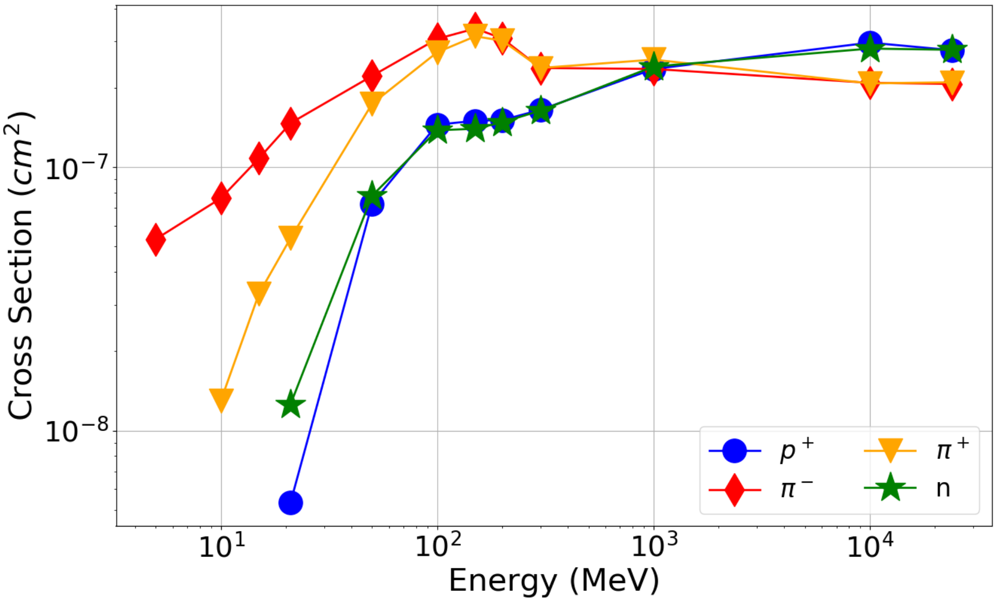

Figure 6.4: SEL cross-sections for the most important hadrons in mixed-field as a function of energy for the SEL SV with 3 μm thickness used as a reference for the Brilliance SRAM as simulated with FLUKA. Reprinted from [110]. © 2021, Coronetti et al., licensed under CC BY 4.0.

neutrons and charged pions are calculated for the full 20 MeV - 20 GeV energy range. Actually, SEL cross-sections were also calculated for charged pions with energies as low as 5 MeV. The figure shows that the proton and neutron SEL cross-sections falls down rather sharply by more than one order of magnitude with respect to their 200 MeV value. On the other hand, the pion SEL cross-sections remain quite high even below 20 MeV, in particular that of negative pions.

It is not that obvious to explain the pion SEL cross-section behaviour considering its divergence with respect to the nuclear reaction cross-section. Therefore, a deeper investigation is conducted within the next section to explain the reason why low-energy pion SEL cross-sections are significantly larger than proton and neutron cross-sections.

Finally, it is noted that, for the Brilliance SRAM, higher energy SEL cross-sections are quite close to the 200 MeV value and do not increase by much at GeV energy. This is because the low LET threshold makes the low-LET products from hadron-silicon interactions dominant over the fission products from hadron-tungsten interactions [16, 152].

6.2 Consequences of pion resonance and absorption on the nature of secondary ions

For HEHs (E > 20 MeV) the sole mechanism capable of triggering SEEs is indirect ionization from the secondary ions generated by hadron-silicon nuclear interactions. As earlier said, the total nuclear reaction cross-sections of charged pions differ from those of protons and neutrons due to the $\Delta(1232)$ resonance and to the pion absorption mechanism.

The two processes have quite different impact on the nature of the secondary ions. Furthermore, these properties vary with the pion energy. Therefore, a further breakdown is needed, one that considers diverse energies between 20 MeV and 1 GeV.

The full transport MC was shown to be fully capable of reproducing the experimental SEU and SEL cross-sections of all particles. However, in a MC simulation only one in a few hundreds of thousand primary particle will experience a nuclear interaction. Therefore, the MC may not be the best way to score secondary ion properties. For this purpose, the FLUKA preex tool was used instead.

6.2.1 Secondary ions as a function of atomic number

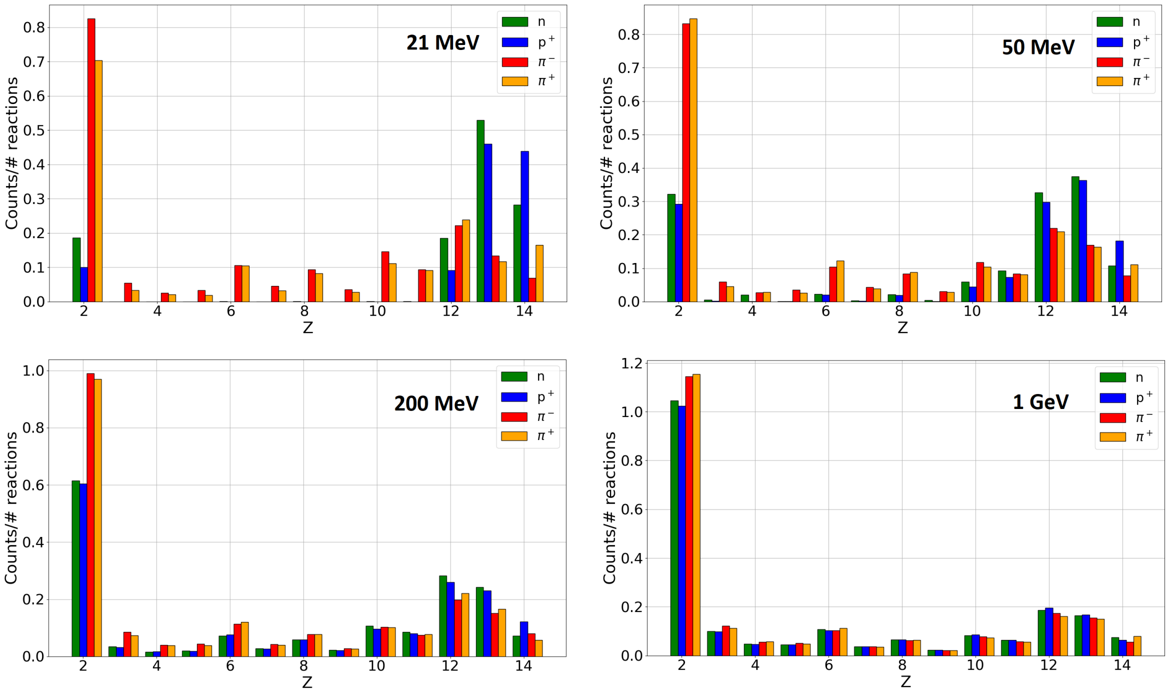

Figure 6.5: Normalized yield of secondary ions as a function of the atomic number for neutrons, protons and charged pions in the 21-1000 MeV primary energy range. Obtained with FLUKA preex. Reprinted from [110]. © 2021, Coronetti et al., licensed under CC BY 4.0.

Fig. 6.5 reports the normalized yield of secondary ions in terms of their atomic number for each primary hadron at various primary energies. Protons and neutrons secondary ions share similar properties at any tested energy and the same apply when comparing positive pions with negative pions. However, while pion and other hadron secondary ion distributions are very similar at high energy, huge differences occur when the primary energy of the hadron is reduced.

At 21 MeV charged pions can deliver quite a large amount of secondary ions with low- and intermediate Z (< 10). On the other hand, with the exception of alphas (which are anyway released in lower amount for protons and neutrons than for pions), proton and neutron nuclear interactions with silicon do not yield a significant amount of ions with Z = 3-10. The stronger level of fragmentation, responsible for the generation of secondary ions with low- and intermediate-Z in pion-silicon reactions, is due to the pion absorption mechanism. Following absorption of the pion, the silicon nucleus is strongly excited and can fragment in various particles. See also Table II in [110] at the end of this thesis showing that charged pions yield about a factor of 2 larger amounts of fragments per reaction at 21 MeV than protons.

The differences between charged pions and the other two hadrons become smoother as the primary energy is increased. However, it is noted that, while for 50 MeV and 1 GeV the total nuclear reaction cross-sections between the two groups are similar, the secondary ions generated differ significantly, given that pions at 50 MeV are still much more effective in generating low- and intermediate-Z secondary ions than protons and neutrons, again due to the pion absorption.

The pion resonance remains on top of these observations. Indeed, the graphs do not consider that pions are more likely to experience a nuclear interaction with the silicon than the other two hadrons above 100 MeV. Conversely, while at 21-50 MeV pions yield a larger amount of low- and intermediate-Z secondary ions, these may or may not be important in absolute terms when everything is rescaled by the total nuclear reaction cross-section, which at these energies is lower for pions.

6.2.2 Secondary ions as a function of their LET

The LET scored upon generation of all secondary ions (Z = 2-15) is a first metric that can be considered.

Fig. 6.6 reports the normalized yield of the secondary ions in terms of their LET upon generation from hadron-silicon nuclear interaction as a function of the particle type and at various energies. The chosen energies are 21 MeV (the lowest in the interval and for which the pion total nuclear reaction cross-sections are smaller than those of protons and neutrons), 50 MeV (for which these cross-sections are very similar), 200 MeV (for which the pion resonance is observed) and 1 GeV (for which, once again, the cross-sections match).

The dissimilarities in the LET distributions arise from the dissimilarities in the secondary ions generated by the various hadron-silicon interactions. Protons and neutrons have quite smooth distributions at 21-50 MeV, likely due to the fact that they do not produce low- and intermediate-Z secondary ions. On the other hand, these low- and intermediate-Z ions are responsible for the peaks in the charged pion distributions. At higher energy (200 MeV and 1 GeV) also protons and neutrons show these peaks and the various distributions almost completely match.

Note that at 21 MeV, despite the absence of secondary ions with LET > 10 MeV/(mg/cm^2) and of the peaks, it is clear that if the distributions are rescaled by the respective total nuclear cross-sections, secondary ions from protons and neutrons (considering the whole LET interval) will be more numerous than those from charged pions.

The latter is an important observation for SEUs. This effect is typically associated with very low LET$_0$ in state-of-the-art memories (typically below 0.5 MeV/(mg/cm^2)). Therefore, the largest part of the ions depicted in the LET distributions will deposit sufficient energy/charge to trigger an SEU. This would indeed be coherent with the SEU cross-sections

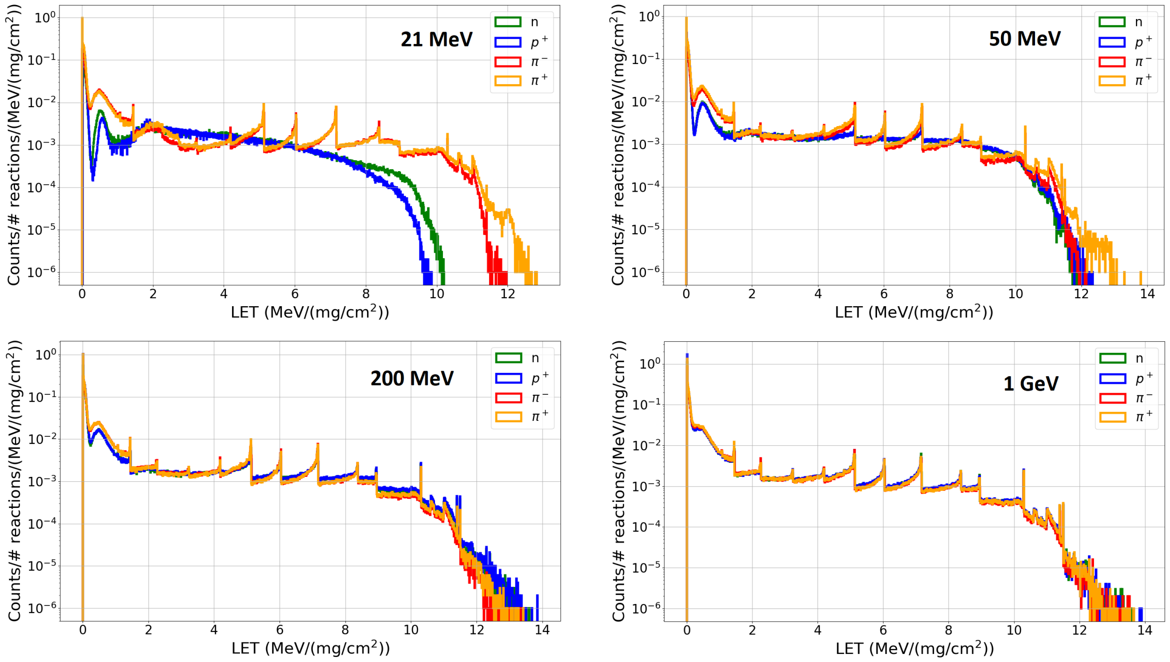

Figure 6.6: Normalized yield of secondary ions as a function of their LET upon generation for neutrons, protons and charged pions in the 21-1000 MeV primary energy range. Obtained from FLUKA preex. Reprinted from [110]. © 2021, Coronetti et al., licensed under CC BY 4.0.

of neutrons and protons growing in the 20-50 MeV range and the fall-off of the charged pion SEU cross-sections.

Similarly, the fact that the LET distributions match at higher energy would return the higher pion SEU cross-sections due to the resonance (or the rescaling of the distributions with respect to the total nuclear reaction cross-section). The same conclusion at high-energy can likely apply to SEL cross-sections.

Triggering SEL requires higher energy deposition than does triggering SEU (this is for instance the reason why 14 MeV neutrons are a good proxy to spallation neutrons for SEUs, but not for SELs [153]). In addition, the experiments showed a higher SEL cross-section for pions at 50 MeV than that of protons and neutrons, but the LET distributions are quite similar.

6.2.3 Secondary ions as a function of their range

The range of the secondary ions yielded by hadron-silicon interactions is another important parameter for heavy ions (both primary and secondary), especially when it comes to potentially destructive SEEs, such as SEL, that require larger amounts of charge to be collected. In addition, the range of the secondary ions was used in the past to explain the differences in the SEL angular cross-section dependency for protons and ions [154].

Fig. 6.7 reports the normalized yield of secondary ions in terms of their range for various hadrons and energies. Similarly to the LET distributions, charged pion distributions differ from those of protons and neutrons the more the primary particle energy is reduced.

Note that the secondary particles whose LET was lower than the LET_0 of the Brilliance SRAM (2.4 MeV/(mg/cm^2)) were filtered out in the range plot as they cannot cause SEL by definition. Therefore, the minimum range of secondary ions having an LET $>$ LET_0 is 500 nm.

The 21 MeV case is quite explicative. Secondary ions from protons do not have range

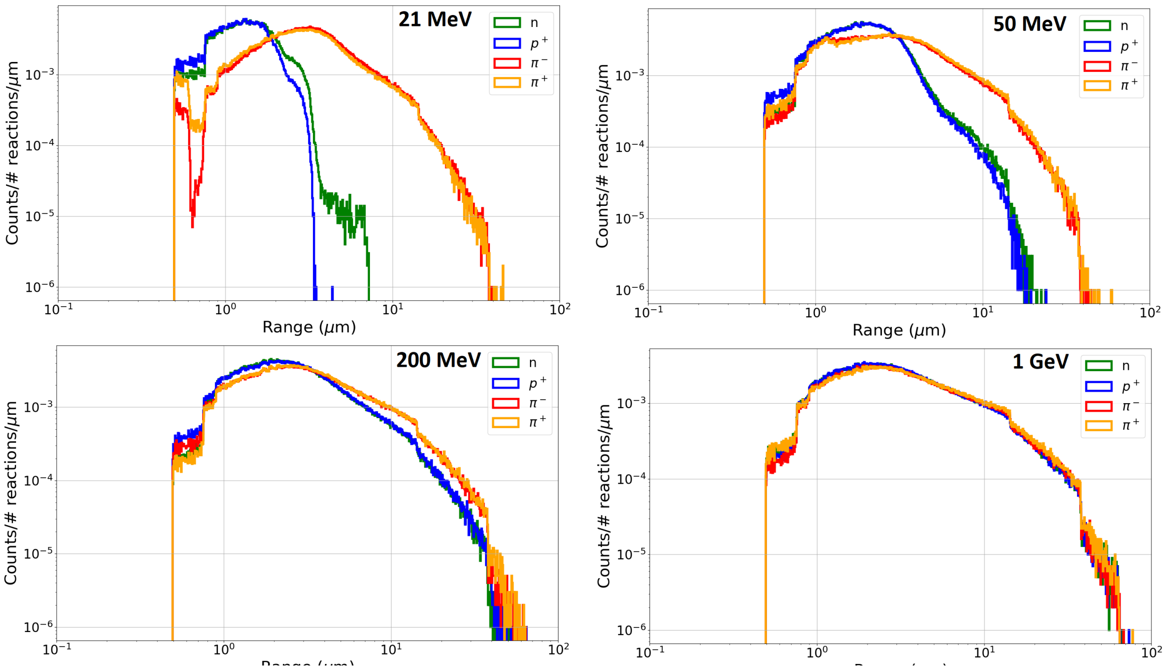

Figure 6.7: Normalized yield of secondary ions as a function of their range in silicon for neutrons, protons and charged pions in the 21-1000 MeV primary energy range. Only ions with LET upon generation above 2.4 MeV/(mg/cm^2) are considered. Obtained with FLUKA preex. Reprinted from [110]. © 2021, Coronetti et al., licensed under CC BY 4.0.

$>$ 4 μm and just a few secondary ions from neutrons can achieve ranges up to 8 μm. On the other hand, secondary ions from pions typically peak at ranges of 4-6 μm and can even have ranges as high as 40 μm.

These differences are somewhat reduced at 50 MeV, although it is noted that once again, secondary ions from protons and neutrons start to be in defect with respect to those from pions above 6 μm and are, then, about one order of magnitude lower for any range bin. Finally, at 200 MeV the differences become basically negligible and the overlap is almost perfect at 1 GeV.

The range distributions give a first indication that energy deposition events may have quite different magnitude at lower energy among charged pions and the other two hadrons. However, it may be first interesting to also compare the kinetic energy of some secondary particles since this is where the difference in range come from.

6.2.4 Secondary ions as a function of their kinetic energy

Fig. 6.8 depicts the normalized yield of secondary protons from hadron-silicon interactions in terms of their kinetic energy for various particles and energies. While high-energy secondary protons do not contribute to the SEU and SEL response (due to the low LET and to the low probability of triggering a new nuclear reaction with another silicon nucleus), they are the particles for which the consequences of the absorption mechanisms are more evident.

Note that the secondary protons from protons and neutrons interactions with silicon always have a hard limit in terms of kinetic energy that corresponds to the energy of the primary. On the other hand, the secondary protons from pions exceed the kinetic energy of the primary [155]. This kinetic energy excess is particularly noticeable at low-energy since it is several times the kinetic energy of the primary. However, the maximum delta in kinetic energy provided to the secondary protons is always in the order of 120 MeV. Therefore, the pion mass (which is given up during the absorption) can be converted in kinetic energy, which

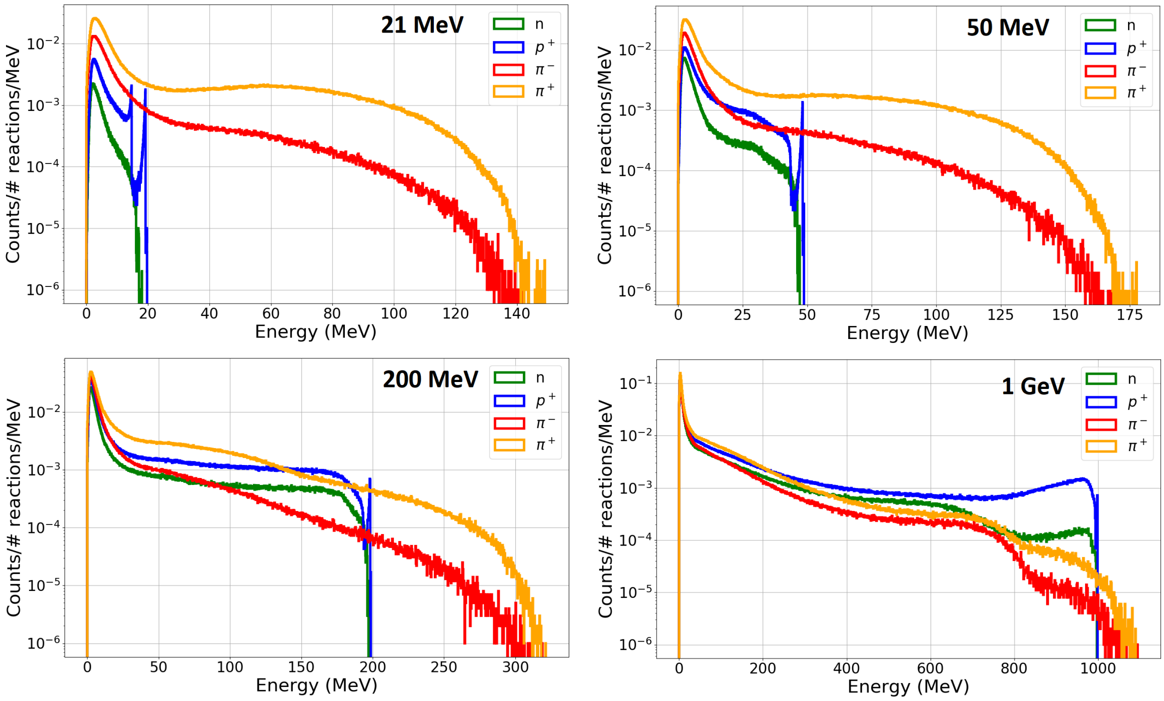

Figure 6.8: Normalized yield of secondary protons as a function of their kinetic energy for neutrons, protons and charged pions in the 21-1000 MeV primary energy range. Obtained with FLUKA preex. Reprinted from [110]. © 2021, Coronetti et al., licensed under CC BY 4.0.

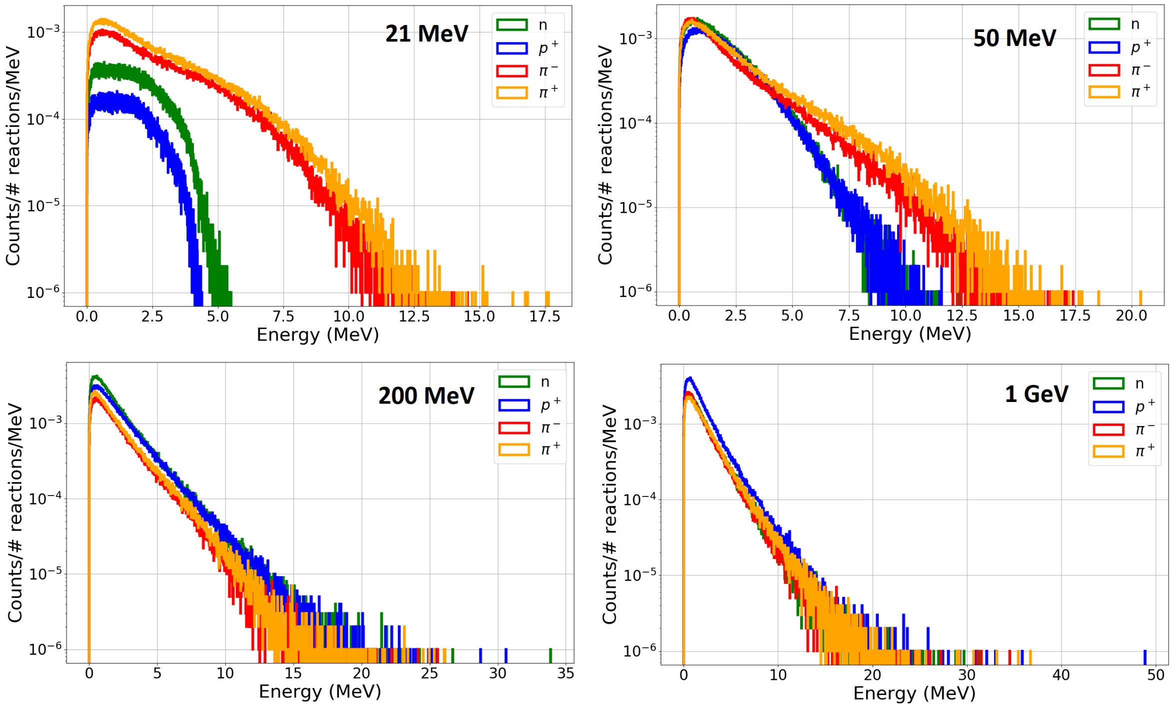

Figure 6.9: Normalized yield of secondary magnesium ions as a function of their kinetic energy for neutrons, protons and charged pions in the 21-1000 MeV primary energy range. Obtained with FLUKA preex. Reprinted from [110]. © 2021, Coronetti et al., licensed under CC BY 4.0.

is made available to secondary protons and ions.

Fig. 6.9 depicts the same normalized yield, but for secondary magnesium ions. It is evident that the kinetic content available to the secondary ion scales with the mass of the secondary ion. Indeed, for magnesium there is a potential excess of $\approx$ 10 MeV available. At the same time, for the magnesium ion, it is noted that this excess becomes smaller with the increasing energy of the primary, inasmuch as at 200 MeV and 1 GeV, the kinetic energy distributions of all hadrons start to match. Therefore, in relative terms, the pion absorption becomes less effective with increasing primary energy. This is likely due to the fact that with increasing primary energy more reaction channels are open for protons and neutrons. And, among these reaction channels, there are some that involve the generation of secondary pions which are re-absorbed into the excited nucleus and give up their mass.

6.2.5 Secondary ions as a function of their volume-equivalent LET

Coming back to the wider range distributions of charged pions at low primary energy, the range of the secondary ions is a key metric when it comes to the triggering of SELs. This is because, differently from SEUs, which are associated with small SVs (a few hundreds of nanometers), SEL SVs of SRAMs are typically quite large, wide and, above all thick (a few microns). Therefore, the range is important when taken in comparison to the size of the SV.

In this context, the LET upon generation is not a reliable metric because secondary ions may have a quite high LET, but very short range when compared to the SV dimensions. A better metric is represented by the volume-equivalent LET, which rescales the ionizing capabilities of each ion by taking into account their range in relative terms with respect to the SV thickness (the thickness is taken because of the mono-directional beams used for the tests and also because secondary ions are preferably emitted in the same direction of the primary particle). In this case the volume-equivalent LET is calculated upon the following formulas:

$$\begin{cases} LET_{eq} = \frac{E_k}{\rho t} & R \leq t \\ LET_{eq} = LET & R > t \end{cases} \tag{6.1}$$

Therefore, if the ion range R is lower than the SV thickness t, the ion will deposit its full kinetic energy and this is redistributed over a characteristic size of the SV to provide the LET$_{eq}$. Otherwise, if the range is longer, it is a fair description to take the LET$_{eq}$ to match the LET of the ion upon generation.

Fig. 6.10 depicts the normalized yield of secondary ions in terms of their volume-equivalent LET for various primaries and energies. In this case, secondary ions that, as a result of the LET$_{eq}$ calculation, have an LET$_{eq}$ below the threshold (2.4 MeV/(mg/cm^2)) have been filtered out.

The importance of the volume-equivalent LET in determining the SEL cross-section is evident. At 21 MeV, there is still a quite large amount of secondary ions from pion-hadron interaction with LET$_{eq}$ higher than the threshold and extending above 12 MeV/(mg/cm^2). On the other hand, secondary ions from protons and neutrons have almost disappeared and a relatively important contribution remains only below 5 MeV/(mg/cm^2) along with a quite narrow peak at $\approx$ 9 MeV/(mg/cm^2).

As demonstrated in Table III in [110], the convolution of these volume-equivalent LET distributions with the SEL heavy ion Weibull function of this SRAM provides a more faithful estimation of the SEL proton and pion cross-sections than the convolution with the LET distributions themselves.

As seen for the other plots, LET$_{eq}$ distributions of protons and neutrons start to resemble more and more to those of pions as the energy of the primary is increased (quite in accordance to the range distributions). Although following the pion distribution shapes,

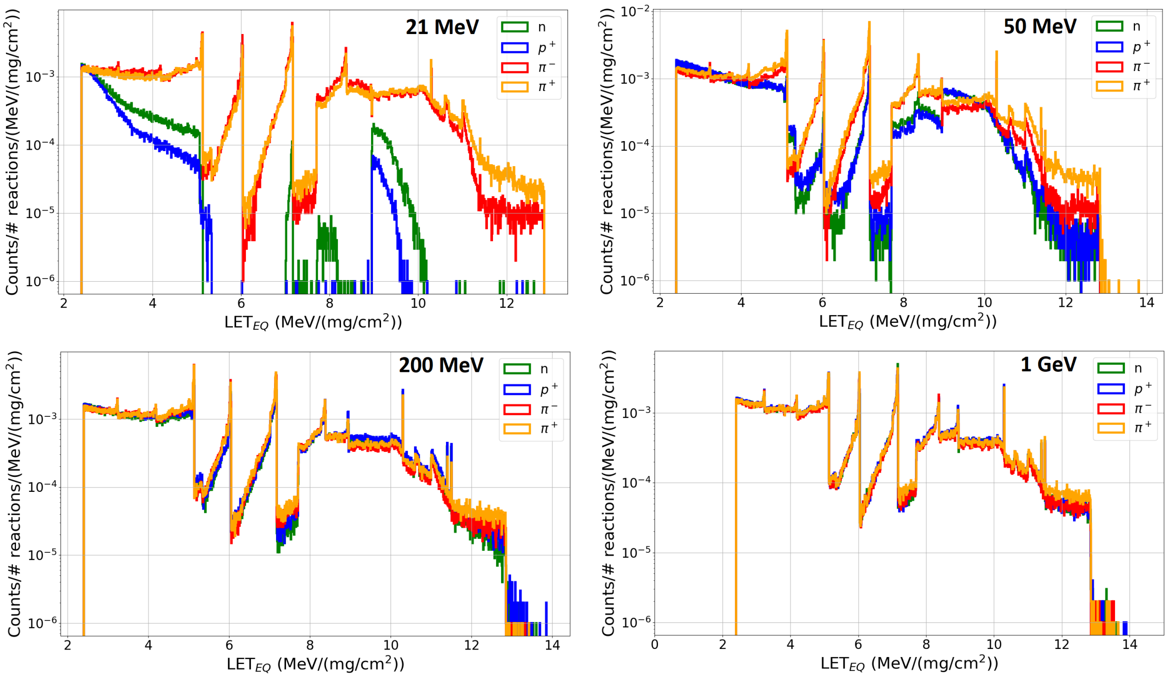

Figure 6.10: Normalized yield of secondary ions as a function of their volume equivalent LET for neutrons, protons and charged pions in the 21-1000 MeV primary energy range. A thickness of 3 μm is considered for calculation of the LET$_{eq}$. Only ions with volume equivalent LET above 2.4 MeV/(mg/cm^2) are considered. Obtained with FLUKA preex. Reprinted from [110]. © 2021, Coronetti et al., licensed under CC BY 4.0.

at 50 MeV, protons and neutrons are still somewhat defective for volume-equivalent LETs above 5 MeV/(mg/cm^2). The differences become nearly negligible at 200 MeV and above.

6.2.6 Conclusions

To answer the first two observations at the beginning of the chapter:

- SEU and SEL cross-sections from pions are indeed higher in the resonance region of the total nuclear reaction cross-section due solely to the higher probability of interaction. The characteristics of the secondary ions are indeed very similar in the resonance region among pions and the other hadrons. Therefore, the pion absorption plays a marginal role, that is to differentiate negative and positive pion cross-sections.

- The SEU cross-section also follows the total nuclear reaction cross-section due to the low LET$_0$ of this mechanism and small SV. On the other hand, the divergence in the SEL cross-section is fully caused by the pion absorption. By giving up the rest mass, pions yield secondary ions with higher kinetic energy than protons and neutrons at low-energy (21-50 MeV). This higher kinetic content results in secondary ions with longer range, so that these ions can typically cross the entire sensitive volume and deposit larger amounts of energy (as the volume-equivalent LET portrays).

6.3 Hardness assurance implications for the accelerator

The aim of this section and this work on pions is to verify whether the HEH equivalence approximation for accelerator environments holds or if the pion resonance and absorption mechanisms have an impact on SEU and SEL predictions extrapolated from testing with high-energy protons (e.g., 200 MeV protons at PSI). Note that this part is meant to cover only the high-energy hadron part of the HEH equivalence (i.e., only particles above 20 MeV are considered since the impact of thermal and intermediate energy neutrons is treated elsewhere [7, 147]).

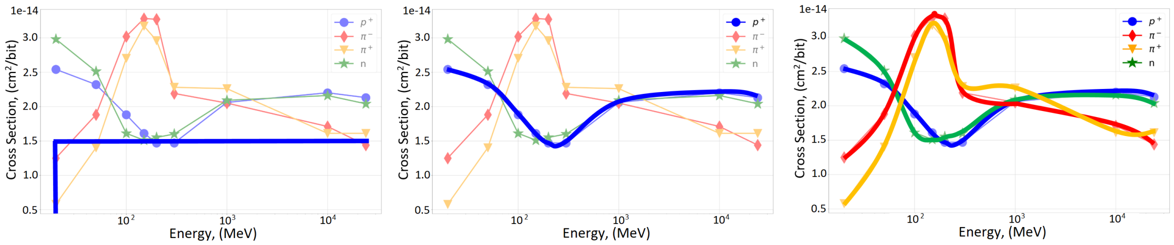

(a) (b) (c)

Figure 6.11: Three approaches to calculate the SEU response in mixed-field: (a) HEH approximation based on a step function with the 200 MeV proton cross-section, (b) convolution of all particle fluxes with the full proton cross-section as a function of energy, (c) convolution of each particle flux with each particle cross-section as a function of energy.

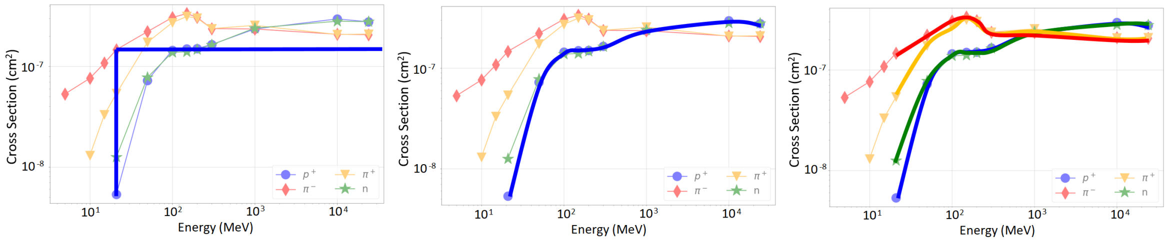

(a) (b) (c)

Figure 6.12: Three approaches to calculate the SEL response in mixed-field: (a) HEH approximation based on a step function with the 200 MeV proton cross-section, (b) convolution of all particle fluxes with the full proton cross-section as a function of energy, (c) convolution of each particle flux with each particle cross-section as a function of energy.

The procedure to test the HEH equivalence approximation is the same for both SEU and SEL and it is exemplified through the plots in Figs. 6.11-6.12. The idea is to calculate the SEE rate in mixed-field following three possible approaches:

- The HEH approximation: based on the multiplication of the integral HEH flux with the proton cross-section measured at 200 MeV;
- The convolution of all particle fluxes with the proton cross-section curve: this is an intermediate step that is meant to take into account at least the cross-section variability with the energy of the protons (and, by consequence, neutrons);
- The convolution of all particle fluxes with the respective cross-section curves: this approach does not provide any approximation and it can be considered the actual mixed-field response.

In order to check both (i) whether the HEH equivalence approximation stands and (ii) whether CHARM can provide comparable results to other facilities, the CHARM mixed-field fluxes were used for these computations. A few CHARM positions, representative of the LHC tunnel environment (R13), of the shielded alcoves (R10) and of the Earth's proton radiation belt (R5) are considered for the calculations.

SEU and SEL rates are reported in Figs. 6.13-6.14 for three CHARM positions. The computations were achieved for the ISSI and the Brilliance SRAM based on the numerical

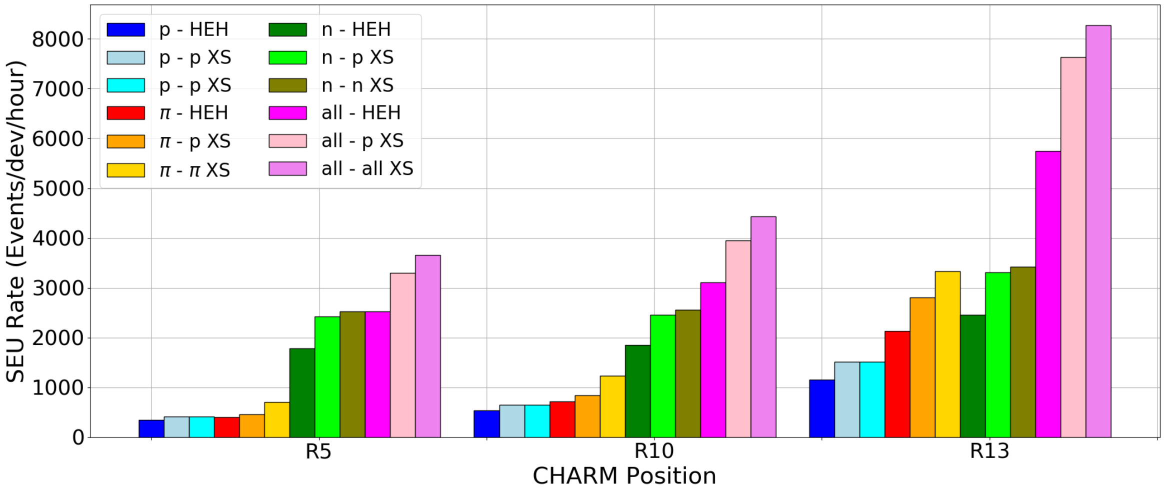

Figure 6.13: Comparison of SEU rates for the ISSI SRAM in three CHARM positions for the three approaches. Data are subdivided per particle.

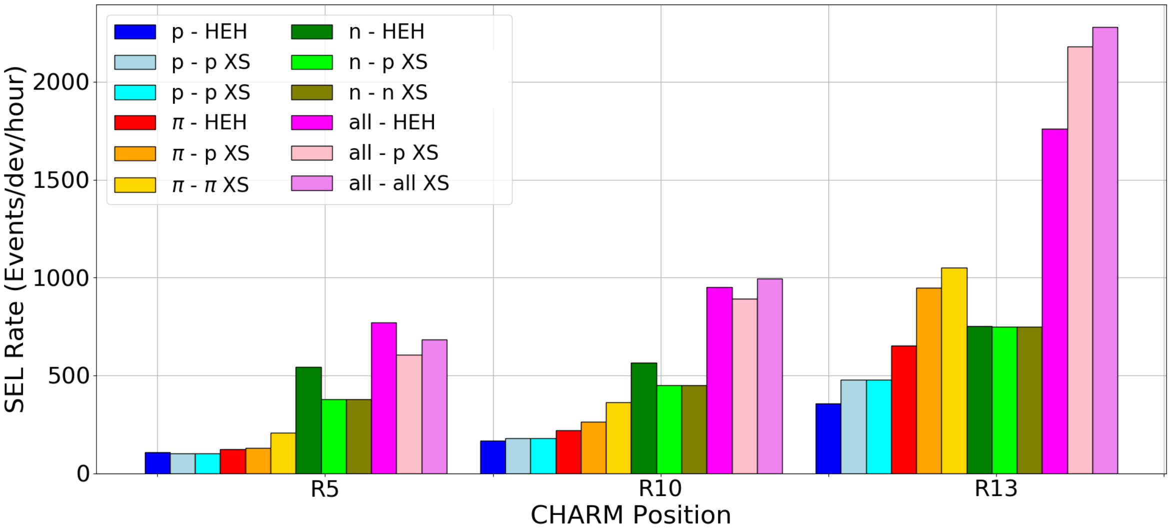

Figure 6.14: Comparison of SEL rates for the Brilliance SRAM in three CHARM positions for the three approaches. Data are subdivided per particle. Reprinted from [110]. © 2021, Coronetti et al., licensed under CC BY 4.0.

SEE cross-sections. The data are broken down by particle and by calculation method. In addition, the overall rates are also reported. In the legend, the part before the hyphen refers to the particle fluxes, whereas the part after the hyphen is the calculation method. Note that pion fluxes are scored together, no matter the charge, so it is assumed that one half of the pion fluxes have negative charge and the other half have positive charge.

Concerning SEUs and the impact of the resonance, it is observed that this phenomenon has mild effects on the upset rate when the pion fluxes are low (e.g., R5 and R10). In such cases, the HEH equivalence approximation usually provides lower estimates (up to 33% less) due to the high neutron fluxes in the 20-100 MeV region. Concerning the impact on the total upset rate it is observed that this can be ameliorated if the whole proton cross-section as a function of energy is used instead of the single 200 MeV point.

Concerning SELs, for R13 pions end up being the largest contributor to the total response, but this does not seem to be due to the observed enhancements below 200 MeV, but rather to the higher pion fluxes at GeV energy. The reason why the impact is contained is that, for SEL, the HEH equivalence approximation is very conservative when it assumes that the proton and neutron SEL cross-sections at 20-50 MeV is as high as that at 200 MeV (indeed the 200 MeV proton cross-section is very similar to the < 50 MeV charged pion cross-sections). This is the reason why for R5 and R10 the HEH equivalence approximation provides very similar results to the actual response and, on the converse, using the whole proton cross-section response yields underestimations.

Table 6.1: Ratios between the total SEE rates calculated with the HEH equivalent approximation and the other two methods and for the three CHARM test positions under consideration.

	HEH$_{eq}$ / proton		**HEH$_{eq}$ / all**	
CHARM position	**SEU**	**SEL**	**SEU**	**SEL**
R5	0.76	1.27	0.69	1.13
R10	0.79	1.06	0.70	0.96
R13	0.75	0.81	0.70	0.77

To conclude on these points, a summary is provided in Table 6.1. The HEH equivalence approximation for SEUs is not much impacted by the pion resonance. Neutrons are responsible for the largest inaccuracy, in this case. Only for position R13, the HEH equivalence approximation provides quite low estimates for the pion contribution. However, globally the impact is reduced to about a 33% underestimation, which is still fairly acceptable. Even lower inaccuracy is found for SEL, with a worst case of about 25%. Therefore, testing with 200 MeV protons can provide a reliable estimation of both the SEU and SEL rate in the accelerator.

Considering the compatibility between the HEH mixed-field SEE cross-sections and those from 200 MeV proton testing, it is clear that using CHARM as a proxy of the space environment can provide very reliable estimates of the proton part of the space SEU and SEL rates. In particular, the use of CHARM enables tests at board- and system-level that cannot be achieved in standard proton facilities (where the beam size is too small).

Chapter 7

HEH testing for space systems

The guideline [46] on system-level testing with HEHs for space missions and the related paper [47] at the end of this thesis provide the working frame and plenty of notions and recommendations on how to conduct system-level testing from the point of view of objectives, implementation and data exploitation.

This chapter will focus on the complementary aspects that can either justify or challenge the use of HEHs as a proxy to heavy ions. As reported in the guideline documents, while the challenges are often unacceptable in the case of standard space missions, there is a growing number of space applications for which those challenges represent less critical constraints than those introduced by the standard RHA approaches. However, discussing these challenges is of primary importance in order for users to be well-aware of the underlying risks.

The analysis performed in Chapter 6 was aimed at ensuring that the CHARM mixed-field could be used as a proxy to high-energy proton irradiation and the other way around. Now, the objective is to determine how to use HEH beams (mono-energetic protons, spallation neutrons and mixed-fields) for the verification of space systems that are typically subject to an environment composed of protons and ions.

7.1 Comparison between HEHIs and HEHs

As a first step it is worthwhile comparing what are the potentialities and limitations of HEHs with respect to one possible alternative, that is high-energy heavy ions. High-energy heavy ions are characterized by much deeper range in matter than ions at standard energy, but are also more limited in terms of LET. For the sake of this comparison, a Pb ion with an energy of 5 GeV/n will be considered. The choice was dictated by the fact that a Pb ion of this energy is available from the standard ion operation of the CHARM facility [52].

Concerning the HEH beams, the analysis is not specifically restricted to the CHARM facility (whose mixed-field operation was described in Chapter 3), but it also includes another two types of beams. The first alternative is spallation neutrons. The ChipIr facility [125, 156] is well suited for the purpose of system-level testing thanks to the deeply penetrating beam that enables irradiation of bulky systems. The second alternative, which is actually the most common for space qualification, is to use mono-energetic HEPs. Cyclotron-accelerated protons with an energy of 200 MeV are quite common and they represent a very good compromise in terms of deep penetration in matter and deposited TID (if compared to lower energy protons).

7.1.1 Beam penetration

For the sake of this initial comparison, the beams will be compared among each other and, in some cases, with the space radiation environment. Given that the use of HEHs and

HEHIs may find wider application in LEO space missions, an orbit with 800 km altitude, 98° inclination, solar minimum conditions is considered. For the beam penetration analysis purposes, only trapped proton and GCR protons are considered. GCR ions are not expected to change the overall picture due to their much lower fluxes with respect to protons, although certainly GCR ions may be more threatening in terms of SEE induction.

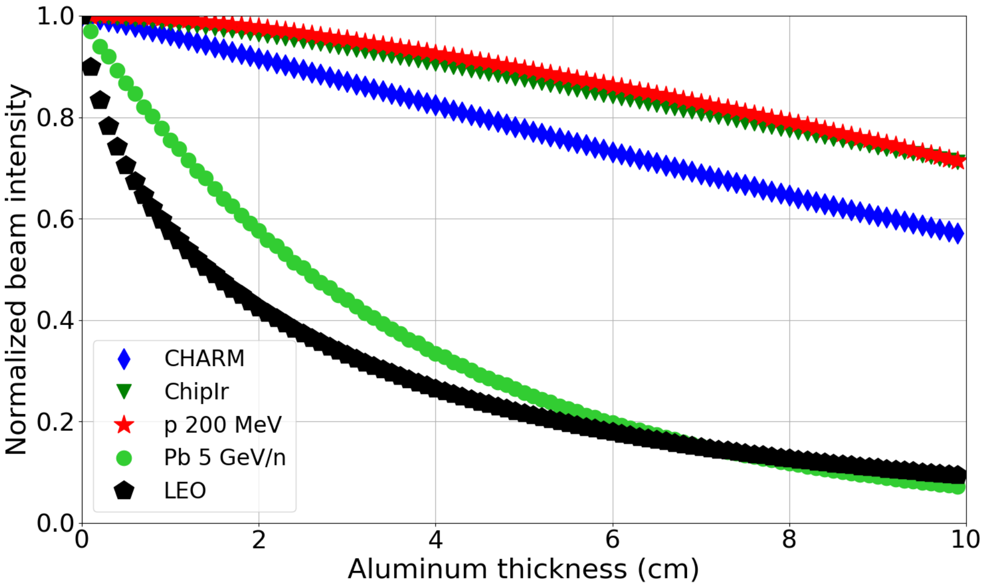

Figure 7.1: Relative fluence of the primary beam as a function of depth in aluminum for the HEH beams (only hadrons above 20 MeV are considered), the HEHI beam and the space trapped proton field (again only protons with energy above 20 MeV). CHARM R4 position was considered.

Space systems can be quite bulky. Typically 100 mils of aluminum are used for transportation of the space environmental fields through the shielding of the satellites. However, if one considers an actual satellite or subsystem that has to be irradiated in a HEH or HEHI beam through a single irradiation, it is necessary to ensure that the fluence of particles received from the backside is similar to that of the front side. Considering the potentially large amount of material within a satellite, it is clear that what stands on the backside will likely be shielded by a few cm of material. Also in this case aluminum can be used as an equivalent to describe all the diverse materials that stand between the beam and the ICs.

Considering for instance a satellite/system with a volume of 50 x 50 x 50 cm^3, since the satellite is not completely full it is realistic to assume that the equivalent thickness of aluminum from one side to the other can be in the order of a few cm.

FLUKA is used to transport the various radiation fields through the various layers of aluminum and determine their penetration capabilities. For the HEH beams and the LEO environment, the comparison is further restricted to hadrons with energy above 20 MeV, although neutrons can still cause some relevant indirect ionization phenomena below 20 MeV.

Fig. 7.1 depicts the relative beam intensity (hadrons with energy above 20 MeV, except for the Pb beam) as a function of depth in aluminum for the five radiation fields under consideration. As the figure shows, the LEO environment is characterized by very high fluxes of trapped protons, which have more limited energy than GCR protons, and, therefore, after 2 cm of aluminum the proton flux would reduce to just 40% of the primary field.

Considering the HEH beams, their penetration capabilities are very promising. At 2 cm all the three beams have retained more than 92% of the original fluence. Therefore, considering that standards typically require a fluence homogeneity of ±10%, if the system has about 2 cm of equivalent aluminum between the front and back sides, the use of these beams will guarantee uniform irradiation. Actually, for ChipIr and 200 MeV protons, this high-level of homogeneity is maintained for up to 4 cm of equivalent aluminum.

Concerning the Pb beam at 5 GeV/n, the range of these ions in aluminum is more than 30 cm. However, the reason why the beam degrades so fast is that the inelastic scattering length of these ions is just about 4 cm. Therefore, after a depth of 4 cm it is expected that a quite large amount of ions would have experienced a nuclear interaction with the aluminum nuclei. As a result, after 2 cm of Al, the primary beam has already reduced to about 56%. A homogeneity of 90% can be ensured only for a depth of less than 4 mm (about 160 mils).

7.1.2 Deposited dose

One of the biggest constraints of HEH irradiation is that charged hadrons are quite ineffective at yielding secondary ions, but, at the same time, each single charged hadron contributes to the deposited TID. On the other hand, in the case of HEHIs, while each of them deposit a much higher TID than a HEH, the beam is much more effective when it comes to triggering SEEs. This is because each individual primary ion can cause SEEs by direct ionization. Therefore, even the TID per primary is higher, a much lower amount of primary HEHIs is needed to trigger as many SEEs as HEHs would do at the same TID.

In standard heavy ion testing the screening against potential destructive SEEs (e.g., SEL) is performed up to an ion fluence of 10^7 ions/cm^2 and it is performed at a fixed LET. This can potentially be easily replicated with HEHIs. A direct comparison with HEHs is not that straightforward. HEHs yield a spectra of secondary ions from their nuclear interactions with silicon (and other materials) that is distributed over a larger range of LETs. Therefore, comparing the yield of secondary ions from HEHs to that of HEHIs requires integrating the HEH secondary ion yield above a certain LET (representative of the device LET threshold). Certainly, a high level of arbitrariness is needed when picking this threshold (given the very wide variability of LET thresholds of EEE devices). For this reason, a parametric analysis of the deposited TID as a function of the LET$_0$ can provide a better perspective about the problem.

As a reference, a yield of 10^4 ions/cm^2 is considered in this analysis. While this can be considered to be quite a low amount of ions, it is worth pointing out that the TID will scale linearly with the ion yield. Therefore, the data in Fig. 7.2 can directly be rescaled if a higher yield is considered by simply multiplying the TID on the y-axis by the ratio between the yield of interest and the used baseline.

In order to aggregate and compare the energy deposition events derived by direct and indirect ionization, it was shown that the LET of the ions cannot be generally considered as a reliable metric when it comes to short range ions as those generated by hadron-silicon interactions. Therefore, the ionization capabilities of the HEH secondary ions have to be quantified through a metric that accounts for the geometry of the SV. The volume equivalent LET is a much more appropriate metric when it comes to large enough volumes typical of potentially destructive SEEs:

$$LET_{eq} = \frac{E_{dep}}{\rho t} \tag{7.1}$$

The use of the LET$_{eq}$ enables performing an even deeper comparison by considering how things change for different geometries of the device SV. FLUKA is used in this analysis to determine the energy deposition event distributions from the three HEH beams and the HEHI beam. The simulated SV is that proposed for the Brilliance SRAM before with 20 x 4 x 3 μm^3 volume. In addition, and to widen the study over a larger amount of devices, a thicker SV is also considered with 20 x 4 x 10 μm^3 volume.

Fig. 7.2 shows the TID as a function of the LET$_{eq}$ threshold above which the integrated yield of ions is of 10^4 ions/cm^2. The dose is shown because it is more relevant than the fluence of protons or neutrons when it comes to the assessment of the HEH and HEHI irradiations (in

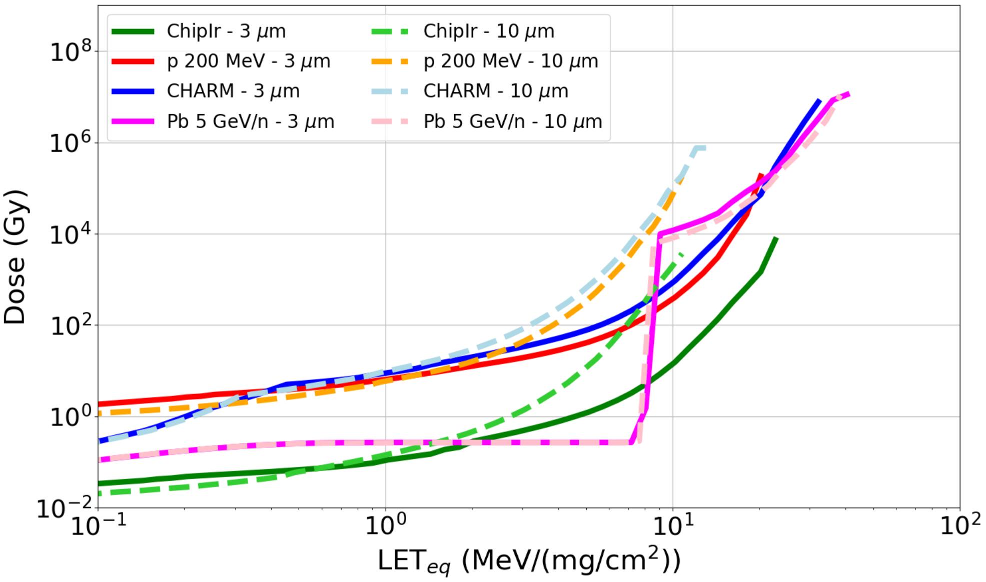

Figure 7.2: TID deposited in the silicon devices as a function of the volume equivalent LET threshold of the device for the three HEH beams and the HEHI beam and for two different SEL SV geometries. The curves are determined for an ion yield of 10^4 ions/cm^2. Note the sharp transition between direct and indirect ionization regime for the HEHI beam.

particular considering that COTS device are typically functional only up to a few hundreds Gy in silicon).

For the 200 MeV protons, the TID is calculated following eq. (2.5). Considering the LET of the protons, each primary will deposit 5.81 x 10^{-10} Gy(Si). For the other HEH beams calculating the TID is more complicated.

For ChipIr, for instance, the neutrons do not directly deposit any dose in the silicon devices, however, the secondary particles generated from nuclear interactions do. Therefore, the dose from a spallation neutron beam is not null. The TID of the ChipIr beam was determined by integrating all energy deposition events obtained from FLUKA that have an energy $>$ 100 keV (it was verified that this approach yields the same dose deposited in the volume and given by the FLUKA standard output). This calcuation yields a TID per primary of 7.30 x 10^{-12} Gy(Si). Note that at ChipIr there is also a γ-ray component (on top of the spallation neutrons) that is received by the devices and that can contribute to the TID. However, precise measurements of neither the gamma-ray flux nor the TID on the ChipIr beamline are available and, for the sake of this analysis, the contribution of γ-rays will be considered negligible.

Concerning CHARM, the beam is composed of a mixed-field of which hadrons are relevant for both SEE triggering and TID. For the latter, both the direct and indirect energy deposition may matter. However, photons and electrons also strongly contribute to the TID in CHARM. From FLUKA simulations available online [123], it is determined that the dose per primary HEH (i.e., by including the contribution of photons and electrons as if it was due to hadrons) at the R4 position is 5.90 x 10^{-10} Gy(Si), which is very similar to that of 200 MeV protons.

Finally, for the Pb 5 GeV/n ions the LET is 8.3 MeV/(mg/cm^2) and it was determined from FLUKA. It shall be specified that this is a restricted LET (i.e., that takes into account only the energy deposited by the delta-rays nearby the ionization track), which differs from that obtained from SRIM ($\approx$ 11 MeV/(mg/cm^2), which also accounts for the long range delta-rays depositing energy far from the ionization track) [30]. The restricted LET yields a dose per primary ion of 1.33 x 10^{-6} Gy(Si).

There are many take-aways from the data portrayed in Fig. 7.2. Sticking to the same

SV geometry (with 3 μm thickness) and comparing the HEH beams among each other and with the HEHI beam, it is clear that the deposited TID to achieve the same number of ions of a certain LET differs a lot. For the Pb 5 GeV/n beam, any LET threshold below the primary LET of the ion will basically yield the required amount of ion with very low dose, e.g., ≈ 0.3 Gy(Si). However, it is still possible to get energy deposition events with higher LET than that of the primary ions from the indirect ionization caused by the nuclear interactions of the primary ions with the silicon nuclei (the same mechanism behind the HEH indirect ionization). However, of course, this would come at a much higher expense in terms of TID than with any HEH beam.

Concerning HEH beams, as expected by the TID per primary, there are not many differences between CHARM and 200 MeV protons. Things change progressively depending on the LET threshold of interest. For instance, to have an ion yield of 10^4 ions/cm^2 with LET$_{eq} > 3$ MeV/(mg/cm^2) one would deposit a TID of $\approx$ 20-30 Gy(Si) (which correspond to $\approx 5 \times 10^{10}$ HEH/cm^2). A TID of 200 Gy(Si) would allow getting an ion yield of 10^4 ions/cm^2 with an LET$_{eq} > 7$ MeV/(mg/cm^2). As an alternative, a yield of 6 x 10^4 ions/cm^2 above 3 MeV/(mg/cm^2) can be attained with a TID of 200 Gy(Si).

Spallation neutrons are much more promising in this respect. If a LET$_{eq}$ threshold of 3 MeV/(mg/cm^2) is considered, then the ion yield of 10^4 ions/cm^2 is already achieved by depositing just 0.5 Gy(Si), i.e., very similar to that of the Pb beam. At 200 Gy(Si) one would have obtained 4 x 10^6 ions/cm^2 above this same LET$_{eq}$, which would be fairly close to the standard ion fluence for testing. Nevertheless, also for spallation neutrons it is hard to shift the LET$_{eq}$ threshold to higher values. If 10 MeV/(mg/cm^2) is taken as threshold, the 10^4 ions/cm^2 yield would be achieved with a dose of ≈ 15 Gy(Si). At 200 Gy(Si), the yield of ions above 10 MeV/(mg/cm^2) would be of 1.3 x 10^5 ions/cm^2.

The effect of the different geometries of the SVs does not have any remarkable effect on the HEHI beam given that the ions have much longer range than the SV size and, therefore, direct ionization phenomena should produce identical energy deposition events. On the other hand, there are remarkable effects when it comes to HEHs and the LET$_{eq}$ of interest. At an LET$_{eq}$ threshold of 3 MeV/(mg/cm^2) the TID necessary to attain 10^4 ions/cm^2 has tripled for all the three HEH beams for the thicker SV. And the dose difference between 10 μm and 3 μm increases exponentially with increasing LET$_{eq}$. For instance, at an LET$_{eq}$ of 7 MeV/(mg/cm^2) one would roughly need a hundred times more primaries to generate the same ion yield for all the three HEH beams and, thus, the dose deposited would also be a hundred times higher.

As it is clear from this graph, due to TID issues, HEH beams will not be very effective in screening devices associated with deep SV. At the same time, looking to get as many ions as possible in this LET$_{eq}$ range for such devices may also be an unworthy effort. Indeed, devices with deeper SV are typically associated with also a higher LET threshold. Therefore, they may even require a much higher amount of ions than 10^4 cm^{-2} for just a few SEEs to be observable.

It is possible to conclude that one of the main value of HEHIs over HEHs is that they provide identical stimuli irrespectively of the geometry of the device SV. This is clearly an issue for HEHs, given that it is not possible to get rid of the geometrical parameters to simplify the analysis and determine whether they would be a suitable proxy to HIs.

As a final take-away, it is noted that given the ratio between the dose per primary of the CHARM (or the 200 MeV proton beam) and the Pb 5 GeV/n beam, a fluence of 10^{11} HEH/cm^2 would deposit the same dose (58 Gy(Si)) than a fluence of 5 x 10^7 ions/cm^2. This will be used in the following analysis.

7.1.3 What kind of sensitivities are exposed by HEHs and HEHIs?

The next question in this comparison stands in understanding whether HEHs and HEHIs are equivalent in terms of device SEE sensitivities that they can expose. Such an analysis requires delving deeper into the wide variability that devices may display in terms of SEE response to heavy ions. Therefore, a parametric analysis is performed to take into account various possible combinations of heavy ion SEE responses based on the potential set of SEL saturation cross-sections and the potential set of LET thresholds.

If only the two previously mentioned parameters are considered, then the heavy ion response is assumed to be a step function (S) starting at the LET threshold and with the HI saturation cross-section as fixed value at any LET > LET$_0$. The use of a step function as a response for a device provides very conservative estimations for the SEE rate in space. However, for the type of analysis that will follow, using a step function response would actually overestimates the capabilities of HEH and HEHI beams in exposing the SEE sensitivity of electronic devices.

This is the reason why, along with the step function response, the 4-parameter Weibull response (W) is used as well. For the 4-parameter Weibull response, in addition to the two earlier mentioned parameters, it is necessary to define also the shape parameter W and the exponent s. Given that these parameters would further complicate the analysis, average values are used. An extensive literature research on device SEL HI data [20, 157–174] (which also includes the data collected during the CNES experiments, see Table 4.4) shows that W = 30 MeV/(mg/cm^2) and s = 3 can be assumed as average values for a quite wide collection of devices.

The SEE response of a device to a HEH or a HEHI beam is determined by convolving the energy deposition distributions as a function of LET$_{eq}$ from these testing environments with the heavy ion SEE response (expressed as either a step or a Weibull function). Therefore, by considering various pairs of LET$_0$-σ_{sat}, it is possible to determine the expected rate for that device in a HEH or HEHI beam after a certain fluence of HEH or ions has been delivered. For the follow-up analysis, CHARM will be considered representative of all HEH beams, as it was earlier shown.

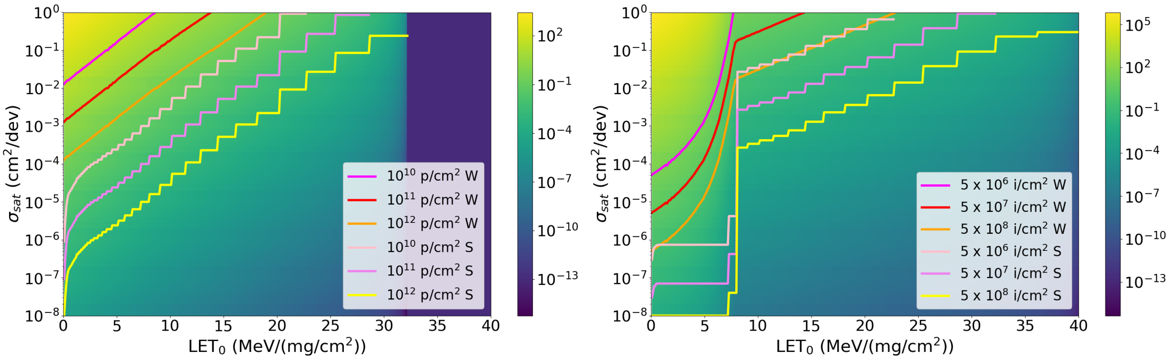

Figure 7.3: Colormaps of the SEE rate for an RPP with 20 x 4 x 3 μm^3 SV at CHARM for a fluence of 10^{11} HEH/cm^2 and with Pb 5 GeV/n ions for a fluence of 5 x 10^7 ions/cm^2 based on MC simulations and the Weibull function. The SEE rate for the Weibull case is shown as a function of the device LET threshold and HI saturation cross-section. The lines on top of the colormap define all the combinations of LET$_0$-σ_{sat} for which at least 3.7 SELs will be observable during the test according to the fluence of HEHs or HEHIs and the SEE response (W = Weibull, S = step). σ_{sat} larger than SV area implies multiple sensitive cells. The minimum LET$_0$ for the parametric analysis was 0.1 MeV/(mg/cm^2).

Fig. 7.3 (left) depicts, by means of a colormap, the SEE rate at CHARM for various combinations of LET$_0$-σ_{sat}. The SEE rate in the colormap expresses the number of events for a fluence of 10^{11} HEH/cm^2. The SEL SV with 3 μm thickness was considered along with the 4-parameter Weibull function, with the aforementioned W and s, to determine the SEE rate. The first noteworthy aspect is that there is a sharp transition at an LET$_{eq}$ of $\approx$ 32 MeV/(mg/cm^2). The reason is that the HEH beam on silicon cannot yield any energy deposition event with higher LET$_{eq}$ than this limit. Therefore, by definition, the SEE rate should be null no matter the σ_{sat} (in the plot this is actually expressed with a very low SEE rate because the colormap scale is logarithmic).

The main interest behind this parametric analysis stands in identifying which sensitivities the HEH beam can expose, or, in other words, for which combinations of LET$_0$-σ_{sat} one can expect to see events in CHARM. Therefore, the interest is in finding the combinations of LET$_0$-σ_{sat} for which > 0 SEEs are expected to occur with an irradiation in the HEH beam. However, since this boundary is affected by very low statistics in terms of SEE occurrence, during an experiment the data retrieved in a HEH beam may fluctuate. Therefore, rather than bounding with respect to 1 SEE, and according to Poisson statistics, it would be better to bound the rate to 3.7 SEEs to increase the level of confidence to 95%. Therefore, it remains only a 5% chance that a combination of LET$_0$-σ_{sat} that is predicted to have 3.7 SEEs will actually suffer 0 SEEs in the HEH beam.

In Fig. 7.3 (left) the combinations of LET$_0$-σ_{sat} for which the SEE rate in CHARM is > 3.7 SEEs for the fluence of 10^{11} HEH/cm^2 is marked by a red line. Therefore, all devices having LET$_0$-σ_{sat} falling above the red line are expected to suffer from SEEs in CHARM and those below are expected not to.

A few more lines have been drawn on the colormap to assess how things change when the fluence is reduced or increased by a factor of 10 or when a step function response is considered in place of the Weibull function.

The former demonstrates that, by means of a higher fluence, it is possible to widen the combinations of LET$_0$-σ_{sat} for which sensitivity to a certain SEE could be exposed by means of HEH experiments. As mentioned, however, this would come at the expenses of a higher TID, therefore it may not be possible to actually test the system/devices up to 10^{12} HEH/cm^2 without experiencing TID failures (580 Gy(Si)).

The latter demonstrates that the use of a step function would provide very high overestimations about the capabilities of a HEH beam in stimulating SEEs, to the point that a fluence of 10^{10} HEH/cm^2 with the step function is expected to provide a wider amount of combinations of LET$_0$-σ_{sat} whose sensitivity would be exposed than a fluence of 10^{12} HEH/cm^2 with the average Weibull.

One of the main take-aways of the plot is that even if a device has a LET$_0$ of 1 MeV/(mg/cm^2), that does not mean that SEEs shall always be expected in CHARM, given that the σ_{sat}, W and s are also determinant.

Fig. 7.3 (right) provides a similar analysis, but for the Pb 5 GeV/n ion. Note that the indicated fluences for this very ion would deliver the same TID as the HEH fluences indicated for the CHARM case. The colormap provides the SEE rate exposed by these HEHIs for various combinations of LET$_0$-σ_{sat} and the same volume as for the CHARM case. Again, the interest stands in finding the combinations of LET$_0$-σ_{sat} for which at least 3.7 SEEs are observed.

As it was for the CHARM case these HEHIs can produce higher energy deposition events than those of the primary LET of the ion. These events are caused by indirect ionization phenomena emerging from the interaction between the Pb ion and the silicon nuclei. As it can be seen, Pb ions can yield indirect ionization energy deposition events beyond those available at CHARM (the actual threshold is about 41 MeV/(mg/cm^2)). However, another sharp transition is visible in the colormap and it occurs at the LET of the primary ion. This is because indirect ionization from ions (as it was for HEH) is much less likely than the own direct ionization.

As a result, when tracing the curve that defines the combinations of LET$_0$-σ_{sat} for which at least 3.7 SEEs will be observed from irradiation with HEHIs, an asymptote appears for LET$_0$ corresponding to the primary LET of the ion. An asymptote that is insensitive with respect to the delivered primary ion fluence. On the one hand, it is clear that the direct ionization contributes only to an increase in coverage in terms of σ_{sat}, but not LET$_0$ (for which it is lower than for HEHs). On the other hand, there are some events from indirect ionization that may extend the combinations of LET$_0$-σ_{sat} that can be exposed in a similar fashion as for HEHs.

The step function also strongly highlights the sharp transition across the primary LET of the HEHIs. Indeed, for a step function, one should obtain very similar rates no matter the actual LET$_0$ of the device if this is lower than the primary LET of the ion. The indirect ionization events from the step function are also very similar to those for HEHs. Therefore, also for HEHIs, the step function response is likely to bring to overestimations in the expected number of events in a HEHI beam.

Coming back to the question expressed in the title of this section, one can conclude that the susceptibilities exposed by HEHs and HEHIs are actually very similar when it comes to the device LET$_0$ sensitivity. However, the main difference is that at LET$_0$ equal or lower than that of the primary HEHI the latter is supposed to expose the SEE susceptibility of more devices because the range of σ_{sat} covered is larger. On the other hand, at LET$_0$ above the LET of the primary HEHI, the two beams can exercise devices in very similar fashions.

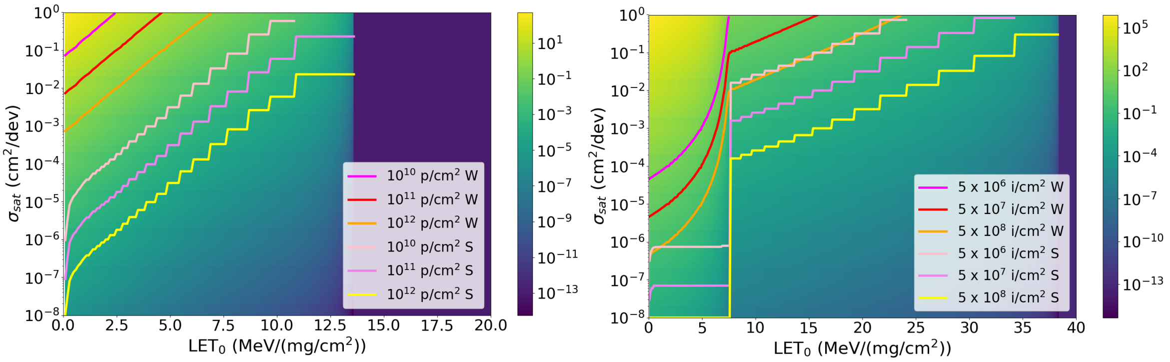

Figure 7.4: Colormaps of the SEE rate for an RPP with 20 x 4 x 10 μm^3 SV at CHARM for a fluence of 10^{11} HEH/cm^2 and with Pb 5 GeV/n ions for a fluence of 5 x 10^7 ions/cm^2 based on MC simulations and the Weibull function. The SEE rate is shown as a function of the device LET threshold and HI saturation cross-section. The lines on top of the colormap define all the combinations of LET$_0$-σ_{sat} for which at least 3.7 SELs will be observable during the test according to the fluence of HEHs or HEHIs and the SEE response (W = Weibull, S = step).

Nevertheless, the picture is not fully complete, given that the 3 μm thickness is not representative of all potentially destructive SEE structures. As it was shown for the delivered dose analysis, a thicker SV has a strong impact on the ion yield for HEHs, while leaving largely unaffected the considerations for HEHIs. Therefore, the analysis is extended to the case with 10 μm thickness.

Fig. 7.4 (left) portrays the same identical analysis as done before for the CHARM environment and Fig. 7.4 (right) for the Pb 5 GeV/n beam. Note that in the CHARM plot the x-axis has been rescaled by almost a half. This is because the energy deposition events for a 10 μm thickness come with a maximum LET$_{eq}$ of just 13 MeV/(mg/cm^2).

The consequences on the capability of HEHs of exposing certain SEE sensitivities also rescale in a similar fashion, i.e., by almost a factor of 3 in terms of LET$_0$ of the device given a certain σ_{sat} and a certain HEH fluence with respect to the 3 μm case. The differences between the Weibull case and the step function case are also enlarged and highlight how optimistic the expectations from a HEH test would be if the latter is considered.

On the other hand, as expected, things go rather unchanged for the HEHI case. For the thicker SV, one would then conclude that HEHI beams can provide a larger set of SEE stimuli to devices than HEH beams can.

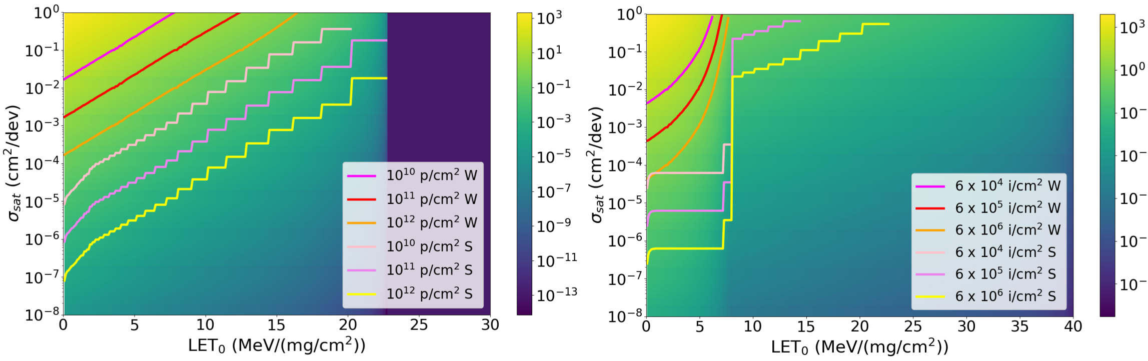

Figure 7.5: Colormaps of the SEE rate for an RPP with 20 x 4 x 3 μm^3 SV at ChipIr for a fluence of 10^{11} HEH/cm^2 and with Pb 5 GeV/n ions for a fluence of 6 x 10^5 ions/cm^2 based on MC simulations and the Weibull function. The SEE rate is shown as a function of the device LET threshold and HI saturation cross-section. The lines on top of the colormap define all the combinations of LET$_0$-σ_{sat} for which at least 3.7 SELs will be observable during the test according to the fluence of HEHs or HEHIs and the SEE response (W = Weibull, S = step).

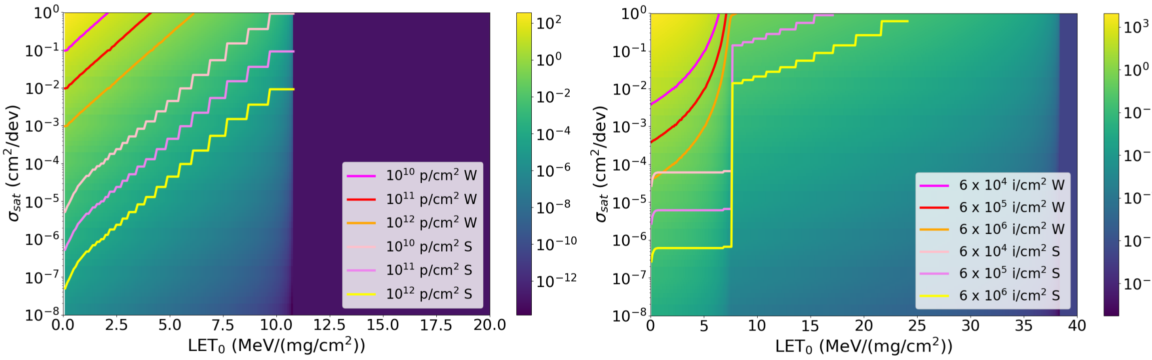

Figure 7.6: Colormaps of the SEE rate for an RPP with 20 x 4 x 10 μm^3 SV at ChipIr for a fluence of 10^{11} HEH/cm^2 and with Pb 5 GeV/n ions for a fluence of 6 x 10^5 ions/cm^2 based on MC simulations and the Weibull function. The SEE rate is shown as a function of the device LET threshold and HI saturation cross-section. The lines on top of the colormap define all the combinations of LET$_0$-σ_{sat} for which at least 3.7 SELs will be observable during the test according to the fluence of HEHs or HEHIs and the SEE response (W = Weibull, S = step).

While CHARM and 200 MeV protons are expected to deposit the same TID, as it was shown above, ChipIr (and spallation neutrons in general) stands out because neutrons deposit TID only through the secondary ions, but not the primary particles. Therefore, the deposited TID is much closer to that of primary HEHIs. Sticking to the same HEH fluence of 10^{11} HEH/cm^2, the ChipIr beam would deposit 0.7 Gy(Si). The same TID would be achieved by HEHIs with a fluence of 6 x 10^5 ions/cm^2. Therefore, the TID for both neutrons and ions is about two orders of magnitude lower than in the CHARM case, for a similar SEE-induction capacity.

Figs. 7.5 and 7.6 provide the same comparisons performed before, but this time for ChipIr and the Pb 5 GeV/n. For ChipIr it is noted that the maximum LET_{eq} available is slightly lower than at CHARM, because the primary proton beam is less energetic. Nevertheless, as expected, the colormap and the curves of SEE susceptibilities based on the 3.7 SEEs are basically the same for CHARM and ChipIr at a given fluence. Therefore, spallation neutrons can indeed achieve the same SEE results as CHARM, but with a much lower TID.

On the other hand, since for the comparison with ChipIr the ion fluence is about 2 orders of magnitude lower than for the comparison with CHARM, the SEE susceptibilities that the ion can highlight have consistently reduced. To the point that for the Weibull response the SEE susceptibilities are actually limited below the primary LET asymptote and there is no possibility of exploiting indirect ionization phenomena. The curves for HEHIs actually move backwards from the asymptote because even if the LET_0 is below that of the primary ion, if the saturation cross-section is low enough no SEEs will occur with this lower fluence, whereas this is certainly not the case for the step function response.

Therefore, for the 3 μm case, spallation neutrons can expose the sensitivity of devices having higher LET_0 than the considered HEHI can.

The picture changes as well for spallation neutrons when considering a thicker SV and, again, the results are very compatible with CHARM even if the maximum LET_{eq} of the secondary ions is lower than at CHARM. HEHIs are again independent on the SV thickness. Therefore, the same situation as for CHARM repeats and, even if less effective at this lower fluence, HEHIs are slightly better in exposing SEE susceptibilities than spallation neutrons.

All considered, and strictly considering the HEHI used in this analysis, one can probably conclude that HEHIs are generally slightly better than CHARM HEHs and slightly worse than ChipIr spallation neutrons (for the same deposited TID) when it comes to exercise the susceptibilities of device whose HI responses would not be known. However, the main issue of HEHIs remains the very scarse penetration that can hardly guarantee homogeneity over more than a single PCB.

7.1.4 High-Z materials

The presence of high-Z materials, such as tungsten or gold, within microelectronics packages, overlayers and contacts can be an important concern when it comes to RHA of electronic devices in space [152, 175]. This is because nuclear fission interactions of HEHs with high-Z nuclei can yield secondary ions with much higher LET_{eq} than those from HEH-silicon interactions.

In order to determine how things change when high-Z materials are located nearby the silicon SV, the previous RPP SVs are used again for the simulations, but, this time, an overlayer of tungsten 0.4 μm thick is added on top of the silicon as it was for the original Brilliance SRAM model in Chapter 6. MC simulations are used to extract the energy deposition distributions as a function of LET_{eq} coming from secondary ions produced by silicon and tungsten.

The previous analysis is repeated to assess how the presence of high-Z materials can have an impact when it comes to provididing SEE stimuli in a HEH or HEHI beam.

Fig. 7.7 provides the SEE rates for CHARM (left) and the Pb 5 GeV/n ion (right) for the model with 3 μm thickness and the tungsten. Note that, in this case, the left plot does not present the sharp transition to 0 SEEs at high LET. Indeed, the presence of tungsten can now release secondary ions with LET_{eq} even above 60 MeV/(mg/cm^2). The other noteworthy aspect is the shape of the curve for 3.7 SEEs as a function of the various fluences. The curves are identical to those when tungsten was not considered for $\mathrm{LET}_0 < 10$ MeV/(mg/cm^2). However, around this LET a transition is observed. As a consequence the range of LET_0

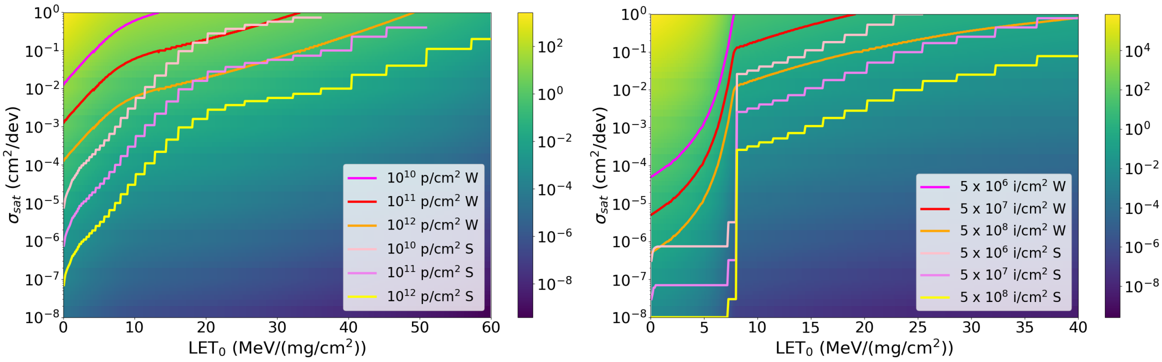

Figure 7.7: Colormaps of the SEE rate for an RPP with 20 x 4 x 3 μm^3 SV with an additional tungsten layer at CHARM for a fluence of 10^{11} HEH/cm^2 and with Pb 5 GeV/n ions for a fluence of 5 x 10^7 ions/cm^2 based on MC simulations and the Weibull function. The SEE rate is shown as a function of the device LET threshold and HI saturation cross-section. The lines on top of the colormap define all the combinations of LET$_0$-σ_{sat} for which at least 3.7 SELs will be observable during the test according to the fluence of HEHs or HEHIs and the SEE response (W = Weibull, S = step).

that the HEH experiment can exercise becomes wider and can reach even 30 MeV/(mg/cm^2) for a fluence of 10^{11} HEH/cm^2 and the Weibull response function. Even higher SEEs with higher LET$_0$ can be stimulated if either a larger fluence or the step function response are considered.

For the Pb 5 GeV/n ions, while it is true that Pb-tungsten nuclear reactions are happening and yielding secondary ions with higher LET, the effect is more limited. Indeed, the presence of the tungsten does not affect what happens due to direct ionization at low LET. At the same time, the additional yield of Pb-tungsten secondary ions is insufficient to change the overall picture. In this case the maximum LET$_0$ exercised for a fluence of 5 x 10^7 ions/cm^2 is 20 MeV/(mg/cm^2), i.e., lower than for HEHs. Therefore, it can be concluded that HEHI beams will also provide results insensitive to the presence or absence of high-Z materials nearby the SV.

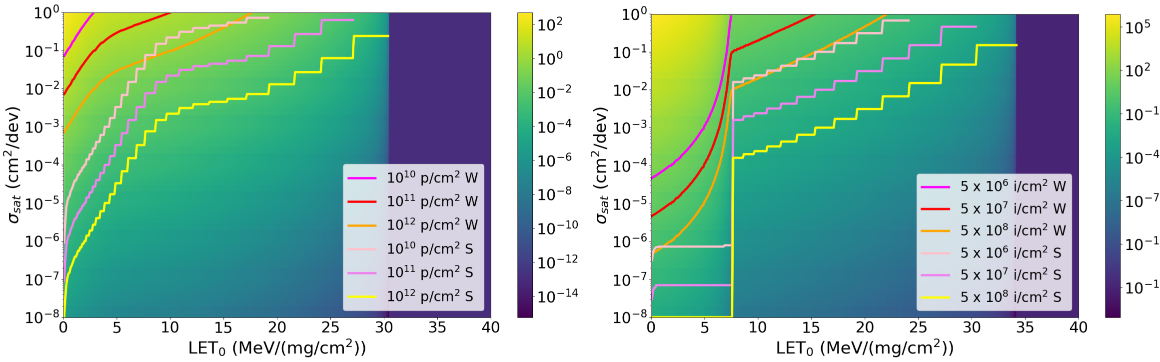

Figure 7.8: Colormaps of the SEE rate for an RPP with 20 x 4 x 10 μm^3 SV with an additional tungsten layer at CHARM for a fluence of 10^{11} HEH/cm^2 and with Pb 5 GeV/n ions for a fluence of 5 x 10^7 ions/cm^2 based on MC simulations and the Weibull function. The SEE rate is shown as a function of the device LET threshold and HI saturation cross-section. The lines on top of the colormap define all the combinations of LET$_0$-σ_{sat} for which at least 3.7 SELs will be observable during the test according to the fluence of HEHs or HEHIs and the SEE response (W = Weibull, S = step).

Similar conclusions can be drawn when it comes to the thicker SV, as shown in Fig. 7.8. In this case, it is possible to see that the presence of tungsten has generated ions with LET_{eq} up to 30 $\text{MeV}/(\text{mg}/\text{cm}^2)$ as opposed to the 13 $\text{MeV}/(\text{mg}/\text{cm}^2)$ in which the tungsten was absent. Also in this case the susceptibility in terms of SEE LET_0 of the devices that the HEH test can expose has increased of about a factor of 2 with respect to the case without tungsten layer. On the other hand, the HEHI case is again only mildly affected.

However, the HEHIs provide still better stimuli for a thickness of 10 μm and the presence of tungsten than the HEHs.

From these observations it is possible to conclude that for those devices for which high-Z materials may be placed nearby the SV, the HEH experiments can sometimes stimulate more SEEs susceptibilities than HEHIs can, but that, again, this capability diminishes as the SV thickness increases. Furthermore, the presence of high-Z material nearby the SV is not the rule. Therefore, the conclusions for the silicon-only case are still the most representative for the HEH vs. HEHI comparison (unless additional information is available from another kind of analysis, e.g., SEM).

7.2 Correlating the HEH SEE cross-section to the space SEE rate

No matter whether mono-energetic protons, spallation neutrons or mixed-fields are used to perform a space system test, the outcomes of such kind of tests are typically one or more system/device SEE cross-sections. The question then becomes how to correlate this cross-section to the space rate, which may comprise proton- and ion-induced SEEs.

A method based once again on LET_{eq} can be proposed to connect the HEH SEE cross-section to the space SEE rate and determine when HEH experiments can be trusted.

7.2.1 VELA: method definition

It is known that the SEE response of a device is strongly affected by several parameters, i.e., some are constructional (e.g., the sensitive volume dimensions) and some are electrical (e.g., the critical charge or LET threshold). As earlier explained, the triggering of an SEE is related to the energy deposition event probability. Therefore, in order to assess the suitability of HEHs in describing SEE phenomena in space a comparative analysis between the energy deposition distribution of the beam available at HEH facilities and of those arising by interaction with the space environment is worthwhile.

When performing such an analysis it is noted that energy deposition events from HEHs will be caused by secondary ions produced in hadron-silicon interactions, whereas for the space environment they will be in part caused, in a similar fashion, by HEPs and, in part by direct ionization from ions (typically more energetic events in terms of energy deposition can be expected).

The LET_{eq} stands at the basis of comparing the HEH facility beams and the space environment through the VELA [100]. This mathematical method makes use of the energy deposition distribution as a function of LET_{eq} determined from MC simulations to calculate a direct correlation between the HEH SEE cross-section and the space rate.

The SEE rate during a test with at a HEH beam is determined as follows:

$$R_{test}[day^{-1}] = \Phi_{HEH}[day^{-1}cm^{-2}] \times \sigma_{HEH}[cm^2] \tag{7.2}$$

The LET_{eq} plays a role in the determination of the acceleration factor of the test with respect to the space environment. In this sense, the acceleration factor is defined as the ratio between the fluence of particles that can generate an event with an LET_{eq} above a certain threshold (marked with *) during the HEH test and the fluence of those same particles in space (also accounting for the isotropic nature of the space environment):

$$acc.factor = \frac{\Phi_{test}(> LET^{*}_{eq})}{\Phi_{space}(> LET^{*}_{eq})} \tag{7.3}$$

Therefore, the simplification here stands in assuming that each particle having an LET$_{eq}$ above the threshold will have identical probability of causing an SEE no matter their LET$_{eq}$. In a similar fashion, all particles having an LET$_{eq}$ below the threshold will be discarded because they cannot trigger that SEE. This is a potentially strong approximation, but in order to maintain the generality of the method it is not possible to apply a generic Weibull function to weigh the two fluxes. Nevertheless, as it will be seen later, the absence of this Weibull function weighting is the reason why the VELA loses precision for devices characterized by an intermediate or high LET$_0$.

It follows that the space SEE rate shall be proportional to the HEH test SEE rate by means of this acceleration factor, which, therefore, directly links the space SEE rate to the HEH SEE cross-section:

$$R_{space}[day^{-1}] = \frac{R_{test}[day^{-1}]}{acc.factor} = \frac{\Phi_{space}(> LET^{*}_{eq})}{\Phi_{test}(> LET^{*}_{eq})} \times \Phi_{HEH} \times \sigma_{HEH} \tag{7.4}$$

Grouping all the elements together so that an expression like R$_{space}$ = α x σ_{HEH} can be obtained, the factor α that relates the space rate to the HEH SEE cross-section is:

$$\alpha(LET^{*}_{eq}) = \Phi_{space}(> LET^{*}_{eq}) \times \frac{\Phi_{HEH}}{\Phi_{test}(> LET^{*}_{eq})} \tag{7.5}$$

In the equation α is a function of the set LET$_{eq}$ threshold. However, as it will be later shown, the choice of the LET$^{*}_{eq}$ weakly affects the value of α for a rather large LET$_{eq}$ range.

In conclusion, the VELA suggests that it is possible to determine an α factor that relates the HEH SEE cross-section to the space SEE rate due to both protons and ions, for a given mission.

Other than with the choice of the LET$^{*}_{eq}$, the value of α can also depend on various other parameters, such as the SV dimensions (the thickness, in particular), the type of SEE, the HEH beam facility as well as the space orbit for which it is calculated.

7.2.2 VELA: application to different facilities and sensitive volumes

MC simulations are used to determine the energy deposition distributions from various radiation fields. Concerning the targeted facilities, the CHARM, ChipIr and 200 MeV monoenergetic proton beams are considered. For this first analysis, their energy deposition distributions are compared with that of a fixed LEO environment based on 800 km altitude, 98° inclination, solar minimum conditions, 100 mils of aluminum of shielding. The LEO environment takes into account both the trapped protons and the GCR protons and ions. The other difference between the space environment and the facility beams is that the energy distribution of the former is determined by simulating a spherically isotropic spectra of particles whereas the energy distributions of the latter are determined using mono-directional beams (to replicate the test conditions).

As introduced throughout the thesis, the SV features can vary depending on the SEE of interest. SEUs and SELs are SEEs that can be stimulated by HEHs. The SVs introduced in the earlier chapters for the ISSI SRAM and Brilliance SRAM are therefore used for the sake of this analysis. As a reminder, the ISSI SRAM was modelled through a cubic RPP with 310 nm side, whereas the Brilliance SRAM was modelled through an RPP with 20 x 4 x 3 μm^3 volume. Since 3 μm can be considered a representative thickness for devices that will display SEL in a HEH environment, but it is likely insufficient for devices displaying SEL only during ion irradiations, a second SEL SV is considered, that is 20 x 4 x 10 μm^3. Concerning the SEL SV, no tungsten is added to the model.

Energy deposition distributions are obtained from FLUKA as probabilities per primary particle. In order to convert them into space SEE rates they have to be normalized based on the beam size and the integral fluxes of protons and ions found in space. In addition, this SEE rate is further normalized to 1 cm^2 device sensitive surface to get rid of the actual device surface dependency. Such normalization is also applied to the space SEE rate for the same reason. As a result, the SEE rates from the HEH test and the space environment as a function of volume equivalent LET are obtained.

In a similar fashion, for the energy deposition distributions of the facilities, a cross-section as a function of LET_{eq} is determined. As earlier mentioned the relationship between the space rate and the HEH SEE cross-section is the α. To determine the α a certain LET_{eq} threshold has to be chosen. For the moment, this will be taken as 3 $MeV/(mg/cm^2)$ and this choice will be verified later on.

By calculating α from eq. (7.5) for $LET^*_{eq} = 3$ $MeV/(mg/cm^2)$ it is possible to multiply the whole HEH SEE cross-section as a function of LET_{eq} so that one can get the predicted space SEE rate from a HEH test, again as a function of LET_{eq}.

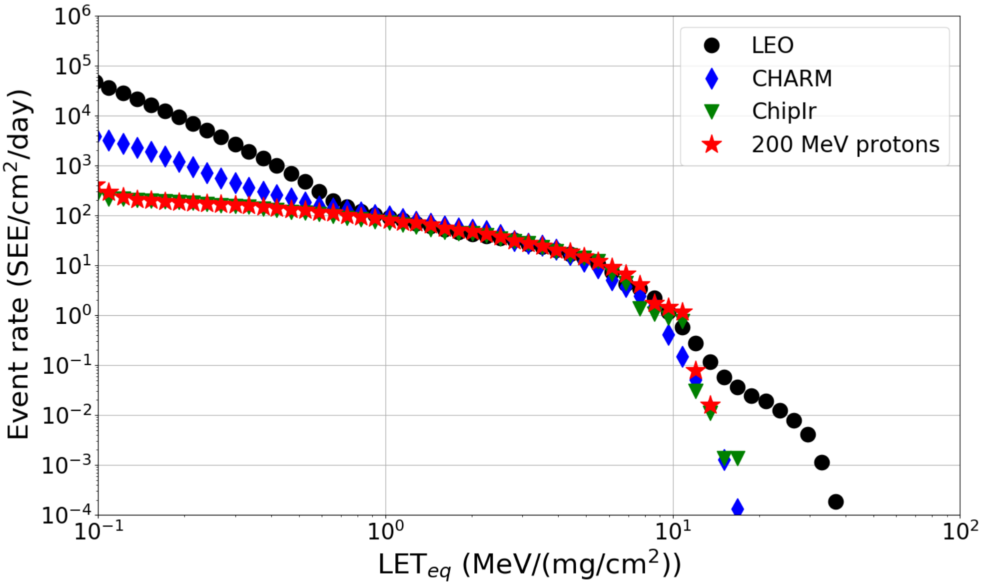

Figure 7.9: Normalized rates per day to a surface of 1 cm^2 for the CHARM, ChipIr, 200 MeV mono-energetic proton beams (and scaled by the respective α) and the LEO environment (800 km, 98°, solar minimum, 100 mils of Al with trapped protons and GCRs). The volume considered for the MC calculations is that of the ISSI SRAM. Obtained with FLUKA. Reprinted from [47]. © 2021, Coronetti et al., licensed under CC BY 4.0.

Figs. 7.9-7.11 depict the normalized space SEE rates as a function of LET_{eq} from the LEO environment and from the three HEH tests for the SEU SV and the two SEL SVs, respectively. As said, the space rates obtained from the HEH experiments have been rescaled by the α and shall thus match the LEO space SEE rate at 3 $MeV/(mg/cm^2)$. However, as it is obvious from the figures, the overlap extends for a much larger range of LET_{eq}.

The plots have several characteristics in common. Apart from the central LET region of overlap, the LEO space rate diverges from that of the HEH tests typically below an $LET_{eq} < 1$ $MeV/(mg/cm^2)$. This is due to direct ionization effects from low-energy protons. These are more significant in space than in the HEH facilities because, e.g., at CHARM

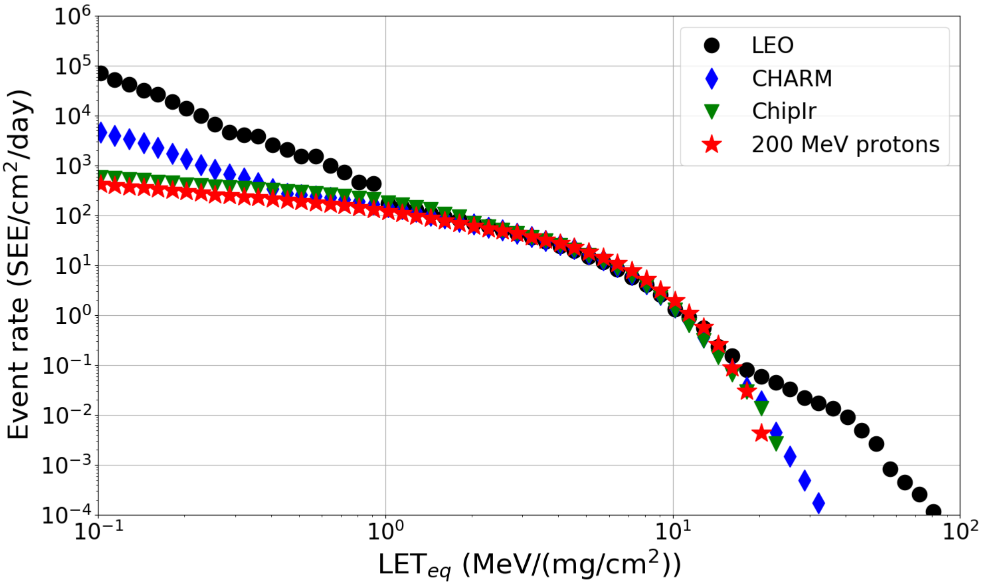

Figure 7.10: Normalized rates per day to a surface of 1 cm^2 for the CHARM, ChipIr, 200 MeV mono-energetic proton beams (and scaled by the respective α) and the LEO environment (800 km, 98°, solar minimum, 100 mils of Al with trapped protons and galactic cosmic rays). The volume considered for the MC calculations is that of the Brilliance SRAM with 3 μm thickness. Obtained with FLUKA. Reprinted from [47]. © 2021, Coronetti et al., licensed under CC BY 4.0.

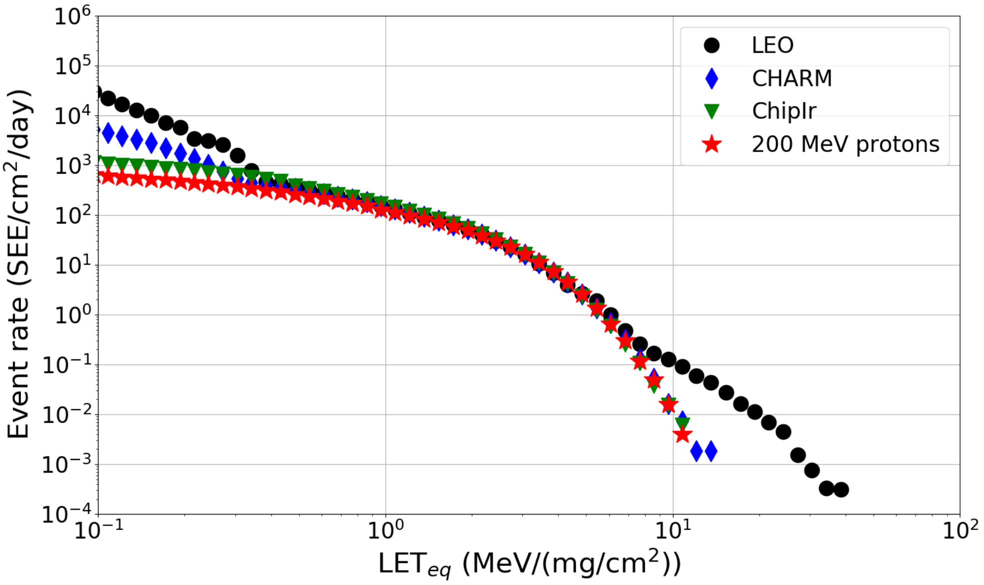

Figure 7.11: Normalized rates per day to a surface of 1 cm^2 for the CHARM, ChipIr, 200 MeV mono-energetic proton beams (and scaled by the respective α) and the LEO environment (800 km, 98°, solar minimum, 100 mils of Al with trapped protons and galactic cosmic rays). The volume considered for the MC calculations is that of the Brilliance SRAM with 10 μm thickness. Obtained with FLUKA.

the LEPs are less abundant in relative terms with respect to HEHs than in space. Clearly, no LEPs are present in the neutron spallation field of ChipIr. Finally, the mono-energetic 200 MeV protons have LET below 0.1 MeV/(mg/cm^2), therefore, their direct ionization would kick in at much lower LET$_{eq}$ than what it is shown in the plot.

The second and more important divergence occurs at high LET$_{eq}$. Space SEE rates devised from the HEH experiments drop down at LET$_{eq}$ of 10-20 MeV/(mg/cm^2). On the other hand, the space SEE rate directly derived from the space environment remains significant at LET$_{eq}$ of 30-50 MeV/(mg/cm^2). This difference is caused by the presence of high LET ions in the space environment.

Excluding PDI effects, if the actual α of each facility is considered, the overlap between the three HEH environments is very good for any LET$_{eq}$. This reinforces the conclusion that testing at either CHARM, ChipIr or with 200 MeV proton will return similar HEH SEE cross-sections and, therefore, similar predicted space rates.

Table 7.1: α factors (units of cm^{-2} day^{-1}) for the considered test facilities with respect to the LEO environment (800 km, 98°, solar minimum, 100 mils of Al, trapped protons and GCRs) for the SEU and the two SEL volumes. Reprinted from [47]. © 2021, Coronetti et al., licensed under CC BY 4.0.

HEH beam	**SEU SV**	**SEL 3 μm SV**	**SEL 10 μm SV**
CHARM	9.27 x 10^6	1.14 x 10^7	1.17 x 10^7
ChipIr	7.25 x 10^6	1.35 x 10^7	1.55 x 10^7
200 MeV protons	1.05 x 10^7	1.08 x 10^7	9.92 x 10^6

Table 7.1 presents the α's used to obtain the plots in the previous figures. For each facility and SV a different α is obtained. However, it can be said, in first approximation, that all α's fall, more or less, around 10^7 cm^{-2}day^{-1} for this orbit no matter whether SEUs or SELs are of concern. Therefore, α remains stable despite variations in (i) the SV size and thickness, (ii) the facility used to calculate the HEH SEE cross-section and (iii) the type of SEE.

This is potentially a very important result for system-level testing, in particular for those cases in which determining the root cause of a system-level fault/failure is either not possible or would require a deeper level of observability. Indeed, the fact that a unique α can be used no matter the nature of the SEE can enable data exploitation out of system-level test with little level of observability.

The paper [47] also shows the application of the VELA to a few devices for which it is possible to have a comparison with either more standard predictions based on the Weibull method and the experimental data or with actual on-orbit data for the LEO here considered.

7.2.3 VELA: dependency with the choice of the LET$_{eq}$ threshold

As earlier mentioned, α depends on the choice of the LET$_{eq}$ threshold. However, some level of arbitrariness exists in the selection of the most appropriate threshold. This is supported by the fact that the overlap between the space SEE rate from the space environment and those calculated after the HEH SEE cross-section extends for quite a large range of LET$_{eq}$.

Fig. 7.12 depicts how the α varies with diverse choices of the LET$_{eq}$ threshold. The figure reports data for the three HEH beams and the two SEL SVs with different thickness.

As indicated by the light and dark grey boundaries (respectively a factor of 1.3 and 2 tolerances with respect to the 10^7 cm^{-2}day^{-1} value considered as the global average before), for both SVs the α is expected to remain stable for nearly a decade when varying the LET$_{eq}$ threshold. However, the decade for which the α is stable shifts towards lower LET$_{eq}$ when the thickness of the SV increases. As a result, the 3 MeV/(mg/cm^2) previously picked stands in the middle of the decade for which the α is stable for the 3 μm thickness (α stable in the 1-10 MeV/(mg/cm^2) range), whereas it is much closer to the upper limit boundary for the 10 μm thickness (α stable in the 0.4-4 MeV/(mg/cm^2) range.

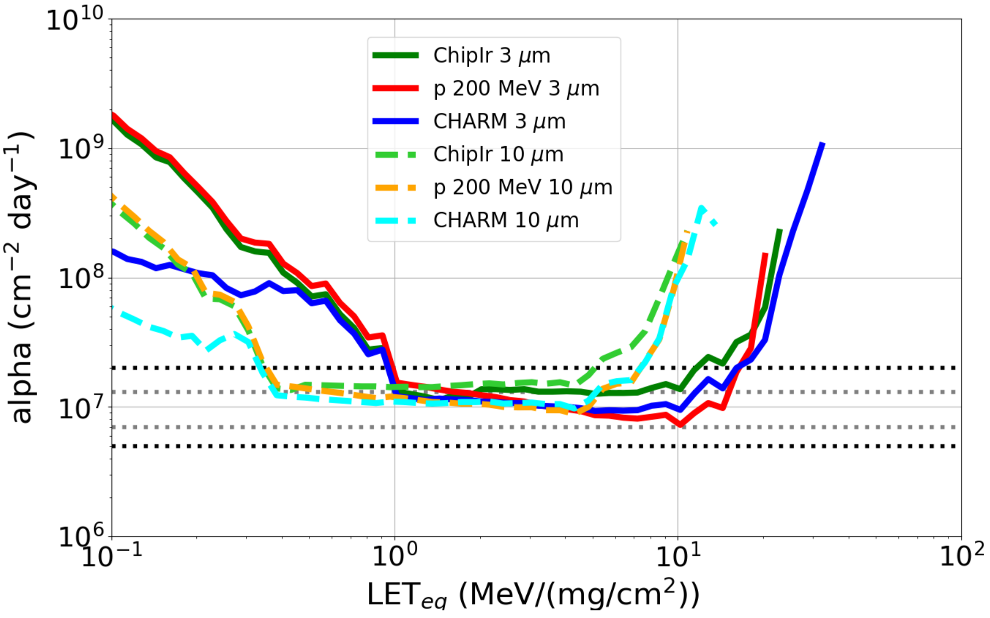

Figure 7.12: α factor as a function of the LET$_{eq}$ for the SEL SV with 3 μm and 10 μm thicknesses for the various facilities. The light and dark grey dashed lines indicate a variation of ±30% and a factor of 2 difference with respect to the 10^7 cm^{-2}day^{-1} value, respectively. Obtained with FLUKA. Reprinted from [47]. © 2021, Coronetti et al., licensed under CC BY 4.0.

Below and above the stable decade the α very quickly diverges either due to direct ionization from LEPs or to the missing heavy ion events, respectively. The situation becomes even more critical as the thickness of the SV increases. For the 10 μm, a violation by a factor of 2 is attained at an LET$_{eq}$ of 7 MeV/(mg/cm^2). Therefore, the VELA becomes less and less representative as the thickness of a device SV grows.

While this is a concern for the capability of the HEH beam field to provide sufficient stimuli to trigger all potential SEEs coming from the space environment, it is moreover true that devices characterized by a very deep SV will typically not exhibit any event during HEH testing. Therefore, the VELA would not be applicable and its decreasing representativeness will be less of a concern.

7.2.4 VELA: dependency with the orbital parameters

The α is a function of the orbit for which it is calculated for. This is because its definition contains the term $\Phi_{space}(> LET^{*}_{eq})$, which directly scales with the proton and ion fluxes of a particular orbit. Proton fluxes may change by more than one order of magnitude in LEO depending on whether the LEO is at low-altitude (e.g., ISS) or deep into the proton radiation belt (> 1000 km). Ion fluxes are also supposed to change based on the geomagnetic shielding, which varies with orbit altitude and inclination.

In the following analysis, orbital altitude and inclination variabilities are considered for a few LEOs that shall encompass the most used orbits. The analysis is restricted to an altitude between 500 km (that of the ISS) and 1400 km. The reason why it may not be worthwhile exploring higher LEO altitudes is related to the TID. Since the HEH testing is mainly proposed for custom-built systems based on COTS devices, at altitudes above 1400 km the TID per year starts to be in the order of 200 Gy(Si) for 100 mils of aluminum. In terms of inclination, the analysis is restricted to 52° and 98°, given that these inclinations should be relevant for most of the LEO missions.

The space proton and ion spectra were simulated with FLUKA and their energy deposition

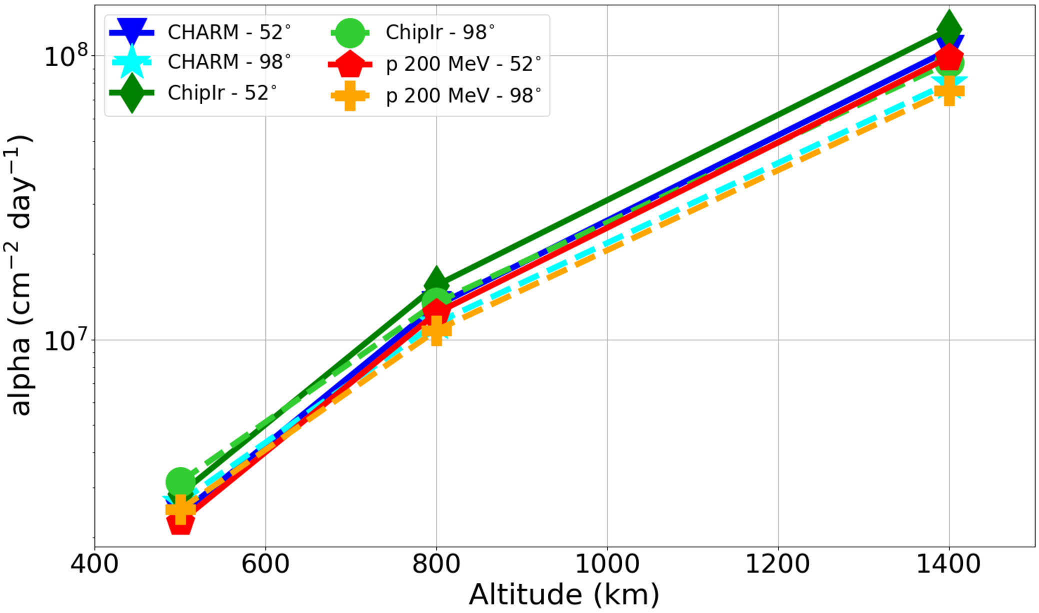

Figure 7.13: α as a function of the orbit altitude and inclination for the SEL SV with 3 μm thickness for the various facilities.

as a function of LET$_{eq}$ extracted for an SEL SV with 3 μm thickness. Fig. 7.13 depicts the α as a function of altitude and inclination for the three HEH beams under consideration. As the plot shows the variability with respect to the altitude dominates over those with respect to the inclination and HEH beams. The α can indeed vary of almost two orders of magnitude between 500 km and 1400 km. As said, the main variability is directly proportional to the higher proton fluxes at higher altitudes. Indeed, the ion contribution to the α is always lower than 10% and even lower than 1% for the highest altitude.

If one was to normalize α with respect to $\Phi_{space}(> LET^*_{eq})$ one would indeed get that the normalized α would be almost constant with the altitude. Therefore, there is no need to calculate all the α for the different orbits, but one can get a reasonable estimation by rescaling α based on the proton fluxes.

The fact that the proton component is dominant is also visible when different inclinations are compared. A higher α is obtained for the lower inclination because the satellite spends more time within the proton belt. On the opposite, the ion fluxes are expected to be higher at the poles due to the lower geomagnetic shielding. However, the ion contribution is largely superseded by the proton contribution. The difference between the two inclinations is in the order of just 20%. Given the small variability, one can assume that for all inclinations in the considered range the lower inclination α should provide a good estimate also for intermediate inclinations.

Although GEO space missions are generally associated with much lower risk acceptance than what this study is targeting, it may be interesting to also assess if it is possible to calculate an α also for an ion dominated orbit like the GEO. Fig. 7.14 depicts the energy deposition distributions of the HEH beams with respect to that of the GEO GCR environment. While it is possible to calculate an α so that the distributions match at 3 MeV/(mg/cm^2), it is noted that the difference at high LET$_{eq}$ is quite strong, i.e., plenty of SEEs caused by events with LET$_{eq}$ > 10 MeV/(mg/cm^2) will be compensated by a larger amount of SEEs in the HEH test environment caused by events with LET$_{eq}$ = 3-10 MeV/(mg/cm^2).

The resulting α for the GEO environment is about 5 x 10^6 cm^{-2} day^{-1} for all the facilities and, in this case, 90% of the α is coming from ion events, and only the remaining 10% from proton events.

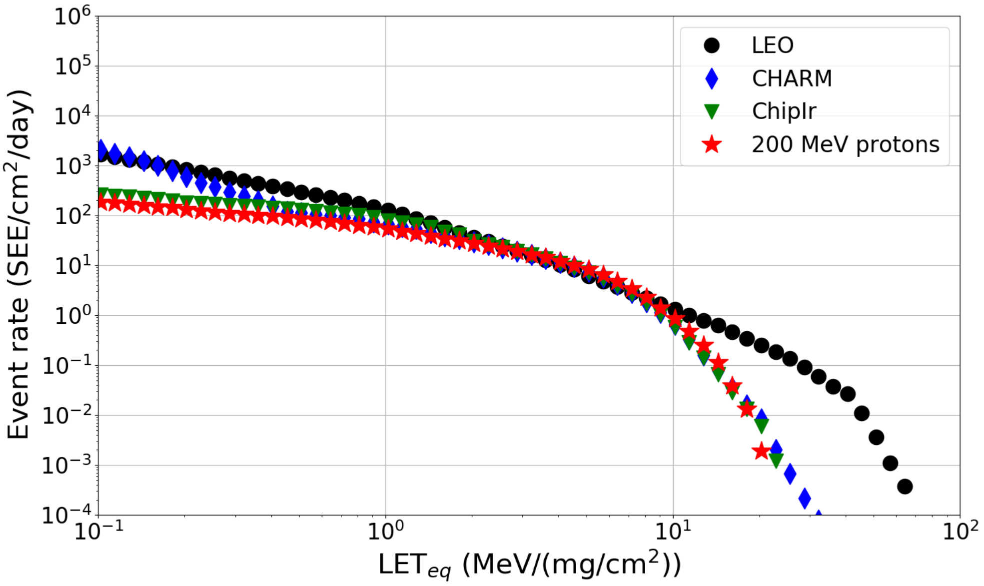

Figure 7.14: Normalized rates per day to a surface of 1 cm^2 for the CHARM, ChipIr, 200 MeV mono-energetic proton beams (and scaled by the respective α) and the GEO environment (35786 km, 0°, solar minimum, 100 mils of Al with galactic cosmic rays). The volume considered for the MC calculations is that of the Brilliance SRAM with 3 μm thickness. Obtained with FLUKA.

7.3 Space SEE rate prediction from the information available through HEH testing

The outcome of HEH testing of devices and systems may be quite variable. One can either observe several hundreds or thousands of events, a few events or no events at all. The statistical uncertainty associated with each of these three cases is quite different and the reliability of the VELA may be impacted by the low amount of events observed during the HEH test. This is because observing just a few or zero events in a HEH environment does not imply that a negligible amount of events will occur in space, but it is just a consequence of the strong limitations arising from the insufficient LET_{eq} of the secondary ions in a HEH experiment.

Therefore, there are still several aspects that have to be assessed. First and foremost, it is necessary to assess when the VELA provides reliable predictions considering that (i) the ion response of the DUTs and their SV characteristics are not known and that (ii) only the number of events (i.e., cross-section) from a HEH test are available. Therefore, the method will actually be applied and tested for a collection of heavy ion responses of real COTS devices and its reliability assessed with respect to the actual response expected in space for those devices. Most of the analysis will therefore rely again on energy depositions as a function of LET_{eq} as determined before.

Since it is already evident that the method will not work for zero events, given that it is impossible to say whether one will actually have zero events from ions in space or not, some complementary information can still be devised from a zero event HEH test at least in terms of an upper bound for those events that were not observed.

For the scope of both points, a set of heavy ion SEL responses from actual commercial devices will be used. Again, the data are collected from the literature [20, 157–174] and from Table 4.4. This database includes parts such as: SRAMs, FPGAs, μCs, ADCs, DACs, transceivers, supervisory ICs, op-amps, voltage references and more. The data-set is depicted in Fig. 7.15 and classifies the devices in terms of their LET$_0$ and σ_{sat}. For the red devices, the

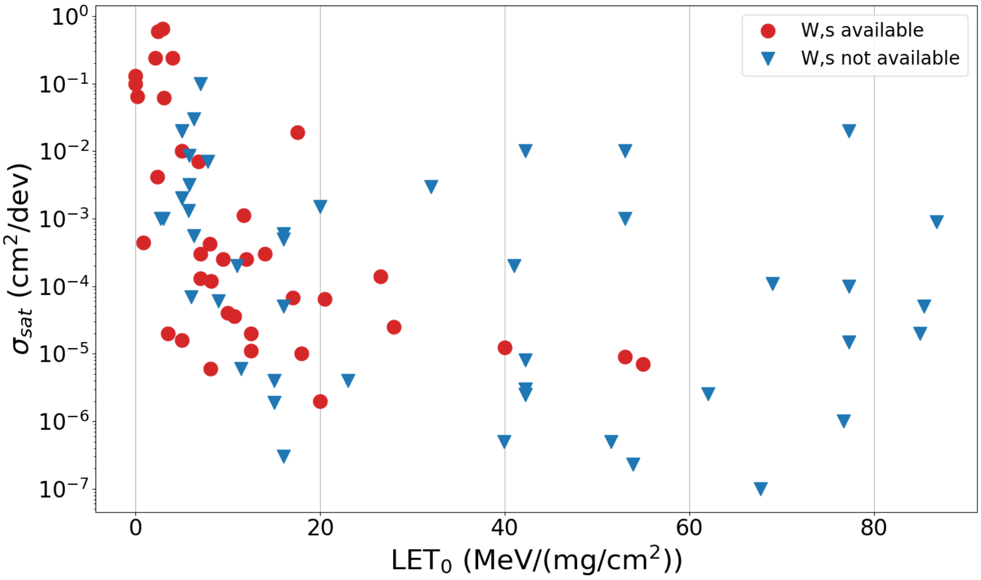

Figure 7.15: Heavy ion SEL response of a set of actual devices (whose data are available in the literature) in terms of their LET$_0$ and σ_{sat}. The data are presented in different colours to show whether the shape and exponent parameters of the Weibull function are also available. Note that the number of SVs is determined by dividing the σ_{sat} by the SV area of the considered SEL volume in the FLUKA simulations.

shape and exponent parameters of the Weibull function are available. For the blue devices, the average values of W = 30 MeV/(mg/cm^2) and s = 3 will be assumed.

7.3.1 VELA: which is the minimum HEH cross-section to get reliable estimation of the space rate?

From the FLUKA energy deposition distributions determined for CHARM and the space environment one can determine which is the number of events (or the HEH cross-section) in a CHARM test of all the targeted devices. This is achieved by convolving the heavy ion response of the device with the energy deposition distribution of CHARM after a certain fluence. While CHARM tests are set to last for a fixed duration of roughly one week, one generally achieves a fluence higher than 10^{11} p/cm^2. However, to be more consistent with proton testing, the fluence for CHARM is also fixed at 10^{11} p/cm^2.

These data are used to mark a separation between the devices which will suffer from more than 3.7 SELs during the CHARM test and those that will suffer less or even zero SELs (because by definition their LET$_0$ is higher than the maximum LET$_{eq}$ of the CHARM secondary ions).

Then, for the devices showing more than 3.7 SELs the VELA is applied to determine the predicted space SEL rate (from protons and ions) for the reference LEO with 800 km altitude and 98° inclination. To determine the accuracy of the VELA for these devices, the space SEL rate is also computed by direct convolution of the space environment energy deposition distribution and the heavy ion response of the device. This second method, called MC convolution, is expected to provide the actual space SEL rate of the device in analogy with other methods such as the Weibull convolution with the LET spectrum.

Fig. 7.16 shows the comparison between the space SEL rate from the VELA and that from the MC convolution of the space environment for the cases of SEL SVs with 3 and 10 μm thickness.

The first noteworthy aspect is that from a data-set comprising more than 80 heavy ion

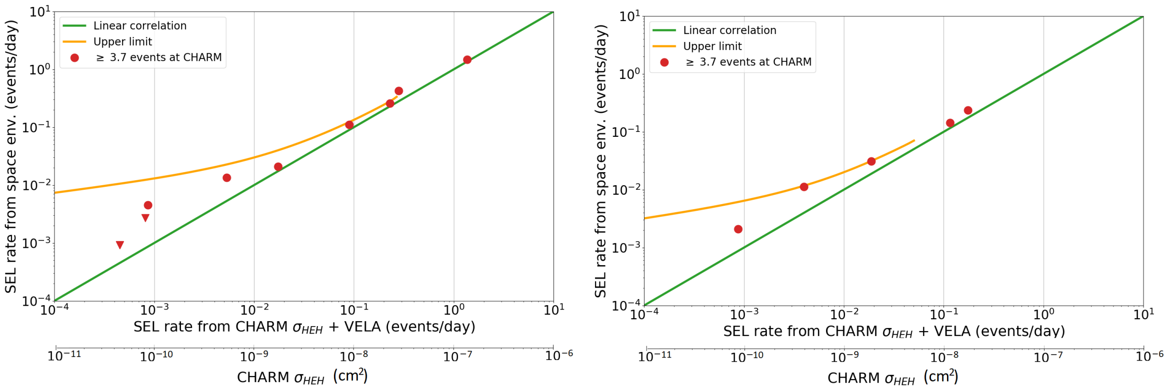

Figure 7.16: Space rate for devices suffering from more than 3.7 SELs at CHARM for a fluence of 10^{11} p/cm^2. The space rate is calculated by means of the VELA and by convolving the device heavy ion response with the space energy deposition distribution. (Left) SEL SV thickness 3 μm, (right) 10 μm.

SEL responses of real devices, CHARM is expected to expose the sensitivity of only 9 if the SEL SV is assumed to be thin, and no more than 5 if the SV is thick, which makes for something between 5% and 10%. Therefore, as a first conclusion, with such kind of HEH tests, based on the literature data-set, one should be able to expose the SEL sensitivity of only a small percentage of commercially available devices.

The second noteworthy aspect is that, certainly, the number of events seen at CHARM for devices having the same heavy ion Weibull response, but different SV thickness is different.

Coming back to the reliability of the VELA at predicting the space rate it is noted that the agreement between the VELA and the MC convolution of the space energy deposition distribution is quite heterogeneous. For about half of the devices the agreement is quite good. However, for the other half there can be discrepancies of up to a factor of 5, and, in all these cases, the VELA is underestimating the actual space rate.

The disagreement between the VELA and the expected space SEL rate grows on the left side of the plots, where the number of events expected in CHARM is lower (i.e., lower measured cross-section). On the other hand, the agreement improves as hundreds of events (or more) are observed in CHARM. On the surface, it appears that the statistical uncertainty on the low amount of events is the main responsible for the growing disagreement. However, the main reason why poor statistics result in unreliable space SEL rate predictions is that the hypothesis in eq. (7.3) of equating events of high LET$_{eq}$ (in space) to events associated with lower LET$_{eq}$ (in the HEH test), though still above the threshold, starts falling apart when the Weibull response of a device actually gives more importance to high LET$_{eq}$ events.

All considered, these observations can be used to define a minimum HEH SEE cross-section above which the VELA is accurate and under which the VELA should not be used.

A wider analysis, involving also the devices that are expected to show less than 3.7 SELs in CHARM is performed to have a wider scale picture about the inaccuracy of the VELA in predicting the actual space SEL rate.

Figs. 7.17-7.18 depict the comparison between the space rate determined from the VELA and that coming from the MC convolution of the space energy deposition environment. Data in red are the devices that showed more than 3.7 events in CHARM, whereas those in blue would show less than 3.7, but more than 0 (here more than 0 refers to devices with less than 3.7 SELs, but also to those having less than 1. The latter are those cases for which the LET$_0$ of the device is lower than the maximum LET$_{eq}$ stimulated by the HEH test, but that would require a much higher fluence to show at least 1 SEL. These devices were thus differentiated with respect to those having a LET$_0$ above the maximum LET$_{eq}$ in a HEH test and that will

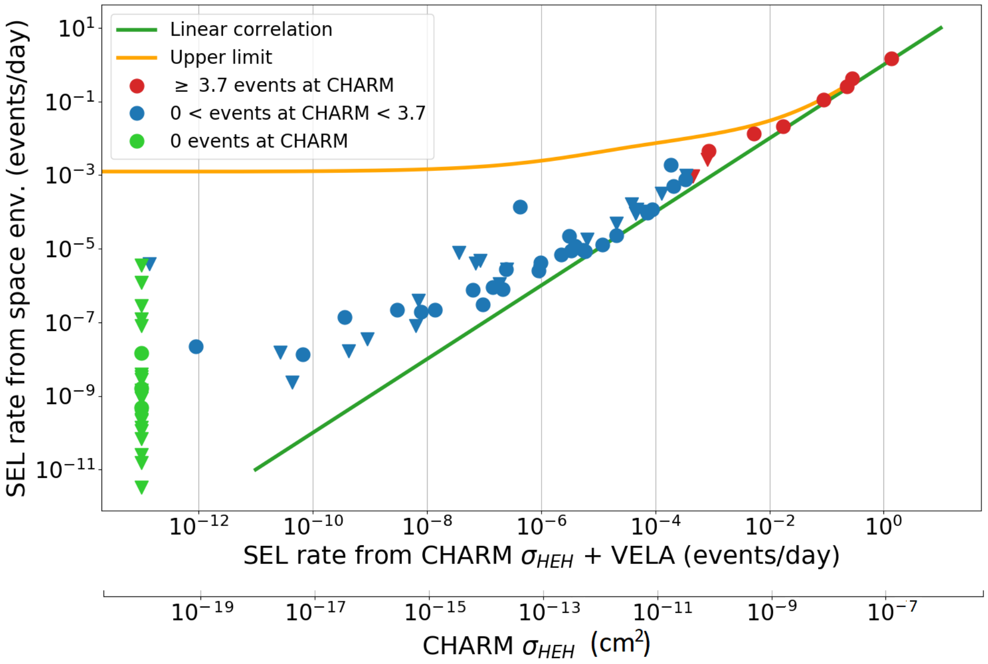

Figure 7.17: Comparison between the space rate calculated with VELA and with the MC convolution of the space energy deposition distribution for all the devices assuming a SEL SV with 3 μm thickness.

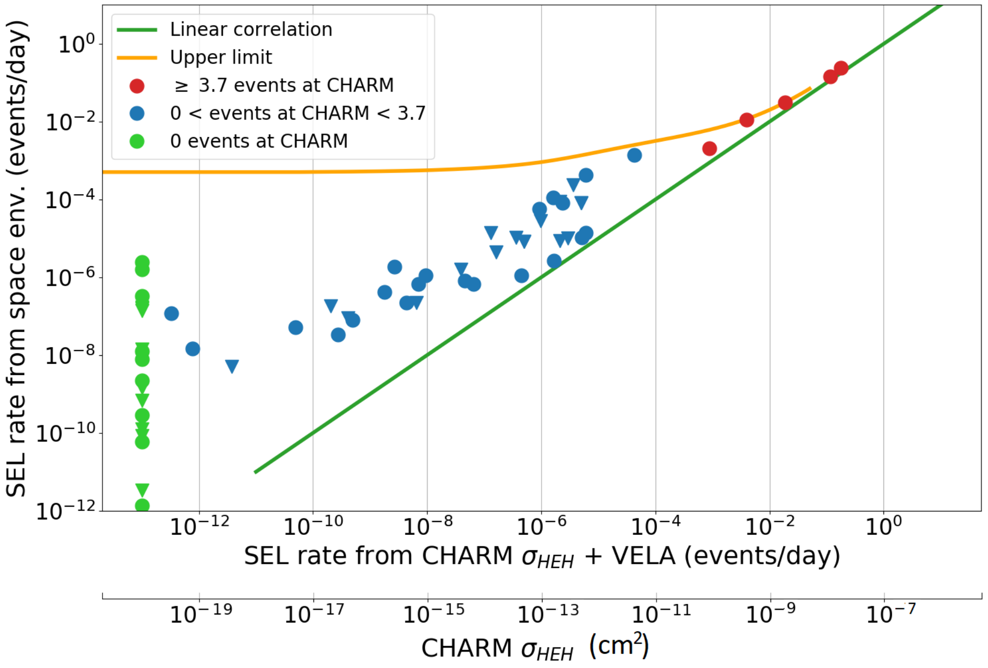

Figure 7.18: Comparison between the space rate calculated with VELA and with the MC convolution of the space energy deposition distribution for all the devices assuming a SEL SV with 10 μm thickness.

display 0 SELs by definition) and the green data are those that by definition would return zero events and that are plotted for convenience at a very low predicted SEL rate (because of the logarithmic scales used in the plots).

The VELA is reliable when there is a linear correspondence between the two space SEL rates (this is indicated by the green line). Therefore, if the points belonging to the various devices fall on this curve, the VELA is expected to be accurate.

Sticking to Fig. 7.17 for the 3 μm thickness, there are several devices satisfying the linear correspondence curve. The maximum deviation would happen towards the lower end of the SEL rate predicted from VELA with differences of even a factor of 100. This also happens for some outliers.

It is also noted that there can be devices showing zero events at CHARM by definition that could be expected to provide a space rate higher than many other devices whose LET_0 is lower (likely because of the higher σ_{sat}).

The differences become more important when considering a thickness of 10 μm for the SEL SV (see Fig. 7.18). The device data are now much farther from the linear correspondence line, by a factor of 10 to a factor of 1000.

The orange curve is set to be the upper limit to the space SEL rate that is calculated upon the very conservative assumption of a σ_{sat} of 1 cm^2 (none of the devices under consideration reach this cross-section) and letting the LET_0 vary. This is assumed to be an upper limit. That is, even if in this data-set there are no devices with such an unfortunate combination of parameters, the worst of them is expected to fall below the orange curve. Therefore, even if the devices are better behaved than the orange curve, one can use this curve to define a rule for when the disagreement between the VELA predicted space SEE rate and the MC convolution space SEE rate becomes unacceptable.

Taking for instance a space SEL rate of 10^{-2} events/day, the linear correspondence would be violated by the upper limit (orange curve) by a factor of 3 for the 3 μm thickness and by a factor of 2 for the 10 μm thickness. Therefore, in this case the 3 μm thickness is worst case. Given that this is a contained violation, which is already margined by the fact that the upper limit is based on a very conservative hypothetical device, the rate of 10^{-2} events/day is considered as the minimum for which the VELA would provide reliable predictions for this orbit.

Given that the space SEE rate from the VELA is connected to the CHARM HEH cross-section by the α alone, it is possible to determine straight away which is the CHARM HEH cross-section above which the VELA is reliable for this orbit. Considering that for the reference LEO orbit the α is 10^7 cm^{-2} day^{-1}, the minimum HEH cross-section for which the VELA will provide reliable results is 10^{-9} cm^2/dev.

Therefore, it is concluded that if the measured CHARM HEH cross-section (or that with protons or spallation neutrons) is $> 10^{-9}$ cm^2/dev one can use the VELA to accurately predict the corresponding space rate caused by protons and ions. On the other hand, whenever only a few events in CHARM are observed and they lead to a HEH SEE cross-section below this threshold, the VELA should not be used, but one can assume that the space SEE rate of that device, and for this very orbit, will be below 10^{-2} events/day (e.g., less than 1 in 100 days) and also higher than the upper bound that will be calculated in the next section and that is generally applicable to devices displaying zero events in a HEH beam.

One potentially important penalty of the VELA is that this minimum HEH SEL cross-section above which the method provides reliable estimations of the space SEL rate is not independent on the targeted mission profile (i.e., the orbit in which the satellite will be launched). Indeed, the VELA is more reliable when the target orbit has relatively higher proton fluxes with respect to ion fluxes.

Fig. 7.19 provides an analysis of how the minimum HEH SEL cross-section for the VELA predictions to be reliable varies with respect to the orbital altitude and inclination. This is again calculated for each orbit by determining for which space SEL rate the orange curves (in Figs. 7.17-7.18) diverge from the linear correspondence line by more than a factor of 3 and by taking the worst case between the 3 μm thick SV and the 10 μm thick SV.

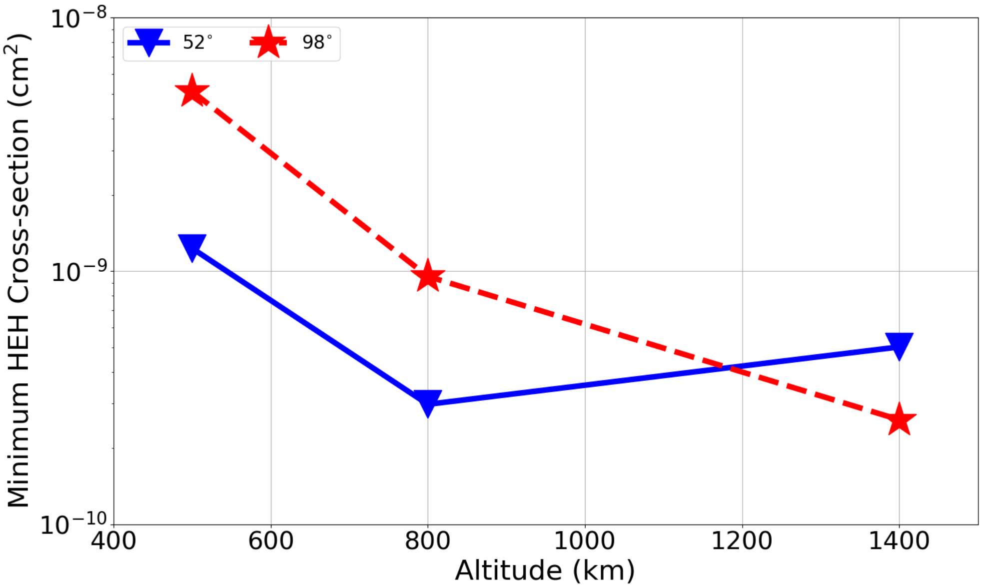

Figure 7.19: Minimum HEH SEL cross-section to consider the VELA reliable as a function of the orbit altitude and inclination. Data for a SEL SV with 3 μm thickness.

As one can see the highest minimum HEH cross-section is achieved at low altitude and high inclination (lower proton fluxes with respect to the ion fluxes) and it reaches 5 x 10^{-9} cm^2/dev. However, for some mission profiles, the minimum HEH cross-section under which the VELA is reliable can be lower than 10^{-9} cm^2/dev and even as low as 2.5 x 10^{-10} cm^2/dev. Therefore, the suitability of the VELA can be strongly dependent on the targeted mission profile and it can be recommended in particular for high-altitude and low inclination orbits.

7.3.2 Upper bound for zero events

As shown in the previous section, the VELA becomes less and less reliable as the number of events observed in a HEH beam is lower. Moreover, the VELA is not really applicable as an upper limit to the rate for zero events if no events are observed during the HEH test (or less than 3.7 SEEs in this case). That is, the fact that no SELs were observed for probably the largest part of the devices of the system during the HEH test does not mean that those devices will be completely safe against SELs from heavy ions.

In this respect, it is worthwhile determining which are the expected heavy ion space rates for those devices that were predicted not to display any SEL sensitivity in a HEH beam. This has a double purpose. On the one hand, it provides an idea of how variable the heavy ion space SEL rate distributions of these devices can be. On the other hand, the idea is to look for the highest heavy ion space SEL rate that would define the upper bound. The worst case SEL rate will provide a further indication on whether HEH testing may be valuable and under which conditions.

The heavy ion SEL rates are calculated following the same procedure as for the VELA. The heavy ion space environment is simulated in FLUKA and energy depositions as a function of LET$_{eq}$ are convolved with the Weibull response of the device to determine the heavy ion space SEL rate of each device.

Note that the heavy ion SEL rate is strongly impacted by the orbit used for the calculation, given that it directly depends on the ion fluxes. Therefore, initial considerations are done for the reference LEO and, then, developed for other orbits.

Fig. 7.20 depicts the heavy ion SEL rates as a function of the LET$_0$ of the device for all

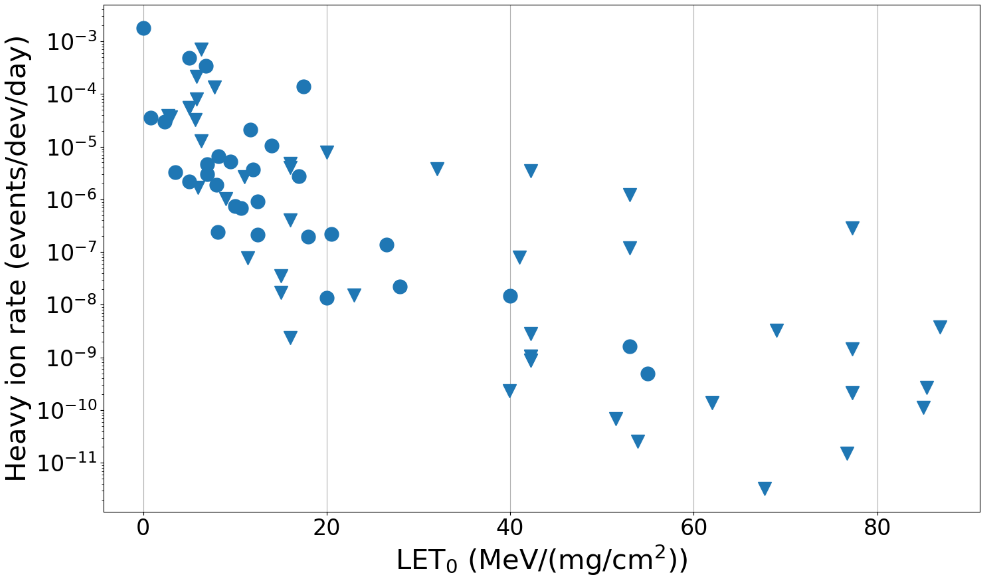

Figure 7.20: Heavy ion SEL rates of the set of devices under consideration for those devices that did not display sensitivity in a HEH beam. Data for a SEL SV with 3 μm thickness. Note that the number of SVs is determined by dividing the σ_{sat} by the SV area of the considered SEL volume in the FLUKA simulations.

the devices that did not display SELs in CHARM according to the previous analysis. The data were calculated from the energy deposition distributions obtained for the 3 μm SEL SV.

The considered data-set provides very different responses spanning about 8 orders of magnitude in terms of space SEL rate. Indeed, the largest amount of devices ($> 85\%$) not showing events in CHARM are expected to have an SEL space rate with a probability of 1 event in 3 or more years (less than 10^{-4} events/dev/day).

When it comes to bounding the space SEL rate, however, the highest SEL rate has to be taken as upper bound. In this case, this is 2 x 10^{-3} events/dev/day, which corresponds to roughly 1 event in 500 days. This is a potentially convenient upper bound for high risk acceptance space missions with a target lifetime of 1-3 years.

Assuming that all the devices in the system not displaying sensitivity in CHARM will have an SEL rate equal to the upper bound would be too much conservative. The calculated distribution, on the other hand, could be better used in a statistical fashion to derive a distribution of SEL sensitivities for all the devices in the system. A further subdivision by device type and technology may even improve the reliability of such an analysis, but would decrease the statistics.

Based on the previous analysis, when the SV becomes thicker, HEHs are less and less capable of reproducing high LET$_{eq}$ events. Therefore, a larger amount of devices remains with an undetermined space rate following the HEH test. However, as shown in Fig. 7.21, devices with thicker SV will also have lower space SEL rate.

As a result, while the worst case device has changed with respect to the 3 μm case the highest heavy ion SEL rate went rather unchanged and it is 1.5 x 10^{-3} events/dev/day. Therefore, the upper bound seems not to be very sensitive with variations on the SV characteristics.

Concerning the possibility of using the statistical distribution to establish potential SEL rates for devices of which the heavy ion response is not known as well as the SV characteristics, one can probably combine distributions obtained with diverse SV characteristics to get a more reliable picture, although, in theory, the distribution with thinner SV provides the highest rates (and it is more conservative).

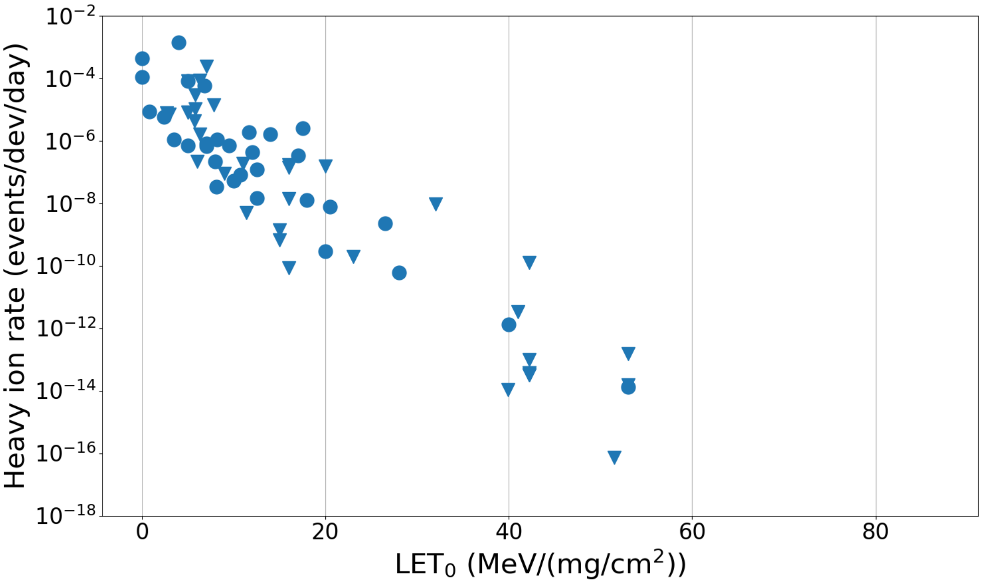

Figure 7.21: Heavy ion SEL rates of the set of devices under consideration for those devices that did not display sensitivity in a HEH beam. Data for a SEL SV with 10 μm thickness. Note that the number of SVs is determined by dividing the σ_{sat} by the SV area of the considered SEL volume in the FLUKA simulations.

As earlier said, an upper bound of 2 x 10^{-3} events/dev/day may be acceptable for the targeted LEO, especially if de-latching circuits or redundancy are implemented. However, this rate is specific to this very orbit. Therefore, it is worthwhile investigating how things change with different orbits.

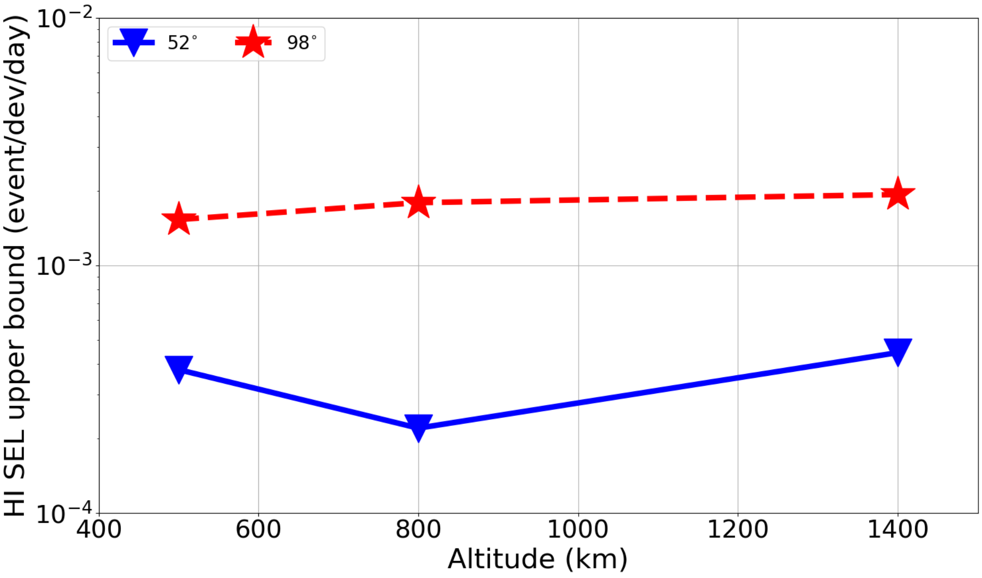

Figure 7.22: Heavy ion SEL upper bound as a function of orbit altitude and inclination. Data for the 3 μm SEL SV.

Fig. 7.22 displays the HI SEL upper bound for the worst case device as a function of the orbital altitude and inclination. As one can see the upper bound changes with the orbital parameters and it is more sensitive with respect to the inclination than the altitude. This is the very opposite of the α.

Variations with respect to the altitude are within a factor of 3 for the targeted orbit set. On the other hand, variations with the inclination can reach up to a factor of 10.

The highest altitude and inclination provide the worst case upper bound (given the lower geomagnetic shielding that allows higher ion fluxes to reach the space system). For this orbit the HI SEL upper bound of the worst case device is 2 x 10^{-3} events/dev/day, i.e., 1 event in 500 days.

A more conservative upper bound can also be calculated following the combinations of LET_0-σ_{sat} for which one would observe 3.7 SELs in a HEH test. These combinations can be extracted from the threshold lines traced over the CHARM SEL rate colormaps in Figs. 7.3 and 7.4 for the 3 and 10 μm thickness and the three fluences (Weibull cases).

Calculating the heavy ion SEL rate in space for devices having these combinations of LET_0-σ_{sat}, one can get a plot like the one in Fig. 7.23. The plot shows how the upper bound varies as a function of the device LET_0 as well as the SV thickness and the HEH fluence attained during the test.

There are some noteworthy features arising from this plot. Clearly, the upper bound reduces as the HEH fluence for the test is increased because a larger set of sensitivities can be exposed through a higher fluence. Moreover, the worst case upper bound is higher for the lower SV thickness by about a factor of 2. This is again due to the fact that also the GCR ions going through the entire thickness of the device are in decreasing amount as the thickness grows.

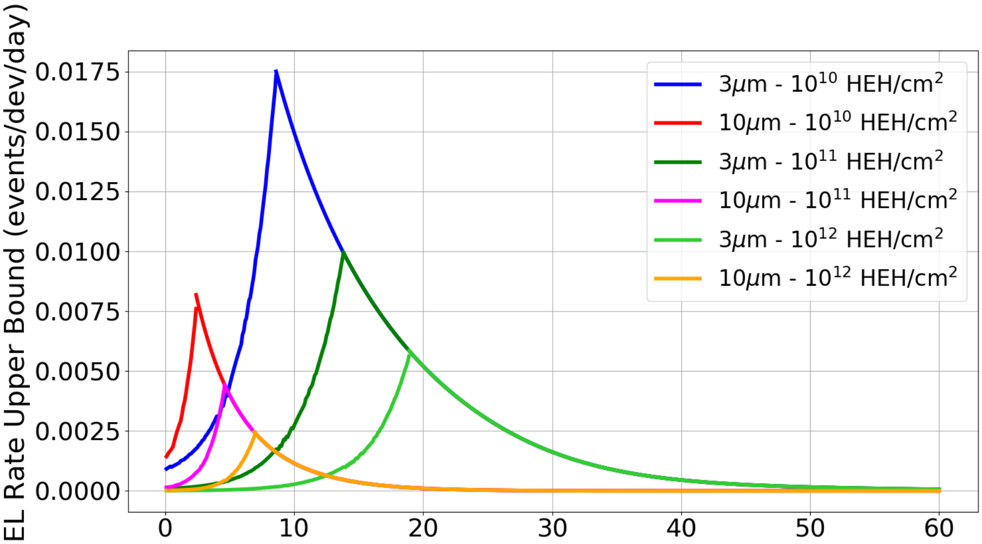

Figure 7.23: Heavy ion SEL upper bound as a function of the LET_0 of the device, the SV thickness and the fluence attained during a HEH test. The data are obtained from the combinations of LET_0-σ_{sat} describing the magenta, red and orange curves (Weibull cases) in Figs. 7.3 and 7.4. The upper bounds refer to an orbit with 800 km altitude and 98° inclination.

The shape of the curve is also peculiar. The upper bound grows with increasing LET_0 to reach an absolute maximum. This absolute maximum is dictated by the maximum LET_0 that can be stimulated in a HEH test for a 1 cm^2 SV surface. For higher LET_0, the upper bound decreases because the corresponding σ_{sat} is kept fixed to 1 cm^2 while varying the LET_0.

In terms of numerical values, this more conservative calculation method shows that, for a fluence of 10^{11} HEH/cm^2, the worst case SEL rate upper bound is about 10^{-2} events/dev/day. For this orbit, this is 5 times higher than the worst case real device, but it also corresponds to the space SEL rate obtained from the minimum HEH SEL cross-section for a reliable use of the VELA.

7.3.3 Space rate prediction summary

To conclude, it was shown that through HEH testing it was possible to resolve for the SEE susceptibility of a restricted number of commercial devices, typically in the order of 10% or less.

For these devices, the actual number of events observed is an important parameter in order to determine whether the VELA would provide reliable estimations for the combined proton-ion SEL response in LEO environments. Independently of the targeted mission, the VELA is shown to be very reliable, thanks to the environmental similitude, if the measured HEH SEL cross-section is above 5 x 10^{-9} cm^2/dev.

For devices displaying no sensitivity to HEHs and for typical target orbits (also considering TID resilience of commercial devices that would make SEEs the most problematic issue), the worst case device in the system can be expected to have a space rate below 2 x 10^{-3} events/dev/day.

The only set of devices that remains in the gray area are those that would display a few events in a HEH beam, but for which the VELA would underestimate the actual space rate. For these devices one can have an interval of possible space SEL rates that goes from the space SEL rate defined by the minimum HEH SEL cross-section and the α for that orbit and the worst case device upper bound, which also varies with the orbit.

Considering the reference LEO, this would mean that for these devices the rate would be comprised in the 2 x 10^{-3} - 10^{-2} events/dev/day range (where the upper limit is the space SEL rate arising from the minimum HEH SEL cross-section for a VELA reliable prediction), which would translate to 1 event in 100 or 500 days, which is not a fully negligible difference for some space missions.

7.3.4 Comparison with no-testing

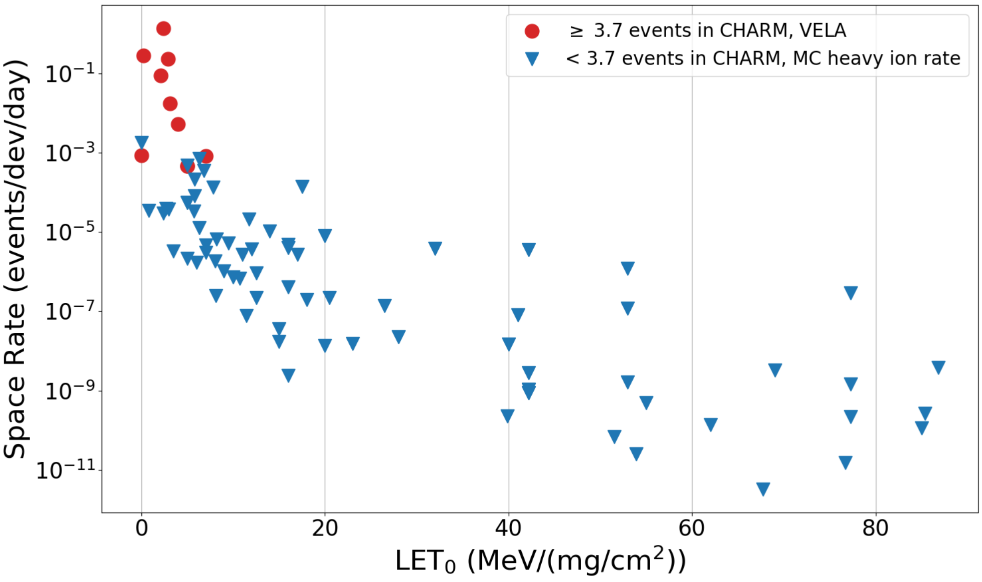

Figure 7.24: Space rates of the device data set according to the VELA for devices with > 3.7 events in CHARM and according to the heavy ion convolution with the Weibull response for those with less. Data for the 3 μm SEL SV.

As it is presented in the guideline [46, 47], system-level testing should be used to verify those systems that would otherwise not undergo any level of radiation verification.

The strength of using system-level testing with respect to no-testing is more obvious when it comes to soft errors, given that system-level testing can provide very reliable estimations through VELA for SEUs [47, 100], while with no-testing nothing can be said. Also, system-level testing brings up information about the potential interplay between an error happening in one device and its propagation into another, as well as concerning the efficacy of fault tolerant schemes.

When it comes to potentially destructive SEEs, there are still some advantages in performing system-level testing over not performing any test.

On the one hand, it is true that the upper bound analysis is perfectly applicable to no-testing as, indeed, no data from HEH testing other than the less than 3.7 events in CHARM was used to run that analysis. On the other hand, missing both the heavy ion and the proton response for typical missions targeted when the no-testing philosophy is followed does not allow one to get reliable figures for the potentially destructive SEEs that are stimulated by HEHs.

In this context, Fig. 7.24 shows the summary of the SEL space rates predicted for the data-set of devices in the two cases discriminated by the number of events observed in CHARM. As one can see, a system composed by these devices would be strongly dominated by SELs happening in the devices whose SEE cross-section could be characterized accurately by means of HEH testing.

With no-testing the only thing that one could assume is again an upper bound that would result in 1.5 events/dev/day, which, indeed does not provide much of an assurance when it comes to the fulfilment of the mission objectives. On the other hand, through HEH testing devices with such negative radiation performance can be identified, disqualified and replaced in the final system.

Chapter 8

Conclusions and future work

Looking back at the initial motivations behind this work, this thesis tackled some specific problems concerning the suitability of the current standards in ensuring radiation hardness assurance of high-reliability equipment to be used in harsh radiation environment as well as the suitability of alternative testing techniques having the goal of supplementing the existing standards for less critical equipment.

8.1 Main observations concerning current and future radiation hardness assurance practices

The first topic that was treated was that of emerging radiation effects in deep sub-micron technologies, such as the PDI effects in space. The thesis provided guidance on how to build representative models for the sensitive volume of the electronic devices that are relevant to study proton direct ionization starting from the experimental data.

While it remains sometimes hard to interpret experimental data discrepancies, the thesis reported that the severity of proton direct ionization effects may become dominant over the standard sensitivities to heavy ions and high-energy protons for devices characterized by low critical charges in more than just a single sample. In particular, the data suggest that the sensitivity to proton direct ionization may be much stronger than it was typically observed before (both high PDI peak cross-section and upset rate in space). And, while an in-space verification is still missing, the breakdown of the CHARM mixed-field SEU cross-section seems to suggest that the sensitivity to proton direct ionization may be a significant concern already in environments whose fluxes are largely dominated by neutrons of various energies.

In this vein, a more pragmatic approach based on specific low-energy proton testing (either through mono-energetic or degraded proton sources) is expected to be more effective than the application of margins on top of the upset rates computed based on heavy ion and high-energy proton cross-sections. An even stronger boost towards this empirical approach may be suggested by the fact that low-energy proton cross-sections may be higher than high-energy low-LET ion cross-sections since the latter may provide a strong underestimation of the proton direct ionization contribution.

In this respect the thesis also pointed out the demand for having simulation tools that are as complete as possible in terms of all the electro-magnetic and nuclear processes that can contribute to the SEU cross-section. While the differences between FLUKA and Geant4 did not have a remarkable impact on the upset rate predictions, the missing physics can often explain the dissimilarities between the experimental data and the numerical data.

The second and third topics that were explored are strictly connected, in that proving that the high-energy hadron equivalence can sustain the challenge brought by some peculiar pion interaction mechanisms (that render their SEE cross-section different from those of proton and neutrons) is an important brick in facilitating the use of mixed-field facilities such as

CHARM for other needs than those of the CERN accelerator complex. It also confirms that what has been developed in the last two decades in terms of radiation hardness assurance for accelerator is still applicable to novel highly integrated technologies (except for PDI), although some subtle differences are always present, but have a marginal impact.

Also for the case of pions relying on valuable simulation tools that can allow exploring what stands behind the triggering of an SEE down to the nuclear level proved to be a huge enabler in explaining experimental data that seemed to initially contradict expectations (e.g., pion SEL cross-section not following the nuclear reaction cross-section as the pion SEU cross-section instead does).

Once the high-energy hadron equivalence was confirmed, the third topic explored the advantages and drawbacks of employing the CHARM mixed-field facility (as well as standard mono-energetic protons or spallation neutron facilities) for the verification of either large ensemble of commercial devices or full systems to be used in space missions characterized by mild radiation environment and high risk acceptance.

The analysis showed that high-energy hadrons stand well the comparison with respect to very high energy ions (high penetration ions), whose LET < 10 MeV/(mg/cm^2), inasmuch as the susceptibilities highlighted by both tests are similar at same dose delivered, with potentially even slight advantages for spallation neutrons over very high energy ions. In addition, HEH beams are currently a more available radiation source than HEHI beams.

The application and limitations of a calculation method based on the environmental similarity between the energy deposition arising from the HEH facilities and the space environment were also developed. This analysis pointed out that it is possible to determine rather accurate predictions for the space rate for both SEUs and SELs when the only experimental data available is the cross-section measured at a HEH facility (and when neither the heavy ion cross-section nor the geometry and parameters of the device sensitive volume are available), though only for devices having a low enough LET threshold.

The simplified calculation method comes with some approximation that may render the method less accurate when the statistics following the HEH radiation test are poor. This is due to the fact that for such devices the small differences between the energy deposition spectra of the HEH facility and that of the space environment grow in significance and can become dominant.

Nevertheless, the use of HEH facilities remains promising for space mission profiles associated to high risk acceptance even when the test returns insensitivity to HEH given that it can at least be guaranteed that the devices passing the HEH test may only suffer ion triggered failures with a relatively low and possibly acceptable frequency.

8.2 Future work

Concerning proton direct ionization effects it will be of central importance to verify that the space upset rates correspond to the predictions derived from experimental and simulation data. Currently, there are several small satellite missions for which it is planned to fly, in different LEO environments, the ISSI SRAM as an SEU radiation monitor. These missions are planned for launch in 2022. Depending on the outcome of these space missions, it will be possible to confirm the existing predictions or to assess whether a revision may be needed and, consequently, also develop some definitive guidelines on how to conduct this kind of characterization for direct exploitation with respect to the mission profile.

Understanding the discrepancy between the LEP and low-LET ion experimental data is also a subject worth further exploration. As pointed out throughout the thesis, solving the issues introduced by diverse dosimetry techniques employed at different facilities may be a good starting point to validate the observed divergences.

It will be worthwhile to examine in deeper detail the SEU cross-section of the RADSAGA

SRAM through the G4SEE tool and additional experimental data in order to understand whether at the minimum voltage the proton direct ionization effects are important even above the 3 MeV (as suggested by the strong differences between the experimental proton and neutron SEU cross-section at 14 MeV, part of an on-going work) that are typically considered as limit for these effects.

Concerning the high-energy hadron equivalence, the robustness of its definition has been now proved against several different challenges. It is not expected that a further major revision will be needed in the coming years because of pion effects. On the other hand, similarly to space, proton direct ionization (as well as other ionization processes associated to electrons and photons) may emerge as an additional effect that may require a separate analysis as it is currently done for the thermal neutrons.

Concerning the use of HEH facilities for component screening and system level testing of space equipment, the whole topic can still be considered to be at an early stage given that the amount of experimental data is still quite limited and the reported analysis would definitely benefit from extended figures of comparison than what it is currently available. The VELA itself may need to follow a stronger level of validation based on this missing experimental and flight data.

In addition, at the moment the VELA has been applied to SEU and SEL, but it may be worthwhile investigating its applicability and limitations when it comes to other DSEEs given that it is not excluded that devices sensitive to DSEEs may be used in high risk acceptance space missions.

Bibliography

[1] R. Garcia-Alia; M. Brugger; F. Cerutti; S. Danzeca; V. Ferlet-Cavrois; R. Gaillard; J. Mekki; C. Poivey; and A. Zadeh. LHC and HL-LHC: present and future radiation environment in the high-luminosity collision points and RHA implications. *IEEE Trans. Nucl. Sci.*, 64(2):882–890, February 2017.

[2] T. Bohlen; F. Cerutti; P. W. Chin; A. Fassò; A. Ferrari; P. Garcia-Ortega; A. Mairani; P. R. Sala; G. Smirnov; and V. Vlachoudis. The FLUKA code: Developments and challenges for high energy and medical applications. *Nuclear Data Sheets*, 120:211–214, June 2014.

[3] G. Battistoni; T. Bohlen; F. Cerutti; P. W. Chin; L. S. Esposito; A. Fassò; A. Ferrari; A. Lechner; A. Empl; A. Mairani; A. Mereghetti; P. Garcia-Ortega; J. Ranft; S. Roesler; P. R. Sala; V. Vlachoudis; and G. Smirnov. Overview of the FLUKA code. *Annals of Nuclear Energy*, 82:10–18, August 2015.

[4] R. Garcia-Alia; M. Brugger; S. Danzeca; F. Cerutti; J. P. de Carvalho-Saraiva; R. Denz; A. Ferrari; L. L. Foro; P. Peronnard; K. Roed; R. Secondo; J. Steckert; Y. Thurel; I. Toccafondo; and S. Uznanski. Single event effects in high-energy accelerators. *Semicond. Sci. Technol.*, 32(034003):1–11, February 2017.

[5] G. Lerner; R. Garcia-Alia; K. Bilko; M. Sabate-Gilarte; C. Bahamonde-Castro; A. Lechner; O. Stein; A. Tsinganis; F. Cerutti; and Y. Kadi. Radiation level specifications for HL-LHC. *CERN EDMS 2302154 V1.0*, October 2020.

[6] K. Roed; D. Kramer; P. Peronnard; C. Pignard; G. Spiezia; and A. Thornton. Method for measuring mixed field radiation levels relevant for SEEs at the LHC. *IEEE Trans. Nucl. Sci.*, 59(4):1040–1047, August 2012.

[7] M. Cecchetto; R. Garcia-Alia; F. Wrobel; A. Coronetti; K. Bilko; D. Lucsanyi; S. Fiore; G. Bazzano; E. Pirovano; and R. Nolte. 0.1-10 MeV neutron soft error rate in accelerator and atmospheric environments. *IEEE Trans. Nucl. Sci.*, 68(5):873–883, May 2021.

[8] J. Martensson; M. Berg; L. Carlen; R. Elmer; A. Fokin; R. Ghetti; B. Jakobsson; B. Noren; A. Oskarsson; H. J. Whitlow; C. Ekstrom; G. Ericsson; J. Romanski; E. J. van Veldhuizen; L. Westerberg; J. Julien; K. Nybo; T. F. Thorsteinsen; S. Amirelmi; M. Guttormsen; G. Lovhoiden; V. Bellini; F. Palazzolo; M. L. Sperduto; C. Sutera; V. Avdeichikov; A. Kuznetsov; and Y. Marin. Pion production excitation functions in proton-nucleus collisions from the absolute threshold to 500 MeV. *Physical Review C*, 62(014610):1–11, June 2000.

[9] S. J. Bates; C. Furetta; M. Glaser; F. Lemeilleur; E. Leon-Florian; C. Gossling; B. Kaiser; A. Rolf; R. Wunstorf; H. Feick; E. Fretwurst; G. Lindstrom; M. Moll; G. Taylor; and A. Chilingarov. Pion-induced damage in silicon detectors. *Nuclear Instruments and Methods in Physics Research A*, 379(1):116–123, November 1995.

[10] S. Danzeca; G. Spiezia; M. Brugger; l. Dusseau; G. Foucard; R. Garcia-Alia; P. Mala; A. Masi; P. Peronnard; J. Soltes; A. Thornton: and L. Viererbl. Qualification and characterization of sram memories used as radiation sensors in the LHC. *IEEE Trans. Nucl. Sci.*, 61(6):3458–3465, December 2014.

[11] G. Spiezia; P. Peronnard; A. Masi; M. Brugger; M. Brucoli; S. Danzeca; R. Garcia-Alia; R. Losito; J. Mekki; P. Oser; R. Gaillard; and L. Dusseau. A new RadMon version for the LHC and its injection lines. *IEEE Trans. Nucl. Sci.*, 61(6):3424–3431, December 2014.

[12] J. Mekki; M. Brugger; R. García Alía; A. Thornton; N. C. Dos Santos Mota; and S. Danzeca. CHARM: a mixed field facility at CERN for radiation test in ground, atmospheric, space and accelerator representative environments. *IEEE Trans. Nucl. Sci.*, 63(4):2106–2114, August 2016.

[13] A. Infantino. FLUKA monte carlo modelling of the CHARM facility's test area: update of the radiation field assessment. *CERN-ACC-NOTE-2017-0059*, November 2017.

[14] A. Coronetti; R. Garcia-Alia; M. Cecchetto; W. Hajdas; D. Soderstrom; A. Javanainen; F. Saigné. The pion single event effect resonance and its impact in an accelerator environment. *IEEE Trans. Nucl. Sci.*, 67(7):1606–1613, July 2020.

[15] R. Garcia-Alia; E. Blackmore; M. Brugger; S. Danzeca; V. Ferlet-Cavrois; R. Gaillard; J. Mekki; C. Poivey; K. Roed; F. Saigné; G. Spiezia; M. Trinczek; S. Uznanski; and F. Wrobel. SEL cross section energy dependence impact on the high energy accelerator failure rate. *IEEE Trans. Nucl. Sci.*, 61(6):2936–2944, December 2014.

[16] R. Garcia-Alia; M. Brugger; S. Danzeca; V. Ferlet-Cavrois; C. Poivey; K. Roed; F. Saigné; G. Spiezia; S. Uznanski; and F. Wrobel. Energy dependence of tungsten-dominated SEL cross sections. *IEEE Trans. Nucl. Sci.*, 61(5):2718–2725, October 2014.

[17] R. Garcia-Alia; M. Brugger; S. Danzeca; V. Ferlet-Cavrois; C. Frost; R. Gaillard; J. Mekki; F. Saigné; A. Thornton; S. Uznanski; and F. Wrobel. SEL hardness assurance in a mixed radiation field. *IEEE Trans. Nucl. Sci.*, 62(6):2555–2562, December 2015.

[18] Vanderbilt University. CREME-MC. *https://creme.isde.vanderbilt.edu*, July 2020.

[19] A. J. Tylka; J. H. Adams; P. R. Boberg; B. Brownstein; W. F. Dietrich; E. O. Flueckiger; E. L. Petersen; M. A. Shea; D. F. Smart; and E. C. Smith. CREME-96: a revision of the cosmic ray effects on microelectronics code. *IEEE Trans. Nucl. Sci.*, 44(6):2150–2160, June 1997.

[20] R. L. Ladbury; M. Bay; and J. Zinchuk. Threats to resiliency of redundant systems due to destructive SEE. *IEEE Trans. Nucl. Sci.*, 68(5):1–9, May 2021.

[21] N. A. Dodds; J. R. Schwank; M. R. Shaneyfelt; P. E. Dodd; B. L. Doyle; M. Trinczek; E. W. Blackmore; K. P. Rodbell; M. S. Gordon; R. A. Reed; J. A. Pellish; K. A. LaBel; P. W. Marshall; S. E. Swanson; G. Vizkelethy; S. Van Deusen; F. W. Sexton; and M. J. Martinez. Hardness assurance for proton direct ionization-induced SEEs using a high-energy proton beam. *IEEE Trans. Nucl. Sci.*, 61(6):2904–2914, December 2014.

[22] M. P. King; R. A. Reed; R. A. Weller; M. H. Mendenhall; R. D. Schrimpf; B. D. Sierawski; A. L. Stenberg; B. Narasimham; J. K. Wang; E. Pitta; B. Bartz; D. Reed; C. Monzel; R. C. Baumann; X. Deng: J. A. Pellish; M. D. Berg; C. M. Seidleck: E. C. Auden; S. L. Weeden-Wright; N. J. Gaspard; C. X. Zhang; D. M. Fleetwood. Electron-induced single event upsets in static random access memories. *IEEE Trans. Nucl. Sci.*, 60(6):4122–4129, December 2013.

[23] M. Tali; R. Garcia-Alia; M. Brugger; V. Ferlet-Cavrois; R. Corsini; W. Farabolini; A. Mohammadzadeh; G. Santin; and A. Virtanen. High-energy electron-induced seus and jovian environment impact. *IBm J. Res. Develop.*, 64(8):2016–2022, August 2017.

[24] J. Barak; and N. M. Yitzhak. SEU rate in avionics: from sea level to high altitude. *IEEE Trans. Nucl. Sci.*, 62(6):3369–3380, December 2015.

[25] H. A. Bethe; and J. Ashkin. in experimental nuclear physics. *Wiley, New York*, page 166, 1953.

[26] European Cooperation for Space Standardization. ECSS-Q-ST-30-11C: space product assurance - derating EEE components. *ESA-ESTEC*, 2011.

[27] N. A. Dodds; N. C. Hooten; R. A. Reed; R. D. Schrimpf: J. H. Warner; N. J.-H. Roche; D. McMorrow; S.-J. Wen; R. Wong; J. F. Salzman; S. Jordan; J. A. Pellish; C. J. Marshall; N. J. Gaspard; W. G. Bennett; E. X. Zhang; and B. L. Bhuva. Effectiveness of SEL hardening strategies and the latchup domino effect. *IEEE Trans. Nucl. Sci.*, 59(6):3085–3092, December 2009.

[28] R. A. Reed; R. A. Weller; M. H. Mendenhall; J.-M. Lauenstein; K. M. Warren; J. A. Pellish; R. D. Schrimpf; B. D. Sierawski; L. W. Massengill; P. E. Dodd; M. R. Shaneyfelt; J. A. Felix; J. R. Schwank; N. F. Haddad; R. K. Lawrence; J.H Bowman; and R. Conde. Impact of ion energy and species on single event effects analysis. *IEEE Trans. Nucl. Sci.*, 54(6):2312–2321, December 2007.

[29] V. Wyrwoll; R. Garcia-Alia; K. Roed; P. Fernandez-Martinez; M. Kastriotou; M. Cecchetto; N. Kerboub; M. Tali; and F. Cerutti. Heavy ion nuclear reaction impact on SEE testing: from standard to ultrahigh energies. *IEEE Trans. Nucl. Sci.*, 67(7):1590–1598, July 2020.

[30] V. Wyrwoll; R. Garcia-Alia; K. Roed; C. Cazzaniga; M. Kastriotou; P. Fernandez-Martinez; A. Coronetti; and F. Cerutti. Longitudinal direct ionization impact of heavy ions on see testing for ultrahigh energies. *IEEE Trans. Nucl. Sci.*, 67(7):1530–1539, July 2020.

[31] B. D. Sierawski; M. H. Mendenhall; R. A. Reed; M. A. Clemens; R. A. Weller; R. D. Schrimpf; E. W. Blackmore; M. Trinczek; B. Hitti; J. A. Pellish; R. C. Baumann: S.-J. Wen; R. Wong; and N. Tam. Muon-induced single event upsets in deep-submicron technology. *IEEE Trans. Nucl. Sci.*, 57(6):3273–3278, December 2010.

[32] J. M. Trippe; R. A. Reed; R. A. Austin; B. D. Sierawski; L. W. Massengill; R. A. Weller; K. M. Warren; R. D. Schrimpf; B. Narasimham; B. Bartz; D. Reed. Predicting muon-induced SEU rates for a 28-nm SRAM using protons and heavy ions to calibrate the sensitive volume model. *IBm J. Res. Develop.*, 65(2):712–718, February 2018.

[33] H. J. Barnaby. Total-ionizing dose effects in modern CMOS technology. *IEEE Trans. Nucl. Sci.*, 53(6):3103–3121, December 2006.

[34] M. R. Shaneyfelt; J. R. Schwank; S.C Witczak; D. M. Fleetwood; R. L. Pease; P. S. Winokur; L. C. Riewe; and G. L. Hash. Thermal-stress effects and enhanced low dose rate sensitivity in linear bipolar ICs. *IEEE Trans. Nucl. Sci.*, 47(6):2539–2545, December 2000.

[35] R. L. Pease. 2008 update to the ELDRS bipolar linear circuit data compendium. *Proc. RADECS Conf.*, pages 75–78, September 2008.

[36] ESCC 22900. Total dose steady-state irradiation test method. *European Space Components Coordination, ESA*, October 2010.

[37] R. Mangeret. Radiation hardness assurance: how well assured do we need to be? *in NSREC Short Course*, July 2018.

[38] J. R. Srour; C. J. Marshall; P. W. Marshall. Review of displacement damage effects in silicon devices. *IEEE Trans. Nucl. Sci.*, 50(3):3653–3670, June 2003.

[39] M. Moll. Displacement damage in silicon detectors for high energy physics. *IEEE Trans. Nucl. Sci.*, 65(8):1561–1582, February 2018.

[40] A. Vasilescu; and G. Lindstroem. Displacement damage in silicon. *https//www.cern.ch/rd-50/*, April 2018.

[41] G. P. Summers; E. A. Burke; P. Shapiro; R. J. Walters; and S. R. Messenger. Damage correlations in semiconductors exposed to gamma, electron and proton radiations. *IEEE Trans. Nucl. Sci.*, 40(6):1372–1379, December 1993.

[42] M. Huhtinen; and P. Aarnio. Pion induced displacement damage in silicon devices. *Nucl. Instrum. Methods Phys. Res. A, Accel. Spectrom. Detect. Assoc. Equip.*, 335(3):580–582, December 1993.

[43] P. J. Griffin. Dosimetry cross section compendium. *Sandia Nat. Lab. Tech. Rep. SAND92-0094*, 1993.

[44] A. Y. Konobeyev; Y. A. Korovin; and V. N Sosnin. Neutron displacement cross-sections for structurak materials below 800 MeV. *J. Nucl. Mater.*, 186(2):117–130, 1992.

[45] R. Ferraro; G. Foucard; A. Infantino; L. Dilillo; M. Brugger; A. Masi; R. Garcia-Alia; and S. Danzeca. COTS optocoupler radiation qualification process for LHC applications based on mixed-field irradiations. *IEEE Trans. Nucl. Sci.*, 67(7):1395–1403, July 2020.

[46] A. Coronetti. RADSAGA system test guideline. *CERN EDMS document 2324146/2.1*, October 2020.

[47] A. Coronetti; R. Garcia-Alia; J. Budroweit; T. Rajkowski; I. da Costa Lopes; K. Niskanen; D. Soderstrom; C. Cazzaniga; R. Ferraro; S. Danzeca; J. Mekki; F. Manni; D. Dangla; C. Virmontois; N. Kerboub; A. Koelpin; F. Saigné; P. Wang; V. Pouget; A. Touboul; A. Javanainen; H. Kettunen; and R. Coq-Germanicus. Radiation hardness assurance through system-level testing: risk acceptance, facility requirements, test methodology and data exploitation. *IEEE Trans. Nucl. Sci.*, 68(5):958–969, May 2021.

[48] J.F. Ziegler; and J.P. Biersack. Stopping and range of ions in matter. *http://www.srim.org*, August 2018.

[49] Brookhaven National Laboratory. NASA space radiation laboratory. *https://www.bnl.gov/nsrl/userguide/*, November 2019.

[50] R. Garcia-Alia; P. Fernandez-Martinez; M. Kastriotou; M. Brugger; J. Bernhard; M. Cecchetto; F. Cerutti; N. Charitonidis; S. Danzeca; L. Gatignon; A. Gerbershagen; S. Gilardoni; N. Kerboub; M. Tali; V. Wyrwoll; V. Ferlet-Cavrois; C. Boatella-Polo; H. Evans; G. Furano; and R. Gaillard. Ultraenergetic heavy-ion beams in the CERN accelerator complex for radiation effects testing. *IEEE Trans. Nucl. Sci.*, 66(1):458–465, January 2019.

[51] P. Fernandez-Martinez; R. Garcia-Alia; M. Cecchetto; M. Kastriotou; N. Kerboub; M. Tali; V. Wyrwoll; M. Brugger; C. Cangialosi; F. Cerutti; S. Danzeca; M. Delrieux; R. Froeschl; L. Gatignon; S. Gilardoni; J. Lendaro; I. Mateu; F. Ravotti; H. Wilkens; and R. Gaillard. SEE tests with ultra energetic Xe ion beam in the CHARM facility at CERN. *IEEE Trans. Nucl. Sci.*, 66(7):1523–1531, July 2019.

[52] M. Kastriotou; P. Fernandez-Martinez; R. Garcia-Alia; C. Cazzaniga; M. Cecchetto; A. Coronetti; G. Lerner; M. Tali; N. Kerboub; V. Wyrwoll; J. Bernhard; S. Danzeca; V. Ferlet-Cavrois; A. Gerbershagen; and H. Wilkens. Single event effect testing with ultrahigh energy heavy ion beams. *IEEE Trans. Nucl. Sci.*, 67(1):63–70, January 2020.

[53] National Academies of Sciences Engineering and Medicine. Testing at the speed of light. *https://www.nap.edu/catalog/24993/testing-at-the-speed-of-light-the-state-of-us*, March 2021.

[54] H. Quinn. Challenges in testing complex systems. *IEEE Trans. Nucl. Sci.*, 61(2):766–786, April 2014.

[55] F. Irom. Guideline for ground radiation testing of microprocessors in the space radiation environment. *JPL publications 08-13 4/08*, March 2008.

[56] NASA. Guidelines for verification strategies to minimize risk based on mission environment, application and lifetime (MEAL). *NASA/TM-2018-220074*, January 2021.

[57] P. M. O'Neill; G. D. Badhwar; and W. X. Culpepper. Risk assessment for heavy ions of parts tested with protons. *IEEE Trans. Nucl. Sci.*, 44(6):2311–2314, December 1997.

[58] K. A. LaBel; P. W. Marshall; T. D. Gruner; R. A. Reed; B. Settles; J. Wilmot; L. F. Dougherty; A. Russo; M. G. Foster; W. Yuknis; and A. Garrison-Darrin. Radiation evaluation method of commercial off-the-shelf (COTS) electronic printed circuit boards (PCBs). *Proc. RADECS Conf.*, pages 528–534, September 1999.

[59] S. M. Guertin. Lessons and recommendations for board-level testing with proton. *Proc. Small Satellite Conf.*, 2018.

[60] S. M. Guertin. Board level proton testing book of knowledge for NASA electronic parts and packaging program. *JPL publications 17-7 11/17*, October 2018.

[61] F. Bezerra; D. Dangla; F. Manni; J. Mekki; D. Standoravski; R. Garcia-Alia; M. Brugger; and S. Danzeca. Evaluation of an alternative low cost approach for SEE assessment of a SoC. *Proc. RADECS Conf.*, pages 418–422, October 2017.

[62] R. Secondo; R. Garcia-Alia; P. Peronnard; M. Brugger; A. Masi; S. Danzeca; A. Merlenghi; E. Chesta; J. R. Vaillè; M. Bernard; and L. Dusseau. System-level radiation characterization of a 1U CubeSat based on CERN radiation monitoring technology. *IEEE Trans. Nucl. Sci.*, 65(8):1694–1699, August 2018.

[63] J. Budroweit; S. Mueller; M. Jaksch; R. Garcia-Alia; A. Coronetti; and A. Koelpin. Insitu testing of a multi-band software-defined radio platform in a mixed-field irradiation environment. *MDPI Aerospace*, 6(10):106, September 2019.

[64] A. Coronetti; F. Manni; J. Mekki; D. Dangla; C. Virmontois; N. Kerboub; and R. Garcia-Alia. Mixed-field radiation qualification of a COTS space on-board computer along with its CMOS camera payload. *Proc. RADECS Conf.*, September 2019.

[65] A. de Bibikoff; and P. Lamberbourg. Method for system-level testing of COTS electronic board under high energy heavy ion. *IEEE Trans. Nucl. Sci.*, 67(10):2179–2187, October 2020.

[66] T. Rajkowski; F. Saigné; V. Pouget; F. Wrobel; A. Touboul; J. Boch; P. Kohler; P. Dubus; and P. X. Wang. Analysis of SET propagation in a system in package point of load converter. *IEEE Trans. Nucl. Sci.*, 67(7):1494–1502, July 2020.

[67] S. Uznanski; B. Todd; A. Dinius; Q. King; and M. Brugger. Radiation hardness assurance methodology of radiation tolerant power converter controls for Large Hadron Collider. *IEEE Trans. Nucl. Sci.*, 61(6):3694–3700, December 2014.

[68] S. Uznanski; R. Garcia-Alia; M. Brugger; P. Moreira; and B. Todd. Qualification of electronics components for a radiation environment: when standards do no exist. *RADECS Short Course*, October 2017.

[69] K. P. Rodbell; D. F. Heidel; H. H. K. Tang; M. S. Gordon; P. Oldiges; and C. E. Murray. Low-energy proton-induced single-event-upsets in 65 nm node, silicon-on-insulator, latched and memory cells. *IEEE Trans. Nucl. Sci.*, 54(6):2474–2479, December 2007.

[70] D. F. Heidel; P. W. Marshall; K. A. LaBel; J. R. Schwank; K. P. Rodbell; M. C. Hakey; M. D. Berg; P. E. Dodd; M. R. Friendlich; A. D. Phan; C. M. Seidleck; M. R. Shaneyfelt; and M. A. Xapsos. Low energy proton single-event-upset test results on 65 nm SOI SRAM. *IEEE Trans. Nucl. Sci.*, 55(6):3394–3400, December 2008.

[71] R. K. Lawrence; J. F. Ross; N. F. Haddad; R. A. Reed; and D. R. Albrecht. Soft error sensitivities in 90 nm bulk CMOS SRAMs. *IEEE Radiation Effects Data Workshop*, pages 123–126, 2009.

[72] B. D. Sierawski; J. A. Pellish; R. A. Reed; R. D. Schrimpf; K. M. Warren; R. A. Weller; M. H. Mendenhall; J. D. Black; A. D. Tipton; M. A. Xapsos; R. C. Baumann; X. Deng; M. J. Campola; M. R. Friendlich; H. S. Kim; A. M. Phan; and C. M. Seidleck. Impact of low-energy proton induced upstes on test methods and rate predictions. *IEEE Trans. Nucl. Sci.*, 56(6):3085–3092, December 2009.

[73] N. Seifert; B. Gill; J. A. Pellish; P. W. Marshall; and K. A. LaBel. The susceptibility of 45 and 32 nm bulk CMOS latches to low-energy protons. *IEEE Trans. Nucl. Sci.*, 58(6):2711–2718, December 2011.

[74] J. R. Schwank; M. R. Shaneyfelt; V. Ferlet-Cavrois; P. E. Dodd; E. W. Blackmore; J. A. Pellish; K. P. Rodbell; D. F. Heidel; P. W. Marshall; K. A. LaBel; P. M. Gouker; N. Tam; R. Wong; S.-J. Wen; R. A. Reed; S. M. Dalton; and S. E. Swanson. Hardness assurance testing for proton direct ionization effects. *IEEE Trans. Nucl. Sci.*, 59(4):1197–1202, August 2012.

[75] C. Weulersee; F. Miller; D. Alexandrescu; E. Schaefer; and R. Gaillard. Assessment and comparison of the low-energy proton sensitivity in 65nm to 28nm SRAM devices. *Proc. RADECS Conf.*, pages 291–296, September 2011.

[76] E. H. Cannon; M. Cabanas-Holmen; J. Wert; T. Amort; R. Brees; J. Koehn; B. Meaker; and E. Normand. Heavy-ion, high-energy and low-energy proton see sensitivity of 90-nm RHBD SRAMs. *IEEE Trans. Nucl. Sci.*, 57(6):3493–3499, December 2010.

[77] P. E. Dodd; M. R. Shaneyfelt; F. W. Sexton; J. D. Black; D. S. Lee; S. E. Swanson; B. L. Bhuva; K. M. Warren; R. A. Reed; J. Trippe; B. D. Sierawski; R. A. Weller; N. Mahatme; N. J. Gaspard; T. Assis; R. Austin; S. L. Weeden-Wright; L. W. Massengill;

G. Swift; M. Wirthlin; M. Cannon; R. Liu; L. Chen; A. T. Kelly; P. W. Marshall; M. Trinczek; E. W. Blackmore; S.-J. Wen; R. Wong; B. Narasimham; J. A. Pellish; N. A. Dodds; M. J. Martinez and H. Puchner. The contribution of low-energy protons to the total on-orbit SEU rate. *IEEE Trans. Nucl. Sci.*, 62(6):2440–2451, December 2015.

[78] N. A. Dodds; P. E. Dodd; R. M. Shaneyfelt; F. W. Sexton; M. J. Martinez; J. D. Black; P. W. Marshall; R. A. Reed; M. W. McCurdy; R. A. Weller; J. A. Pellish; K. P. Rodbell; and M. S. Gordon. New insight gained on mechanisms of low-energy proton-induced SEUs by minimizing energy straggle. *IEEE Trans. Nucl. Sci.*, 62(6):2822–2829, December 2015.

[79] ESCC 25100. Single event effects test method and guidelines. *European Space Components Coordination, ESA*, October 2014.

[80] L. D. Edmonds; and K. J. Edmonds. A method for estimating SEU rates from protons by direct ionization. *IEEE Trans. Nucl. Sci.*, 55(5):2666–2678, October 2008.

[81] D. Kobayashi. Scaling trends of digital single-event effects: a survey of SEU and SET parameters and comparison with transistor performance. *IEEE Trans. Nucl. Sci.*, 68(2):124–148, February 2021.

[82] A. Akkerman; J. Barak; and N. M. Yitzhak. Role of elastic scattering of protons, muons, and electrons in inducing single event upsets. *IEEE Trans. Nucl. Sci.*, 64(10):2648–2660, August 2017.

[83] P. Caron; C. Inguimbert; L. Artola; R. Ecoffet; and F. Bezerra. Physical mechanisms of proton-induced single-event upsets in integrated memory devices. *IEEE Trans. Nucl. Sci.*, 66(7):1404–1409, July 2019.

[84] Z. Wu; S. Chen; J. Yu; J. Chen; P. Huang; and R. Song. Recoil-ion-induced single event uspets in nanometer CMOS SRAM under low-energy proton radiation. *IEEE Trans. Nucl. Sci.*, 64(1):654–664, January 2017.

[85] J. A. Pellish; P. W. Marshall; K. P. Rodbell; M. S. Gordon; K. A. LaBel; J. R. Schwank; N. A. Dodds; C. M. Castaneda; M. D. Berg; H. S. Kim; A. M. Phan; C. M. Seidleck. Criticality of low-energy protons in single-event effects testing of highly-scaled technologies. *IEEE Trans. Nucl. Sci.*, 61(6):2896–2903, December 2014.

[86] L. W. Massengill; M. L. Alles; S. E. Kerns; and K. L. Jones. Effects of process parameter distributions and ion strike location on SEU cross-section data (CMOS SRAMs). *IEEE Trans. Nucl. Sci.*, 40(6):1804–1811, December 1993.

[87] T. Heijmen; and B. Kruseman. Alpha-particle-induced SER of embedded SRAMs affected by variations in process parameters and by the use of process options. *Solid-State Electronics*, 49(11):1783–1790, November 2005.

[88] D. Kobayashi; N. Hayashi; K. Hirose; Y. Kakehashi; O. Kawasaki; T. Makino; T. Ohshima; D. Matsuura; Y. Mori; M. Kusano; T. Narita; S. Ishii; and. K. Masukawa. Process variation aware analysis of SRAM SEU cross sections using data retention voltage. *IEEE Trans. Nucl. Sci.*, 66(1):155–162, January 2019.

[89] D. Kobayashi; K. Hirose; K. Sakamoto; S. Okamoto; S. Baba; H. Shindou; O. Kawasaki; T. Makino; T. Ohshima; Y. Mori; D. Matsuura; M. Kusano; T. Narita; and S. Ishii. Data-renention-voltage-based analysis of systematic variations in SRAM SEU hardness: a possible solution to synergistic effects of TID. *IEEE Trans. Nucl. Sci.*, 67(11):328–335, January 2019.

[90] J. M. Cannon; T. D. Loveless; R. Estrada; R. Boggs; S. P. Lawrence; G. Santos; W. McCurdy; A. L. Sternberg; D. R. Reising; T. Finzell; and A. Cannon. Electrical measurement of cell-to-cell variation of critical charge in sram and sensitivity to single-event upsets by low-energy protons. *IEEE Trans. Nucl. Sci.*, 68(5):1–9, May 2021.

[91] J. A. Pellish; M. A. Xapsos; C. A. Stauffer; T. M. Jordan; A. B. Sanders; R. L. Ladbury; T. R. Oldham; P. W. Marshall; D. F. Heidel; and K. P. Rodbell. Impact of spacecraft shielding on direct ionization soft error rates for sub-130 nm technologies. *IEEE Trans. Nucl. Sci.*, 57(6):3183–3189, December 2010.

[92] J. Guillermin; N. Sukhaseum; P. Pourrouquet; N. Chatry; F. Bezerra; and R. Ecoffet. Worst-case proton contribution to the direct ionization SEU rate. *Proc. RADEC Conf.*, pages 330–337, September 2017.

[93] R. Garcia-Alia; M. Tali; M. Brugger; M. Cecchetto; F. Cerutti; A. Coronetti; S. Danzeca; L. Esposito; P. Fernandez-Martinez; S. Gilardoni; A. Infantino; M. Kastriotou; N. Kerboub; G. Lerner; V. Wyrwoll; V. Ferlet-Cavrois; C. Boatella; A. Javanainen; H. Kettunen; Y. Morilla; P. Martin-Holgado; R. Gaillard; F. Wrobel; C. Cazzaniga; D. Alexandrescu; M. Glorieux; and H. Puchner. Direct ionization impact on accelerator mixed-field soft error rate. *IEEE Trans. Nucl. Sci.*, 67(1):345–352, January 2020.

[94] G. J. Hofman; R. J. Peterson; C. J. Gelderloos; R. A. Ristinen; M. E. Nelson; A. Thompson; J. F. Ziegler; and H. Mullfeld. Light-hadron induced SER and scaling relations for 16- and 64-Mb DRAMs. *IEEE Trans. Nucl. Sci.*, 47(2):403–407, April 2000.

[95] S. Duzellier; D. Falguere; M. Tverskoy; E. Ivanov; R. Dufayel; and M.-C. Calvet. SEU induced by pions in memories from different generations. *IEEE Trans. Nucl. Sci.*, 48(6):41960–1965, December 2001.

[96] ESA. ESA COTS initiative, WG2-3 synthesis. *ESA-ESTEC*, November 2019.

[97] E. L. Petersen. The SEU figure of merit and proton upset rate calculations. *IEEE Trans. Nucl. Sci.*, 45(6):2550–2562, December 1998.

[98] D. M. Hiemstra; and E. W. Blackmore. LET spectra of proton energy levels from 50 to 500 MeV and their effectiveness for single event effects characterization of microelectronics. *IEEE Trans. Nucl. Sci.*, 50(6):2245–2250, December 2003.

[99] C. C. Foster; P. M. O'Neill; and C. K. Kouba. Risk assessment based on upset rates from high energy proton tests and monte carlo simulations. *IEEE Trans. Nucl. Sci.*, 55(6):2962–2969, December 2008.

[100] R. Garcia-Alia; M. Brugger; F. Cerutti; S. Danzeca; A. Ferrari; S. Gilardoni; Y. Kadi; M. Kastriotou; A. Lechner; C. Martinella; O. Stein; Y. Thurel; A. Tsinganis; and S. Uznanski. Simplified SEE sensitivity screening for COTS components in space. *IEEE Trans. Nucl. Sci.*, 65(1):448–456, January 2018.

[101] R. L. Ladbury; J.-M. Lauenstein; and K. P. Hayes. Use of proton SEE data as a proxy for bounding heavy-ion SEE susceptibility. *IEEE Trans. Nucl. Sci.*, 62(6):2502–2510, December 2015.

[102] R. L. Ladbury; and J.-M. Lauenstein. Evaluating constraints on heavy-ion SEE susceptibility imposed by proton SEE testing and other mixed environments. *IEEE Trans. Nucl. Sci.*, 64(1):301–308, January 2017.

[103] N. Kerboub; R. Garcia-Alia; J. Mekki; F. Bezerra; A. Monteuuis; P. Fernandez-Martinez; S. Danzeca; M. Brugger; D. Standarovski; and J. Rauch. Comparison between in-flight SEL measurements and ground estimation using different facilities. *IEEE Trans. Nucl. Sci.*, 66(7):1541–1547, July 2019.

[104] H. H. K. Tang. Nuclear physics of cosmic ray interaction with semiconductor materials: particle-induced soft errors from a physicist's perspective. *IBm J. Res. Develop.*, 40(1):91–108, January 2018.

[105] D. Ashery; I. Navon; G. Azuelos; H.K. Walter; H.J. Pfeiffer; and F.W. Schleputz. True absorption and scattering of pions on nuclei. *Phys. Rev. C*, 23(5):2173–2185, May 1981.

[106] D. Lucsanyi. G4SEE. *https://g4see.web.cern.ch*, May 2021.

[107] J. Allison; K. Amako; J. Apostolakis; H. Araujo; P. Arce-Dubois; M. Asai; G. Barnard; R. Capra; S. Chauvie; R. Chytracek; G. A. P. Cirrone; G. Cooperman; G. Cosmo; G. Cuttone; G. G. Daquino; M. Donszelmann; M. Dressel; G. Folger; F. Foppiano; J. Generowicz; V. Grichine; S. Guatelli; P. Gumplinger; A. Heikkinen; I. Hrivnacova; A. Howard; S. Incerti; V. Ivanchenko; T. Johnson; F. Jones; T. Koi; R. Kokoulin; M. Kossov; H. Kurashige; V. Lara; S. Larsson; F. Lei; O. Link; F. Longo; M. Maire; A. Mantero; B. Mascialino; I. McLaren; P. Mendez-Lorenzo; K. Minamimoto; K. Murakami; P. Nieminen; L. Pandola; S. Parlati; L. Peralta; J. Perl; A. Pfeiffer; M. G. Pia; A. Ribon; P. Rodrigues; G. Russo; S. Sadilov; G. Santin; T. Sasaki; D. Smith; N. Starkov; S. Tanaka; E. Tcherniaev; B. Tome; A. Trindade; P. Truscott; L. Urban; M. Verderi; A. Walkden; J. P. Wellisch; D. C. Williams; D. Wright; and H. Yoshida. Geant4 developments and applications. *IEEE Trans. Nucl. Sci.*, 53(1):270–278, February 2006.

[108] B. D. Sierawski; M. H. Mendenhall; R. A. Weller; R. A. Reed; J. H Adams; J. W. Watts; and A. F. Barghouty. CREME-MC: a physical-based single event effect tool. *Nucl. Sci. Symp. Conference Rec.*, pages 1258–1261, 2010.

[109] A. Coronetti; R. Garcia-Alia; J. Wang; M. Tali; M. Cecchetto; C. Cazzaniga; A. Javanainen; F. Saigné; and P. Leroux. Assessment of proton direct ionization for the radiation hardness assurance of deep sub-micron SRAMs used in space applications. *IEEE Trans. Nucl. Sci.*, 68(5):937–948, May 2021.

[110] A. Coronetti; R. Garcia-Alia; F. Cerutti; W. Hajdas; D. Soderstrom; A. Javanainen; and F. Saigné. The pion single-event latch-up cross-section enhancement: mechanisms and consequences for accelerator hardness assurance. *IEEE Trans. Nucl. Sci.*, 68(8):1613–1622, August 2021.

[111] E. L. Petersen; J. C. Pickel; J. H. Adams; and E. C. Smith. Rate prediciton for single event effects. *IEEE Trans. Nucl. Sci.*, 39(6):1577–1599, December 1992.

[112] D. Hansen; D. Czajkowski; and B. Vermeire. Proton cross-sections from heavy-ion data: a review of the models. *Proc. RADECS Conf.*, September 2021.

[113] P. Calvel; C. Barillot; P. Lamothe; R. Ecoffet; S. Duzellier; and D. Falguère. An empirical model for predicting proton induced upsets. *IEEE Trans. Nucl. Sci.*, 43(6):2827–2832, December 1996.

[114] B. Doucin; T. Carriere; C. Poivey; P. Garnier; J. Beaucour; and Y. Patin. Model of single event upsets induced by space protons in electronic devices. *Proc. of the RADECS Conf.*, September 1995.

[115] R. Ecoffet; and S. Duzellier. Estimation of latch-up sensitive thickness and critical energy using large inclination heavy ion beams. *IEEE Trans. Nucl. Sci.*, 44(6):2378–2385, December 1997.

[116] V. Pouget; P. Fouillat; D. Lewis; H. Lapuyade; F. Darracq; and A. Touboul. Laser cross section measurement for the evaluation of single-even effects in integrated circuits. *Microelectron. Reliab.*, 40(8):1371–1375, August 2000.

[117] A. J. Burnell; A. M. Chugg; R. Harboe-Sorensen. Laser SEL sensitivity mapping of SRAM cells. *IEEE Trans. Nucl. Sci.*, 57(4):1973–1977, August 2010.

[118] E. Faraud; V. Pouget; K. Shao; C. Larue; F. Darracq; D. Lewis; A. Samaras; F. Bezerra; E. Forfevre; and R. Ecoffet. Investigation on the SEL sensitive depth of an SRAM using linear and two-photon absorption laser testing. *IEEE Trans. Nucl. Sci.*, 58(6):2637–2643, December 2011.

[119] N. A. Dodds; N. C. Hooten; R. A. Reed; R. D. Schrimpf: J. H. Warner; N. J.-H. Roche; D. McMorrow; S. Buchner; S. Jordan; J. A. Pellish; W. G. Bennett; N. J. Gaspard; and M. P. King. SEL-sensitive area mapping and the effects of reflection and diffraction from metal lines on laser SEE testing. *IEEE Trans. Nucl. Sci.*, 60(4):2550–2558, August 2013.

[120] Y.-T. Yu; J.-W. Wan; G.-Q. Feng; M.-H. Cai; and R. Chen. Correction of single-event latchup rate prediction using pulsed laser mapping test. *IEEE Trans. Nucl. Sci.*, 62(2):565–570, April 2015.

[121] P. Wang; A. L. Stenberg; J. A. Kozub; E. X. Zhang; N. A. Dodds; S. L. Jordan; D. M. Fleetwood; R. A. Reed; R. D. Schrimpf. Analysis of TPA pulsed-laser-induced single-event latchup sensitive-area. *IEEE Trans. Nucl. Sci.*, 65(1):2502–509, January 2018.

[122] P. Wang; A. L. Stenberg; D. B. Sierawski; E. X. Zhang; K. M. Warren; A. M. Tonigan. R. M. Brewer: N. A. Dodds; G. Vizkelethy; S. L. Jordan; D. M. Fleetwood; R. A. Reed; and R. D. Schrimpf. Sensitive-volume model of single-event latchup for a 180-nm SRAM test structure. *IEEE Trans. Nucl. Sci.*, 67(9):2015–2020, September 2020.

[123] CERN. CHARM toolkit. *https://charmtoolkit.web.cern.ch/*, February 2021.

[124] Y. Morilla; P. Martin-Holgado; A. Romero; J. A. Labrador; B. Fernandez; J. Praena; A. Lindoso; M. Garcia-Valderas; M. Pena-Fernandez; and L. Entrena. Progress of CNA to become the spanish facility for combined irradiation testing in aerospace. *Proc. RADECS Conf.*, pages 250–254, September 2018.

[125] C. Cazzaniga; R. Garcia-Alia; M. Kastriotou; M. Cecchetto; P. Fernandez-Martinez; and C. D. Frost. Study of deposited energy spectra in silicon by high-energy neutron and mixed fields. *IEEE Trans. Nucl. Sci.*, 67(1):175–180, January 2020.

[126] A. Coronetti; C. Cazzaniga; and R. Garcia-Alia. RADSAGA test report 07 v1.1 CNA. *EDMS document 2215710*, July 2020.

[127] E. R. van der Graaf; R. W. Ostendorf; M. J. van Goethem; H. H. Kiewiet; M. A. Hofstee; and S. Brandenburg. AGORFIRM, the AGOR facility for irradiations of material. *Proc. RADECS Conf.*, pages 451–454, September 2009.

[128] A. Coronetti; D. Soderstron; J. Wang; I. Lopes. RADSAGA test report 12 v1.1 KVI. *EDMS document 2339432*, March 2021.

[129] W. Hajdas; L. Desorgher; K. Deiters; D. Reggiani; T. Rauber; M. Tulej; P. Wurz; M. Luethi; K. Wojczuk; and P. Kalaczynski. High energy electron radiation exposure facility at PSI. *Journal of Applied Mathematics and Physics*, 2:910–917, August 2014.

[130] A. Coronetti and D. Söderström. RADSAGA test report 03 v1.3 PSI. *EDMS document 2133326*, March 2020.

[131] W. Hajdas; F. Burri; C. Eggel; R. Harboe-Sorensen; and R. de Marino. Radiation effects testing facilities in psi during implementation of the PROSCAN project. *IEEE Radiation Effects Data Workshop*, pages 160–164, January 2002.

[132] A. Virtanen; R. Harboe-Sorensen; A. Javanainen; H. Kettunen; H. Koivisto; and I. Riihimaki. Upgrades for the RADEF facility. *IEEE Radiation Effects Data Workshop*, pages 38–41, 2007.

[133] H. Kettunen; V. Ferlet-Cavrois; P. Roche; M. Rossi; A. Bosser; G. Gasio'; F.-X. Guerre; J. Jaatinen; A. Javanainen; F. Lochon; and A. Virtanen. Low energy protons at RADEF - application to advanced eSRAMs. *IEEE Radiation Effects Data Workshop*, 2014.

[134] A. Coronetti; M. Cecchetto; J. Wang; M. Tali; P. Fernandez-Martinez; M. Kastriotou; A. Papadopoulou; K. Bilko; F. Castellani; M. Sacristan; R. Garcia-Alia; C. Cazzaniga; Y. Morilla; P. Martin-Holgado; M. J. van Goethem; H. Kiewiet; E. van der Graaf; S. Brandenburg; W. Hajdas; L. Sinkunaite; M. Marszalek; H. Kettunen; M. Rossi; J. Jaatinen; A. Javanainen; M.-H. Moscatello; A. Dubois; S. Fiore; G. Bazzano; C. Frost; M. Letiche; W. Farabolini; A. Gilardi; R. Corsini; and H. Puchner. SEU characterization of commercial and custom-designed SRAMs based on 90-nm technology and below. *IEEE Radiation Effects Data Workshop*, pages 56–63, December 2020.

[135] R. Harboe-Sorensen; C. Poivey; N. Fleurinck; K. Puimege; A. Zadeh; F.-X. Guerre; F. Lochon; M. Kaddour; L. Li; D. Walter; A. Keating; A. Jaksic; and M. Poizat. The technology demonstration module on-board PROBA-II. *IEEE Trans. Nucl. Sci.*, 58(3):1001–1007, June 2011.

[136] D. F. Heidel; P. W. Marshall; J. A. Pellish; K. P. Rodbell; K. A. LaBel; J. R. Schwank; S. E. Rauch; M. C. Hakey; D. Berg; C. M. Castaneda; P. E. Dodd; M. R. Friendlich; A. D. Phan; C. M. Seidleck; M. R. Shaneyfelt; and M. A. Xapsos. Single event upsets and multiple bit upsets on a 45 nm SOI SRAM. *IEEE Trans. Nucl. Sci.*, 56(6):3499–3504, December 2009.

[137] J. Wang; J. Prinzie; A. Coronetti; and P. Leroux. Study of the SEU sensitivity of an SRAM-based radiation monitor in a 65-nm CMOS technology. *IEEE Trans. Nucl. Sci.*, 68(5):913–920, May 2021.

[138] D. M. Fleetwood. Radiation effects in a post-Moore world. *in NSREC Short Course*, December 2020.

[139] G. M. Swift. SEE testing lessons from Dickens, Scounting and Oz. *SEE Symposium Conf.*, May 2006.

[140] B. Ye; J. Liu; T. S. Wang; T. Q. Liu; K. Maaz; J. Luo; B. Wang; Y. N. Yin; Q. G. Ji; Y. M. Sun; M. D. Hou. Low energy proton induced single event upset in 65 nm DDR and QDR commercial SRAMs. *Nucl. Instr. and Methods in Phys. Res. B*, 406:443–448, September 2017.

[141] NIST National Institute of Standards and Technology. PSTAR. *https://physics.nist.gov/PhysRefData/Star/Text/PSTAR.html*, May 2020.

[142] G. Gasiot; D. Giot; and P. Roche. Multiple cell upsets as the key contribution to the total SER of 65 nm CMOS SRAMs and its dependence on well engineering. *IEEE Trans. Nucl. Sci.*, 54(6):2468–2473, December 2007.

[143] G. Tsiligiannis; L. Dilillo; A. Bosio; P. Girard; S. Pravossoudotovitch; A. Todri; A. Virazel; H. Puchner; C. Frost; F. Wrobel; and F. Saigné. Multiple cell upsets classification in commercial SRAMs. *IEEE Trans. Nucl. Sci.*, 61(4):1747–1754, August 2014.

[144] A. Bosser; V. Gupta; G. Tsiligiannis; A. Javanainen; H. Kettunen; H. Puchner; F. Saigné; A. Virtanen; F. Wrobel; and L. Dilillo. Laser SEL sensitivity mapping of SRAM cells. *IEEE Trans. Nucl. Sci.*, 62(6):2620–2626, December 2015.

[145] D. Giot; P. Roche; G. Gasiot; J.-L. Autran; and R. Harboe-Sorensen. Heavy ion testing and 3d simulations of multiple cell upsets in 65nm standard SRAMs. *Proc. of RADECS Conf.*, 2007.

[146] WikiChip. 65 nm litography process. *https://en.wikichip.org/wiki/65_nm_litography_process*, January 2021.

[147] M. Cecchetto; R. Garcia-Alia; F. Wrobel; M. Tali; O. Stein; G. Lerner; K. Bilko; L. Esposito; C. Bahamonde-Castro; Y. Kadi; S. Danzeca; M. Brucoli; C. Cazzaniga; M. Bagatin; S. Gerardin; and A. Paccagnella. Thermal neutron-induced SEUs in the LHC accelerator environment. *IEEE Trans. Nucl. Sci.*, 67(7):1412–1420, July 2020.

[148] M. Tali. Single-event radiation effects in hardened and state-of-the-art components for space and high-energy accelerator applications. *PhD Dissertation, Department of Physics, University of Jyväskylä, Finland*, 2019.

[149] A. Fassò; A. Ferrari; J. Ranft; and P. R. Sala. FLUKA: performances and applications in the intermediate energy range. *Proc. 1st AEN/NEA Specialists' Meeting on Shielding Aspects of Accelerators, Targets and Irradiation Facilities (SATIF)*, pages 287–304, April 1994.

[150] A. Fassò; A. Ferrari; J. Ranft; and P. R. Sala. An update about FLUKA. *Proc. 2nd Workshop on Simulating Accelerator Radiation Environment*, pages 158–170, October 1997.

[151] A. Ferrari; J. Ranft; S. Roesler; and P. R. Sala. Cascade particles, nuclear evaporation, and residual nuclei in high energy hadron-nucleus interactions. *Zeitschrift für Physik C Particles and Fields*, 70:413–426, January 1996.

[152] J. R. Schwank; M. R. Shaneyfelt; J. Baggio; P. E. Dodd; J. A. Felix; V. Ferlet-Cavrois; P. Paillet; D. Lambert; F. W. Sexton; G. L. Hash; and E. Blackmore. Effects of particle energy on proton-induced single-event latchup. *IEEE Trans. Nucl. Sci.*, 52(6):2622–2629, December 2005.

[153] C. Weulersee; N. Guibbaud; A.-L. Beltrando; J. Galinat; C. Beltrando; F. Miller; P. Trochet; and D. Alexandrescu. Preliminary guidelines and predictions for 14-MeV neutron SEE testing. *IEEE Trans. Nucl. Sci.*, 64(8):2268–2275, August 2017.

[154] J. R. Schwank; M. R. Shaneyfelt; J. Baggio; P. E. Dodd; J. A. Felix; V. Ferlet-Cavrois; P. Paillet; G. K. Lum; S. Girard; and E. Blackmore. Effects of angle of incidence on proton and neutron-induced single-event latchup. *IEEE Trans. Nucl. Sci.*, 53(6):3122–3131, December 2006.

[155] R. D. McKeown; S. J. Sanders; J. P. Schiffer; H. E. Jackson; M. Paul; J. R. Specht; E. J. Stephenson; R. P. Redwine; R. E. Segel. Inclusive reactions of pions on nuclei. *Physical Review C*, 24(1):211–220, July 1981.

[156] C. Cazzaniga; M. Bagatin; S. Gerardin; A. Costantino; and C.D. Frost. First tests of a new facility for device-level, board-level and system-level neutron irradiation of microelectronics. *IEEE Trans. Emerg. Topics Comput.*, 9(1):104–108, March 2021.

[157] R. Garcia-Alia. Radiation fields in high energy accelerators and their impact on single event effects. *PhD Dissertation, Institute d'Électronique et des Systèmes, Université de Montpellier*, 2013.

[158] V. S. Anashin; A. S. Kuznetsov; A. E. Kozyukov; L. R. Bakirov; A. A. Kazyakin; and K. A. Artemyev. Compilation of electronic components SEE test results. *IEEE Radiation Effect Data Workshop*, July 2013.

[159] S. Uznanski; B. Todd; A. Dinius; Q. King; K. Motala; M. Brugger; G. Spiezia; and E. Gousiou. SEE and TID test results of candidate electronics for LHC power converter control. *IEEE Radiation Effects Data Workshop*, July 2013.

[160] M. V. O'Bryan; D. Chen; M. J. Campola; M. C. Casey; A. D. Topper; K. A. LaBel; J. A. Pellish; J.-M. Lauenstein; R. A. Gigliuto; E. P. Wilcox; R. L. Ladbury; M. Berg; and R. R. Davies. Compendium of current single event effects for candidate spacecraft electronics for NASA. *IEEE Radiation Effects Data Workshop*, July 2013.

[161] V. S. Anashin; A. E. Koziukov; A. A. Kazyakin; A. S. Kuznetsov; L. R. Bakirov; V. S. Korolev; K. A. Artemyev; and K. Z. Faradian. SEE test results of electronic components performed on Roscosmos test facilities. *IEEE Radiation Effect Data Workshop*, July 2014.

[162] G. V. Chukov; V. V. Elesin; G. N. Nazarova; A. Y. Nikiforov; D. V. Boychenko; V. A. Telets; A. G. Kuznetsov; K. M. Amburkin. SEE testing results for RF and microwave ICs. *IEEE Radiation Effects Data Workshop*, July 2014.

[163] G. R. Allen; l. Z. Scheick; F. Irom; S. M. Guertin; P. C. Adell; M. Amrbar; S. Vartanian; M. O'Connor. 2015 compendium of recent test results of single event effects conducted by the Jet Propulsion Laboratory's radiation effects group. *IEEE Radiation Effect Data Workshop*, pages 54–66, July 2015.

[164] M. V. O'Bryan; K. A. LaBel; D. Chen; M. J. Campola; M. C. Casey; J.-M. Lauenstein; J. A. Pellish; R. L. Ladbury; and M. Berg. Compendium of current single event effects for candidate spacecraft electronics for NASA. *IEEE Radiation Effects Data Workshop*, July 2015.

[165] F. Irom; S. Vartanian; and G. Allen. Single-event latchup measurements on wireless and powerline network communication devices for use in Mars missions. *IEEE Radiation Effects Data Workshop*, July 2018.

[166] S. C. Davis; D. J. Mabry; R. Koga; and J. S. George. SEE and TID testing of components for the near infrared airglow camera (NIRAC). *IEEE Radiation Effects Data Workshop*, July 2018.

[167] A. C. Daniel; and G. Allen. Heavy-ion test results of several commercial components for use in class D interplanetary mission payload. *IEEE Radiation Effects Data Workshop*, July 2018.

[168] C. Virmontois; J.-M. Belloir; M. Beaumel; A. Vriet; N. Perrot; C. Sellier; J. Bezine; D. Gambart; D. Blain; E. Garcia-Sanchez; W. Mouallem; and A. Bardoux. Dose and single event effects on a color CMOS camera for space exploration. *IEEE Trans. Nucl. Sci.*, 66(1):104–110, January 2019.

[169] A. C. Daniel; S. Vartanian; and G. R. Allen. Radiation effects characterization of commercial multi-channel digital to analog converters for spaceflight applications. *IEEE Radiation Effects Data Workshop*, July 2019.

[170] S. C. Davis; D. J. Mabry; A. D. Yarbrough; R. Koga; A. W. Wright; C. A. Langford; and J. S. George. The Aerospace Corporation's compendium of recent single event effect results. *IEEE Radiation Effects Data Workshop*, July 2019.

[171] C. H. Pham; D. F. Caughran; and J. J Likar. Compendium of recent radiation test results from the Johns Hopkins University applied physics laboratory. *IEEE Radiation Effects Data Workshop*, July 2019.

[172] J. Budroweit; M. Jaksch; R. Garcia-Alia; A. Coronetti; and A. Koelpin. Heavy ion induced single event effects characterization on an RF-agile transceiver for flexible multiband radio systems in NewSpace avionics. *MDPI Aerospace*, 7(2):14, February 2020.

[173] S. C. Davis; D. J. Mabry; A. D. Yarbrough; R. Koga; K. S. MacGowan; J. R. Scarpulla; V. T. Hunt; A. W. Wright; and J. L. Taggart. The Aerospace Corporation's compendium of recent radiation effect results. *IEEE Radiation Effects Data Workshop*, December 2020.

[174] S. Vartanian; F. Irom; G. R. Allen; W. P. Parker; M. D. O'Connor. Single event latchup results for COTS devices used on SmallSat missions. *IEEE Radiation Effects Data Workshop*, December 2020.

[175] R. L. Ladbury. Risk methodology for SEE caused by proton-induced fission of high-Z materials in microelectronics packaging. *IEEE Trans. Nucl. Sci.*, 67(6):1152–1160, June 2020.

INCLUDED ARTICLES

Publication I

A. Coronetti, R. García Alía, M. Cecchetto, W. Hajdas, D. Söderström, A. Javanainen, and F. Saigné, "The pion single event effect resonance and its impact in an accelerator environment," *IEEE Trans. Nucl. Sci.*, vol. 67, no. 7, pp. 1606-1613, July 2020.

© 2020, Coronetti et al., licensed under CC BY 4.0.

The Pion Single-Event Effect Resonance and Its Impact in an Accelerator Environment

Andrea Coronetti, Rubén García Alía, Matteo Cecchetto, Wojtek Hajdas, Daniel Söderström,
Arto Javanainen, and Frédéric Saigné

***Abstract*— The pion resonance in the nuclear reaction cross section is seen to have a direct impact on the single-event effect (SEE) cross section of modern electronic devices. This was experimentally observed for single-event upsets and single-event latchup. Rectangular parallelepiped (RPP) models built to fit proton data confirm the existence of the pion SEE cross-section resonance. The impact on current radiation hardness assurance (RHA) soft error rate (SER) predictions is, however, minimal for the accelerator environment since this is dominated by high neutron fluxes. The resonance is not seen to have a major impact on the high-energy hadron equivalence approximation established for testing in mixed-field facilities.**

***Index Terms*— Accelerator, cross section, FLUKA, neutrons, pions, protons, radiation hardness assurance (RHA), single-event effect (SEE), soft error rate (SER).**

I. INTRODUCTION

ALIKE protons and neutrons, pions can interact with silicon nuclei by inelastic collisions. The consequent indirect energy deposition along the recoil ionization track can lead to single-event effects (SEEs) in electronic devices. The pion soft error rate (SER) is expected to be similar or higher than those from proton and neutron indirect energy depositions. The potentially higher SER from pions is due to the resonance in the inelastic collision reaction cross section in the 100–250-MeV energy region [1]. Typically, the p–Si interaction has a reaction cross section of 400 mb in this energy region. In the resonance, the π–Si interaction can reach up to 800 mb.

Pions differ from protons and neutrons because they are lighter (rest mass 139.47 MeV/c^2) and they can have positive, negative, or neutral charge. The inelastic collision mechanism is dominant when it comes to SEE generation. However, negative pions can also be absorbed by the nucleus. The consequent deexcitation leads to secondary emission of particles capable of causing SEEs. Different from protons and neutrons, charged pions decay into muons or electrons within a few nanoseconds. Neutral pions decay even faster, making their flux completely negligible.

With such a short lifespan, pions can provide an important contribution to the SER only if electronic devices are located nearby pion generation points. This is the case of particle accelerators where electronics is subject to pion fluxes in amounts comparable to those of protons and neutrons [2], [3]. Pions can also be found in the atmospheric environments since they are part of the cosmic ray cascade, which is responsible for the formation of high neutron and muon fluxes. Most of the muons in the atmosphere are generated by the decay of pions. The pion fluxes in the atmosphere are more important at higher altitudes [4], but these fluxes are still a few orders of magnitude lower than those of neutrons.

Even when pion fluxes are important, the standard radiation hardness assurance (RHA) approach is to assume that pion SEE cross sections are identical to those of protons and neutrons at energies above 20 MeV. For this reason, the 200-MeV proton data point is commonly used to predict the mixed-field SER in the accelerator [5]. Not many experimental radiation data for pion-induced SEE exist in the literature, and none of such experiments was performed within the last 15 years, despite the emerging challenges introduced by recent deep submicrometer technologies. The existing radiation data are also rather contrasting. A first work on dynamic random access memories (DRAMs) single-event upsets (SEUs) [6] pointed out a quite predominant increase in the pion SEU cross section when compared to that of protons. Depending on the technology employed by the different manufacturers, the pion cross section was found to be as high as three times that of protons. A second work on static random access memories (SRAMs) and DRAMs' SEUs [7], though showing that the reaction cross-section resonance is somewhat reflected in an increase in the SER, still shows that this increase is much less pronounced. Thus, no conclusion concerning a pion enhancement of the SER was confirmed.

This article aims at extending the knowledge about the pion reaction resonance and its possible effects on the SER in the mixed field. Experimental data collected at the Paul Scherrer Institute (PSI) with monoenergetic pion beams show that the pion SEE cross section of commercial SRAMs is typically higher than the proton SEE cross sections at energies above 75 MeV. The experimental investigation dealt not only with SEUs but also with single-event latchups (SELs). The pion reaction resonance was investigated through FLUKA2011

Manuscript received November 28, 2019; revised January 27, 2020 and February 9, 2020; accepted February 29, 2020. Date of publication March 4, 2020; date of current version July 16, 2020. This work was supported by the European Union's Horizon 2020 Research and Innovation Programme through the Marie Sklodowska-Curie (MSC) under Grant 721624.

Andrea Coronetti, Rubén García Alía, and Matteo Cecchetto are with CERN, 1211 Geneva, Switzerland (e-mail: andrea.coronetti@cern.ch).

Wojtek Hajdas is with the Paul Scherrer Institute, Forschungsstrasse 111, 5232 Villigen, Switzerland.

Daniel Söderström and Arto Javanainen are with the Jyväskylän Yliopisto, 40500 Jyväskylä, Finland.

Frédéric Saigné is with the Institut d'Électroniqe et des Systèmes, Université de Montpellier, 34090 Montpellier, France.

Color versions of one or more of the figures in this article are available online at http://ieeexplore.ieee.org.

Digital Object Identifier 10.1109/TNS.2020.2978228

This work is licensed under a Creative Commons Attribution 4.0 License. For more information, see https://creativecommons.org/licenses/by/4.0/

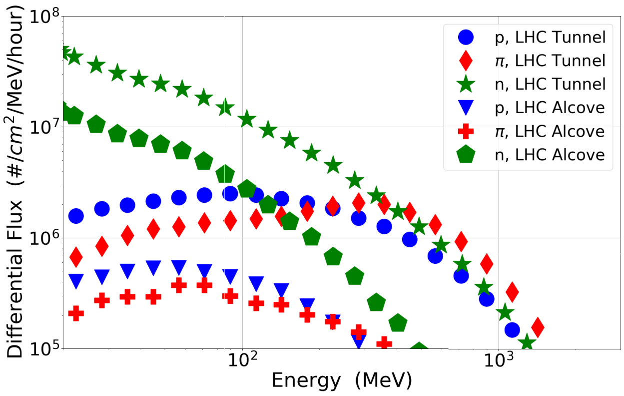

Fig. 1. Pion, proton, and neutron differential fluxes in typical accelerator mixed-field environment for two CHARM configurations representative of the LHC tunnel and the shielded alcoves [11].

2x.6 Mar 19 [8] simulations to understand why pions have a higher probability of inducing SEEs over the wide range of technological processes under analysis. The fundamental implications for RHA SER predictions of accelerator electronics are reasserted to account for this effect. The impact on the high-energy hadron (HEH) equivalence [3] for mixed-field SER predictions is also reassessed.

II. High-Energy Accelerator Environment

Along with protons and neutrons, pions are an important contributor to the overall mixed-field environment typical of the CERN accelerator complex. They are released over a widespread energy spectrum by the high-energy spallation reactions (production threshold energy = 141 MeV [9]) of the primary proton beam at the interaction points in p–p collisions [10] but also in collisions with beam intercepting devices (e.g., collimators) and with the residual gas in the vacuum pipes.

Fig. 1 shows a comparison of the pion, proton, and neutron differential energy spectra for a typical CERN Highly AcceleRated Mixed-field facility (CHARM) [12] configuration representative of the large hadron collider (LHC) tunnel and the shielded alcoves. The graph shows that the differential pion flux is similar to the proton flux. However, the peak pion flux is located between 300 MeV and 1 GeV, i.e., above the resonance region.

Table I reports on the hadronic abundance of each type of hadron and only accounts for energies above 20 MeV. This is the minimum energy that charged pions and protons must have to overcome the Coulomb barrier (when considering also their energy loss through standard microelectronic packaging structures). When it comes to SEEs, neutrons tend to dominate most of the accelerator relevant environments. However, in R13, the pion abundance is very similar to that of neutrons. This position is used for the qualification of equipment to be located in very energetic radiative environments at CERN.

Traditionally, electronic systems used at CERN are qualified at CHARM because of its environment representativeness. Component qualification is alternatively performed using monoenergetic proton beams or neutron spallation sources. While the latter is quite similar to the CHARM qualification approach, monoenergetic proton testing covers only a small part of the actual spectrum. These monoenergetic data are then used to account also for the pion flux, under the assumption that the pion SEE cross section can be considered equivalent to that of protons.

TABLE I

Hadronic Abundance of HEHs ($E > 20$ MeV) for Some Test Positions Inside CHARM [11]. All Charged Pions Are Grouped Together

Position	Pions	Protons	Neutrons	Kaons
R5	15.7%	13.8%	69.9%	0.6%
R10	22.7%	17.3%	58.9%	1.1%
R13	37.0%	20.2%	42.8%	0.0%

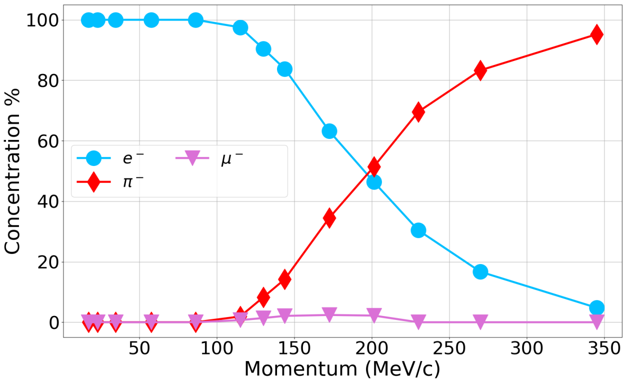

Fig. 2. Concentration of electrons, pions, and muons for negative polarity in percentage as a function of the momentum. Measurements performed with time-of-flight measurements [15].

III. Experimental Investigation

The experimental investigation focuses on SRAMs since these memories are widely used for the detection of radiation levels in the CERN LHC accelerator complex [13], as well as, in actual accelerator equipment designs exposed to radiation [14]. Since SRAMs are used to determine the HEH fluence in the mixed field, a direct assessment of their response to monoenergetic pions and protons was the best option.

A. Facilities

The PSI offers a wide range of particle beams for radiation to electronics effects' studies. Pions are produced at the piM1 facility [15] by the nuclear spallation of a 590-MeV proton monoenergetic beam from the high-intensity proton accelerator on a target. The secondary particles that are transported at the test position are pions, electrons, and muons. Pions can be found only with a momentum ranging from 115 to 345 MeV/c. However, the beam is not fully composed of pions, but its composition changes with the momentum. Fig. 2 shows the time-of-flight measurements performed by the facility to determine the beam composition at various momenta. Data were also extracted for the used momenta (130, 200, 270, and 345 MeV/c), which correspond, respectively, to 51, 104, 164, and 233 MeV in terms of pion energy.

The particles momentum is selected by a double bending magnet structure. The dosimetry instruments cannot differentiate among particles, and therefore, the beam compositions reported in Fig. 2 have to be accounted for when considering the actual flux of pions at the device under test (DUT). The maximum pion flux that can be extracted is 3×10^6 $\pi^-/\mathrm{cm}^2/\mathrm{s}$ at 233 MeV, but it gets as low as 5×10^4 $\pi^-/\mathrm{cm}^2/\mathrm{s}$ at 51 MeV.

Even for such cases when the beam is mostly composed of electrons (90% at 51 MeV), it is assumed that all the recorded events are induced by pions since electrons have SEU and SEL cross sections, which are at least three orders of magnitude lower [16].

Given the wide flux range, it was not possible to perform flux measurements at the facility using a single set of instruments. Three different methods were employed for pion flux logging. A first method, used for high energy (>100 MeV) and high flux ($>5 \times 10^5$ $\pi^-/\mathrm{cm}^2/\mathrm{s}$), made use of an ionization chamber positioned at the beam exit just before the DUT. A second method, used for lower energy beams (51 MeV only), made use of the proton current measurements upstream the spallation target which were converted into a pion flux by calibration with a scintillator. A final method, employed for high-energy beams (>100 MeV) and low flux ($<5 \times 10^5$ $\pi^-/\mathrm{cm}^2/\mathrm{s}$), consisted in measuring the beam intensity from the current produced by a scintillator. This was first located in place of the DUT for calibration means and then positioned behind the DUT during the tests.

Considering the uncertainties on the beam composition measurements and the use of various sets of instruments to retrieve the flux, a global uncertainty of ±20% on the beam fluence is accounted for the cross-sectional error bars. The spatial homogeneity of the beam (±10%) was attained only for a spot size with 10 mm diameter and was measured using a pixelated ionization chamber.

Proton testing has been performed at the Kernfysisch Versneller Instituut (KVI-CART facility) and the proton irradiation facility (PIF) in PSI. For KVI-CART, the same cyclotron can be tuned to provide protons with a primary energy of 190 or 66.5 MeV. The PIF cyclotron can accelerate proton up to a primary energy of 230 MeV. At both cyclotrons, the primary energies were also degraded into lower and intermediate energies (30–164 MeV) using aluminum or copper slabs of several thicknesses. For proton irradiation, the experiments were conducted using fluxes in the order of 10^7 $\mathrm{p/cm}^2/\mathrm{s}$ for SEU and $3 \times 10^5 - 10^6$ $\mathrm{p/cm}^2/\mathrm{s}$ for SEL. In both facilities, the beam is homogeneous within ±10% over a large area (5–10 cm^2). The beam intensity is monitored with ionization chambers and the fluence is determined within an uncertainty of ±10%.

B. Experimental Results

This study was performed by analyzing the SEE response of a set of six commercial complementary metal–oxide–semiconductor (CMOS) SRAMs with technological nodes varying from 250 to 40 nm. Four of these six memories were characterized against their SEU response, whereas the other two were known to have a relatively high SEL proton cross section that could be relevant for the limited pion flux available. The main data about these memories are reported in Table II. The first three SRAMs in Table II were irradiated lid-off, and the last three were irradiated lid-on. This is not expected to have a significant impact on the beam energy with these particles. The same date codes were irradiated with both protons and pions. In some cases, exactly, the same part was irradiated.

TABLE II

LIST OF TESTED DEVICES AND THEIR FEATURES

Reference	Array size, Mbits	Technology	Lid
AT86166H-YM20-E	4	250nm	off
CY62157EV30LL-45ZSXI	8	90nm	off
CY62167EV30LL-45ZXA	16	90nm	off
IS61WV204816BLL	32	40nm	on
BS62LV1600EIP55	16	180nm	on
LY62W20488ML	16	180nm	on

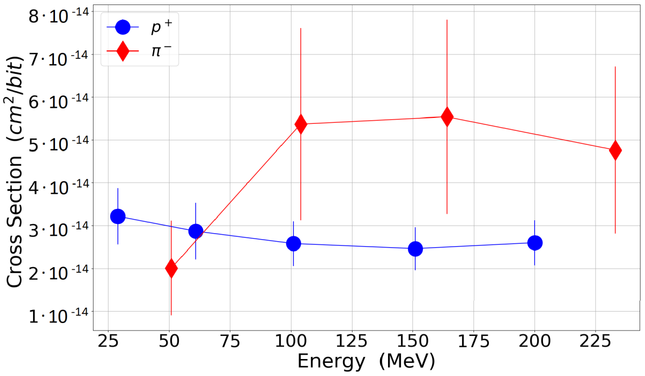

Fig. 3. Pion and proton SEU cross section for the Atmel SRAM with 95% confidence level error bars.

The same test logic was applied to both pion and proton irradiations. For SEU measurements, the SRAMs were programmed with a checkerboard pattern and a fixed fluence of 10^{10} π^-/cm^2 ($\mathrm{p/cm}^2$) was targeted. This was sufficient to accumulate a statistically valuable amount of upsets. For SEL measurements, the test was stopped once at least 100 events had been observed. Tests were performed only at room temperature and within the datasheet nominal voltage. The current threshold was set to 10 mA with a hold time of 0.6 s and a reset time of 0.9 s.

All SRAMs have been irradiated under negative pions at four energies ranging from 51 to 233 MeV. For protons, four to six energies were selected in the 30–200-MeV range.

A direct comparison of proton and pion SEU cross sections is available in Figs. 3–6 for each of the commercial references previously listed. No matter the actual sensitivity of the single part, the technological process or the fact that they were lid-on or lid-off, all the data point out that the pion cross section at energies above 75 MeV is about a factor of 1.5–2.5 higher than its proton counterpart. Some of the measurements were repeated during a second run and their outcomes were very consistent with the first round of measurements. This seems to indicate that the uncertainty on the fluence is lower than what was shown by the error bars for the pion data.

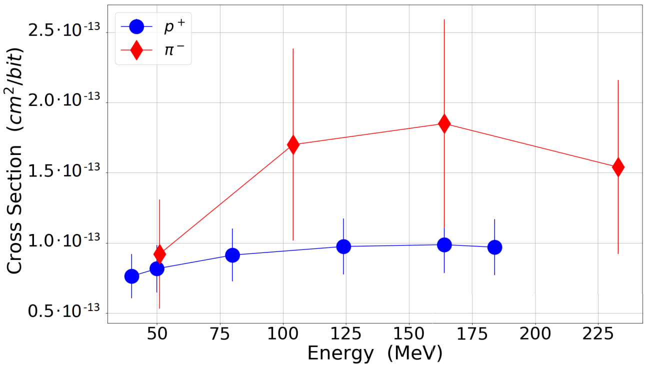

Fig. 4. Pion and proton SEU cross section for the cypress-45ZSXI SRAM with 95% confidence level error bars.

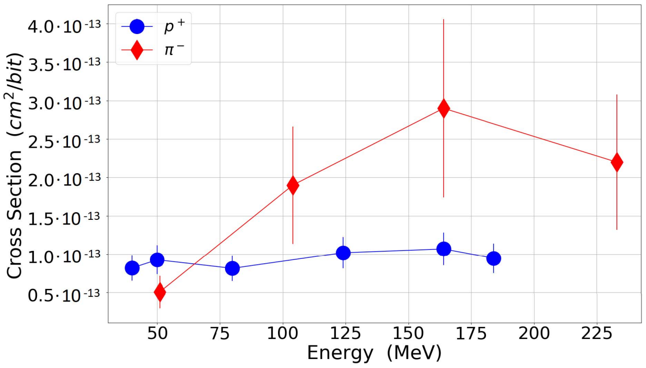

Fig. 5. Pion and proton SEU cross section for the cypress-45ZXA SRAM with 95% confidence level error bars.

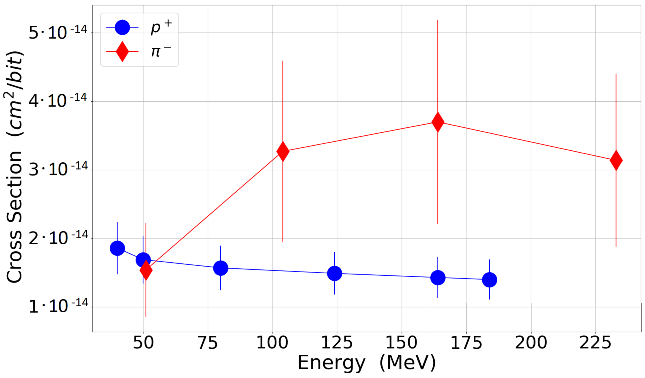

Fig. 6. Pion and proton SEU cross section for the ISSI SRAM with 95% confidence level error bars.

Concerning SEL measurements, data are compared in Figs. 7 and 8. The data seem to confirm the same trend that was observed with SEU for energies above 75 MeV. However, in the SEL case, the cross section does not drop so sharply and it is still higher than that of proton at 51 MeV for both SRAMs by a factor 2 and 3.

IV. SIMULATIONS OF PION SEU CROSS SECTIONS

The numerical data are retrieved through FLUKA-based Monte Carlo simulations. The basis of the simulations stands in finding suitable parameters for the sensitive volume (SV) model that would provide energy deposition events probability whose fitting matches the proton experimental cross section at 184 MeV. The 184-MeV proton point is chosen because it is used for the HEH approximation in mixed field, and for SEU, it is a good reference for the saturation cross section. The attained rectangular parallelepiped (RPP) model size and critical charge are then implemented for the simulations with all other hadrons: charged pions, neutrons, and charged kaons.

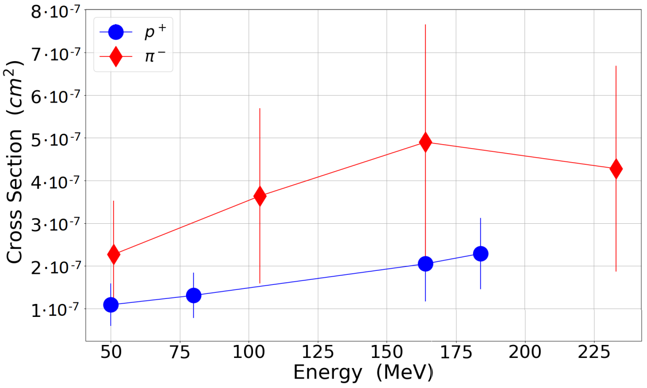

Fig. 7. Pion and proton SEL cross section for the brilliance SRAM with 95% confidence level error bars.

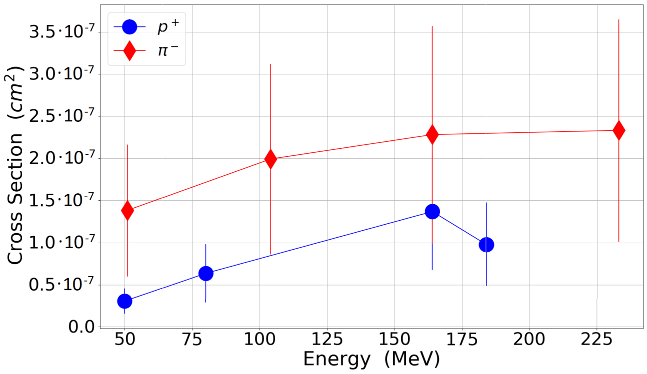

Fig. 8. Pion and proton SEL cross section for the Lyontek SRAM with 95% confidence level error bars.

The analysis focuses on the Integrated Silicon Solution Inc. (ISSI) SRAM, which is a state-of-the-art technology. Its radiation response and RPP modeling were benchmarked in [17]. A critical charge of ≈0.75 fC was found to be suitable in describing direct ionization phenomena from low-energy protons, and it is retained for this article. That article also proposed an SV size of 250 nm for the 40-nm technological node. A back end of line (BEOL) SiO_2 layer 6 μm thick is also added on top of the SV.

In this article, the SV size is taken as the free parameter of the cubic RPP for the high-energy proton data fitting. A side of 310 nm was chosen since it better approximates the 184-MeV proton experimental point, 1.4×10^{-14} cm^2/bit, whereas the 250-nm returned a cross section of 0.9×10^{-14} cm^2/bit. A larger volume better accounts from more spread drift and diffusion collection mechanisms from higher energies. A validation of the proposed model is reported in Fig. 9. The figure shows that both proton and pion experimental cross sections are well reproduced

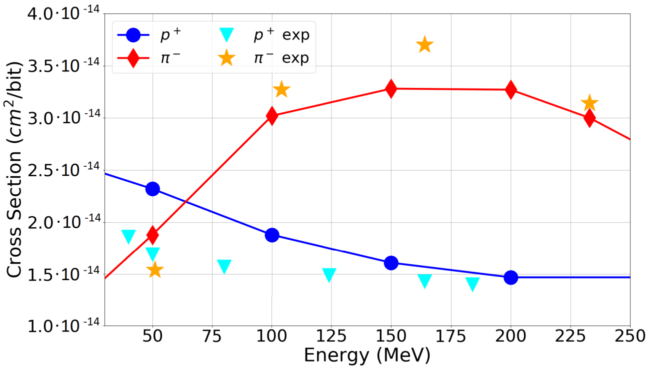

Fig. 9. Simulated cross sections for protons and negative pions and comparison with experimental data for the ISSI memory.

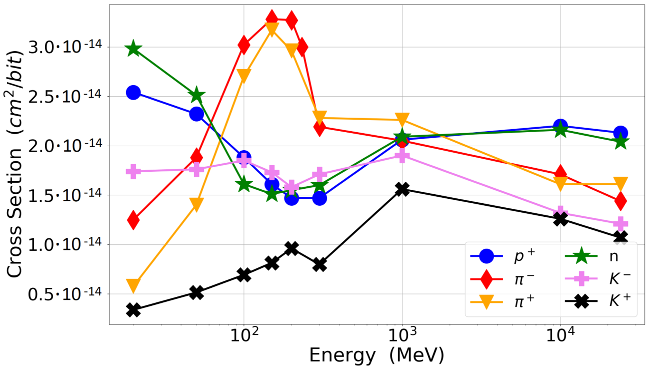

Fig. 10. Simulated cross sections for protons, charged pions, neutrons, and charged kaons over typical CHARM energy distributions for an RPP with 310-nm side and 0.75-fC critical charge.

within a worst case factor 2 for protons at 50 MeV. Discrepancies at this energy are likely due to the presence of the plastic packaging as well as the absence of a detailed BEOL material description. The numerical pion SEU cross sections are calculated within an error of 25% at 100 MeV and 45% at 50 MeV.

The model was run for six particles and nine energies each to cover the 20 MeV–24-GeV energy interval typical of the CHARM mixed field. The data are shown in Fig. 10. According to the simulations, the pion SEU resonance is restricted to the 75–250-MeV region. The resonance peak well reproduces the factor 2 increase, which was experimentally observed.

The pion SEU experimental decrease below 100 MeV is also reproduced by the strong lowering of the simulated pion cross section at 20 and 50 MeV if compared to the enhanced proton and neutron cross sections. However, the 50-MeV pion point has the same magnitude as the 200-MeV proton point. After the numerical results, this simple RPP seems capable of grasping all of the nuclear mechanisms affecting the pion SEU cross section. The use of a nested RPP model [18] did not provide significant differences.

The proposed RPP model with 0.75-fC critical charge and 310-nm size is retained for the later RHA implications since it very well describes the resonance.

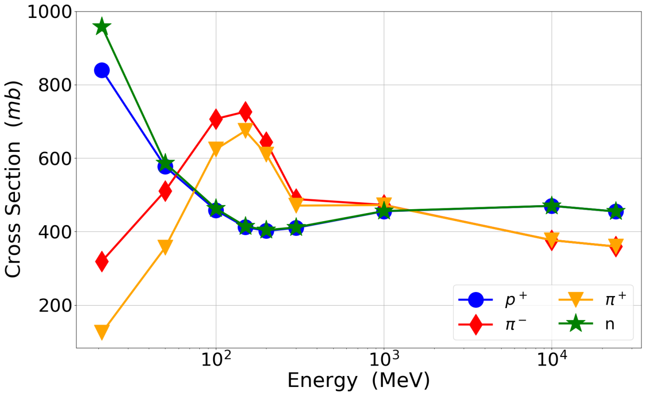

Fig. 11. Reaction cross section in silicon of protons, pions, and neutrons showing a resonance in the 100–250-MeV energy region (obtained from FLUKA).

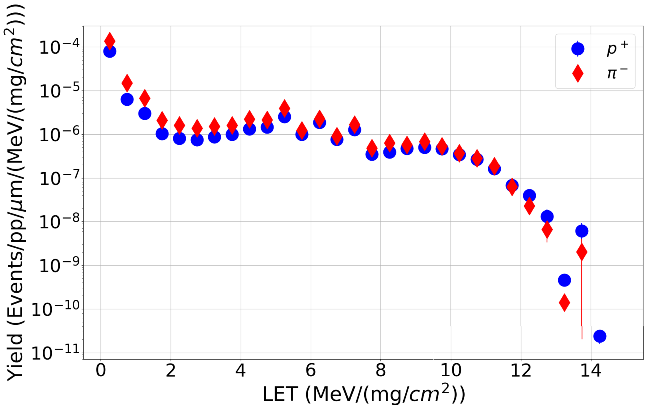

Fig. 12. Yield of secondary ions produced by nuclear reactions as a function of their LET for negative pions and protons at 200 MeV.

V. NUCLEAR INTERACTION MECHANISMS

The observed pion SEE cross-section resonance is the reflection of the nuclear inelastic cross section (see Fig. 11) for these particles. This figure shows that within the concerned energy range, pions have a much higher probability of interacting with the Si nuclei than the other hadrons do.

The characteristics of the secondary ions from π-Si collisions are responsible for the SEU cross section behavior too. Such quantities were scored in FLUKA upon production to quantify the differences between protons and negative pions' secondary recoils. Fig. 12 shows a quantification of the event probabilities per incident particles for various linear energy transfer (LET) intervals at 200 MeV. Pions are twice as effective as protons in generating low LET [<5 MeV/(mg/cm^2)] secondary ions and up to 50% more effective for intermediate LET [<10 MeV/(mg/cm^2)] secondary ions. Similarly, there is an excess of low Z recoils for pions if compared to protons (see Fig. 13). A similar higher fragmentation mechanism with more low LET secondary ions is responsible for the proton and neutron SEU cross-sectional enhancements above 1 GeV.

On the contrary, pion nuclear interactions release a smaller amount of high-Z (and high LET) recoils than protons. At 200 MeV, this yield is not that effective in limiting the

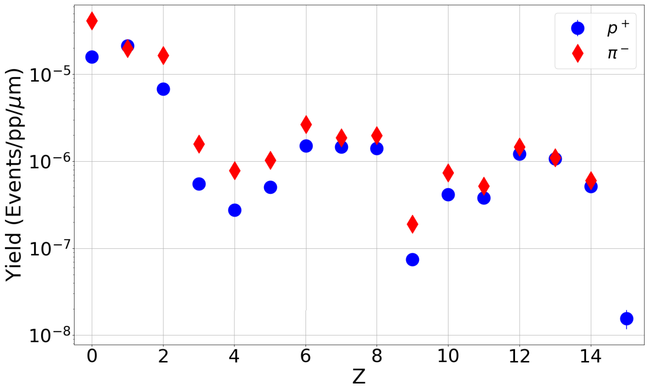

Fig. 13. Yield of secondary ions produced by nuclear reactions as a function of their atomic number for negative pions and protons at 200 MeV.

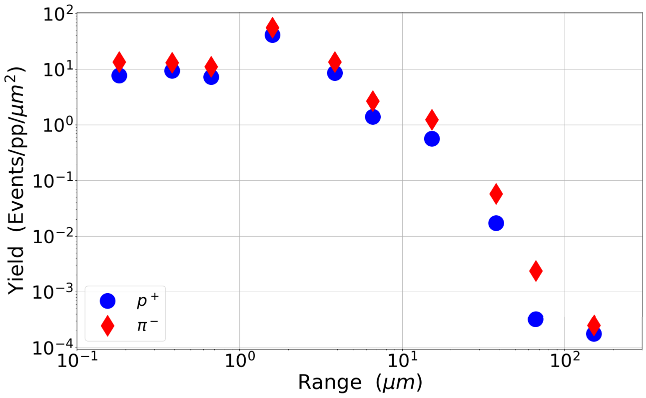

Fig. 14. Yield of secondary ions produced by nuclear reactions as a function of their range for negative pions and protons at 200 MeV.

pion SEU resonance. Fig. 14 also reports on the range of secondary ions having an LET $>$ 1 MeV/(mg/cm^2), which confirms that pion recoils are usually associated with a longer range than proton recoils.

Fig. 15 shows the event probability distribution as a function of LET when the energy of the incident particles is reduced to 50 MeV. The pion yield is very similar to that of protons for low LET secondary ions but becomes $>$50% lower for intermediate and high LET secondary ions. This is further stressed by the comparison of LET distributions of the Si recoils, as shown in Fig. 16. Pions are ineffective in producing these recoils at intermediate and high LET since the kinetic energy content that is imparted to the Si ions is below 100 keV/n. As a result, Si recoils from π–Si interactions above 6 MeV/(mg/cm^2) have negligible probability of being created when compared to the same recoils released by p–Si interaction, which have high production probability up to an LET as high as 12 MeV/(mg/cm^2). Fig. 17 also shows the ranges of the secondary recoils with LET $>$ 1 MeV/(mg/cm^2) at 50 MeV. This figure also shows that even though protons produce a larger number of short-ranged recoils, pions can still produce recoils with quite extended range.

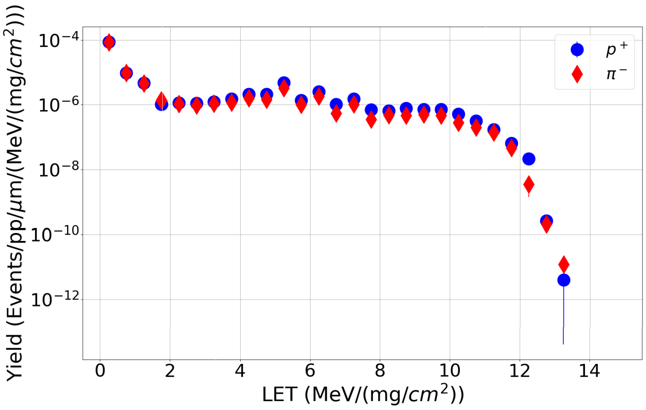

Fig. 15. Yield of secondary ions produced by nuclear reactions as a function of their LET for negative pions and protons at 50 MeV.

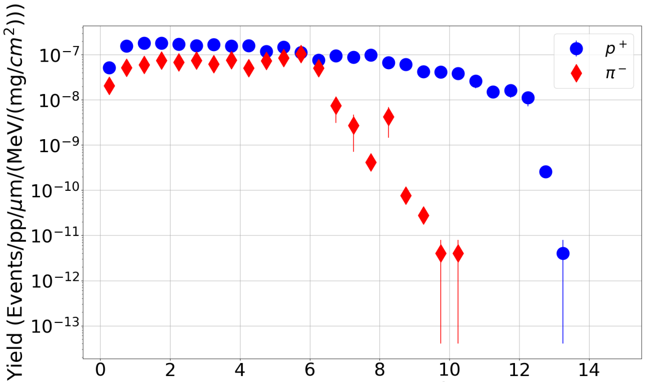

Fig. 16. Yield of secondary ions produced by nuclear reactions as a function of their LET for Si recoils for negative pions and protons at 50 MeV.

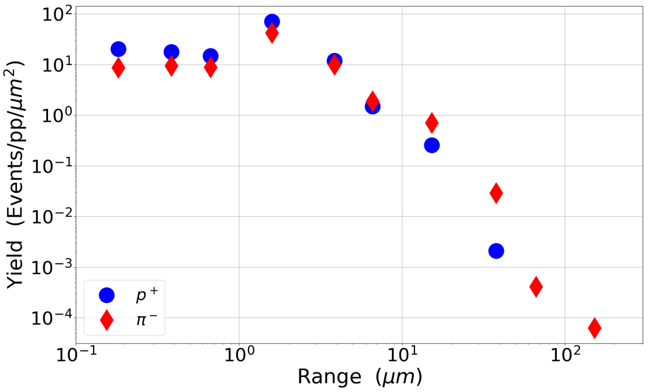

Fig. 17. Yield of secondary ions produced by nuclear reactions as a function of their range for negative pions and protons at 50 MeV.

The excess in low and intermediate LET recoils from $>$100-MeV pions is thus justified by higher π-Si interaction probability and by larger fragmentation of the silicon nuclei. This may also explain why, in previous studies based on older technologies [7], the pion resonance was sometimes not observed. If the heavy-ion LET threshold of the device is indeed higher than 6 MeV/(mg/cm^2), then the enhanced production of low LET secondary ions will not contribute to an increase in the SEU cross section.

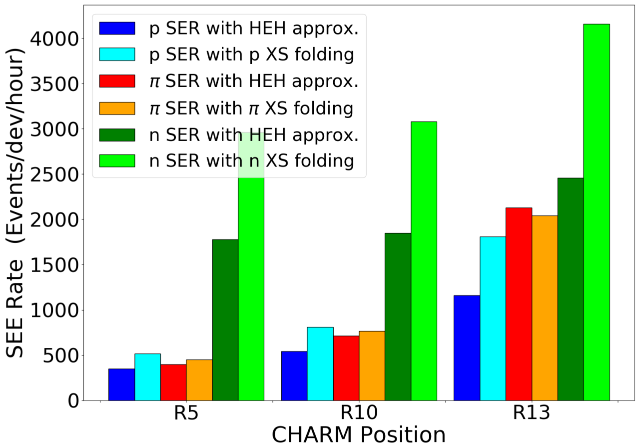

Fig. 18. SER comparison between the HEH approximation approach and the full particle folding approach. Data are reported by the CHARM position and further subdivided for protons (blue), pions (red), and neutrons (green).

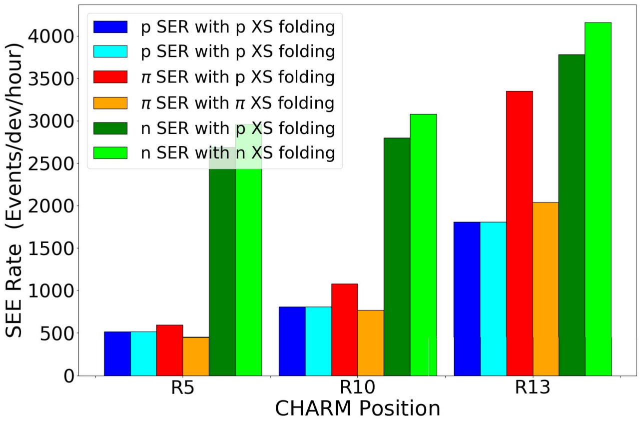

Fig. 19. SER comparison between the proton only folding approach and the full particle folding approach. Data are reported by the CHARM position and further subdivided for protons (blue), pions (red), and neutrons (green).

VI. RHA Implications

The CHARM mixed field is certainly a valuable mean to assert RHA practices devoted to the accelerator equipment qualification. The many different positions with respect to the target in the irradiation room allow maintaining the representativeness of many radiative environments within the CERN accelerator complex, but they can also be extended to various electronic equipment tests for other environments, e.g., space. In this context, the interest is to assess if the pion SEU resonance can affect the radiation response when compared to a standardized qualification made with monoenergetic protons [19].

The actual HEH SEU cross section is a single value determined by the contribution of a wide energetic multiparticle spectrum. The HEH approximation claims that this HEH SEU cross section can be assumed to be equivalent to the 200-MeV proton SEU cross section. The approximation stands in assuming that all the particles' responses are identical, no matter the particle types and their energy above 20 MeV.

The nuclear interaction analysis and simulations performed for the ISSI SRAM allows implementing a set of comparison to determine the SER of this specific device based on the simulated cross sections. Fluxes from each particle inside the CHARM irradiation room are scored by simulating the model of the facility. The SER can be obtained according to the following approaches:

1) by the integral of all particle fluxes above 20 MeV multiplied by the 200-MeV proton cross section (HEH approximation);
2) by folding all particle fluxes above 20 MeV with the proton cross-sectional curve as a function of energy (approach typical of standards [19]);
3) by folding each particle flux above 20 MeV with its own particle cross section (the actual HEH cross section with no approximation other than using simulation data and excluding the neutron contribution below 20 MeV).

Fig. 18 shows a first comparison between the first and the third SER calculation philosophies. This first comparison allows drawing conclusions about the suitability of using monoenergetic proton facilities for testing electronic equipment to be installed in the accelerator. The comparison is made for three significant positions inside CHARM (R5: low-Earth orbit (LEO) space-like spectra, R10: accelerator and atmospheric-like spectra, and R13: accelerator-like spectra for very energetic environments) and on a particle-by-particle basis. The graph shows that no matter which approach is pursued, neutrons will dominate the SER response in positions R5 and R10 and they stand out as the main contributor for position R13 too.

The pion response is the one that is less affected by the HEH approximation. The differences between protons and neutrons are higher. This is due to their increased cross section between 20 and 100 MeV, shown in Fig. 10, compared to their 200-MeV value which is taken as energy reference for the HEH approximation. The SER of pions from the HEH approximation is underestimated by just 10%, whereas those for protons and neutron by 33% and 42%, respectively. When all contributions are summed up, the HEH approximation is underestimating the SER by 33% in R5 and by 28% in R13.

A similar comparison between the folding of the proton cross section (second approach) and the folding of all the cross sections (third approach) yields very similar SERs (Fig. 19). In this case, the folding of the proton cross section may lead to slight overestimations of the SER. Pions are also the particles whose SER differs the most. This is mainly due to the 20–50-MeV proton cross section being higher than the 20–50-MeV pion cross section in an energy region where pion fluxes are not negligible. The differences resulting from this comparison is a 3% underestimation for R5 and a 10% overestimation for R13.

To conclude, the pion SEU resonance is seen not to be the main factor affecting the cross-sectional estimations in a mixed-field environment because, first, the SER is dominated by neutrons (in the 20–100-MeV range, in particular) and, second, because the peak pion flux does not correspond to the resonance region. Testing an electronic device to be used in the accelerator at a monoenergetic proton facility with 200 MeV protons (first approach) brings to an accelerator SER

TABLE III

COMPARISON BETWEEN APPROACHES 2 AND 3 FOR LEO SER PREDICTIONS

Orbit	**SER proton test** (events/dev/hour)	**SER CHARM** (events/dev/hour)	**Ratio**
400 km, 98°, Solar min	$2.80 \cdot 10^{-2}$	$2.57 \cdot 10^{-2}$	1.09
400 km, 51°, Solar min	$4.21 \cdot 10^{-2}$	$3.84 \cdot 10^{-2}$	1.10
800 km, 98°, Solar min	$3.62 \cdot 10^{-1}$	$3.35 \cdot 10^{-1}$	1.08
800 km, 51°, Solar min	$5.35 \cdot 10^{-1}$	$4.92 \cdot 10^{-1}$	1.09

underestimation of up to 33%, which is still quite satisfactory. Performing standard proton cross-sectional measurements at multiple energies and folding the cross section with the actual mixed-field fluxes (second approach) would lead to an even better fit. This shows that there is no particular information lost if pion and neutron responses are unknown. Fitting of experimental data is expected to be even better since there is no experimental evidence of such a strong increase in the proton and neutron cross sections at 20–100 MeV.

Another analysis can be done to study which is the level of approximation introduced by testing a device in a mixed field for a different environment than the accelerator, e.g., space. Still using simulation data, the actual HEH SEU cross section that would be retrieved from a CHARM experiment for the ISSI SRAM is 2.29×10^{-14} cm^2/bit. Multiplying this cross section for some typical space fluxes (above 20 MeV and obtained from OMERE [20]) would lead to proton-induced SERs that are underestimated by 10% or less (see Table III).

VII. CONCLUSION

Measurements of pion SER have been often overlooked, assuming that their cross section would match that of protons and neutrons. Pions are, nonetheless, a central contributor to the SEE response in accelerators. Their cross section was experimentally observed to differ from that of protons for both SEU and SEL in the energy region between 50 and 230 MeV.

The proposed numerical model confirmed that the SEU response of pions strictly reflects the inelastic cross section of π–Si collisions. The increased SEU cross section in the 75–250-MeV region was seen to be related to an enhancement in the production of low and intermediate LET secondary ions. The <75-MeV drop in the pion SEU cross section is also justified by the less effective production of intermediate and high LET secondary ions at these lower incident energies.

The impact of the pion SEU resonance in a mixed-field environment was assessed for the sake of RHA practices. The resonant pion SEE cross section was found not to affect the radiation response of a device in the mixed field. Due to their higher fluxes, neutrons remain the dominating contributor to the SEE global response.

Both the HEH approximation (200-MeV proton testing only) and the proton cross-sectional folding approaches were shown to be reliable techniques for the SER prediction of electronic devices to be used in the accelerator environment. At the same time, the mixed-field response was demonstrated to be similar to that of a radiative field mainly composed of protons, proving the suitability of using CHARM for qualification of electronics to be used in proton- or neutron-dominated environments.

REFERENCES

[1] H. H. K. Tang, "Nuclear physics of cosmic ray interaction with semiconductor materials: Particle-induced soft errors from a physicist's perspective," *IBM J. Res. Develop.*, vol. 40, no. 1, pp. 91–108, Jan. 1996.

[2] R. Garcia Alia *et al.*, "LHC and HL-LHC: Present and future radiation environment in the high-luminosity collision points and RHA implications," *IEEE Trans. Nucl. Sci.*, vol. 65, no. 1, pp. 448–456, Jan. 2018.

[3] K. Roeed *et al.*, "Method for measuring mixed field radiation levels relevant for SEEs at the LHC," *IEEE Trans. Nucl. Sci.*, vol. 59, no. 4, pp. 1040–1047, Aug. 2012.

[4] J. Barak and N. M. Yitzhak, "SEU rate in avionics: From sea level to high altitudes," *IEEE Trans. Nucl. Sci.*, vol. 62, no. 6, pp. 3369–3380, Dec. 2015.

[5] R. G. Alía *et al.*, "Single event effects in high-energy accelerators," *Semicond. Sci. Technol.*, vol. 32, no. 3, 2017, Art. no. 034003.

[6] G. J. Hofman *et al.*, "Light-hadron induced SER and scaling relations for 16- and 64-mb DRAMS," *IEEE Trans. Nucl. Sci.*, vol. 47, no. 2, pp. 403–407, Apr. 2000.

[7] S. Duzellier, D. Falguere, M. Tverskoy, E. Ivanov, R. Dufayel, and M.-C. Calvet, "SEU induced by pions in memories from different generations," *IEEE Trans. Nucl. Sci.*, vol. 48, no. 6, pp. 1960–1965, Dec. 2001.

[8] *FLUKA*. Accessed: Feb. 2020. [Online]. Available: http://fluka.cern

[9] J. Mårtensson *et al.*, "Pion production excitation functions in proton-nucleus collisions from the absolute threshold to 500 MeV," *Phys. Rev. C*, vol. 62, Jun. 2000, Art. no. 014610.

[10] S. J. Bates *et al.*, "Pion-induced damage in silicon detectors," *Nucl. Instrum. Methods Phys. Res. A, Accel., Spectrometers, Detectors Associated Equip.*, vol. 379, no. 1, pp. 116–123, Sep. 1996.

[11] A. Infantino, "FLUKA Monte Carlo modelling of the CHARM facility's test area: Update of the radiation field assessment," CERN, Geneva, Switzerland, Tech. Rep. CERN-ACC-NOTE-2017-0059, Nov. 2017.

[12] J. Mekki, M. Brugger, R. G. Alia, A. Thornton, N. C. Dos Santos Mota, and S. Danzeca, "CHARM: A mixed field facility at CERN for radiation tests in ground, atmospheric, space and accelerator representative environments," *IEEE Trans. Nucl. Sci.*, vol. 63, no. 4, pp. 2106–2114, Aug. 2016.

[13] G. Spiezia *et al.*, "A new RadMon version for the LHC and its injection lines," *IEEE Trans. Nucl. Sci.*, vol. 61, no. 6, pp. 3424–3431, Dec. 2014.

[14] S. Danzeca *et al.*, "Qualification and characterization of SRAM memories used as radiation sensors in the LHC," *IEEE Trans. Nucl. Sci.*, vol. 61, no. 6, pp. 3458–3465, Dec. 2014.

[15] W. Hajdas *et al.*, "High energy electron radiation exposure facility at PSI," *J. Appl. Math. Phys.*, vol. 2, no. 9, pp. 910–917, Aug. 2014.

[16] M. Tali *et al.*, "High-energy electron-induced SEUs and Jovian environment impact," *IEEE Trans. Nucl. Sci.*, vol. 64, no. 8, pp. 2016–2022, Aug. 2017.

[17] R. G. Alía, M. Tali, M. Cecchetto, F. Cerutti, and A. Cononetti, "Direct ionization impact on accelerator mixed-field soft-error rate," *IEEE Trans. Nucl. Sci.*, vol. 67, no. 1, pp. 345–352, Jan. 2020.

[18] B. D. Sierawski *et al.*, "Impact of low-energy proton induced upsets on test methods and rate predictions," *IEEE Trans. Nucl. Sci.*, vol. 56, no. 6, pp. 3085–3092, Dec. 2009.

[19] *Single Event Effects Test Method and Guidelines*, ESA ESTEC, Noordwijk, The Netherlands, Oct. 2014.

[20] *OMERE*. Accessed: Aug. 2019. [Online]. Available: http://www.trad.fr/spatial/logiciel-omere

Publication II

A. Coronetti, R. García Alía, J. Wang, M. Tali, M. Cecchetto, C. Cazzaniga, A. Javanainen, F. Saigné, and P. Leroux, ”Assessment of proton direct ionization for the radiation hardness assurance of deep sub-micron SRAMs used in space applications,” *IEEE Trans. Nucl. Sci.*, vol. 68, no. 5, pp. 937-948, May 2021.

© 2021, Coronetti et al., licensed under CC BY 4.0.

Assessment of Proton Direct Ionization for the Radiation Hardness Assurance of Deep Submicron SRAMs Used in Space Applications

Andrea Coronetti, *Student Member, IEEE*, Rubén Garcìa Alìa, *Member, IEEE*,
Jialei Wang, *Graduate Student Member, IEEE*, Maris Tali, Matteo Cecchetto, Carlo Cazzaniga,
Arto Javanainen, *Member, IEEE*, Frédéric Saigné, and Paul Leroux, *Senior Member, IEEE*

***Abstract*— Proton direct ionization (PDI) from low-energy protons has been shown to have a potentially significant impact on the accuracy of prediction methods used to calculate the upset rates (URs) of memory devices in space applications for state-of-the-art deep submicron technologies. The general approach nowadays is to consider a safety margin to apply over the UR computed from high-energy proton and heavy-ion experimental data. The data reported here present a challenge to this approach. Different UR prediction methods are used and compared in order to establish the impact of PDI on the total UR. Regardless of the method employed, the findings suggest that PDI can contribute to up to 90% of the total UR, on average, for a general selection of space orbits, with peaks of up to 99%. Such results suggest that an approach based on the characterization of the low-energy portion of the proton spectrum would be more convenient for similar technologies than the application of a general safety margin. Based on data presented here, the previously proposed margin of 5 is exceeded, by large amounts in some cases.**

***Index Terms*— Low-energy protons (LEPs), Monte-Carlo (MC) simulations, prediction methodologies, proton direct ionization (PDI), radiation hardness assurance (RHA), space environment, upset rate (UR).**

I. INTRODUCTION

THE potential impact of direct ionization phenomena arising from singly charged particles, such as protons [1], [2], electrons [3], and muons [4], on the upset rate (UR) of memory devices has been a matter of concern for more than a decade. When it comes to space applications, low-energy protons (LEPs) are one of the main threats challenging the standard UR prediction methodologies based on high-energy proton (HEP) and heavy-ion (HI) single-event upset (SEU) characterizations. Although not specifying how to calculate the UR from LEPs, space standards for single-event effects [5] are starting to mention procedures for SEU characterization under LEP irradiation.

While it is common to refer to HEPs as those protons with energy above 20 MeV, the energy range for LEPs is not clearly defined. One of the reference studies in this subject [6] suggests to account only for protons having energies in the 0–3 MeV range because these are the only energies relevant for direct ionization. Such an observation arose from those previous experimental observations.

An additional source of uncertainty on the total UR may arise from proton elastic scattering, occurring at energies below 20 MeV [7]–[9], which is generally neglected as well.

Both direct ionization and elastic scattering are phenomena that can cause SEUs in deep submicron technologies, regardless of whether they are based on bulk Si or silicon-on-insulator (SOI) processes [10]. Angular dependence was also shown to be an important factor for the triggering of SEU mechanisms. Normal incidence is considered worst case for bulk silicon and 90° tilting worst case for SOI [10].

SEUs from proton direct ionization (PDI) are triggered by the energy directly deposited by protons within the device-sensitive volume (SV). This mechanism becomes more and more remarkable for those protons having an energy near the Bragg peak, that is, those protons that either stop within the SV or that pass through it while depositing most of their energy. These are protons that enter the SV with energies on the order of 50 keV.

In terms of radiation hardness assurance (RHA) for space missions, several approaches have been proposed in the past

Manuscript received December 31, 2020; revised February 15, 2021; accepted February 17, 2021. Date of publication February 22, 2021; date of current version May 20, 2021. This work was supported in part by the European Union's Horizon 2020 Research and Innovation Program through the Marie Sklodowska Curie (MSC) under Grant 721624 and in part by the European Space Agency [ESA/European Space Research and Technology Center (ESTEC)] at the University of Jyväskylä under Contract 4000124504/18/NL/KML/zk.

Andrea Coronetti is with CERN, 1211 Geneva, Switzerland, and also with the Department of Physics, University of Jyväskylä, 40014 Jyväskylä, Finland (e-mail: andrea.coronetti@cern.ch).

Rubén Garcìa Alìa, Maris Tali, and Matteo Cecchetto are with CERN, 1211 Geneva, Switzerland.

Jialei Wang and Paul Leroux are with the Department of Electrical Engineering (ESAT), KU Leuven, 2440 Geel, Belgium.

Carlo Cazzaniga is with the Science and Technology Facilities Council, Didcot OX11 0QX, U.K.

Arto Javanainen is with the Department of Physics, University of Jyväskylä, 40014 Jyväskylä, Finland, and also with the Department of Electrical Engineering and Computer Science, Vanderbilt University, Nashville, TN 37235 USA.

Frédéric Saigné is with the Institute d'Électronique et des Systèmes, Université de Montpellier, 34090 Montpellier, France.

Color versions of one or more figures in this article are available at https://doi.org/10.1109/TNS.2021.3061209.

Digital Object Identifier 10.1109/TNS.2021.3061209

This work is licensed under a Creative Commons Attribution 4.0 License. For more information, see https://creativecommons.org/licenses/by/4.0/

years for PDI UR predictions starting from ground test data [6], [10]–[13]. One of the main studies [6] proposes the use of a degraded HEP beam as an enabler for LEP SEU ground testing. In this case, the main advantage is the possibility to exploit the energetic spread introduced by the degraders in the beamline to irradiate the device with a spectra replicating that found in a typical Earth space mission in the 0–3 MeV energy range.

The main conclusion of the study was that for static random access memories (SRAM) operated down to 10% undervoltage, the PDI contribution to the total UR could be counted by applying a conservative margin of 5 to the UR calculated from the conventional HEP and HI SEU cross sections determined through ground testing [10].

The present work explores very strong PDI enhancements observed in the SEU cross sections of a few SRAMs that can break the previous assumptions about the severity of PDI for space missions RHA. When considering the two commercial devices in the accelerator context [14], it was found that UR enhancements due to PDI up to a factor of 5 were expected. This despite the minor contribution of LEPs to the overall accelerator radiative environment (largely neutron-dominated) if compared to the larger abundance of LEPs in the space environment. Thus, the objective is to determine whether the standard RHA approaches for PDI are challenged by this specific set of devices and by how much the previous safety margins might be violated.

This article is structured as follows. The experimental investigation performed for this work is briefly introduced. The experimental data are fed into models to be used in Monte-Carlo (MC) simulation tools. These are used, along with other prediction tools to estimate the UR of the characterized devices for a few selected space orbits in order to evaluate the impact of PDI UR in typical space missions.

II. EXPERIMENTAL INVESTIGATION

One of the three characterized devices is a custom-developed SRAM designed by one of the authors of this article and the other two are commercial SRAMs. The custom-developed SRAM will henceforth be referred as RADSAGA 65-nm SRAM. As the name suggests, it is based on a 65-nm technology and it was manufactured according to the standard commercial Taiwan Semiconductor Manufacturing Company (TSMC) process. The only difference is that the cell size is three times larger than that of the standard. One of the commercially available SRAMs, reference CY62167GE30-45ZXI (henceforth called Cypress SRAM), is also based on this technology. The other commercial SRAM, reference IS61WV204816BLL-10TLI (henceforth called Integrated Silicon Solutions Inc. (ISSI) SRAM), is based on a 40-nm technology. The main features of these memories are summarized in Table I.

TABLE I
SRAMs Under Consideration in This Work

Name	Technology (nm)	Size (bits)	Core Voltage (V)
RADSAGA	65	32k	0.3
ISSI	40	32M	1.1
Cypress	65	16M	1.1

Note that the RADSAGA 65-nm SRAM [15] has a tunable core voltage that can be used to vary the sensitivity of the memory chip, spanning in the 0.3–1.2 V range. For the scope of this article, the presented data and the main focus will be devoted to a core voltage of 0.3 V. The data presented for the commercial SRAMs all refer to their nominal core voltages of 1.1 V. Note that the Cypress SRAM has an internal error-correction code (ECC), which has been disabled for the purposes of this study.

TABLE II
Main Characteristics of the HIs Used to Characterize the SEU Cross Sections

Ion	Energy (MeV)	LET (MeV/(mg/cm^2))	Range (mm)
C	1080	0.22	11.78
C	720	0.31	5.73
C	360	0.52	1.67
Ar	1050	5.2	0.55
Ar	548	8.1	0.20
Xe	2700	43.5	0.22

The SRAMs have been tested with several beams [16] and most of the experimental details are reported in that article. All the SRAMs have been irradiated through the back-end-of-line (BEOL). This was shown to have an impact for SOI SRAMs [17] with respect to irradiation from the substrate. For the presented bulk SRAMs, however, such configuration could not be achieved.

For the purpose of this work, data referring to LEP, HEP, and HI irradiations are reported. Concerning LEPs, the core of the experimental work was completed at the Centro Nacional de Aceleradores (CNA) [18]. There, the SRAMs have been irradiated with mono-energetic proton beams in the 0.5–5 MeV energy range. LEP data for the ISSI SRAM were collected at the Radiation Effects Facility (RADEF) [19], [20] at the University of Jyväskylä. HEP testing was accomplished at the Kernfysisch Versneller Instituut (KVI) [21] for the ISSI and Cypress SRAMs and at the Paul Scherrer Institute (PSI) [22] for the RADSAGA 65-nm SRAM. HI testing was performed at KVI for all the SRAMs. Table II reports the HI characteristics in terms of species, energy, linear energy transfer (LET), and range. Only the LEP testing at CNA and RADEF were performed in vacuum. All the data have been obtained at normal incidence and room temperature. Different from other experiments and measurement techniques [23], [24], mono-energetic LEP data have not been obtained by beam degradation.

Error bars for all experimental data are calculated at 95% confidence level, assuming a fluence uncertainty of 10% and based on the actual number of events. If not visible in the plots, they are smaller than the markers.

The experimental proton cross sections as a function of energy for the RADSAGA 65-nm SRAM are depicted in Fig. 1. The peak direct ionization cross section was found for 900 keV and it reaches up to 4×10^{-9} cm^2/bit. The cross section is still higher than 10^{-12} cm^2/bit at 5 MeV. The HEP cross section lowers down to 1.5×10^{-13} cm^2/bit

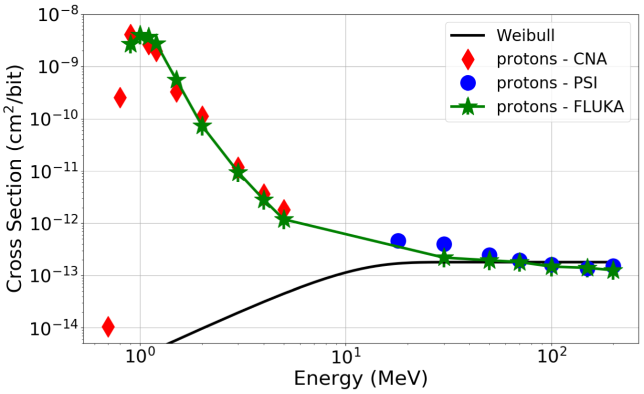

Fig. 1. Low and HEP experimental cross sections as a function of proton energy for the RADSAGA 65-nm SRAM when tuned at 0.3 V. The HEP data are fit with a Weibull with the following parameters: $\sigma_{\text{sat}} = 1.8 \times 10^{-13}$ cm^2/bit, $E_0 = 0$ MeV, $W = 10$ MeV, $s = 1.8$. The data are compared with the FLUKA simulated cross sections.

at 200 MeV. It is seen to grow from below 100 MeV to reach up to 4.7×10^{-13} cm^2/bit at 18 MeV. This may indicate a potential influence of direct ionization at energies around 20 MeV. For the Weibull fit, the saturation cross section is taken to be 1.8×10^{-13} cm^2/bit to better account for this enhancement below 100 MeV. Overall, the peak PDI cross section is about 2.2×10^4 times the HEP saturation cross section used for the Weibull fit.

The experimental proton cross sections as a function of energy for the ISSI SRAM are depicted in Fig. 2. The peak direct ionization cross section was observed at 600–800 keV, probably indicating a thinner BEOL than the previous SRAM. The fact that the LEP cross section is almost constant for an interval of energies (600–800 keV) more strongly points out the reaching of the physical limit imposed by the SV size. The peak cross section is 5×10^{-10} cm^2/bit. The HEP saturation cross section is 1.5×10^{-14} cm^2/bit, resulting in a ratio between the peak PDI and high-energy saturation cross sections of 3.3×10^4.

The indicated ratios are among the highest that could be found in the literature. In one case [25], ratios up to a factor of 10^5–10^6 were observed. However, different from these data, the peaks were quite steep and narrow, indicating a higher critical charge than for the devices here considered.

The experimental proton cross sections as a function of energy for the Cypress SRAM are depicted in Fig. 3. The peak direct ionization cross section is seen to occur between 800 keV and 1 MeV, stretching up to 1.2×10^{-9} cm^2/bit. The HEP saturation cross section is 8×10^{-14} cm^2/bit. As a result, the ratio between the peak PDI and high-energy saturation cross sections is 1.5×10^4.

Fig. 4 presents the same PDI data for the RADSAGA 65-nm SRAM as a function of LET compared to cross sections obtained with long range ions. Other than the data points at high LET, which define the HI saturation cross section, the main purpose of the figure is to compare the cross sections of LEPs with those of long-range high-energy light ions (carbon in the 30–90 MeV/u energy range).

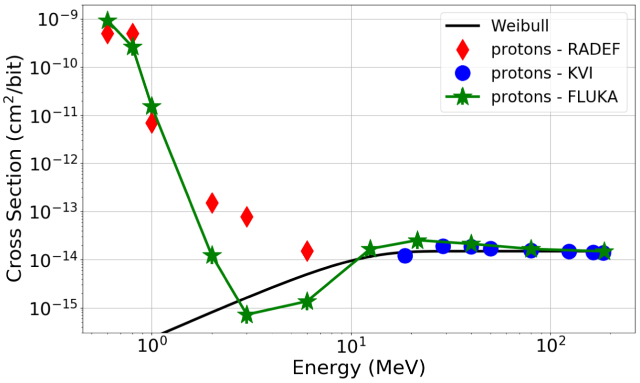

Fig. 2. Low and HEP experimental cross sections as a function of proton energy for the ISSI SRAM. The HEP data are fit with a Weibull with the following parameters: $\sigma_{\text{sat}} = 1.5 \times 10^{-14}$ cm^2/bit, $E_0 = 10$ MeV, $W = 0$ MeV, $s = 1.8$. The data are compared with the FLUKA simulated cross sections.

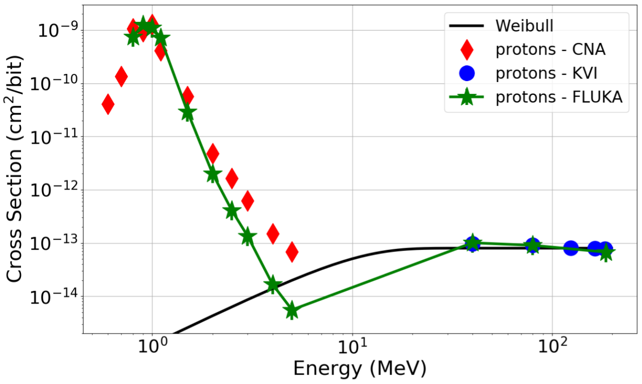

Fig. 3. Low and HEP experimental cross sections as a function of proton energy for the Cypress SRAM. The HEP data are fit with a Weibull with the following parameters: $\sigma_{\text{sat}} = 8 \times 10^{-14}$ cm^2/bit, $E_0 = 10$ MeV, $W = 0$ MeV, $s = 1.8$. The data are compared with the FLUKA simulated cross sections.

In the figure, ion data points have been placed at an LET corresponding to that before the BEOL. It is assumed that, given their longer range, the ions will reach the SV while losing a negligible amount of energy in the BEOL. On the contrary, LEPs have a shorter range that may bring them to stop either inside the SV or in its vicinity. Thus, LEP data points have not been placed at the tabulated LET [26] for that primary energy before the BEOL. A more realistic LET has been estimated based on the interaction with the BEOL. While the latter cannot be known for the commercial memories, the experimental cross section helped deducing their SiO_2 equivalent BEOL thicknesses. On the other hand, for the RADSAGA 65-nm SRAM, it is known from manufacturing documentation that the BEOL would be equivalent to a layer of SiO_2 12-μm thick.

Whether known or deduced from the data, this equivalent thickness was used to calculate the energy lost by the primary protons while passing through the BEOL by means of the stopping and range of ions in matter (SRIM) software [27]. Once this was known, SRIM was again used to determine the range in silicon of a proton having the residual kinetic energy and calculate an LET based on this residual kinetic energy

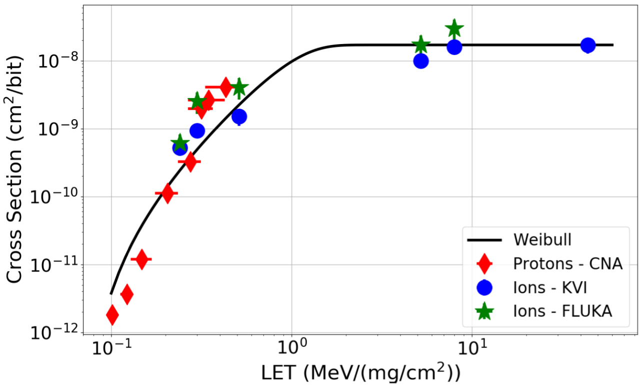

Fig. 4. LEP and HI cross sections as a function of LET for the RADSAGA 65-nm SRAM when tuned at 0.3 V. Weibull parameters: $\sigma_{\text{sat}} = 1.7 \times 10^{-8}$ cm^2/bit, LET$_0$ = 0.07 MeV/(mg/cm^2), W = 1 MeV/(mg/cm^2), $s = 2.4$. The data are compared with the FLUKA simulated cross sections.

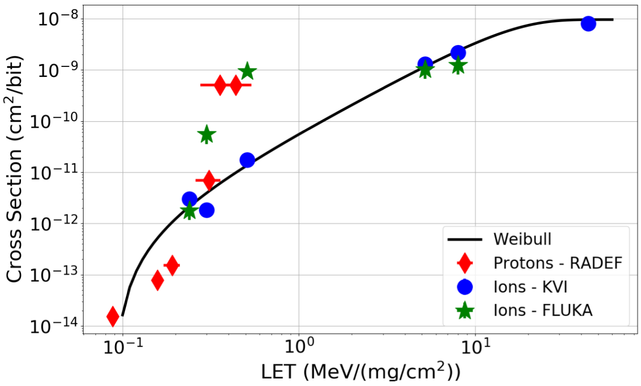

Fig. 5. LEP and HI cross sections as a function of LET for the ISSI SRAM. Weibull parameters: $\sigma_{\text{sat}} = 9.56 \times 10^{-9}$ cm^2/bit, LET$_0$ = 0.09 MeV/(mg/cm^2), W = 16 MeV/(mg/cm^2), and s = 1.8. The data are compared with the FLUKA simulated cross sections.

and the range. This LET is exclusively used to show the LEP points in the plots.

Note that this method introduces an approximation, since it considers that all the protons transiting through the BEOL will experience the same identical energy loss. Fluktuierende Kaskade (FLUKA) 4.0 [28], [29] was used to simulate mono-energetic 900-keV protons traveling through the BEOL oxide. Due to straggling, the resulting spectra after the BEOL and at the entry of the SV were found to be continuous between 0 and 200 keV. This was also observed in [30]. At the same time, the residual kinetic energy obtained from SRIM for this case was about 290 keV. Considering the energy straggling, using a single LET derived from a single proton energy may result in an underestimation of the LET of less than 0.1 MeV/(mg/cm^2), which will not alter the general picture.

Coming back to Fig. 4, it is clear that the peak PDI cross sections are not fully reproduced by long-range light ions, as was found before [31]. In this case, the peak PDI cross section can be three times higher than the respective carbon cross section at a similar LET.

Fig. 5 shows the LEP and HI cross sections as a function of LET for the ISSI SRAM. The same procedure, as for the previous case, was implemented for the LEP LET determination, this time with a BEOL as thick as 6 μm. The PDI peak is seen to exceed the carbon cross sections for similar LET by even a factor of 50. Indeed, the peak PDI cross sections are even closer to the argon ion cross sections obtained with LETs above 5 MeV/(mg/cm^2) than to the carbon ion cross sections.

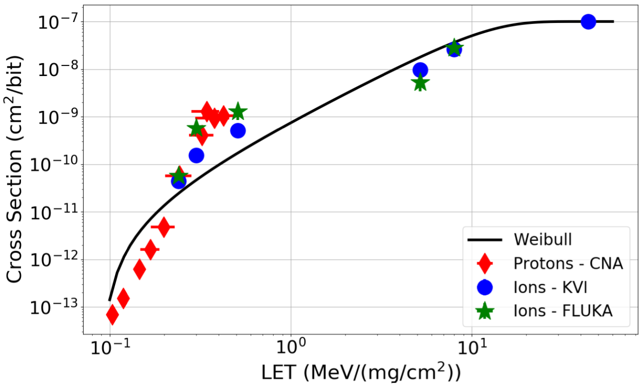

Fig. 6. LEP and HI cross sections as a function of LET for the Cypress SRAM. Weibull parameters: $\sigma_{\text{sat}} = 1 \times 10^{-7}$ cm^2/bit, LET$_0$ = 0.09 MeV/(mg/cm^2), W = 12 MeV/(mg/cm^2), and s = 1.9. The data are compared with the FLUKA simulated cross sections.

Fig. 6 depicts the LEP and HI cross sections as a function of LET for the Cypress SRAM. The LETs for LEPs were calculated assuming a BEOL 10-μm thick. This was chosen because the PDI peak cross section is maximum between 0.8 and 1 MeV and it starts fading only below 800 keV. Hence, at an energy lower than where the fading is observed for the RADSAGA 65-nm SRAM. The situation is similar to the RADSAGA 65-nm SRAM, with a maximum difference among peak PDI and carbon ion cross sections of a factor of 3.

The reason for the observed experimental behaviors is not fully clear, but it is not caused by the presence of multiple-bit upsets (MBUs, occurring in the same word), while nothing can be said about multiple-cell upsets (MCUs, occurring in physically adjacent cells) given that the physical mapping of the memories is not available. It may be a topic of future investigations. The presented HI LET Weibull functions are derived to follow the HI data at both low and high LET and will be later used to calculate the HI contributions to the total UR.

Carbon and argon ion interactions were also simulated with FLUKA and are reported in the figures. For all the models, the FLUKA-simulated cross sections for carbon (low LET) tend to follow the LEP experimental data rather than the carbon experimental data at similar LET. This is particularly evident for the ISSI SRAM (Fig. 5). On the other hand, the agreement between argon experimental data and simulated data is within a factor of 2 for all the models.

III. MODELING OF THE SVS

SV models are proposed for the memory cells of the three SRAMs. They will be used as input in the MC simulations used to determine the UR of the SRAMs in the space environment.

TABLE III

NESTED RPP DATA OF THE SVs OF EACH SRAM ALONG WITH THE COLLECTION EFFICIENCY (ALPHA), BEOL THICKNESS, AND CRITICAL CHARGE

RADSAGA 65 nm SRAM		
BEOL 12 μm, Q_{crit} = 0.55 fC		
SV side (nm)	**SV thickness (nm)**	**alpha**
638	250	1
996	250	0.077
1304	250	0.050

ISSI SRAM		
BEOL 6 μm, Q_{crit} = 0.96 fC		
SV side (nm)	**SV thickness (nm)**	**alpha**
310	310	1

Cypress SRAM		
BEOL 10 μm, Q_{crit} = 0.86 fC		
SV side (nm)	**SV thickness (nm)**	**alpha**
360	360	1
984	360	0.057
1612	360	0.037
3160	360	0.007

TABLE IV

COMPARISON OF THE ENERGY CONVOLUTION OF THE EXPERIMENTAL AND RPP MODEL PROTON RESPONSES FOR LOW- (0–3 MeV), INTERMEDIATE- (3–20 MeV), AND HIGH-ENERGY (>20 MeV) REGIONS FOR THE THREE SRAMs WITH THE ISS ENVIRONMENT AND 100 MILS OF ALUMINUM SHIELDING. DATA ARE REPORTED IN SEU/bit/day

Data	**0-3 MeV**	**3-20 MeV**	**> 20 MeV**	**Total**
RADSAGA 65 nm SRAM				
Exp	8.00 x 10^{-6}	4.37 x 10^{-7}	5.90 x 10^{-7}	9.03 x 10^{-6}
RPP	9.06 x 10^{-6}	2.94 x 10^{-7}	4.59 x 10^{-7}	9.81 x 10^{-6}
ISSI SRAM				
Exp	6.22 x 10^{-7}	5.38 x 10^{-9}	4.14 x 10^{-8}	6.69 x 10^{-7}
RPP	6.76 x 10^{-7}	3.80 x 10^{-9}	4.53 x 10^{-8}	7.25 x 10^{-7}
Cypress SRAM				
Exp	1.89 x 10^{-6}	2.34 x 10^{-8}	2.22 x 10^{-7}	2.14 x 10^{-6}
RPP	2.11 x 10^{-6}	7.64 x 10^{-9}	2.08 x 10^{-7}	2.33 x 10^{-6}

All the SRAM models here considered are based on rectangular parallelepiped (RPP) that are built based on the experimental data. LEP data are very useful when building such models since they can give direct indications of the SV size, that is, the direct ionization cross section tends to be equal to the SV surface normal to the beam. In addition, the lowering of the cross section at energies below the PDI peak can give indications about the BEOL thickness. Finally, the slope of the cross section curve from the PDI peak toward higher energies can give indications about the SV thickness and the critical charge Q_{crit} [14].

Even when these LEP data are correctly fit, often a single RPP can be representative of the LEP cross section, but it can underestimate the HEP cross section. Given that the models will be used for the estimations of the UR due to LEPs and HEPs, as well as HIs, it is crucial to build models that could reproduce in the best possible way also the high-energy part of the proton cross section. A nested RPP technique [11], [32] based on HI data can be used to better fit the HEP cross section while not affecting the low-energy part.

The nested RPP technique was used for the RADSAGA 65-nm and Cypress SRAMs. On the other hand, a single RPP was found to be suitable for the ISSI SRAM since it fairly reproduces both the LEP and HEP responses. The data of the RPP models for all the SRAMs are reported in Table III. The BEOL are assumed to be made with SiO_2 for all the cases.

For the nested RPPs, the external volume sides are obtained directly by a few high-LET HI (>5 MeV/(mg/cm^2)) cross section data points. The collection efficiency (alpha) is obtained by making the ratio between the LET of the PDI peak data point and the LET of that HI. For the RADSAGA 65-nm SRAM, the reference proton LET is 0.4 MeV/(mg/cm^2), whereas for the Cypress SRAM, this is 0.3 MeV/(mg/cm^2). The thickness is kept constant [33] and equal to that of the innermost SV (targeted to reproduce the PDI enhancement).

The RADSAGA 65-nm SRAM has the largest SV side (640 nm) for the innermost volume. At the same time, this is the only model for which the SV thickness (250 nm) did not coincide with the SV side. The reason is the matching of the proton cross section at energies of 1–5 MeV. Using a larger thickness would lead the simulated cross section to fall down much quicker with increasing energy. The critical charge is also the lowest (0.55 fC), given the lower core voltage. For the outermost volumes, only the argon ion data are retained, since the xenon data point has the same cross section as the argon ion with the highest LET.

The ISSI SRAM has the lowest PDI peak cross section, hence the lowest RPP side (310 nm). It also has the thinner BEOL (6 μm) since the memory was experimentally observed to be sensitive down to just 600 keV. Finally, it also relies on the highest critical charge (0.96 fC), which, in spite of the smaller technology, is likely due to differences in the manufacturing processes among companies.

For the innermost volume, the Cypress SRAM model has the SV side and thickness of 360 nm. The critical charge is 0.86 fC. To complete the model, three larger volumes are added based on the argon and xenon cross sections. In this case, the HI saturation cross section is much larger than that of the RADSAGA 65-nm SRAM, resulting in volumes with sides as large as 3 μm.

FLUKA MC simulations were performed for all the models and for several mono-energetic proton cases to assess the consistency of the model with respect to the experimental data. The uncertainty on the calculated cross sections varies with each energy. On average, an uncertainty of ±35% can be taken for all the data points and models based on the energy deposition distributions. Other uncertainties may be present on the parameters chosen for the SV such as BEOL thickness, critical charge, SV size, and thickness.

Figs. 1–3 present the comparison among the mono-energetic experimental and simulated cross sections for the RADSAGA 65-nm SRAM, ISSI SRAM, and Cypress SRAM, respectively.

For the RADSAGA 65-nm SRAM, the consistency is verified at low (0–3 MeV), intermediate (3–20 MeV), and high energy (>20 MeV). For the ISSI and Cypress SRAMs, the agreement between the models and the experiments is good for LEPs and HEPs. For the intermediate-energy region, the agreements are less optimal. However, this region is not an important contributor when it comes to the proton UR since it contributes less than 1%, at least for these two SRAMs.

As a further verification of the validity of the proposed RPP models to describe the proton cross section response over different sets of energies, a first UR calculation was performed. cosmic-ray environment and effects models (CREME) 96 [34] was used to determine the trapped proton flux for the International Space Station (ISS) orbit. The flux was transported by means of the online tool through 100 mils of aluminum. The data were then divided into the three energy regions described before. Both the experimental data and the RPP model data were convolved along with the proton fluxes in the three energy regions. Both data sets are determined for normal incidence only, for both the data and the radiation field. For this simple calculation, the angular response is not considered because no such experimental data were collected and a fair comparison would not be possible.

Table IV reports the comparison of all three devices and for each energy region. The agreement for each region is quite satisfactory. The largest discrepancies are seen for the ISSI and Cypress SRAMs for intermediate-energy protons. However, given that, for these memories, this region is expected to contribute 1% or less to the total UR, the related inaccuracy can be assumed to be negligible. Globally, the total URs from these models are about 10% higher than their experimental counterparts.

IV. UR PREDICTION METHODS

UR prediction methods based on the measurements of HEP and HI cross sections are nowadays well standardized, for example, the Weibull [35] method, among others. Existing methods on HEPs and HIs are all based on the assumptions made from the typical test results that cross section curves are null below the energy/LET threshold and tend to reach a saturation cross section at high energy/LET while maintaining a monotonic dependence with energy/LET.

PDI, however, introduces the problem that the cross section is no longer monotonic with energy. Hence, the established prediction methods can hardly help out in predicting the UR from LEPs. In principle, some of these methods can be mimicked in some other way, because they are basically convolutions of a cross section function defined as a function of energy/LET with an environmental particle spectrum, similarly defined as a function of energy/LET.

The LEP experimental mono-energetic cross sections can, for instance, be convolved with the environmental flux without a need to define a function that would describe the whole cross section curve as a function of energy, that is, by performing linear interpolation for intermediate points. This is supposed to provide a more accurate estimation than that obtained by multiplying the cross section peak for the proton flux in the relevant energy range, as proposed in [36].

Still, among the problems introduced by energy convolution, there is the assumption that the proton will reach the SV with normal incidence, which is not the case since the space environmental proton fluxes are isotropic. For instance, when folding the cross sections presented in Fig. 1, all protons within the environment having an energy below 700 keV will not contribute to the response. However, when considering an isotropic spectrum, there will always be protons arriving at the SV with an energy in the 0-700-keV range, which, in principle, are associated with a cross section similar with that of the PDI peak. Such a method, based on the energy and range of protons arriving at the SV, was also proposed in the past [37].

Another possibility would be to treat the LEPs in a similar fashion as HIs and to perform an LET convolution. However, in this case, determining the LET of the protons used during the experiments can, as was shown before, be complicated and the uncertainty introduced by the straggling may lead to much higher inaccuracy than for the determination of the actual proton energy.

A promising method, proposed by Dodds [6], to calculate the UR from PDI consists of measuring the cross section of a degraded high-energy beam containing a known spectrum of LEPs. The method also requires performing measurements at various angles of incidence to cover the effects related to the isotropic nature of the space spectra. The PDI UR is then compared to those attained through the Weibull method for HEPs and HIs. However, when data from such an experiment are not available, approximate methods may be introduced based on the observed mono-energetic proton cross sections in order to retrieve the UR.

Finally, MC simulations can also be considered for UR predictions. The earlier introduced RPP models of the SV can be used to extract the cross sections derived from the environmental proton and HI spectra. The advantage of MC simulations is that the models used are assumed to be a valid representation of the device response regardless of the particle or energy. In addition, they may also provide further indications about potential variations introduced by varying the parameters in the chosen models. Note that the MC simulations are run with isotropic spectra as input, hence accounting for the angular response of the modeled component. A certain degree of uncertainty, which is not so easy to quantify, is present, anyhow. This is due to the lack of experimental data at different angles of incidence. That is, the angular dependence here considered is that emerging as a result of the modeling at normal incidence, but no verification with respect to experimental data was possible.

For this first assessment, the data refer to a single orbit and a single shielding configuration. The environment under consideration is that of the ISS for solar minimum conditions. Both proton and HI fluxes are transported through 100 mils of aluminum with the CREME/universal heavy ion propagation code (UPROP) online tool. The fluxes are then used to perform energy convolution calculations (applicable only to protons), the Weibull fit calculations (applicable only to HEPs and HIs), FLUKA MC simulations (applicable to every particle and energy), and an approximated Dodds' method (applicable only to LEPs).

For the heavy-ion Weibull methods, the Weibull curves presented in Figs. 4–6 were used. For the HEPs, the same identical Weibull functions were used for the three devices, but with a different saturation cross section ($E_{\mathrm{th}} = 0$ MeV, $W = 10$ MeV, $s = 1.8$). The saturation cross sections were 1.8×10^{-13}, 1.5×10^{-14}, and 8×10^{-13} cm^2/bit for the RADSAGA 65-nm ISSI and Cypress SRAMs, respectively (Figs. 1–3).

TABLE V

COMPARISON OF UR PREDICTION METHODS FOR LOW AND HEPS AND HIS FOR THE THREE SRAMS AT 0.3 V FOR THE LISTED METHODS. THE ISS ENVIRONMENT IS USED FOR ALL METHODS (500 km, 51.6°, SOLAR MIN, 100 MILS ALUMINUM). THE UR UNITS ARE SEU/bit/day

RADSAGA 65 nm SRAM			
Method	**High-E protons**	**Low-E protons**	**Heavy ions**
Energy convolution	5.42 x 10^{-7}	8.49 x 10^{-6}	X
Weibull	4.57 x 10^{-7}	X	2.65 x 10^{-7}
Monte-Carlo	3.04 x 10^{-7}	1.47 x 10^{-5}	4.07 x 10^{-7}
Approx. Dodds'	4.57 x 10^{-7}	1.43 x 10^{-5}	2.65 x 10^{-7}

ISSI SRAM			
Method	**High-E protons**	**Low-E protons**	**Heavy ions**
Energy convolution	4.06 x 10^{-8}	6.27 x 10^{-7}	X
Weibull	3.81 x 10^{-8}	X	3.90 x 10^{-9}
Monte-Carlo	2.33 x 10^{-8}	5.76 x 10^{-7}	5.34 x 10^{-8}
Approx. Dodds'	3.81 x 10^{-8}	1.20 x 10^{-6}	3.90 x 10^{-9}

Cypress SRAM			
Method	**High-E protons**	**Low-E protons**	**Heavy ions**
Energy convolution	2.25 x 10^{-7}	1.92 x 10^{-6}	X
Weibull	2.03 x 10^{-7}	X	4.02 x 10^{-8}
Monte-Carlo	1.58 x 10^{-7}	1.88 x 10^{-6}	1.10 x 10^{-7}
Approx. Dodds'	2.03 x 10^{-7}	3.41 x 10^{-6}	4.02 x 10^{-8}

The idea behind the approximated Dodds' method is to retrieve a rough estimate of the cross section that would have been measured for the devices presented in this work if experimental measurements in a high-energy degraded beam were performed. Note that the Dodds' method can be used to calculate the LEP contribution to the UR, whereas for the HEP and HI contributions, the method also relies on the Weibull fits.

The approximated Dodds' method consists in the convolution of the experimental LEP cross section with the spectrum experimentally measured at Tri-University Meson Facility (TRIUMF) [6] when degrading the 70-MeV proton beam to an average energy of 6 MeV. Once this cross section is estimated, the approximated method follows the same steps as the original Dodds' method.

Table V presents the UR calculated for the three contributors: LEPs, HEPs, and HIs with the various methods. Note that in this case all protons in the environment below 20 MeV are considered as LEPs, as they are typically irrelevant in the traditional methods based on HEP and HI characterizations only.

For all three devices, the energy convolution, Weibull, and MC methods deliver very similar HEP URs, always within less than a factor of 2 difference. For HIs, the Weibull and the MC methods are quite in disagreement for the ISSI SRAM, with even one order of magnitude lower UR delivered by the Weibull fit. For the other two SRAMs, the differences are much smaller, within a factor of 1.5 for the RADSAGA 65-nm SRAM and less than a factor of 3 for the Cypress SRAM. The larger HI UR arising from MC simulations is due to the fact that the RPP models of the SVs are built so that they follow the experimental LEP cross sections at low LET rather than the light ion cross sections. As was shown earlier, the difference is not negligible, in particular, for the ISSI SRAM, for which the discrepancy between different HI UR estimation methods is the highest.

Concerning the comparison among LEP UR prediction methods, the results are not always consistent among devices. For the RADSAGA 65-nm SRAM, the energy convolution delivers a UR which is about half that of the MC simulations and the approximated Dodds' method, which, in turn, are very similar. This effect may be related to the isotropic nature of the environment, which is neglected in the energy convolution method. However, although this is indeed always the case for all the memories when comparing energy convolution and approximated Dodds' method, for the ISSI and Cypress SRAMs, the MC LEP UR is similar to that obtained through energy convolution.

Since the combined Weibull/Dodds' method and the MC simulations provide data for all three contributors to the total UR, these two approaches are followed to perform the following RHA assessments. One of the main differences between the two methods is that the approximated Dodds' method considers only protons with energy below 3 MeV, whereas the MC simulations consider the full proton spectra below 20 MeV.

V. PDI IMPACT ON THE TOTAL UR

Generally, the UR of a digital device in any space orbit is defined by two main contributions, that is, direct HI ionization and proton indirect ionization. PDI can be considered as a separate contributor since the proton-induced SEUs are, in this case, triggered in a similar fashion as those from HIs. In order to evaluate the impact of PDI on the total UR, let us define a parameter D as

$$D = \frac{\mathrm{UR_{HI}} + \mathrm{UR_{HEP}} + \mathrm{UR_{LEP}}}{\mathrm{UR_{HI}} + \mathrm{UR_{HEP}}}. \tag{1}$$

The D factor will define the relative contribution of PDI to the UR with respect to the UR estimated when PDI is neglected. It can also be seen as a safety margin to apply to the estimated UR when LEP data are not available.

The analysis is made considering the three devices presented in this article, four different space radiation environments, and two different shielding configurations. All the environments are calculated through the CREME96 online tools. The ISS environment (I1 and I5) is calculated at 500-km altitude, 51.6° inclination, solar minimum, quiet conditions; the low-Earth orbit (LEO) environment (L1 and L5) at 1400-km altitude, 52°, solar minimum, quiet conditions; the geostationary orbit (GEO) environment is calculated for both quiet (GQ1 and GQ5) and stormy solar conditions (GW1 and GW5, worst day). The shielding configurations are with 100 and 500 mils of aluminum.

For the RADSAGA 65-nm SRAM, the contributions to the UR (both in absolute and percentage terms) are reported in Table VI for both the MC simulations and for the approximated Dodds' method. PDI effects are found to be negligible only for the GEO quiet conditions, for which both methods, regardless of the shielding, yield a PDI UR in the order of 1%. For all other radiation environments, the PDI contribution to the UR is never below 85%. The most affected orbits are the LEO and GEO in stormy conditions and the situation does not change much when a thicker shielding is considered. Generally, the two methods yield very similar results for

TABLE VI

UR OF THE **RADSAGA 65 -nm SRAM** FROM PROTON INDIRECT AND DIRECT IONIZATION AND HIs (WITH PERCENTAGE CONTRIBUTIONS TO THE TOTAL UR IN BRACKETS) FOR EIGHT COMBINATIONS OF ORBITS AND SHIELDING CONFIGURATIONS. UR IN SEU/bit/day

Monte-Carlo			
Env.	**UR**$_{HEP}$ **(%)**	**UR**$_{LEP}$ **(%)**	**UR**$_{HI}$ **(%)**
I1	3.04 x 10^{-7} (2%)	1.47 x 10^{-5} (96%)	2.65 x 10^{-7} (2%)
I5	2.41 x 10^{-7} (6%)	3.72 x 10^{-6} (89%)	2.39 x 10^{-7} (6%)
L1	2.38 x 10^{-5} (2%)	1.03 x 10^{-3} (98%)	3.98 x 10^{-7} (0%)
L5	7.72 x 10^{-6} (4%)	2.07 x 10^{-4} (96%)	3.59 x 10^{-7} (0%)
GQ1	3.94 x 10^{-8} (2%)	1.89 x 10^{-8} (1%)	1.84 x 10^{-6} (97%)
GQ5	4.09 x 10^{-8} (3%)	1.79 x 10^{-8} (1%)	1.46 x 10^{-6} (96%)
GW1	3.92 x 10^{-4} (0%)	1.44 x 10^{-1} (96%)	6.04 x 10^{-3} (4%)
GW5	5.98 x 10^{-5} (1%)	5.04 x 10^{-3} (98%)	6.27 x 10^{-5} (1%)

Approximated Dodds' method			
Env.	**UR**$_{HEP}$ **(%)**	**UR**$_{LEP}$ **(%)**	**UR**$_{HI}$ **(%)**
I1	4.57 x 10^{-7} (3%)	1.43 x 10^{-5} (95%)	2.65 x 10^{-7} (2%)
I5	3.32 x 10^{-7} (9%)	3.32 x 10^{-6} (85%)	2.39 x 10^{-7} (6%)
L1	2.29 x 10^{-5} (2%)	9.79 x 10^{-4} (98%)	3.98 x 10^{-7} (0%)
L5	1.64 x 10^{-5} (9%)	1.76 x 10^{-4} (91%)	3.59 x 10^{-7} (0%)
GQ1	5.96 x 10^{-8} (3%)	1.48 x 10^{-8} (1%)	1.84 x 10^{-6} (96%)
GQ5	5.77 x 10^{-8} (4%)	1.72 x 10^{-8} (1%)	1.46 x 10^{-6} (95%)
GW1	3.89 x 10^{-4} (0%)	1.36 x 10^{-1} (96%)	6.04 x 10^{-3} (4%)
GW5	9.65 x 10^{-5} (2%)	4.94 x 10^{-3} (97%)	6.27 x 10^{-5} (1%)

TABLE VII

UR OF THE **ISSI SRAM** FROM PROTON INDIRECT AND DIRECT IONIZATION AND HIs (WITH PERCENTAGE CONTRIBUTIONS TO THE TOTAL UR IN BRACKETS) FOR EIGHT COMBINATIONS OF ORBITS AND SHIELDING CONFIGURATIONS. UR IN SEU/bit/day

Monte-Carlo			
Env.	**UR**$_{HEP}$ **(%)**	**UR**$_{LEP}$ **(%)**	**UR**$_{HI}$ **(%)**
I1	2.33 x 10^{-8} (4%)	5.76 x 10^{-7} (96%)	3.90 x 10^{-9} (1%))
I5	3.94 x 10^{-8} (32%)	8.13 x 10^{-8} (65%)	3.45 x 10^{-9} (3%)
L1	2.47 x 10^{-6} (6%)	4.00 x 10^{-5} (94%)	5.77 x 10^{-9} (0%)
L5	8.27 x 10^{-7} (14%)	5.54 x 10^{-6} (86%)	5.14 x 10^{-9} (0%)
GQ1	6.01 x 10^{-9} (14%)	2.50 x 10^{-9} (6%)	3.50 x 10^{-8} (80%)
GQ5	2.40 x 10^{-9} (8%)	3.44 x 10^{-9} (11%)	2.49 x 10^{-8} (81%)
GW1	8.81 x 10^{-5} (2%)	5.04 x 10^{-3} (97%)	4.46 x 10^{-5} (1%)
GW5	8.62 x 10^{-6} (4%)	4.14 x 10^{-4} (96%)	4.35 x 10^{-7} (0%)

Approximated Dodds' method			
Env.	**UR**$_{HEP}$ **(%)**	**UR**$_{LEP}$ **(%)**	**UR**$_{HI}$ **(%)**
I1	3.81 x 10^{-8} (3%)	1.20 x 10^{-6} (97%)	3.90 x 10^{-9} (0%)
I5	2.77 x 10^{-8} (8%)	3.04 x 10^{-7} (91%)	3.45 x 10^{-9} (1%)
L1	1.91 x 10^{-6} (6%)	8.20 x 10^{-5} (94%)	5.77 x 10^{-9} (0%)
L5	1.37 x 10^{-6} (8%)	1.48 x 10^{-5} (92%)	5.14 x 10^{-9} (0%)
GQ1	5.44 x 10^{-9} (13%)	1.24 x 10^{-9} (3%)	3.50 x 10^{-8} (84%)
GQ5	5.26 x 10^{-9} (17%)	1.44 x 10^{-9} (5%)	2.49 x 10^{-8} (78%)
GW1	3.24 x 10^{-5} (1%)	1.14 x 10^{-2} (99%)	4.46 x 10^{-5} (0%)
GW5	7.97 x 10^{-6} (2%)	4.14 x 10^{-4} (98%)	4.35 x 10^{-7} (0%)

TABLE VIII

UR OF THE **CYPRESS SRAM** FROM PROTON INDIRECT AND DIRECT IONIZATION AND HIs (WITH PERCENTAGE CONTRIBUTIONS TO THE TOTAL UR IN BRACKETS) FOR EIGHT COMBINATIONS OF ORBITS AND SHIELDING CONFIGURATIONS. UR IN SEU/bit/day

Monte-Carlo			
Env.	**UR**$_{HEP}$ **(%)**	**UR**$_{LEP}$ **(%)**	**UR**$_{HI}$ **(%)**
I1	1.58 x 10^{-7} (8%)	1.88 x 10^{-6} (91%)	4.02 x 10^{-8} (1%)
I5	1.21 x 10^{-7} (21%)	4.17 x 10^{-7} (73%)	3.58 x 10^{-8} (6%)
L1	7.46 x 10^{-6} (5%)	1.37 x 10^{-4} (95%)	1.63 x 10^{-7} (0%)
L5	7.32 x 10^{-6} (23%)	2.41 x 10^{-5} (77%)	5.37 x 10^{-8} (0%)
GQ1	2.98 x 10^{-8} (11%)	1.14 x 10^{-9} (0%)	2.44 x 10^{-7} (89%)
GQ5	2.66 x 10^{-8} (12%)	2.31 x 10^{-10} (1%)	1.87 x 10^{-7} (87%)
GW1	2.70 x 10^{-4} (2%)	1.54 x 10^{-2} (96%)	3.34 x 10^{-4} (2%)
GW5	7.21 x 10^{-5} (11%)	5.48 x 10^{-4} (88%)	4.29 x 10^{-6} (1%)

Approximated Dodds' method			
Env.	**UR**$_{HEP}$ **(%)**	**UR**$_{LEP}$ **(%)**	**UR**$_{HI}$ **(%)**
I1	2.03 x 10^{-7} (6%)	3.41 x 10^{-6} (93%)	4.02 x 10^{-8} (1%)
I5	1.48 x 10^{-7} (14%)	8.65 x 10^{-7} (83%)	3.58 x 10^{-8} (3%)
L1	1.02 x 10^{-5} (4%)	2.33 x 10^{-4} (96%)	1.63 x 10^{-7} (0%)
L5	7.31 x 10^{-6} (15%)	4.20 x 10^{-5} (85%)	5.37 x 10^{-8} (0%)
GQ1	3.09 x 10^{-8} (11%)	3.54 x 10^{-9} (1%)	2.44 x 10^{-7} (88%)
GQ5	2.99 x 10^{-8} (14%)	4.10 x 10^{-9} (2%)	1.87 x 10^{-7} (84%)
GW1	1.73 x 10^{-4} (1%)	3.25 x 10^{-2} (98%)	3.34 x 10^{-4} (1%)
GW5	4.25 x 10^{-5} (4%)	1.18 x 10^{-3} (96%)	4.29 x 10^{-6} (0%)

the PDI contribution to the UR, pointing out the potential dominance of PDI over the other two SEU mechanisms.

For the ISSI SRAM, the contributions to the UR (both in absolute and percentage terms) are reported in Table VII for both the MC simulations and for the approximated Dodds' method. PDI UR for GEO quiet conditions is found to contribute for a maximum of 11% to the total UR, again pointing out that PDI effects can be considered negligible in this environment. For the other three environments, when considering the MC simulations, PDI is still the major contributor to the UR. However, it is not dominant in all the cases. At the lowest, PDI contributes to 65% for the I5 orbit and can reach 97% for the GW1 environment. The situation is quite different when considering the approximated Dodds' method. In this case, PDI never contributes less than 91% for each orbit, with a peak of 99% for GW1.

For the Cypress SRAM, the contributions to the UR (both in absolute and percentage terms) are reported in Table VIII for both the MC simulations and for the approximated Dodds' method. In this case as well, PDI contributes to the GQ UR by 0%–2%, pointing out that PDI will not contribute to the total UR in this environment. For the other three environments, when considering MC simulations, PDI is the main contributor to the UR, it is never below 73% and it can peak at 96% for the GW1 environment. One peculiarity for the Cypress SRAM is that the HEP component of the UR is, in percentage, higher than for the other two memories. Similar to the ISSI SRAM, when considering the approximated Dodds' method, the PDI contribution to the UR becomes dominant, with an 83% lowest percentage contribution for the I5 orbit and a maximum of 98% for the GW1 environment.

The *D* factors for the RADSAGA 65-nm SRAM for both the MC and the approximated Dodds' methods are reported in Fig. 7. The plot is made to compare how the *D* factor changes with orbit, shielding, and calculation method. The RADSAGA 65-nm SRAM shows quite consistent *D* factors for almost all the orbits when calculated either using MC or with the approximated Dodds' method. Letting the GEO quiet conditions aside, regardless of the calculation method, the orbit or the shielding, the *D* factor is never below 5 and can reach up to 43 for the L1 and GW5 orbits.

The *D* factors for the ISSI SRAM for both the MC and the approximated Dodds' method are reported in Fig. 8. Note that, in this case, the data are reported in logarithmic scale to improve readability. In the case of the ISSI SRAM, the two methods may disagree by even a factor of 4 for the I5 and GW1 environments. The approximated Dodds' method predicts the highest *D* factor to be roughly 150 (for the GW1 environment). For the same orbit, the MC simulations

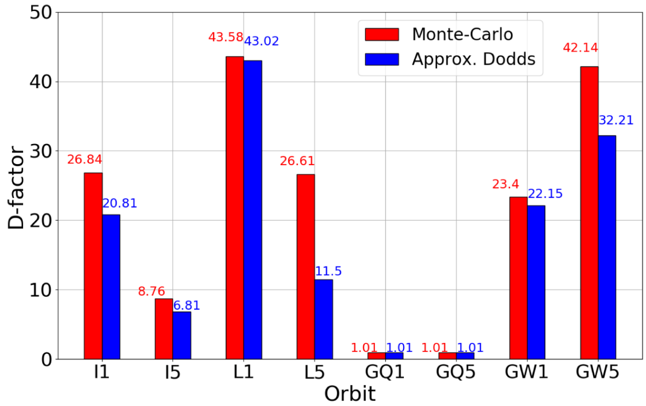

Fig. 7. *D* factors of the RADSAGA 65-nm SRAM calculated for eight combinations of orbit and shielding with the MC simulations and the approximated Dodds' method.

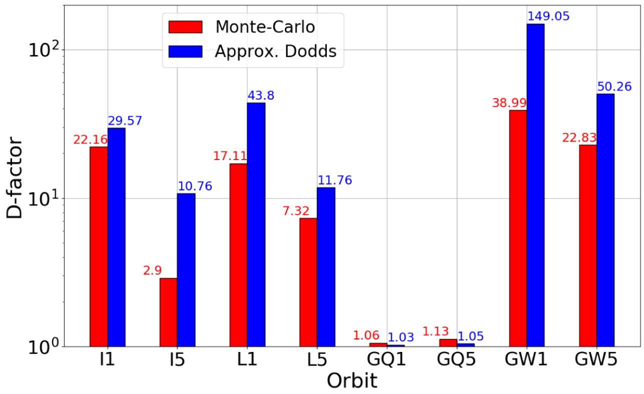

Fig. 8. *D* factors of the ISSI SRAM calculated for eight combinations of orbit and shielding with the MC simulations and the approximated Dodds' method.

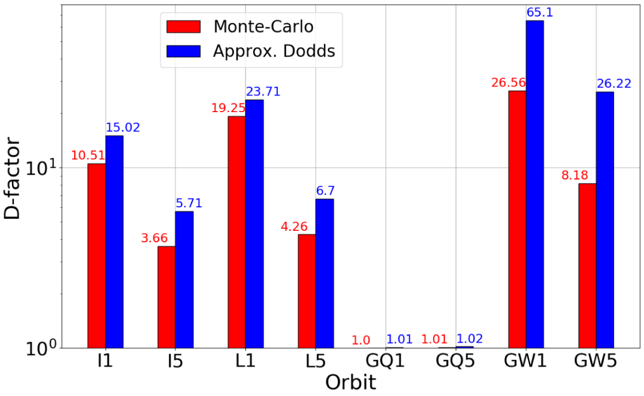

Fig. 9. *D* factors of the Cypress SRAM calculated for eight combinations of orbit and shielding with the MC simulations and the approximated Dodds' method.

predicts a factor of 39. The minimum *D* factors are found for the GQ conditions (just above 1). Letting this environment aside, the minimum would otherwise be 3 for the I5 orbit. For this same orbit, the approximated Dodds' method provides the lowest *D* factor, which is as high as 11.

The *D* factors for the Cypress SRAM for both the MC and the approximated Dodds' method are reported in Fig. 9, also in logarithmic scale. The comparison between the two methods yields similar observations as for the ISSI SRAM, though the difference, in this case, is moderate, that is, the approximated Dodds' method yields less than a factor of 2 higher *D* factors than MC for the ISS and LEO cases, with the only exception of GEO worst day. With the exception of the GQ cases, for which the *D* factor is 1 or just above, all other *D* factors are higher than 5. For MC, the highest *D* factor is 27 for the GW1 orbit and the lowest is 4 for the I5 orbit. For the approximated Dodds' method, the highest *D* factor is 65 for the GW1 orbit and the lowest is 6 for the I5 orbit.

The two methods point out quite heterogeneous contributions to the UR. In general, the MC simulations bring factors which are equal to or lower than the approximated Dodds' method. Despite representing the most optimistic prediction case, the MC simulations still yield *D* factors that violate the safety margin of 5 established in the literature [10].

The shielding is almost always seen to provide a benefit in terms of UR in absolute value. However, it does have a quite limited impact on the *D* factors. At best, for the ISSI SRAM, the *D* factor for I5 was 7 times smaller than for I1. For the other conditions, the effect is no higher than a factor of 2. The RADSAGA 65-nm SRAM and the GEO stormy environment represent the only exception. For this case alone, the *D* factor for 500 mils is seen to be higher than for 100 mils for both methods. The reason is likely related to the wider PDI cross section peak of the RADSAGA 65-nm SRAM with respect to the other two devices, which render the RADSAGA 65-nm SRAM also more sensitive to intermediate-energy protons. Hence, 500 mils of aluminum are likely not enough to mitigate the effects of a large part of the intermediate-energy protons. In the literature [38], more realistic shielding configurations were found to yield a reduction in the PDI UR by up to a factor of 25 with respect to the spherical 100 mils aluminum shielding.

VI. *D* FACTOR AS A FUNCTION OF THE CRITICAL CHARGE

One advantage of the MC simulations is that they provide data over a wide range of critical charges. While losing the link to the data of these specific devices, such analysis can allow exploring how the *D* factor would vary when changing the critical charge of the model, which can be used to assess whether the device may be sensitive to direct ionization from HEPs and how the picture may change for other devices having a different critical charge. Note that the other parameters of the modeled SVs may also play a role, so this analysis will focus strictly on common observations among devices and models.

In order to use the MC data as a function of critical charge, the L1 orbit was chosen. The HI contribution to the UR was found to be negligible for this orbit. This allows neglecting the overestimated (but still negligible) low-LET HI response from MC, so that the *D* factor simplifies further

$$D(Q_{\text{crit}}) = \frac{\text{UR}_{\text{HEP}}(Q_{\text{crit}}) + \text{UR}_{\text{LEP}}(Q_{\text{crit}})}{\text{UR}_{\text{HEP}}(Q_{\text{crit}})}. \tag{2}$$

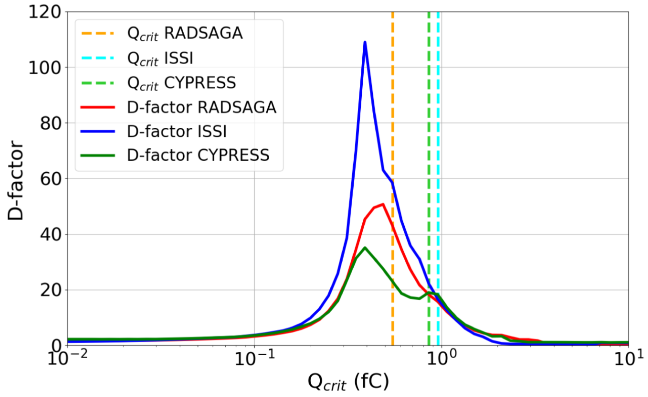

Fig. 10. *D* factors of the three devices calculated for the LEO orbit with 100 mils of aluminum shielding with the MC simulations as a function of the critical charge.

In general terms, the *D* factor will converge to 1 at high critical charge because LEPs would not deposit enough charge to trigger SEUs. At the same time, it will converge to 1 also at very low critical charge (below 0.1 fC) because such a device would also be sensitive to direct ionization from HEPs. The latter would be covered through HEP testing and would make the LEP contribution less important in relative terms.

Thus, the *D* factor is expected to reach an absolute maximum, usually at critical charges in between 0.1 and 1 fC. If the chosen critical charge is lower than that corresponding to the absolute maximum, direct ionization effects may be relevant also at energies above 20 MeV.

Fig. 10 reports the *D* factor as a function of critical charge for the three devices under consideration. For the RADSAGA 65-nm SRAM, the chosen critical charge falls very close to the peak region (which is at around 0.5 fC). This shows that this device is likely sensitive to direct ionization effects above 3 MeV and, potentially, up to 20 MeV.

For the ISSI SRAM, the chosen critical charge is just placed at the onset of the range of critical charges for which PDI becomes dominant. However, the ISSI SRAM shows an absolute maximum that can stretch up to more than 100.

The Cypress SRAM has the lowest peak in absolute value among the three devices. Another peculiarity is represented by the secondary peak located at the chosen critical charge (0.86 fC), for which the *D* factor reaches a relative maximum, which is as high as 60% of the absolute maximum at 0.4 fC. The chosen critical charge (0.86 fC) places the model almost halfway between the absolute maximum and the onset, indicating that direct ionization from HEPs is unlikely for this device.

In general, the critical charge at which the *D* factor reaches the absolute maximum is seen not to vary much among the different SV models and it occurs for a critical charge of 0.4–0.5 fC. However, the absolute value of the *D* factor may vary by far, from 35 for the Cypress SRAM to 110 for the ISSI SRAM and it seems to be strictly related to the ratio between the PDI cross section peak and the HEP saturation cross section observed experimentally.

VII. DISCUSSION

The three devices under consideration have all proved, to different extents, to be very susceptible to direct ionization from LEPs. Experiments with mono-energetic protons exhibit ratios between the peak PDI cross sections and the high-energy saturation cross sections higher than 10^4.

When brought into an environmental context, such high and wide PDI effects were predicted to provide not only a significant contribution to the total UR, but, in most of the cases, they dominated the total UR response. Regardless of the prediction method used, the considered orbit or the shielding, PDI was found to contribute about 90% of the total UR on average, with maxima of 99%.

The corresponding *D* factors calculated for these devices in the considered environments were always on the order of a few tens, reaching maximum values above 100 for the worst case orbits. These were either low-Earth orbits for which the trapped proton fluxes are quite high or the GEO environments under the intensification of the proton fluxes provided by a strong solar activity. Shielding (varying from 100 to 500 mils of Al) was seen to have an impact, but just to a limited extent, often sufficient to reduce the *D* factor by a factor of 2.

The *D* factor is assumed to be a safety margin that one can apply to the UR calculated through Weibull fitting of the HEP and HI experimental cross sections. It is clear that safety margins make sense if they are small compared to the quantity that is margined. At least for the considered devices, this is not the case for basically any space environment (even the supposedly mild ISS environment). Considering the potential uncertainty of the UR calculation methods for PDI effects, a method based on the application of safety margins over the UR calculated from HEPs and HIs is unlikely to work. Bounding the UR with the highest *D* factor found among all the devices would mean applying always a factor of 150 to the UR calculated excluding LEPs, which will often be unrealistically pessimistic.

From the experimental data reported in other works [6], [13], it is clear that such a safety margin would provide a huge overshoot over the actual contribution of PDI to the UR of memory devices in general. More than providing a revision to the required safety margins to account for PDI when calculating the UR from HEP and HI responses, the presented data rather reinforce the need to perform experimental characterization of memory devices with either mono-energetic LEPs [31] or degraded HEP beams [6].

Some further considerations can be made on the accuracy of the proposed calculation methods. The RPP models calibrated over LEPs and HEPs proved to be very accurate for the two proton contributors, but provided some overestimation of the HI contribution with respect to the Weibull-predicted UR, which, in turn, would have reduced the *D* factor. However, for the RADSAGA 65-nm SRAM, the *D* factor would have not reduced by more than a factor of 1.5, still pointing out a quite strong PDI enhancement.

Concerning the approximated Dodds' method, it is clear that it would not exactly correspond to the experimental measurements attained by degradation of a high-energy beam.

However, this approximated method is likely not overestimating the UR by more than a factor of 5. Even when considering such a strong inaccuracy, it would still yield D factors higher than 10 for certain devices and certain orbits.

In this respect, the simplicity of the approximated Dodds' method is counterbalanced by a higher degree of inaccuracy in the UR prediction, whereas the MC simulations can be considered to provide a higher-fidelity estimation within a factor of ± 2.

As a matter of fact, it will not be possible to draw conclusion about the accuracy of current UR prediction methods for PDI unless the devices are actually tested in the space environment. Currently, the devices analyzed in this work have been considered for launch in LEO space missions. If proved to be that sensitive to the actual space radiation environment, they could be considered as a baseline to have very sensitive radiation monitors to characterize the LEP fluxes in space.

The analysis of the D factor as a function of critical charge showed that for the RADSAGA 65-nm SRAM, the worst case scenario was already reached, being the chosen critical charge so close to that of the D factor absolute maximum. This may point out an influence from direct ionization above 3 MeV, potentially extending up to 20 MeV and above. The analysis for the other two devices showed that they are still positioned at about the onset of the PDI sensitivity and still quite far from the absolute maximum.

VIII. CONCLUSION

Novel data and soft error prediction methods on the impact of PDI in SRAMs based on deep submicron technology and bulk Si were presented to report on the strong enhancement to the UR that would come from the observed PDI effects. The big impact seems to be related to both the relatively high peak PDI cross section, compared to the HEP saturation cross section, and to the wide energy range for which direct ionization phenomena play a role, which may extend even above 3 MeV.

Regardless of the calculation method employed, PDI contributes, on average, about 90% of the total UR. The resulting safety margins (D factors) to be applied to the UR calculated from HEP and HI experimental data generally exceed the factor of 5 previously established in the literature and can get as high as 150. Although the analyzed devices could just represent a worst case for PDI, it is suggested to pursue experimental characterization for PDI effects whenever the HI LET threshold of the device is lower than 0.4 MeV/(mg/cm^2), rather than stick to the application of a general safety margin.

ACKNOWLEDGMENT

The authors acknowledge Yolanda Morilla and Pedro Martìn-Holgado from CNA; Heikki Kettunen, Mikko Rossi, and Jukka Jaatinen from RADEF; Marc-Jan van Goethem, Harry Kiewiet, Emil van der Graaff, and Sytze Brandenburg from KVI; and Wojtek Hajdas, Laura Sinkunaite, and Miroslaw Marszalek from PSI for their support during data collection at the respective facilities.

Special thanks go to Helmut Puchner, from Cypress Semiconductors, for providing the information required to disable the embedded ECC within the Cypress 65-nm chip.

REFERENCES

[1] K. P. Rodbell, D. F. Heidel, H. H. K. Tang, M. S. Gordon, P. Oldiges, and C. E. Murray, "Low-energy proton-induced single-event-upsets in 65 nm node, silicon-on-insulator, latches and memory cells," *IEEE Trans. Nucl. Sci.*, vol. 54, no. 6, pp. 2474–2479, Dec. 2007.

[2] D. F. Heidel *et al.*, "Low energy proton single-event-upset test results on 65 nm SOI SRAM," *IEEE Trans. Nucl. Sci.*, vol. 55, no. 6, pp. 3394–3400, Dec. 2008.

[3] M. P. King *et al.*, "Electron-induced single event upsets in static random access memories," *IEEE Trans. Nucl. Sci.*, vol. 60, no. 6, pp. 4122–4129, Dec. 2013.

[4] B. D. Sierawski *et al.*, "Muon-induced single event upsets in deep-submicron technology," *IEEE Trans. Nucl. Sci.*, vol. 57, no. 6, pp. 3273–3278, Dec. 2010.

[5] *Single Event Effects Test Method and Guidelines*, Standard ESCC 25100, European Space Components Coordination, ESA, Oct. 2014.

[6] N. A. Dodds *et al.*, "Hardness assurance for proton direct ionization-induced SEEs using a high-energy proton beam," *IEEE Trans. Nucl. Sci.*, vol. 61, no. 6, pp. 2904–2914, Dec. 2014.

[7] A. Akkerman, J. Barak, and N. M. Yitzhak, "Role of elastic scattering of protons, muons, and electrons in inducing single-event upsets," *IEEE Trans. Nucl. Sci.*, vol. 64, no. 10, pp. 2648–2660, Oct. 2017.

[8] P. Caron, C. Inguimbert, L. Artola, R. Ecoffet, and F. Bezerra, "Physical mechanisms of proton-induced single-event upset in integrated memory devices," *IEEE Trans. Nucl. Sci.*, vol. 66, no. 7, pp. 1404–1409, Jul. 2019.

[9] Z. Wu, S. Chen, J. Yu, J. Chen, P. Huang, and R. Song, "Recoil-ion-induced single event upsets in nanometer CMOS SRAM under low-energy proton radiation," *IEEE Trans. Nucl. Sci.*, vol. 64, no. 1, pp. 654–664, Jan. 2017.

[10] N. A. Dodds *et al.*, "The contribution of low-energy protons to the total on-orbit SEU rate," *IEEE Trans. Nucl. Sci.*, vol. 62, no. 6, pp. 2440–2451, Dec. 2015.

[11] B. D. Sierawski *et al.*, "Impact of low-energy proton induced upsets on test methods and rate predictions," *IEEE Trans. Nucl. Sci.*, vol. 56, no. 6, pp. 3085–3092, Dec. 2009.

[12] J. R. Schwank *et al.*, "Hardness assurance testing for proton direct ionization effects," *IEEE Trans. Nucl. Sci.*, vol. 59, no. 4, pp. 1197–1202, Aug. 2012.

[13] J. Guillermin, N. Sukhaseum, P. Pourrouquet, N. Chatry, F. Bezerra, and R. Ecoffet, "Worst-case proton contribution to the direct ionization SEU rate," in *Proc. 17th Eur. Conf. Radiat. Effects Compon. Syst. (RADECS)*, Geneva, Switzerland, Oct. 2017, pp. 330–337.

[14] R. G. Alia *et al.*, "Direct ionization impact on accelerator mixed-field soft-error rate," *IEEE Trans. Nucl. Sci.*, vol. 67, no. 1, pp. 345–352, Jan. 2020.

[15] J. Wang, J. Prinzie, A. Coronetti, and P. Leroux, "Study of the SEU sensitivity of an SRAM-Based Radiation Monitor in a 65-nm CMOS Technology," *IEEE Trans. Nucl. Sci.*, to be published.

[16] A. Coronetti *et al.*, "SEU characterization of commercial and custom-designed SRAMs based on 90 nm technology and below," in *Proc. IEEE Radiat. Effects Data Workshop Rec.*, Santa Fe, NM, USA, Nov./Dec. 2020, pp. 56–63.

[17] N. A. Dodds *et al.*, "New insights gained on mechanisms of low-energy proton-induced SEUs by minimizing energy straggle," *IEEE Trans. Nucl. Sci.*, vol. 62, no. 6, pp. 2822–2829, Dec. 2015.

[18] Y. Morilla *et al.*, "Progress of CNA to become the Spanish facility for combined irradiation testing in aerospace," in *Proc. 18th Eur. Conf. Radiat. Effects Compon. Syst. (RADECS)*, Gothenburg, Sweden, Sep. 2018, pp. 250–254.

[19] A. Virtanen, R. Harboe-Sorensen, A. Javanainen, H. Kettunen, H. Koivisto, and I. Riihimaki, "Upgrades for the RADEF facility," in *Proc. IEEE Radiat. Effects Data Workshop*, Honolulu, HI, USA, Jul. 2007, pp. 38–41.

[20] H. Kettunen *et al.*, "Low energy protons at RADEF—Application to advanced eSRAMs," in *Proc. IEEE Radiat. Effects Data Workshop (REDW)*, Paris, France, Jul. 2014, pp. 147–150.

[21] E. R. van der Graaf, R. W. Ostendorf, M.-J. van Goethem, H. H. Kiewiet, M. A. Hofstee, and S. Brandenburg, "AGORFIRM, the AGOR facility for irradiations of materials," in *Proc. Eur. Conf. Radiat. Effects Compon. Syst.*, Bruges, Belgium, Sep. 2009, pp. 451–454.

[22] W. Hajdas, F. Burri, C. Eggel, R. Harboe-Sorensen, and R. D. Marino, “Radiation effects testing facilities in PSI during implementation of the proscan project,” in *Proc. IEEE Radiat. Effects Data Workshop*, Phoenix, AZ, USA, Jul. 2002, pp. 160–164.

[23] C. Weulersse, F. Miller, D. Alexandrescu, E. Schaefer, and R. Gaillard, “Assessment and comparison of the low energy proton sensitivity in 65 nm to 28 nm SRAM devices,” in *Proc. 12th Eur. Conf. Radiat. Effects Compon. Syst.*, Seville, Spain, Sep. 2011, pp. 291–296.

[24] N. Seifert, B. Gill, J. A. Pellish, P. W. Marshall, and K. A. LaBel, “The susceptibility of 45 and 32 nm bulk CMOS latches to low-energy protons,” *IEEE Trans. Nucl. Sci.*, vol. 58, no. 6, pp. 2711–2718, Dec. 2011.

[25] R. K. Lawrence, J. F. Ross, N. F. Haddad, R. A. Reed, and D. R. Albrecht, “Soft error sensitivities in 90 nm bulk CMOS SRAMs,” in *Proc. IEEE Radiat. Effects Data Workshop*, Quebec City, QC, Canada, Jul. 2009, pp. 123–126.

[26] PSTAR. *National Institute of Standards and Technology*. Accessed: May 2020. [Online]. Available: https://physics.nist.gov/PhysRefData/Star/Text/PSTAR.html

[27] J. F. Ziegler and J. P. Biersack. *Stopping and Range of Ions in Matter*. Accessed: Aug. 2018. [Online]. Available: http://www.srim.org

[28] G. Battistoni *et al.*, “Overview of the FLUKA code,” *Ann. Nucl. Energy*, vol. 82, pp. 10–18, Aug. 2015.

[29] T. T. Böhlen *et al.*, “The FLUKA code: Developments and challenges for high energy and medical applications,” *Nucl. Data Sheets*, vol. 120, pp. 211–214, Jun. 2014.

[30] B. Ye *et al.*, “Low energy proton induced single event upset in 65 nm DDR and QDR commercial SRAMs,” *Nucl. Instrum. Meth. Phys. Res. B, Beam Interact. Mater. At.*, vol. 406, pp. 443–448, Sep. 2017.

[31] J. A. Pellish *et al.*, “Criticality of low-energy protons in single-event effects testing of highly-scaled technologies,” *IEEE Trans. Nucl. Sci.*, vol. 61, no. 6, pp. 2896–2903, Dec. 2014.

[32] J. M. Trippe *et al.*, “Predicting muon-induced SEU rates for a 28-nm SRAM using protons and heavy ions to calibrate the sensitive volume model,” *IEEE Trans. Nucl. Sci.*, vol. 65, no. 2, pp. 712–718, Feb. 2018.

[33] R. A. Reed *et al.*, “Impact of ion energy and species on single event effects analysis,” *IEEE Trans. Nucl. Sci.*, vol. 54, no. 6, pp. 2312–2321, Dec. 2007.

[34] CREME. *Vanderbilt University*. Accesses: May 2020. [Online]. Available: https://creme.isde.vanderbilt.edu

[35] E. L. Petersen, J. C. Pickel, J. H. Adams, and E. C. Smith, “Rate prediciton for single event effects,” *IEEE Trans. Nucl. Sci.*, vol. 39, no. 6, pp. 1577–1599, Dec. 1992.

[36] E. H. Cannon *et al.*, “Heavy ion, high-energy, and low-energy proton SEE sensitivity of 90-nm RHBD SRAMs,” *IEEE Trans. Nucl. Sci.*, vol. 57, no. 6, pp. 3493–3499, Dec. 2010.

[37] L. D. Edmonds and K. J. Edmonds, “A method for estimating SEU rates from protons by direct ionization,” *IEEE Trans. Nucl. Sci.*, vol. 55, no. 5, pp. 2666–2678, Oct. 2008.

[38] J. A. Pellish *et al.*, “Impact of spacecraft shielding on direct ionization soft error rates for sub-130 nm technologies,” *IEEE Trans. Nucl. Sci.*, vol. 57, no. 6, pp. 3183–3189, Dec. 2010.

Publication III

A. Coronetti, R. García Alía, J. Budroweit, T. Rajkowski, I. da Costa Lopes, K. Niskanen, D. Söderström, C. Cazzaniga, R. Ferraro, S. Danzeca, J. Mekki, F. Manni, D. Dangla, C. Virmontois, N. Kerboub, A. Koelpin, F. Saigné, P. Wang, V. Pouget, A. Touboul, A. Javanainen, H. Kettunen, and R. Coq Germanicus, "Radiation hardness assurance through system-level testing: risk acceptance, facility requirements, test methodology and data exploitation," *IEEE Trans. Nucl. Sci.*, vol. 68, no. 5, pp. 958-969, May 2021.

© 2021, Coronetti et al., licensed under CC BY 4.0.

Radiation Hardness Assurance Through System-Level Testing: Risk Acceptance, Facility Requirements, Test Methodology, and Data Exploitation

Andrea Coronetti, *Student Member, IEEE*, Rubén García Alía, *Member, IEEE*, Jan Budroweit, *Associate Member, IEEE*, Tomasz Rajkowski, *Member, IEEE*, Israel Da Costa Lopes, Kimmo Niskanen, *Member, IEEE*, Daniel Söderström, *Student Member, IEEE*, Carlo Cazzaniga, Rudy Ferraro, Salvatore Danzeca, Julien Mekki, Florent Manni, David Dangla, Cedric Virmontois, Nourdine Kerboub, *Graduate Student Member, IEEE*, Alexander Koelpin, *Senior Member, IEEE*, Frédéric Saigné, Pierre Wang, *Member, IEEE*, Vincent Pouget, *Member, IEEE*, Antoine Touboul, Arto Javanainen, *Member, IEEE*, Heikki Kettunen, *Member, IEEE*, and Rosine Coq Germanicus

***Abstract*—Functional verification schemes at a level different from component-level testing are emerging as a cost-effective tool for those space systems for which the risk associated with a lower level of assurance can be accepted. Despite the promising potential, system-level radiation testing can be applied to the functional verification of systems under restricted intrinsic boundaries. Most of them are related to the use of hadrons as opposed to heavy ions. Hadrons are preferred for the irradiation of any bulky system, in general, because of their deeper penetration capabilities. General guidelines about the test preparation and procedure for a high-level radiation test are provided to allow understanding which information can be extracted from these kinds of functional verification schemes in order to compare them with the reliability and availability requirements. The use of a general scaling factor for the observed high-level cross sections allows converting test cross sections into orbit rates.**

***Index Terms*—Commercial off-the-shelf (COTS), facilities, neutrons, protons, radiation hardness assurance, risk acceptance, single-event effect (SEE), small satellites, system-level testing, test methodology, total ionizing dose (TID).**

I. Introduction

COMMERCIAL OFF-THE-SHELF (COTS) devices have been gaining popularity within the radiation community during the last two decades, thanks to their higher electrical and electronic performance, when compared to similar rad-hard parts, and to their reduced price and lead time. Similarly, interest has been growing around highly integrated solutions manufactured within the same package (e.g., system-on-chip, SoC) or assemblies of discrete devices and integrated circuits (ICs) on printed circuit boards (PCBs), boxes, or modules.

The radiation testing single-event effect (SEE) [1], [2] and total ionizing dose (TID) [3] standards developed by the community are in a continuous struggle when it comes to keeping up with the innovation introduced by brand new devices (e.g., flip-chips, multiple chips stacked within the same package, 3-D layouts) which outperform those devices the standards were tailored for. Among the main criticalities stands the necessity of making the sensitive volumes (SVs) of the devices and ICs accessible to those beams, such as heavy ions, which are typically characterized by high linear energy

---

Manuscript received January 20, 2021; revised February 12, 2021 and February 15, 2021; accepted February 18, 2021. Date of publication February 22, 2021; date of current version May 20, 2021. This work was supported by the European Union's Horizon 2020 Research and Innovation Program through the Marie Sklodowska Curie (MSC) under Grant 721624.

Andrea Coronetti is with CERN, 1211 Geneva, Switzerland, and also with the Department of Physics, University of Jyväskylä, 40014 Jyväskylä, Finland (e-mail: andrea.coronetti@cern.ch).

Rubén García Alía, Rudy Ferraro, and Salvatore Danzeca are with CERN, 1211 Geneva, Switzerland.

Jan Budroweit is with DLR, 28359 Bremen, Germany.

Tomasz Rajkowski and Pierre Wang are with 3D Plus, 78530 Buc, France.

Israel Da Costa Lopes, Kimmo Niskanen, Frédéric Saigné, Vincent Pouget, and Antoine Touboul are with the Institute d'Électronique et des Systèmes, Université de Montpellier, 34090 Montpellier, France.

Daniel Söderström and Heikki Kettunen are with the Department of Physics, University of Jyväskylä, 40014 Jyväskylä, Finland.

Carlo Cazzaniga is with the Science and Technology Facilities Council, Didcot OX11 0QX, U.K.

Julien Mekki, Florent Manni, David Dangla, and Cedric Virmontois are with CNES, 31400 Toulouse, France.

Nourdine Kerboub is with CERN, 1211 Geneva, Switzerland, and also with CNES, 31400 Toulouse, France.

Alexander Koelpin is with the Institut für Hochfrequenztechnik, TUHH, 21073 Hamburg, Germany.

Arto Javanainen is with the Department of Physics, University of Jyväskylä, 40014 Jyväskylä, Finland, and also with the Department of Electrical Engineering and Computer Science, Vanderbilt University, Nashville, TN 37235 USA.

Rosine Coq Germanicus is with Crismat, Iut, Unicaen, Ensicaen, CNRS, Normandie University, 14000 Caen, France.

Color versions of one or more figures in this article are available at https://doi.org/10.1109/TNS.2021.3061197.

Digital Object Identifier 10.1109/TNS.2021.3061197

This work is licensed under a Creative Commons Attribution 4.0 License. For more information, see https://creativecommons.org/licenses/by/4.0/

transfer (LET), but short range in matter. It is noted that for some of these layouts, decapsulation may be unachievable in some cases.

In view of the emerging challenges, the radiation community started questioning whether it was possible to perform qualification of devices and ICs that could overcome the usual inconveniences associated with standard testing (e.g., use of vacuum chambers, decapsulation) by using deeper penetrating beams, such as high-energy protons, as a proxy for heavy ions. An effort that started more than two decades ago [4], [5] and whose potentialities and limitations are summarized in a book-of-knowledge for proton board-level irradiation [6], [7].

Among the potentialities stands the verification of the soft error response of an entire set of devices at a reduced cost. At the same time, very loose bounds can be applied to hard and destructive SEEs (DSEEs) coverage without heavy-ion testing [8], [9] and, likely, the information extracted is not sufficient to perform a rigorous TID worst case analysis (WCA) for the considered devices [10].

Nevertheless, due to its cost competitiveness, system-level testing may find wider applications when it comes to space missions associated with higher risk acceptance, for example, CubeSats and NanoSats. Due to schedule and cost constraints, such space missions may not afford the cumbersome qualification based on component-level testing and the mentioned standards, often running into the highly disputable no-testing approach. For such missions, system-level testing on either a radiation model or the flight model itself may provide a higher level of confidence on the mission success likelihood while being compatible with schedule and cost restrictions.

Approaches based on system-level testing are nowadays already in use for terrestrial applications, for which neutrons can provide a sufficient coverage for DSEEs, and TID degradation is not an issue. In the accelerator field [11], system-level testing is used in a complementary fashion with respect to component-level testing in that it is used as a qualification tool only for those devices which are not critical within the design of the system and as a final verification of the system functionality.

A few examples for space applications have been reported in the literature by CNES [12], [13], DLR [14], and University of Montpellier [15]. System-level radiation testing may find wider applications in the future for space missions having criticality classes Q1 and Q2 as defined in the European Space Agency (ESA) COTS initiative review [16].

Under such promises, this work aims at synthesizing guidelines on how to perform system-level radiation testing with hadrons as a verification tool for high-risk acceptance space missions. This will include providing a common language among actors in system design, development, and verification, a guidance among the various criteria to be borne in mind in order to decide whether to go for system-level testing (and under which conditions), the best suited facilities to perform system-level testing, the test logic and procedure to follow, as well as the usage of the high-level data extracted from the test.

II. "SYSTEM" AND SYSTEM-LEVEL RADIATION TESTING

A component can be defined as any electronic device which cannot be physically partitioned without affecting its capability of delivering the intended functionality [17]. In this context, anything that is manufactured on a single chip has to be considered as a component, for example, SoC.

If the terminology "system" is applied to everything else at a higher integration level than a component, then a system can be anything from a PCB, with a few discrete components, to a whole satellite. In terms of exposing such assemblies to a radiation field, the challenges are somewhat similar over this full scale (i.e., not easy to ensure uniform irradiation with heavy ions, not easy to access all the SVs by decapsulation once all devices are placed within the system layout, not easy to perform standard TID testing). In addition, any assembly of two or more devices can lead to the generation of radiation-chain effects, that is, malfunctioning of a device which is caused from a radiation effect occurring in another device, which is feeding signals or information to the device in which the malfunctioning is observed (e.g., data corruption in a memory fed to a microprocessor).

Systems can be classified according to the following categories:

1) custom-designed based on COTS, graded, or rad-hard components;
2) modified off-the-shelf (MOTS) systems;
3) fully commercial.

Custom-designed systems based on COTS are built in-house by the satellite designer/integrator. In this case, the developer has control over part screening and selection, traceability of components, architecture, and can include radiation effects tolerance and mitigation within the system design. A typical example is the Function Generator Controller Lite (FGCLite) system for the CERN large hadron collider [18].

Fully commercial systems are manufactured by a third party (likewise components) and are intended to be used as they are. Similar to COTS devices, the satellite designer/integrator may not be provided with more information than those listed in the data sheet. Thus, part selection and traceability as well as the system architecture are often not available.

MOTS systems are an intermediate category. They are commercial systems whose radiation tolerance is improved by the end-user, thanks to collaboration agreements with the manufacturer allowing access to information related to the internal architecture and the Bill-of-Materials (BoM) to either apply mitigations or part replacement.

In general, a satellite can be thought of as a custom-designed system. However, this does not exclude some of its subsystems from being based on MOTS or fully commercial solutions. The radiation tolerance of custom-designed systems in space is generally attained through component-level testing and screening. At the other end of the spectrum, the radiation response of fully commercial systems can be established only though system-level testing, with the only alternative of a cumbersome reverse engineering process.

System-level radiation testing consists in the experimental verification of the compliance of the system to the reliability

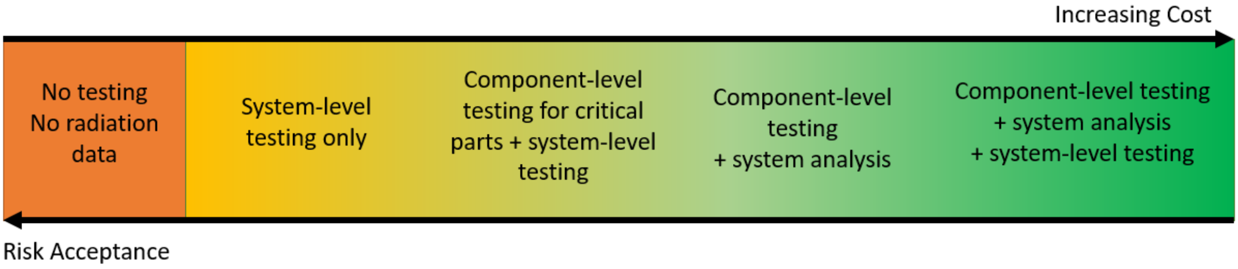

Fig. 1. System-level radiation testing with respect to risk acceptance and cost.

and availability requirements defined for the mission by operating the finished system under radiation. The extent to which the previous definition can be applied depends on whether the system-level test can provide the necessary insight to the radiation performances.

System-level radiation testing can be, in general, used to shed light upon:

1) functional reliability with the existing set of components and architecture;
2) functional availability with the embedded software and firmware and for the selected space environment;
3) criticalities arising from the radiation effects of single components or dependent faults and failures;
4) criticalities due to the design itself;
5) whether the system can perform self-recovery;
6) whether other implemented mitigation techniques (e.g., derating, transient filtering, error correction codes) are effective;
7) additional system-level mitigations to be implemented at hardware or software level.

Other than a verification tool for high-risk acceptance space missions that would alternatively follow a no-testing scheme, system-level testing can also be considered as a complement to component-level characterization for noncritical subsystems and as a final verification tool for very complex systems whose components previously sustained a complete component-level screening. For the latter, it is noted that the radiation response of complex systems in the working configuration (although they are designed following a rigorous qualification) may still be dominated by dependent faults and failures or synergistic effects that were not easy to anticipate by modeling (e.g., fault-tree analysis or failure mechanism effects and analysis). In this case, system-level testing can exercise the system as a stochastic fault injection tool in accordance with the actual probability of fault occurrence. Fig. 1 summarizes some of these concepts by positioning the various available options in terms of risk acceptance and costs.

III. RISK ACCEPTANCE

When facing the decision on whether to go for system-level radiation testing, the user shall carefully assess what kind of coverage is achievable through system testing and what are its limitations. NASA provides recommendations on this subject [19] while accounting for mission environment, application, and lifetime.

The mission environment plays a significant role in defining the risk acceptance. The two main threats to the mission reliability and success are 1) cumulative TID and total nonionizing dose (TNID) effects and 2) the stochastic DSEEs related to a single particle strike. Note that not all DSEEs are stimulated by hadrons (due to the limited energy imparted to the secondary ions [20]), whereas they can be stimulated by heavy ions provided that the LET is high enough. The reasons why these two threats may be very critical when it comes to system-level radiation testing are that:

1) this test cannot provide the wide insight necessary to perform WCA following parametric drifts induced by TID and TNID;
2) the use of hadrons does not cover the full spectra of particles encountered in the space environment and responsible for DSEEs.

These radiation effects are not only critical when it comes to determining and verifying the radiation response, but have implications on the design of the system itself by, for example, derating [21] of the components in order to avoid DSEEs. That is why whenever components susceptible to DSEEs [such as single-event burnout (SEB) or single-event gate rupture (SEGR)] have to be used in the system, a preliminary characterization at component level is always mandatory. This is in order to establish the correct derating to apply to the system. Use of default derating factors, for example, 50% in the case of aviation [22] may not provide sufficient coverage due to the presence of heavy ions in the space environment. The costs associated with a change in the design upon discovery of a failure at a late stage in the development, as it would be for verification by system-level testing only, would overpass the initially predicted cost benefits of the verification [23].

The radiation response variability over different technologies and semiconductor materials is also an important factor to consider because of several subtle radiation effects that may characterize certain devices. One of them is the enhanced low-dose-rate sensitivity (ELDRS) [24], the effect of which is to produce a larger degradation when the dose rate is lower (like in the application) than usually applied in accelerated testing. Component-level standards [3] provide recommendations for testing devices that may be susceptible to ELDRS. However, if the system-level radiation testing is performed through a single verification in a hadronic environment (i.e., an environment obtained by nuclear spallation of a high-energy proton beam with a high-Z target and usually composed of a wide spectra of protons, neutrons, and pions or a selection of them), the dose rate may represent a lower constraint than the suitable hadron flux for the SEE screening. Thus, ELDRS may end up being untested and unassessed. At the same time, ELDRS does not usually appear below a TID of 10 krad(Si) [25]. Hence, there are space missions for which it can be neglected.

Variability in the degradation among materials may be a big deal when it comes to displacement damage (DD) [26] where variability cannot only be observed in how the materials degrade, but also in the different effects produced by different particles, for example, protons as opposed to neutrons, making the non-ionizing energy loss (NIEL) approximation fall apart. Once again, these effects are likely to happen when significant TNID has to be delivered to the devices, which may not be the case for most of the systems whose reliability could be verified through system-level radiation testing.

Similar to component-level radiation testing, the outcome of a system-level radiation test is described on a pass/fail basis when it comes to reliability. The main difference is the severity that a “fail” outcome has on the system design choices. Discarding a component through prescreening comes mainly at the cost of the beam time and test preparation. A fail outcome for the entire system may, in the best case, lead to a reiteration in the design in order to solve the issue encountered during the test by mitigation and, in the worst case, may require a full redesign of an already developed prototype.

Observing only high-level radiation effects on the system without delving deeper into the component characterization may also be problematic when it comes to implement solutions that could mitigate or solve a potential source of unreliability emerging as an outcome of the test. The failure of a device in the system makes it quite easy to identify the culprit. However, there may be other failures for which clear root causes may be hard to spot, for example, when failures are caused by the concurrent degradation of several devices or by other SEE-related dependent failures. Hence, also the depth of observability in system-level radiation testing may need to be calibrated in order to increase the number of observable parameters for a correct outcome interpretation. Clearly, this may lead to longer test-bench preparations and potential compatibility issues with the facility.

Generally, a “pass” outcome from system-level radiation testing comes with a limited level of confidence. The aforementioned component-level testing standards for TID suggest performing tests over 10 parts to assess and account for the intralot variability. The outcome of a single system-level test may not be replicable over other units (even when the traceability of the single components is respected) due to:

1) one or more units may fail due to unlikely radiation effects that cannot be reproduced on all units with the targeted fluence;
2) the units may be tested under different conditions of voltage, frequency, temperature, and application, which can impact both cumulative degradation and stochastic event probability [27].

For TID and TNID, the only possibility to increase the confidence on the outcome would be to test up to margined doses, whereas for SEEs, as long as the irradiation source provides negligible levels of TID and TNID, testing the flight model may mitigate the associated risk (although testing flight equipment shall also be carefully assessed and traded based on the risk of suffering DSEEs during the verification test itself).

TABLE I

CRITICALITY CLASSES TO DEFINE SYSTEM-LEVEL EFFECTS

Class	**Impact on the system**	**Action**	**Radiation effect naming**
0	Transparent to the system functionality	No action needed	-
1	Temporary impact on functionality	No action or simple mitigation through existing equipment	Soft loss of functionality
2	Availability impacted, but no mission loss	Supervisory circuitry added to have only temporary impact	Hard loss of functionality
3	Mission reliability not achieved	May require intervention on the system design and parts	Permanent loss of functionality

IV. RADIATION EFFECTS AT SYSTEM-LEVEL AND RADIATION-TOLERANT SYSTEM

Similar to component-level effects, a common language for system-level radiation effects, may be introduced to facilitate information exchange and data portability. The aim is to describe the radiation effects so that they are strictly connected to the functional reliability and availability of the system (hence, more promptly linked to the system requirements).

The main system-level radiation effect is the loss of functionality, that is, the condition under which the system stops either temporarily or permanently to deliver its intended top-level functionality or starts delivering it outside of specifications. A classification can be made based on the criticality chart in Table I.

Class 0 effects are radiation effects occurring on a device that do not propagate up to the top-level functionality because they are either filtered, masked, or unasserted at the moment they happen. All such effects will not have any impact on the system availability or reliability. Class 0 effects are generally attained once system mitigation is implemented.

Class 1 effects can produce visible, though very mild, effects on the system functionality, which in turn may affect the system availability. They are usually originated at component level by either single-event upsets (SEUs), single-event transients (SETs), multiple-cell upsets (MCUs), or single-event functional interrupts (SEFIs). Their limited impact is due to the fact that they may last one iteration in a digital processing system or that they can last for a few fractions of a second as analog signals. Note that not all SEFIs can be included in this category. SEFIs will be classified as soft losses of functionality (SLF) only if the system can recover from them without relying on power cycling.

Class 2 effects differ from class 1 because they may have a stronger impact, mainly due to the fact that the associated downtime for the system is longer. The larger downtime is usually associated with the need of performing a power cycle of the whole system in order to remove the undesired radiation effect. This is the case of single-event latchups (SELs) and SEFIs. Note that both these events require the use of supervising circuitry to be removed. For the SEL, to detect the current increase and, for the SEFI, to detect the interruption of the function. Unless mitigated (by, e.g., scrubbing), some SEUs in the configuration logic and memory of digital devices may lead to continuous malfunctioning of the system that may not result in an SEFI. In this case, probably a power cycling will be needed as well to remove these uncorrectable SEUs. Hence, they may also be considered as hard losses of functionality (HLF).

Class 3 effects can affect the reliability of the system. Class 3 effects can have as root causes the degradation induced by TID and TNID, DSEEs, unmitigated milder SEEs, or even dependent failures. This includes SEBs, SEGRs, unprotected SELs, and unrecoverable SEFIs. In any case, the end effect observed during the test or the mission is that the system functionality is lost and cannot be recovered by any means. Note that this does not apply only to sudden failures due to stochastic events, but it also applies to continuous degradation imparted by TID and TNID. That is, the system may still be operating, but outside of the specifications that are set in the requirements (e.g., system unable to provide high enough voltage, provided output signals with too low margin with respect to noise).

The proposed classification is meant to provide a common taxonomy among users. However, other classifications [28] can be considered given their complementarity.

Other than the various degrees of loss of functionality, several degraded modes can be observed during a test. The simplest is the degradation of performance due to the parametric degradation from TID and TNID. That is, the system keeps on providing its full functionality, but nominally, this is provided at lower speed, with the system working at higher temperature or with the system requiring a higher power consumption. As long as the variations are still within the specifications, these effects are not to be considered losses, but just degradations.

Other degraded modes may be more impactful, but still not bring to end effects comparable to a loss of functionality. For instance, a few stuck bits in a memory device may reduce the total throughput of the memory, but this may be tolerable because the system does not make full use of the memory resources available. Even the failure of a single device due to SEB can be considered only a degradation if either the impact to the global functionality is limited (because the system used several of those same devices to accomplish its duty) or if there are redundancies.

Based on the pure top-level radiation effects, a radiation-tolerant system is a system that can provide its functionality under the declared specifications in the defined radiation environment while not suffering from permanent loss of functionality (PLF), that is, it is compliant with the reliability requirements. A radiation-tolerant system may suffer from HLF and SLF and manifest degraded modes of operation as long as their impact is compliant with the availability requirements.

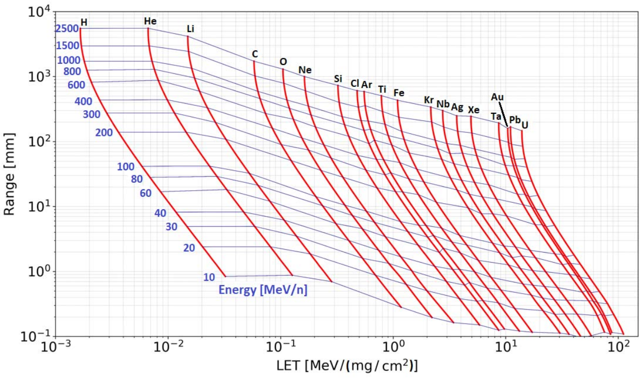

Fig. 2. Range and LET of heavy ions at various energies that are within the current ground test capabilities.

V. BEAM AND FACILITY REQUIREMENTS FOR SYSTEM-LEVEL RADIATION TESTING

Concerning the most suitable beam conditions, some requirements are provided based on the cases for which the system under consideration can be as complex as a small satellite having a 3-D layout arrangement resulting in a volume of $50 \times 50 \times 50$ cm^3. The considerations made and beam requirements proposed for such kind of system can be relaxed depending on the geometry and layout configuration of the system the user is willing to test.

Since the space environment cannot be reproduced with fidelity at ground-level accelerators (in terms of the full spectra of particles involved as well as dose rate over proton and heavy-ion fluxes ratio), some compromises have to be made in order to propose a system-level radiation testing methodology which can be applicable to the existing facilities.

The main driver for facility selection is the beam homogeneity, both depth-wise and over a wide enough surface. In order to ensure uniformity of the irradiation of the system, what standards typically require is that the homogeneity is kept within ±10%.

Homogeneous depth-wise irradiation is quite critical, as it can be ensured only by highly energetic and highly penetrating beams. In addition, the selected beam shall not be prone to strong fragmentation while traversing various layers of material at the penalty of decreasing the beam intensity and significantly altering its composition.

Fig. 2 reports the main features of protons and ions available at ground-level facilities (considering Europe and North America, although the whole state space is achieved only at NASA Space Radiation Laboratory (NSRL) [29]) nowadays based on the ion species and the primary energy. The LETs and ranges reported in the figure were calculated with Stopping and Range of Ions in Matter (SRIM) [30] using silicon as reference material. Note that if the range is used as a metric to qualify which ions may be suitable, no ions can be found that have both a surface LET of 30 MeV/(mg/cm^2) and a penetration in silicon of 5 mm. This means that it is not very likely to find ions suitable for the radiation testing of systems having an even not so deep volume. Suitable ions in terms of range would have

LETs which can indeed be found in hadron secondary ions in silicon.

Note that considering only range and surface LET of the ions is not sufficient. Indeed, the figure does not provide any information about:

1) the ion beam fragmentation as the ions traverse the various layers of material, which results in a high-intensity reduction of the primary beam;
2) the fact that even for a single one-sided PCB, the various SVs may be under diverse thicknesses of packaging and shielding material, resulting in a nonhomogeneity of the surface LET at the SV [31];
3) the SVs of the devices may be shallower or deeper, resulting in further variable energy deposition event probability.

As a result, when using ions to irradiate a system, the devices composing the system will be subjected to spectra of particles, whose LET, Bragg peak distribution, and local flux will not guarantee homogeneity.

In terms of depth-wise homogeneity, high-energy protons are a better fit for energies of a few hundreds of MeV. In this case, it is not the primary LET of the proton that matters, rather it is the LET of the secondary ions generated by hadron–silicon interactions, which can be in the range 0–15 MeV/(mg/cm^2). In addition, these ions are generated within the SV itself or in its close proximities. Protons do well for soft SEE testing; however, the initial LET of the secondary ions can often be insufficient to trigger those events requiring deep ionization tracks such as SEL, SEB, and SEGR [8], [9] because they would result in lower energy deposition events than with shallower volumes. That is why DSEE coverage cannot be ensured with proton testing.

Other than mono-energetic protons, depth-wise homogeneity can be ensured by beams with similar characteristics. This is the case of neutrons produced through nuclear spallation and of mixed fields made of protons, neutrons, and pions. This is, for instance, the case of the ChipIr [32] and the CERN Highly-AcceleRated Mixed-field (CHARM) [33] facilities. Both facilities are characterized by spectra of particles from very low energies to very high energies (up to 800 MeV at ChipIr and up to 24 GeV at CHARM).

Fig. 3 provides a comparison of penetration capabilities of the hadronic beams available in a few selected facilities with respect to the penetration capabilities of the low-Earth orbit (LEO) proton environment. The LEO proton environment was calculated with the Cosmic-Ray Environment and Effects Models (CREME) online tool [34]. It accounts for both trapped proton and galactic cosmic proton spectra determined for an orbit with 800-km altitude, 98° inclination, and solar minimum conditions. Note that for the considered CHARM spectrum in the figure, the maximum hadron energy is 3 GeV. Also, for both the LEO environment and the facilities, the plotted beam intensity accounts only for hadrons having a minimum energy of 20 MeV.

The figure is meant to compare the penetration capabilities of the various fields into growing thickness of aluminum, which is taken as a representative of the diverse shielding provided by the various layers of materials of a typical space system. The LEO proton spectrum decays very fast. After 2 cm of aluminum, its intensity is reduced to just 40% of that of the original. This is mainly due to the limited energy of trapped protons, making the most part of the environment. The three facility beams are not as strongly affected. After 2 cm of aluminum, the 200-MeV proton and ChipIr field will preserve more than 95% of the intensity of the primary beam, whereas CHARM is above 90%.

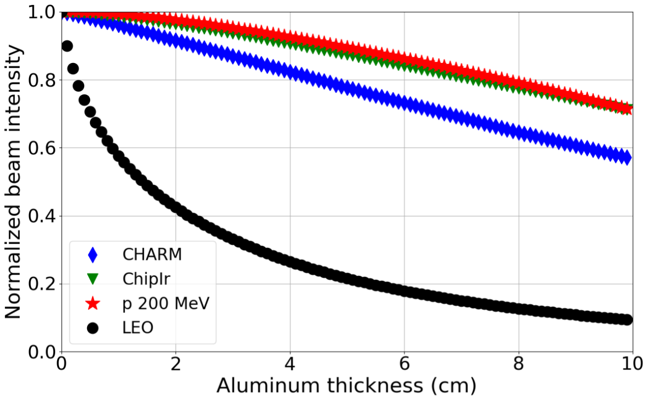

Fig. 3. Penetration depth of protons in aluminum in the LEO proton environment compared to that of the mixed field available at CHARM, that of spallation neutrons available at ChipIr and that from a 200-MeV mono-energetic proton beam. Only hadrons with energy above 20 MeV are considered for both space and facility environments.

Hence, when irradiating a system in these facilities, and provided there is no more than 2 cm of aluminum of equivalent material between the front face and the back face, the beam intensity would reduce by less than 10%, ensuring depth-wise homogeneity. For 200-MeV protons and ChipIr that homogeneity would be maintained for up to 4 cm of equivalent aluminum.

Other than depth-wise homogeneity, beams produced by nuclear spallation are widely emitted in every direction. Hence, at sufficient distance from the source, the resulting beam will be homogeneous over a large surface. This is quantified in 70 × 70 cm^2 for ChipIr and 100 × 100 cm^2 for CHARM. Mono-energetic proton beams are usually developed to irradiate devices and are associated with small field sizes. The only mono-energetic proton beam facility that can provide a field up to 60 × 60 cm^2 is NSRL.

Flux is also an important parameter for the selection of facilities for system-level radiation testing, in particular, for digital architectures. However, it is not always easy to find facilities that can provide the most appropriate test conditions. The problem is dual, since it may be due to (i) the pulsed time structure of the beam (that all the mentioned facilities have to various extents) and (ii) to the average flux itself, which is not always tunable over several orders of magnitude, thus not allowing to find an optimum for the system under test (SUT). For these two reasons, radiation effects strictly related to the beam configuration may occur that are not relevant for the final application. While it is still possible (in some cases) to have some play on the average flux, not much can be done for the time structure of the beam. This is because it is very rare (and quite impractical) to build accelerating structures reaching 1-GeV energy with continuous beam acceleration.

In conclusion, an optimal fit for all the parameters at play to perform system-level radiation testing could not be found and, in the context of this guideline, best trade-offs have been selected in order to propose a methodology that could be implemented with what is nowadays available in terms of facilities.

If the purpose of the system-level radiation test is TID, most of the classic Co-60 sources can provide both depth-wise and surface-wide homogeneity for irradiation of a system having the aforementioned volume. The existing standard for devices [3] may be of direct application in this case.

VI. DESIGN OF THE TEST

System-level testing can be quite challenging also in terms of test preparation. At a minimum, even when using the flight model as is, the user may be capable of observing and logging the following parameters (depending on the system input and output):

1) system-level SELs (sudden current increase over one of the power domains of the system);
2) SEFIs on the main control element;
3) SETs on the output voltage/current;
4) data corruption of output data streams;
5) frequency reduction;
6) drifts of input voltage and current.

Other localized effects leading to the failure of the system (e.g., device failure due to SEB) may be identified after the test.

Increasing the radiation effect observability at a lower level (i.e., down to single critical devices) would be desirable in order to better understand radiation effects and potential remedies. However, a balance has to be kept. Overloading the system with points of measurement or code-level instrumentation may alter the original system functionality and, thus, either produce new artificial radiation effects or alter the severity or rate of occurrence of the actual system-level effects. Hence, proper testing of the radiation model of the system prior to irradiation shall be accomplished in order to exclude any malfunctioning arising from the setup itself.

Other than the intrinsic non-observability of some effects (e.g., TID-induced drifts in worst case scenarios), some effects may not be observed due to constraints imposed by how the test equipment should comply with the facility interfaces and regulations. Usually, test equipment has to be kept far from the beam, thus relying on long cables. These may lead to two undesired effects: voltage drop and signal-to-noise ratio decrease. The former resulting in an insufficient biasing of the system that may even trigger undesired setup-related effects [35]. The latter resulting in data reception corruption that is not produced within the system as a radiation effect, but rather in the cable as a parasitic setup effect.

DSEE mitigation at test-bench level should be implemented when possible, or, as an alternative, at the level of the equipment in order to avoid that unprotected effects may end the test very early. Several mitigations can be implemented directly within the system or at the equipment level [36].

VII. TEST LOGIC

One of the main challenges for the execution of a proper system-level radiation test is under which conditions the system has to be tested in order to provide representative information about reliability and availability, while not masking fault/failure modes due to the way the system is operated. In component-level testing, one can perform device radiation testing and data analysis based on worst case conditions (e.g., of biasing, temperature, frequency). However, when operated in a system, the devices are set to work under a specific envelope of conditions (if not just a single one that can be quite far from worst case).

While it is sometimes suggested to test under real working conditions, it is also true that systems are very rarely designed to work under a unique set of parameters or modes. For instance, when testing a satellite, this may have several different modes of operation (scientific acquisition, data downlink, telemetry and command uplink and downlink, battery recharging, etc.), which may not employ all parts of the system at the same time or may employ those parts under different loads.

At the same time, even finding a single system, worst case condition may not be so easy due to competing effects and sensitivities among devices within the system. For instance, device-level standards [1], [2] mention that the worst case for SEL would be high temperature, whereas for SEB it would be room temperature.

The situation becomes even more critical when only one SUT is available and the radiation source also provides cumulative degradation by TID/TNID. Some drivers that can help defining the best test configuration within the operating state space that would provide a representative insight for a system functional verification are:

1) the types of radiation effects that the system is expected to be prone to during the test and whose occurrence would potentially set a critical situation for the system;
2) the conditions under which the system is supposed to be operated for most of the time during its intended mission;
3) the conditions imposing the largest electrical loads on the widest set of devices;
4) performing a multipurpose test (whenever low TID/TNID is deposited in the system):
    a) to exclude DSEEs;
    b) running under highest data load and frequency to find upper bounds to data corruption rates.

Generally, performing a “duty-cycle” radiation testing of the satellite encompassing the various operating modes may be suitable in order to exercise the system under representative conditions whenever a clear worst case condition for the whole system cannot be found. Defining a parametric envelope for the set of variables under test can also provide a valuable option.

One critical aspect of the system-level test is to select a flux that does not lead the system into HLF with a too high rate. In addition, a moderate flux can ensure that the observed events are linear with the fluence and not the combination of accumulated events over a short time period due to the high flux of the accelerated test, which would not be representative of the low-flux conditions found in space.

The last two points are particularly critical when testing a system whose component radiation data are not known because it would be much harder to interpret whether the observed radiation effects are caused by the beam configuration or actual system faults. In order to mitigate that it is strongly advised to start the test with a low flux and then ramp it up and decide upon the observed system response. Generally, full analog systems can sustain stronger fluxes than digital systems, but it is advised not to go above 10^7 hadrons/cm^2/s. Full digital systems, on the other hand, are often plagued by flux-induced effects for fluxes higher than 10^6 hadrons/cm^2/s.

Additionally, when using the duty-cycle radiation testing scheme, it is recommended to set the flux so that, on average, at least ten consecutive duty cycles can be completed between two consecutive HLFs. For other cases, in general, it is recommended to set the flux so that the time between two HLFs is, on average, at least a 100 times the recovery time of the system.

When more than one SUT unit is available for testing (in general, for systems to be produced in hundreds or thousands of units), the worst case condition for the system can be found empirically by testing the various SUTs under different conditions. Some of the facilities previously mentioned allow performing the parallel irradiation of many systems, thanks to their broad beam. A few additional units can then be tested under the identified worst case condition to improve the level of confidence on the positive outcome of the first SUT unit.

VIII. TEST OUTCOME AND DATA EXPLOITATION

A. Functional Reliability

As earlier said, the test outcome on reliability is defined on a pass/fail basis. For the pass case (no PLF) against stochastic events of radiation, a cross section with 2σ level of confidence can be determined based on the statistical Poisson distribution [37] and the test fluence

$$\sigma_{\mathrm{PLF}} \leq \frac{3.7}{\Phi_{\mathrm{HEH}}} \quad \mathrm{cm}^2/\mathrm{system}. \tag{1}$$

The high-energy hadron (HEH) fluence Φ_{HEH} can be used as a general measurement of the flux for a hadronic environment. The general approximation behind the definition of HEH [38] is that all hadrons (in N_p amount) from an energy above 20 MeV can be considered equivalent for SEE triggering, so that

$$\Phi_{\mathrm{HEH}} = \sum_{i=1}^{N_p} \int_{20\,\mathrm{MeV}}^{\infty} \Phi_i(E)\,dE. \tag{2}$$

The main justification is that DSEEs can be triggered only by hadrons with energy above 20 MeV. Note that when combined with this fluence, the previously defined σ_{PLF} is assumed to be a step function starting at 20 MeV. This may generally yield higher rates than expected, although it was shown that usually these are within a factor of 1.5 for irradiations done at CHARM [39], [40].

TABLE II

ALPHA FACTORS (UNITS OF $\mathrm{cm}^{-2}\,\mathrm{day}^{-1}$) FOR THE CONSIDERED TEST FACILITIES WITH RESPECT TO THE LEO ENVIRONMENT (800 km, 98°, SOLAR MINIMUM, 100 MILS OF AL, TRAPPED PROTONS, AND GALACTIC COSMIC RAYS) FOR THE SEL-LIKE AND SEU-LIKE VOLUMES

	SEL SV	**SEU SV**
CHARM	1.03 x 10^7	8.82 x 10^6
ChipIr	1.35 x 10^7	7.25 x 10^6
200 MeV protons	1.08 x 10^7	1.05 x 10^7

When it comes to TID/TNID, the test outcome is pass if the system did not experience PLF up to the targeted (and potentially margined) doses. The level of confidence on the outcome can even be increased if the test is prolonged to the ultimate dose required to observe the ultimate failure of the system.

Only for failures due to unprotected SELs and unmitigated SEFIs can the user easily implement mitigation out of a fail outcome. Failure by TID/TNID and DSEEs may, on the other hand, require either part replacement or system design reiteration, which are not straightforward.

B. Functional Availability

Cross sections for HLF and SLF can be determined similar to component-level cross sections. The actual root cause of the system-level effect may not be required to be determined (e.g., whether it was an SEFI or SEL) as long as the system is protected against permanent damage. Root causes may, on the other hand, be crucial whenever the loss of functionality rate is too high and a reduction or solution could be found by mitigation.

Other than the cross section, the typical system downtime associated with the observed interruption can be used to determine the actual availability of the system. Note that the calculated availability for the mission based on environmental fluxes, test cross sections, and downtime may be strongly impacted by the mode of operation set for the system. Hence, calculating a rate for each mode of operation may be better.

C. Environmental Similitude for Stochastic Events

The similitude in terms of energy deposition event response among space proton-dominated environments and the proposed facility hadronic environments can allow calculation of the expected on-orbit rates whenever events are observed during the test [41], [42]. This concerns only those events that can be triggered by hadron–silicon nuclear recoils, that is, it is applicable to those devices with a low enough volume equivalent LET ($\mathrm{LET}_{\mathrm{eq},V}$) threshold. Not much can be said about those events that cannot be stimulated by the hadronic environment of the test and only very weak upper bounds on the worst device response to heavy ions can be applied, typically in the order of 0.01 event/device/day for mild environments and even weaker for harsher ion environments.

The on-orbit event rate can be directly obtained from the measured cross section during the test in the proposed facilities by multiplication of the latter for an appropriate factor called α [42] obtained from the following derivation:

$$R_{\text{test}}\left[\text{day}^{-1}\right] = \Phi_{\text{HEH}}\left[\text{day}^{-1}\text{cm}^{-2}\right] \cdot \sigma_{\text{HEH}}\left[\text{cm}^{2}\right] \tag{3}$$

$$\text{acc. factor} = \frac{\Phi_{\text{test}}\left(>\text{LET}^{*}_{\text{eq},V}\right)}{\Phi_{\text{space}}\left(>\text{LET}^{*}_{\text{eq},V}\right)} \tag{4}$$

$$\begin{aligned} R_{\text{space}}\left[\text{day}^{-1}\right] &= \frac{R_{\text{test}}\left[\text{day}^{-1}\right]}{\text{acc. factor}} \\ &= \frac{\Phi_{\text{space}}\left(>\text{LET}^{*}_{\text{eq},V}\right)}{\Phi_{\text{test}}\left(>\text{LET}^{*}_{\text{eq},V}\right)} \cdot \Phi_{\text{HEH}} \cdot \sigma_{\text{HEH}} \end{aligned} \tag{5}$$

$$\alpha\left(\text{LET}^{*}_{\text{eq},V}\right) = \Phi_{\text{space}}\left(>\text{LET}^{*}_{\text{eq},V}\right) \cdot \frac{\Phi_{\text{HEH}}}{\Phi_{\text{test}}\left(>\text{LET}^{*}_{\text{eq},V}\right)}. \tag{6}$$

Note that this can be applied also to heavy-ion on-orbit rate predictions whenever the LET threshold of the device is low enough.

Fluktuierende Kaskade (FLUKA) 4.0 [43], [44] is used to perform Monte-Carlo (MC) simulations of the energy deposition event response of a LEO environment for an orbit of 800 km, 98°, solar minimum conditions, 100 mils of aluminum, and including both the trapped protons and the galactic cosmic-ray heavy ions with angular isotropic distribution. MC simulations are also used to extract the energy deposition event response for the CHARM mixed field, the ChipIr spallation neutron beam, and a mono-energetic 200-MeV proton beam. The SVs under consideration are two: a first one is representative of certain SEL structures (20 × 4 μm surface with 3 μm thickness [45]) and the second one is representative of highly scaled SEU structures (0.31 × 0.31 μm surface with 0.31-μm thickness [46]).

Note that, unlike soft errors, the use of hadrons for the test is insufficient to screen against SELs for all those devices that may be characterized by either a low heavy-ion saturation cross section or a high LET threshold. This limitation mainly comes from the fact that hadrons are quite inefficient at producing secondary ions of sufficient $\text{LET}_{\text{eq},V}$. For instance, about 10^4 ions/cm^2 having a $\text{LET}_{\text{eq},V} > 3$ MeV/(mg/cm^2) will be generated for a fluence of 10^{11} HEH/cm^2 and a volume with 3-μm thickness, that is, much lower than the typical ion fluence used for standard heavy-ion component-level testing. More ions can be produced with a higher fluence, but this has to be traded off with the increased ionizing and non-ionizing dose deposited by the primary charged hadrons. In this respect, 10^{11} HEH/cm^2 can be considered a good trade-off value considering the deposited dose of 56 Gy(Si) for a pure proton beam and the amount of secondary ions generated, also considering that little can be gained in terms of $\text{LET}_{\text{eq},V}$ of the secondary ions themselves. The same neutron fluence will deposit less than 5 Gy(Si) while providing secondary ions in similar amount.

The choice of 3-μm thickness for the SEL SV is also representative of only a few devices, but it can be considered representative for those devices that can suffer from SELs in hadronic environment as this size would be quite compatible with typical secondary ion ranges from hadrons' inelastic reactions. In other words, devices with thicker SVs would typically not experience events in hadronic environments, unless having an extremely low LET onset.

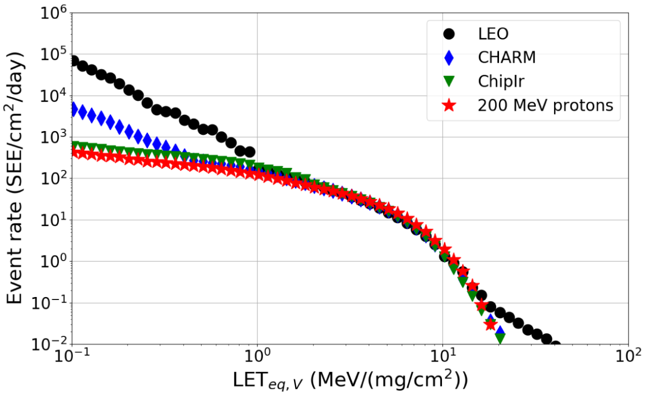

Fig. 4. Event rate normalized to a device surface of 1 cm^2 per day for the LEO environment (800 km, 98°, solar minimum, 100 mils of Al, trapped protons, and galactic cosmic rays) compared with those from CHARM, ChipIr, and 200-MeV protons scaled by the respective alpha factors. The volume considered for the MC calculations is typical of certain SEL structures.

For these reasons, the proposed analysis has to be taken as a reliable event rate prediction tool for the space environment of concern only and solely when a significant amount of events are seen with hadron testing.

The purpose of using very different structures is to check whether a general alpha factor can be derived no matter the SV and whether this can be used to calculate on-orbit rates affecting availability even whenever the originating cause of the observed system-level fault is unknown.

One of the main assumptions is the choice of the $\text{LET}^{*}_{\text{eq},V}$ at which the facility energy deposition distributions have to be scaled with respect to that of the space environment. However, α weakly varies for $\text{LET}^{*}_{\text{eq},V}$ in the 1–10 MeV/(mg/cm^2) range, regardless of the considered facility. Thus, a value of 3 MeV/(mg/cm^2) [42] can suitably represent both the events originating from proton indirect ionization and heavy-ion direct ionization.

The alpha factors for the two SVs and the three facilities for the mentioned LEO environment are reported in Table II. From these calculations, 200-MeV protons provide basically the same α regardless of the considered volumes, whereas CHARM and ChipIr are supposed to provide a lower estimate for SEU than SEL.

The respective α are used to calculate the plots in Figs. 4 and 5, for the SEL SV and the SEU SV, respectively. The plots show the event rate in units of SEE/day normalized to a device-sensitive surface of 1 cm^2. The facility rates are also divided by the acceleration factors of the test. By selecting $\text{LET}^{*}_{\text{eq},V} = 3$ MeV/(mg/cm^2) for α, the event rate curves tend to overlap for $\text{LET}_{\text{eq},V} > 1$ MeV/(mg/cm^2) with just a small bunch of heavy-ion events at high $\text{LET}_{\text{eq},V}$ not covered.

Fig. 6 shows the alpha factor as a function of $\text{LET}_{\text{eq},V}$ for various facilities and SEL SVs with 3- and 10-μm thicknesses. Other than reinforcing the generality for the choice of the

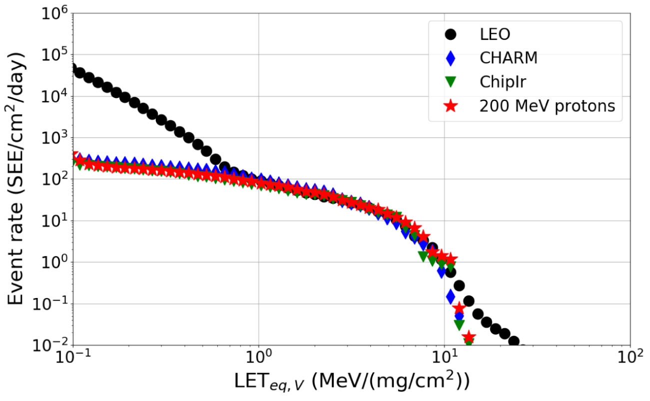

Fig. 5. Event rate normalized to a device surface of 1 cm^2 per day for the LEO environment (800 km, 98°, solar minimum, 100 mils of Al, trapped protons, and galactic cosmic rays) compared with those from CHARM, ChipIr, and 200-MeV protons scaled by the respective alpha factors. The volume considered for the MC calculations is typical of certain highly scaled SEU structures.

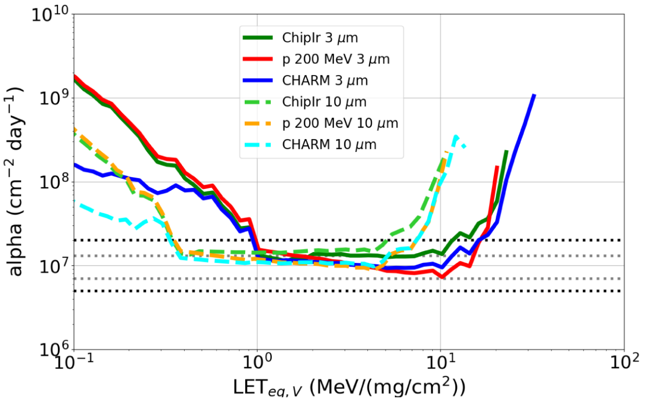

Fig. 6. Alpha factor as a function of the volume equivalent LET for the SEL SV with 3 μm and 10 μm thicknesses for the various facilities.

$LET^*_{eq,V}$ for the 3-μm thickness, the plot shows that for thicker volumes, the alpha factor diverges rather swiftly above 3 MeV/(mg/cm^2). This shows that the method works well for those devices whose SEL SV is rather thin. These are usually the devices for which SELs in hadron environment can be observed. So, the validity of the method is not compromised. Devices having thicker volumes, on the other hand, usually do not display SELs in hadron environment. To this end, it is reminded that the alpha method can be considered accurate only if events are seen with hadrons, whereas not much can be concluded for 0 events.

All in all, despite the use of very different volumes and test environments, the α is not seen to vary much, to the point that a general value of (1 ± 0.3) × 10^7 cm^{-2} day^{-1} can be assumed for the derivation of on-orbit rates from the event cross section attained at one of the proposed test facilities.

As a verification of the suitability of this method for predicting on-orbit event rates, a couple of comparisons are performed. In the first, for SEU, a few state-of-the-art devices are chosen [46]. Both the heavy-ion and high-energy proton responses of these devices are known, so that it is possible to calculate the predicted event rates through the standard Weibull fits [47] and then compare them with those calculated with $\alpha = 1 \times 10^7$ cm^{-2} day^{-1} and the 200-MeV proton data-point. The data are compared in Table III. For all the considered devices, the rate calculated through α is within ±30%, which is in agreement with the earlier specified uncertainty.

TABLE III

Expected Event Rates (in Units of Events/Device/Day) for Some Devices Sensitive to SEU [46] Based on the Weibull Fits of the Known Heavy-Ion and High-Energy Proton Cross Sections and on the Use of the α Factor From the Cross Sections Measured in a 200-MeV Proton Facility

	Weibull ions and protons	α x $\sigma_{proton-200MeV}$
ISSI	6.08	5.03
Cypress	16.84	13.42
RADSAGA	1.63	1.42

TABLE IV

Comparison of the Event Rates (in Units of Events/Device/Day) for Some Devices Sensitive to SEL [42] With the Expected Event Rates From the Multiplication of the α Factor and the Cross Sections Measured at CHARM

	On-orbit rate	α x $\sigma_{HEH-CHARM}$
IS61LV5128AL-12	1.81 x 10^{-1}	1.46 x 10^{-1}
K6R4008V1D	2.57 x 10^{-3}	2.66 x 10^{-3}
AS7C34096A	1.36 x 10^{-3}	1.73 x 10^{-3}

For SEL, on-orbit event rates are available [42], so that it is possible to compare the proposed prediction method with actual in-space observations. In this case, the same $\alpha = 1 \times 10^7$ cm^{-2} day^{-1} is used to predict the event rate from the cross section measured at the CHARM facility. The data are compared in Table IV. The agreement with the predicted data and the in-space measured data is again within ±30%.

Note that the α changes with the orbit, although it is possible to calculate it for various orbits and just perform a rescaling of the value here proposed. The other limitation is that this method can work well for proton-dominated environments, which are usually those for which system-level testing is anyway best suited. Finally, the coverage is not guaranteed for SEL associated with thicker volumes (e.g., 10 μm), although it is also quite unlikely to observe any event during hadron testing for such deep SVs.

This method can be generally extended to high-level losses of functionality observed during the test to calculate their expected rate on orbit and the impact on availability.

IX. SUMMARY AND CONCLUSION

Cost-effective radiation testing schemes adapted to the functional verification of large ensembles of devices, subsystems, and full small satellites are flourishing. A general top-down approach to functional verification through system-level radiation testing that can be employed for higher risk acceptance space missions was proposed.

Risk acceptance is the key parameter when it comes to decide whether to pursue a system-level radiation verification scheme. Several aspects of standard space qualification are intrinsically overlooked for this kind of qualification scheme, including TID WCA, ELDRS, and DD deviations from the NIEL scaling among different materials and DSEE coverage.

In addition, system-level testing of one or a few units is associated with limited level of confidence even following a pass outcome, and observability of root cause events may not always be achieved. For all these reasons, system-level radiation testing shall be seen as a tool that can cover for the functional verification of those systems lying in the gray area between "no-testing" and qualification based on standards for component-level testing. Given the long list of intrinsic limitations associated with system-level radiation testing, this methodology shall not be seen as a cheap replacement of standard qualification whenever risk acceptance would not allow so.

A taxonomy for system-level radiation effects based on their criticality was proposed. The state space of system-level radiation testing is wider than the proposed top-level functional verification given that the latter can be combined with some standard component-level qualification. However, the scope of this work was to take the very opposite end of the state space and propose guidelines on how to extract precious information about functional verification even when using the simplest radiation model possible, that is, the system "as is." Engineering and radiation models of the system shall be consistent and should be carefully verified prior to irradiation as well as the test setup.

The proposed methodology is based on the use of deeply penetrating beams (i.e., protons, neutrons, or mixed fields) due to the intrinsic low penetration and fragmentation of ions and to the relatively large volumes considered. Currently, there are only a handful of facilities fulfilling the requirements for the irradiation of bulky systems. Other considerations related to beam characteristics such as the flux may have to be assessed when choosing the most suitable facility for the test. Sometimes, even the test infrastructure available at the facility (e.g., cabling length, test equipment shielding) may play a role on whether to pursue this kind of qualification due to radiation effects observability limitations. Other test methodologies can be built upon these general considerations to, for instance, irradiate portions of the system or by making use of heavy ions for the irradiation of single boards.

Test preparation for these kinds of tests may be as critical as the test itself. A good balance between what it is expected to be observed and in-depth observability shall be kept in order not to affect the system radiation response in other ways. Whenever the system itself is not equipped with protections from potentially destructive radiation effects, it is good practice to protect it at the level of the monitoring equipment.

Tailoring an effective test plan to fulfill all the objective of the test is also similarly important. Testing the system in a large enough set of configurations may help in identifying worst case conditions and may provide more confidence than simply testing the system in the "real" condition (which is probably just an educated guess of how the system will most likely be used). Whenever radiation data of the system and its components are not available, it is suggested to always start from a low enough flux and ramp up only when flux-dependent events cannot be observed. In addition, the frequency of HLFs shall be much smaller than the standard duty-cycle execution time of the system.

Data exploitation in terms of reliability comes with a limited level of confidence whenever a single unit is tested. More confidence can be built on availability provided a sufficient amount of events is observed with hadrons and for those mission environments dominated by protons. The environmental similitude among the test facility energy deposition environments and those of certain space orbits (both in terms of proton and heavy-ion energy depositions) can, if events are seen during the test, allow the calculation of expected on-orbit rates relying on the use of the alpha factor method. This was shown to return mission rates compatible with actual on-orbit measurements and the classic Weibull prediction. While the alpha factor varies with the orbit, it was shown to vary just slightly among the different hadronic beams and SVs considered, meaning that the alpha factor could be easily rescaled just based on the orbit. Nonetheless, it shall be borne in mind that the hadron test may be blind to certain potentially destructive events triggered by heavy ions and that the proposed rate calculation method can be used to predict only and solely events that could be observed during the test with hadrons.

ACKNOWLEDGMENT

The authors recognize the valuable feedback provided by Renaud Mangeret from Airbus, Françoise Bezerra from CNES, and Jonathan Pellish and Anthony Sanders from NASA during the write-up of the guideline document related to this article.

REFERENCES

[1] *Single Event Effects Test Method and Guidelines*, Eur. Space Compon. Coordination, ESCC 25100, ESA, Paris, France, Oct. 2014.

[2] *Single-Event Burnout and Single-Event Gate Rupture*, document MIL-STD-750-1 Method 1080.1, United States Dept. Defense, Nov. 2006.

[3] *Total Dose Steady-State Irradiation Test Method*, Eur. Space Compon. Coordination, ESCC 22900, ESA, Paris, France, Oct. 2010.

[4] P. M. O'Neill, G. D. Badhwar, and W. X. Culpepper, "Risk assessment for heavy ions of parts tested with protons," *IEEE Trans. Nucl. Sci.*, vol. 44, no. 6, pp. 2311–2314, Dec. 1997.

[5] K. A. LaBel *et al.*, "Radiation evaluation method of commercial off-the-shelf (COTS) electronic printed circuit boards (PCBs)," in *Proc. 5th Eur. Conf. Radiat. Effects Compon. Syst. (RADECS)*, Fontevraud, France, Sep. 1999, pp. 528–534.

[6] S. M. Guertin. *Board Level Proton Testing Book of Knowledge for NASA Electronic Parts and Packaging Program*. Accessed: Oct. 2018. [Online]. Available: https://trs.jpl.nasa.gov/handle/2014/45964

[7] S. M. Guertin, "Lessons and recommendations for board-level testing with proton," in *Proc. Small Satell. Conf.*, Logan, UT, USA, 2018, pp. 1–7. Accessed: Jun. 2019. [Online]. Available: https://digitalcommons.usu.edu/smallsat/2018/all2018/446/

[8] R. Ladbury, J.-M. Lauenstein, and K. P. Hayes, "Use of proton SEE data as a proxy for bounding heavy-ion SEE susceptibility," *IEEE Trans. Nucl. Sci.*, vol. 62, no. 6, pp. 2505–2510, Dec. 2015.

[9] R. L. Ladbury and J.-M. Lauenstein, "Evaluating constraints on heavy-ion SEE susceptibility imposed by proton SEE testing and other mixed environments," *IEEE Trans. Nucl. Sci.*, vol. 64, no. 1, pp. 301–308, Jan. 2017.

[10] R. Mangeret, "Radiation hardness assurance: How well assured do we need to be?" in *Proc. NSREC Short Course, Part II*, Waikoloa, HI, USA, Jul. 2018, pp. 1–64.

[11] S. Uznanski *et al.*, "Qualification of electronics components for a radiation environment: When standards do not exist," in *Proc. RADECS Short Course, Part 4B*, Geneva, Switzerland, Oct. 2017, pp. 1–55.

[12] F. Bezerra *et al.*, "Evaluation of an alternative low cost approach for SEE assessment of a SoC," in *Proc. 17th Eur. Conf. Radiat. Effects Compon. Syst. (RADECS)*, Geneva, Switzerland, Oct. 2017, pp. 418–422.

[13] A. Coronetti *et al.*, “Mixed-field radiation qualification of a COTS space on-board computer along with its CMOS camera payload,” in *Proc. RADECS Conf.*, 2019.

[14] J. Budroweit, S. Mueller, M. Jaksch, R. G. Alía, A. Coronetti, and A. Koelpin, “*In-situ* testing of a multi-band software-defined radio platform in a mixed-field irradiation environment,” *Aerospace*, vol. 6, no. 10, Sep. 2019, Art. no. 106.

[15] R. Secondo *et al.*, “System level radiation characterization of a 1U CubeSat based on CERN radiation monitoring technology,” *IEEE Trans. Nucl. Sci.*, vol. 65, no. 8, pp. 1694–1699, Aug. 2018.

[16] *ESA COTS Initiative, WG2-3 Synthesis*, ESA-ESTEC, Noordwijk, The Netherlands, Nov. 2019.

[17] *Electropedia, IEC*. Accessed: Jan. 2020. [Online]. Available: http://www.electropedia.org

[18] S. Uznanski, B. Todd, A. Dinius, Q. King, and M. Brugger, “Radiation hardness assurance methodology of radiation tolerant power converter controls for large hadron collider,” *IEEE Trans. Nucl. Sci.*, vol. 61, no. 6, pp. 3694–3700, Dec. 2014.

[19] *Guidelines for Verification Strategies to Minimize Risk Based on Mission Environment, Application and Lifetime (MEAL)*. NASA/TM-2018-220074. Accessed: Jan. 2021. [Online]. Available: https://ntrs.nasa.gov/citations/20180007514

[20] C. Weulersee *et al.*, “Preliminary guidelines and predictions for 14-MeV neutron SEE testing,” *IEEE Trans. Nucl. Sci.*, vol. 64, no. 8, pp. 2268–2275, Aug. 2017.

[21] *ECSS-Q-ST-30-11C: Space Product Assurance—Derating EEE Components*, ESA-ESTEC, Noordwijk, The Netherlands, 2011.

[22] International Electrotechnical Commission, *Process Management for Avionics—Atmospheric Radiation Effects—Part 4: Design of Hugh Voltage Aircraft Electronics Managing Potential Single Event Effects*, Standard IEC 62396-4, Sep. 2013.

[23] M. Campola and J. Pellish, “Radiation hardness assurance: Evolving for new space,” in *Proc. RADECS Short Course, Part V*, Montpellier, France, Sep. 2019, pp. 1–35.

[24] M. R. Shaneyfelt *et al.*, “Thermal-stress effects and enhanced low dose rate sensitivity in linear bipolar ICs,” *IEEE Trans. Nucl. Sci.*, vol. 47, no. 6, pp. 2539–2545, Dec. 2000.

[25] R. L. Pease, “2008 update to the ELDRS bipolar linear circuit data compendium,” in *Proc. Eur. Conf. Radiat. Effects Compon. Syst.*, Jyväskylä, Finland, Sep. 2008, pp. 75–78.

[26] R. Ferraro *et al.*, “COTS optocoupler radiation qualification process for LHC applications based on mixed-field irradiations,” *IEEE Trans. Nucl. Sci.*, vol. 67, no. 7, pp. 1395–1403, Jul. 2020.

[27] F. Irom. *Guideline for Ground Radiation Testing of Microprocessors in the Space Radiation Environment*. Accessed: Mar. 2019. [Online]. Available: https://trs.jpl.nasa.gov/handle/2014/40790

[28] *SEECA, Single Event Effect Criticality Analysis*. NASA. Accessed: Jan. 2021. [Online]. Available: https://radhome.gsfc.nasa.gov/radhome/papers/seeca2.htm

[29] *NASA Space Radiation Laboratory, Brookhaven National Laboratory*. Accessed: Nov. 2019. [Online]. Available: https://www.bnl.gov/nsrl/userguide/

[30] J. F. Ziegler and J. P. Biersack. *Stopping and Range of Ions in Matter*. Accessed: Aug. 2018. [Online]. Available: http://www.srim.org

[31] A. de Bibikoff and P. Lamberbourg, “Method for system-level testing of COTS electronic board under high-energy heavy ions,” *IEEE Trans. Nucl. Sci.*, vol. 67, no. 10, pp. 2179–2187, Oct. 2020.

[32] C. Cazzaniga and C. D. Frost, “Progress of the scientific commissioning of a fast neutron beamline for chip irradiation,” *J. Phys., Conf. Ser.*, vol. 1021, May 2018, Art. no. 012037.

[33] J. Mekki, M. Brugger, R. G. Alia, A. Thornton, N. C. D. S. Mota, and S. Danzeca, “CHARM: A mixed field facility at CERN for radiation tests in ground, atmospheric, space and accelerator representative environments,” *IEEE Trans. Nucl. Sci.*, vol. 63, no. 4, pp. 2106–2114, Aug. 2016.

[34] *CREME, Vanderbilt University*. Accessed: Jul. 2020. [Online]. Available: https://creme.isde.vanderbilt.edu

[35] T. Rajkowski *et al.*, “Analysis of SET propagation in a system in package point of load converter,” *IEEE Trans. Nucl. Sci.*, vol. 67, no. 7, pp. 1494–1502, Jul. 2020.

[36] H. Quinn, “Challenges in testing complex systems,” *IEEE Trans. Nucl. Sci.*, vol. 61, no. 2, pp. 766–786, Apr. 2014.

[37] G. M. Swift, “SEE testing lessons from Dickens, Scounting and Oz,” in *Proc. SEE Symp.*, May 2006.

[38] K. Roeed *et al.*, “Method for measuring mixed field radiation levels relevant for SEEs at the LHC,” *IEEE Trans. Nucl. Sci.*, vol. 59, no. 4, pp. 1040–1047, Aug. 2012.

[39] A. Coronetti *et al.*, “The pion single-event effect resonance and its impact in an accelerator environment,” *IEEE Trans. Nucl. Sci.*, vol. 67, no. 7, pp. 1606–1613, Jul. 2020.

[40] N. Kerboub *et al.*, “Comparison between in-flight SEL measurement and ground estimation using different facilities,” *IEEE Trans. Nucl. Sci.*, vol. 66, no. 7, pp. 1541–1547, Jul. 2019.

[41] C. C. Foster, P. M. O’Neill, and C. K. Kouba, “Risk assessment based on upset rates from high energy proton tests and Monte Carlo simulations,” *IEEE Trans. Nucl. Sci.*, vol. 55, no. 6, pp. 2962–2969, Dec. 2008.

[42] R. G. Alia *et al.*, “Simplified SEE sensitivity screening for COTS components in space,” *IEEE Trans. Nucl. Sci.*, vol. 64, no. 2, pp. 882–890, Feb. 2017.

[43] G. Battistoni *et al.*, “Overview of the FLUKA code,” *Ann. Nucl. Energy*, vol. 82, pp. 10–18, Aug. 2015.

[44] T. T. Böhlen *et al.*, “The FLUKA code: Developments and challenges for high energy and medical applications,” *Nucl. Data Sheets*, vol. 120, pp. 211–214, Jun. 2014.

[45] R. G. Alia *et al.*, “SEL cross section energy dependence impact on the high energy accelerator failure rate,” *IEEE Trans. Nucl. Sci.*, vol. 61, no. 6, pp. 2936–2944, Dec. 2014.

[46] A. Coronetti *et al.*, “Assessment of proton direct ionization for the radiation hardness assurance of deep sub-micron SRAMs used in space applications,” *IEEE Trans. Nucl. Sci.*, to be published.

[47] E. L. Petersen, J. C. Pickel, J. H. Adams, and E. C. Smith, “Rate prediciton for single event effects,” *IEEE Trans. Nucl. Sci.*, vol. 39, no. 6, pp. 1577–1599, Dec. 1992.

Publication IV

A. Coronetti, R. García Alía, F. Cerutti, W. Hajdas, D. Söderström, A. Javanainen, and F. Saigné, "The pion single-event latch-up cross-section enhancement: mechanisms and consequences for accelerator hardness assurance," *IEEE Trans. Nucl. Sci.*, vol. 68, no. 8, pp. 1613-1622, August 2021.

© 2021, Coronetti et al., licensed under CC BY 4.0.

The pion single-event latch-up cross-section enhancement: mechanisms and consequences for accelerator hardness assurance

Andrea Coronetti, Rubén García Alía, Francesco Cerutti, Wojtek Hajdas, Daniel Söderström, Arto Javanainen, and Frédéric Saigné

***Abstract*—Pions make up a large part of the hadronic environment typical of accelerator mixed-fields. Characterizing device cross-sections against pions is usually disregarded in favour of tests with protons, whose single-event latch-up cross-section is, nonetheless, experimentally found to be lower than that of pions for all energies below 250 MeV. While Monte-Carlo simulations are capable of reproducing such behavior, the reason of the observed pion cross-section enhancement can only be explained by a deeper analysis of the underlying mechanisms dominating proton-silicon and pion-silicon reactions. The mechanisms dominating the single-event latchup response are found to vary with the energy under consideration. While a higher pion nuclear reaction rate, i.e., probability of interaction, can explain the observed latchup cross-section enhancement at energies $>$ 100 MeV, it is the volume-equivalent linear energy transfer (LET$_{EQ}$) of the secondary ions that keeps the pion latchup response high at lower energies. The higher LET$_{EQ}$ of secondary ions from pion-silicon interactions are caused by the pion absorption mechanism, which is highly exothermic. In spite of the observed higher cross-section for pions, the high-energy hadron approximation is found to still provide reliable estimations of the latch-up response of a device in mixed-field.**

***Index Terms*—Pions, protons, neutrons, accelerator, SEL, cross-section, radiation hardness assurance, FLUKA, nuclear interactions.**

I. INTRODUCTION

CHARGED pions are hadrons which, by inelastic interaction with the target nuclei, can release secondary ions capable of causing hazards as critical as single-event latch-up (SEL) in electronic devices. Although SEL hardening techniques exist [1], they are rarely applied in commercial static random access memories (SRAMs), which are typically characterized by very high heavy ion cross-sections [2] and can exhibit latchup also in hadron environments [3], [4].

An experimental study on pion single-event upset (SEU) and SEL cross-sections was performed in [5]. For SEU, the pion cross-section shape directly reflected the typical reaction cross section resonance in silicon in the 75-250 MeV energy region [6]. However, for SEL, the measured pion cross-section enhancement was not limited to the established resonance region, but extended at lower energies without any straightforward explanation.

While there are at least a few papers in the literature [7], [8] dealing with pion cross-section measurements, and one [5] directly dealing with their impact in an accelerator environment, all these studies focused on SEUs. SEL rate predictions in the accelerator environment were shown to be quite a concern for certain memories characterized by strong energy dependence in the proton cross section [9], [10]. This was shown to be caused by the fragments released by the primary particles interacting with the tungsten layers nearby the sensitive volume (SV) of the device [11], [12]. The effect was very relevant at energies above the typical 200 MeV proton energy, used as a reference for testing, and extended up to 3 GeV.

For typical accelerator environments, the pion fluxes peak at 1 GeV [13]. For the SEU case [5] it was concluded that the effect on the soft error rate (SER) was limited because the pion resonance was not extending beyond 250 MeV. However, this conclusion has to be verified for SELs in order to confirm that their rates in the accelerator are not underestimated.

Furthermore, the high-energy hadron equivalence approximation [14] neglects the impact of charged hadrons at energies below 20 MeV. There is no experimental indication that the pion SEL cross-section would reduce similarly to that of protons around and below this energy. Hence, this may provide a further source of inaccuracy.

This work delves in more detail into the nuclear mechanisms with the aim of understanding what stands behind the experimentally observed enhancement of the pion SEL cross-section with respect to that of protons. In order to achieve that, this work strongly relies on the numerical analysis of SEL cross-section responses as well as on the study of basic pion-silicon and proton-silicon nuclear interactions. The obtained simulation benchmarks are also used to calculate the SEL rate expected in mixed-field environments and to assess the conse-

---

Manuscript received November 13, 2020; revision submitted February 9, 2021.

This study has received funding from the European Union's Horizon 2020 research and innovation programme under the MSC grant agreement no. 721624.

Andrea Coronetti (andrea.coronetti@cern.ch) is with CERN, CH-1211 Geneva 23, Switzerland, and with the Department of Physics, University of Jyväskylä, 40014 Jyväskylä, Finland.

Rubén García Alía and Francesco Cerutti are with CERN, CH-1211 Geneva 23, Switzerland.

Wojtek Hajdas is with the Paul Scherrer Institute, Forschungsstrasse 111, 5232 Villigen, Switzerland.

Daniel Söderström and Arto Javanainen are with the Department of Physics, University of Jyväskylä, 40014 Jyväskylä, Finland. Arto Javanainen is also with the Electrical Engineering and Computer Science Department, Vanderbilt University, Nashville, TN 37235 USA.

Frédéric Saigné is with Institute d'èlectronique et des systemès, Université de Montpellier, 34090 Montpellier, France.

quences of the extended pion SEL cross-section enhancement on the high-energy hadron (HEH) equivalence.

II. EXPERIMENTAL INVESTIGATION

SRAMs are extensively used in the CERN Large Hadron Collider (LHC) complex for radiation detection purposes [15] as well as in the equipment exposed to the harsh radiation environment [16]. In the former case, components having a rather weak radiation tolerance are a better fit, in the latter, harder devices are more suited. Nevertheless, in both cases, the pion SEL cross-section enhancement may have a negative impact. On the one hand, by overpredicting the hadronic flux, and, on the other hand, by underestimating the rate of power-cycles in the electronic equipment, which would result in an availability underperformance for fundamental physics experiments.

The pion experimental tests have been performed at the Paul Scherrer Institute (PSI), at the piM1 facility. The facility and the flux calibration are extensively described in [5], [17]. Currently, the facility cannot provide pion fluxes well suited for extensive SEL testing. This limited the number of devices for which a statistically significant amount of events at various energies could be collected in reasonable time.

Information on the tested references is reported in Table I. The rather high cross-section of the two tested references allowed covering the whole available energy range at the facility (51-233 MeV).

The high-energy proton SEL measurements were performed at KVI-CART [18] in an energy range of 50-186 MeV and at PSI [19] for 30 and 230 MeV. The data acquisition procedure was the same as for the pions.

During the tests the SRAM were biased at 3.3 V, irradiated with the package on and at room temperature. One device per reference was tested with both pions and protons. The input current was monitored with a Keysight E3648A, whose maximum current was set to 0.5 A in order to protect the devices under test (DUT). The nominal current of these memories is typically below 1 mA. A latchup was recorded whenever the input current increased above 10 mA. In order for the event to be counted as a SEL, the high-current state was kept for 600 ms. Then, the equipment automatically cut the supply to the memory for 900 ms in order to remove the high-current state. Typically, the observed high-current states were between 300 and 500 mA for both devices no matter the primary particle or its energy. The tests were stopped whenever about 100 SELs were detected for each tested particle and energy. No device characterization was performed after the test to check whether it was still possible to correctly write and read the DUTs, but no power consumption variations were observed.

The experimental data are reported with error bars with 95% confidence level. For both the pion and the proton error bars an uncertainty on the fluence of ± 10% is considered.

Fig. 1 reports the SEL cross-section of the Brilliance SRAM as a function of the tested energies for both pions and protons. The pion SEL cross-section is a factor of 2-2.5 higher than that of protons for the entire tested energy range.

TABLE I
LIST OF TESTED DEVICES AND THEIR FEATURES.

Manufacturer	Reference	Datecode	Technology
Brilliance	BS62LV1600EIP55	9254	180 nm
Lyontek	LY62W20488ML	1529	180 nm

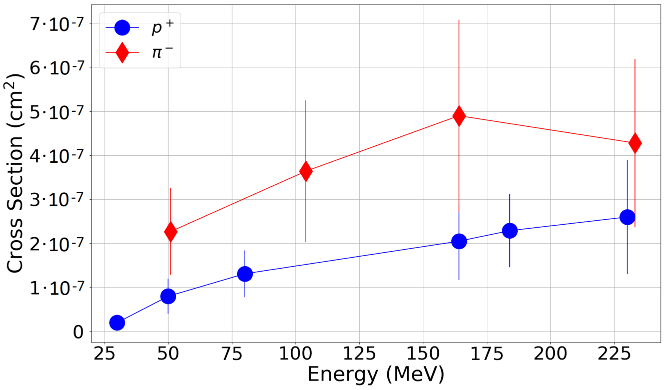

Fig. 1. Negative pion and proton SEL cross-sections for the Brilliance SRAM with 95% confidence level error bars [5].

Fig. 2 shows the SEL cross-section of the Lyontek SRAM as a function of the tested energies for both pions and protons. In this case, the pion SEL cross-section is more than a factor of 3 higher at 50 MeV and is generally up to a factor of 2 higher for the other energies.

III. MODELING AND MONTE-CARLO SIMUALTIONS OF PION SEL CROSS-SECTIONS

An integral rectangular parallelepiped (IRPP) model can be used to replicate the sensitive volume (SV) of the device and determine the energy deposition events contributing to the SEL response. The heavy ion SEL cross-section as a function of LET (described in terms of its Weibull function [20]) is convolved with the energy deposition distribution probability, produced by secondary ions of protons or pions, to retrieve the numerical SEL cross-section from a beam of protons or pions. For the Brilliance SRAM, the heavy ion Weibull fitting parameters are: σ_{sat} = 0.6 cm^2, LET$_0$ = 2.4 MeV/(mg/cm^2), W = 13.7 MeV/(mg/cm^2), s = 1.8. However, they are not known for the Lyontek SRAM. Hence, the following analysis focuses on the Brilliance SRAM.

The sensitive size for the memory in the model was derived from the observations on SEL induction regions achieved on SRAM structures of 180 nm [21] performed with laser testing, which was proven to provide reliable results for proton and neutrons [9]. Laser testing was shown to be a valuable complementary tool in the qualification process of integrated circuits as it can enable determining the characteristics of the sensitive volume such as the size [21], [22], and the thickness [23] as well as to correlate it with the heavy ion response for determining the LET threshold [24], the cross-section [25] or even the number of sensitive cells within the device [26]. All these information can be used to retrieve a better estimation of expected SEL rates in application.

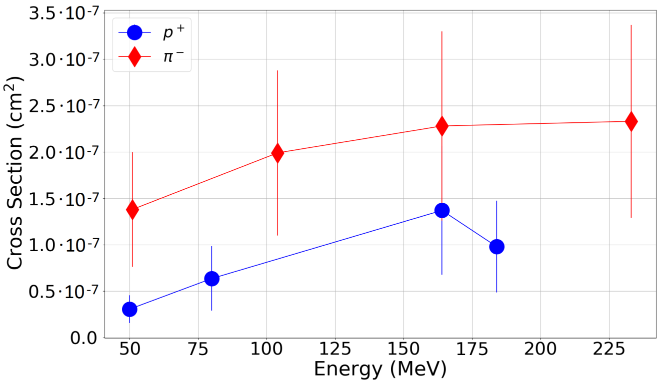

Fig. 2. Negative pion and proton SEL cross-sections for the Lyontek SRAM with 95% confidence level error bars [5].

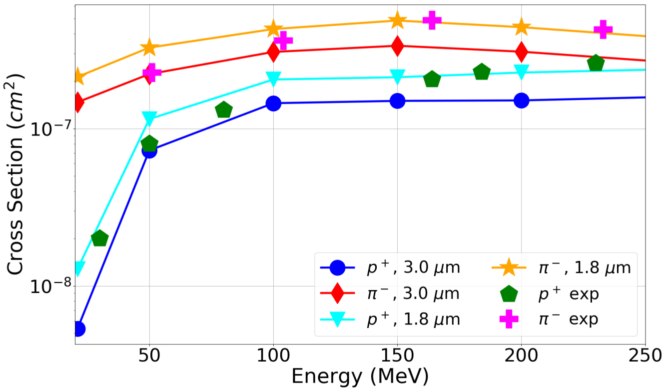

Fig. 3. Proton and negative pion SEL cross-sections simulated with FLUKA for a SV thickness of 3.0 and 1.8 μm and compared to the Brilliance experimental data.

A surface of 20x4 μm^2, representative of an array of 10x2 cells, is then used. Other than that, the simulations employ a 6 μm silicon back-end-of-line (BEOL) and a tungsten overlayer 0.4 μm thick. The thickness of the SV is kept as the free parameter for fitting the energy deposition events into an actual SEL hadron cross-section. A SV thickness between 1.8 and 3 μm can fairly represent the SRAM SEL response and is compatible with thicknesses proposed for similar models in SRAMs manufactured in 180 nm technology [27] and it is also in good agreement with the observation that SEL strcutures in SRAMs are usually wider and longer rather than thicker [28].

Fig. 3 presents the FLUKA 4.0 [29], [30] simulations data for two thicknesses and the two particles compared to experimental data. No perfect thickness matching for both the lower ($<$ 100 MeV) and higher ($>$ 100 MeV) energy part of the cross-section curves was found.

The largest thickness was found to better describe the lower energy part, whereas the smallest was found to better replicate the higher energy part. These observations both apply to protons and negative pions. The disagreement between the models is small, i.e., the model based on the smaller thickness returns, on average, cross-sections which are 33% higher than those from the model with the larger thickness.

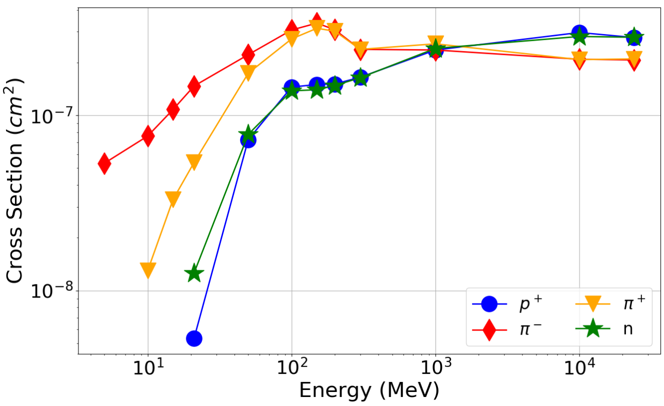

Fig. 4. FLUKA simulated SEL cross-sections as a function of energy for protons, charged pions and neutrons. The energy range is meant to cover that of the CHARM facility.

The larger thickness model is taken as a baseline, which will be verified in the nuclear interaction mechanisms and used for the accelerator radiation hardness assurance (RHA) considerations.

SEL cross-sections are simulated for other particles making up the accelerator mixed-field, i.e., positive pions and neutrons and for an extended range of energies meant to cover the whole spectra of spallation products typically found in the accelerator environment. Those cross-sections are reported in Fig. 4. No significant differences are found between protons and neutrons all along the energy range (except at 21 MeV). On the other hand, the pion cross-sections are always higher than those from the other two hadrons starting from well below 20 MeV up to 1 GeV, where the pion, proton and neutron SEL cross-section finally match.

Note that while the proton and neutron cross-sections fade by more than one order of magnitude at 20 MeV with respect to their high-energy value, the negative pion cross-section remains as high as the 50 MeV proton cross-section even down to 5 MeV.

In the HEH approximation, the cross-section of all hadrons is taken to be a step function starting at 20 MeV and equal to the proton cross-section at 200 MeV. This would be quite conservative when considering protons and neutrons due to the observed fallout. However, ignoring the fact that pions can induce SEL even at energies below 20 MeV may lead to underestimations of the expected SEL cross-section in mixed-fields, although the presence of packaging may compensate for that.

The other interesting observation is that, while positive pions have the same charge as protons, their SEL cross-section is about ten times higher at 21 MeV than that of proton and fades by one order of magnitude with respect to high-energies only at 10 MeV.

IV. NUCLEAR INTERACTION MECHANISMS BEHIND THE OBSERVED ENHANCEMENTS

A. *Nuclear reaction cross-section*

One of the main parameters that can affect the SEL cross-section response of pions with respect to protons is the nuclear

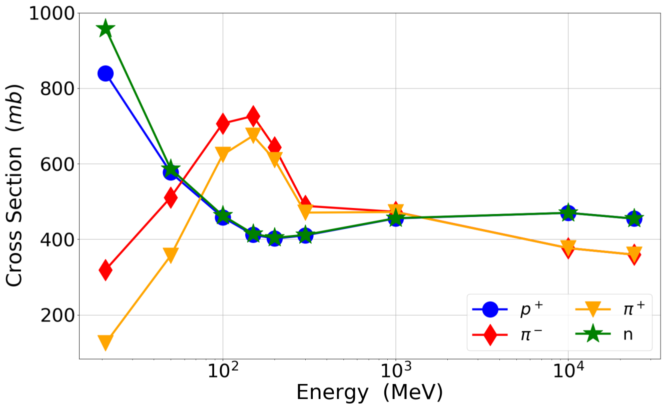

Fig. 5. Reaction cross-section in millibarns (1 mb = 10^{-27} cm^2) of protons, neutrons, negative pions and positive pions when interacting with Silicon nuclei as a function of energy.

reaction cross-section. This is the probability that a pion or a proton of a certain energy will interact by either elastic or inelastic scattering with a silicon nucleus.

Fig. 5 reports the reaction cross-sections of protons, neutrons and charged pions in silicon as a function of the primary energy. Protons and pions exhibit very contrasting behaviours when it comes to their primary energy. At 200 MeV, both negative pions and positive pions have a reaction cross-section which is at least 50% higher than that of protons. At 21 MeV, the situation is reversed with protons now having a cross-sections more than twice as high as that at 200 MeV, whereas the negative pion reaction cross-section halves and the positive pion reaction cross-section is four times lower than at 200 MeV. As a result, the proton reaction cross-section is about a factor of 2.5 higher than that of negative pions and a factor of 7 higher than that of positive pions.

Higher probability of interaction means higher yield of secondary ions capable of depositing a sufficiently high amount of energy to trigger a single-event effect (SEE) at the same primary particle fluence. What the reaction cross-section by itself does not say is how many secondary particles are released due to the nuclear interaction and which are their properties. For instance, the interaction may release a proton and an aluminum ion, of which only the second (if provided with enough kinetic energy) can directly deposit enough charge to trigger a SEE. On the other hand, there may be reactions breaking up the silicon nucleus so that an alpha particle, a carbon ion and an oxygen ion are released and all of them may deposit enough energy to trigger a SEE.

B. *Scoring of secondary ions by atomic number*

TABLE II

AVERAGE NUMBER OF REACTION PRODUCTS RELEASED BY PROTON, NEGATIVE PION AND POSITIVE PION INTERCATIONS WITH SILICON NUCLEI FOR UNIT NUCLEAR REACTION.

Primary energy [MeV]	By-products p^+-Si	By-products π^--Si	By-products π^+-Si
21	2.60	5.17	4.95
200	5.11	6.13	6.10

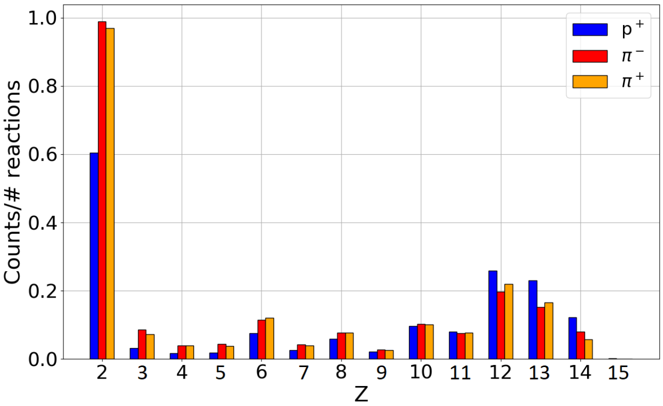

Fig. 6. Yield of secondary ions produced by nuclear reactions as a function of their atomic number normalized to the number of interactions for mono-energetic protons, negative pions and positive pions at 200 MeV.

The preex tool available in FLUKA allows resolving for all the possible nuclear interactions between primary particles and target nuclei on a statistical basis. The underlying physics is based on pre-equilibrium and evaporation models. The physics model for pion nuclear interaction in FLUKA are described in detail in [31] and [32]. Preex allows the extrapolation of distributions of by-products in terms of species, kinetic energy, linear energy transfer (LET) and range. The numerical simulations are performed by forcing the interaction of one million primary particles with one million silicon nuclei. Natural silicon is used as a target material. Hence, its isotopic composition is: 92.23% of ^{28}Si, 4.67% of ^{29}Si and 3.10% of ^{30}Si.

Table II reports the average number of reaction products produced by forcing the nuclear interaction of one million primaries with the silicon nuclei as a function of the primary particle and its energy.

Note that the minimum number of reaction products for each nuclear reaction is two, for which the products would be the original primary particle and the Si nucleus after having exchanged momentum. Clearly, the value of 2.6 for 21-MeV protons indicates that it is quite common for protons of this energy, and the nuclei they interact with, to simply experience an exchange of momentum. Both charged pions at 21 MeV release on average 5 by-products.

The situation is more homogeneous among protons and pions at 200 MeV, with protons releasing up to 5 by-products and pions up to 6, in average. The open inelastic interaction channels are probably similar among protons and pions at high-energy, yielding the release of similar amounts of reaction products (mainly secondary ions).

Figs. 6-7 propose the comparison of the yield of secondary ions released in proton-silicon and pion-silicon nuclear interactions at 200 and 21 MeV, respectively. The ions are identified by their atomic number and the yield is normalized by the one million simulated reactions.

There are not many differences at 200 MeV among the secondary ions released by p-Si and π-Si interactions. That is, similar reaction channels are open. Note that pions seem to

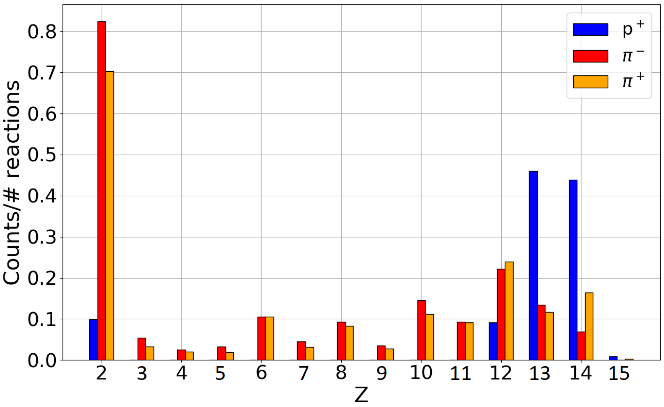

Fig. 7. Yield of secondary ions produced by nuclear reactions as a function of their atomic number normalized to the number of interactions for mono-energetic protons, negative pions and positive pions at 21 MeV.

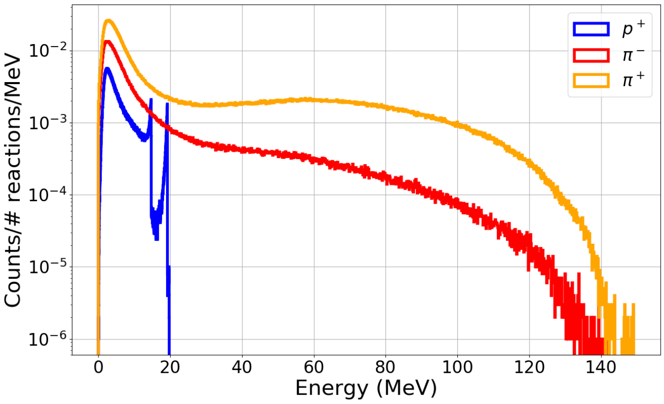

Fig. 8. Yield of secondary protons normalized to the number of interactions as a function of their kinetic energy for mono-energetic protons, negative pions and positive pions at 21 MeV.

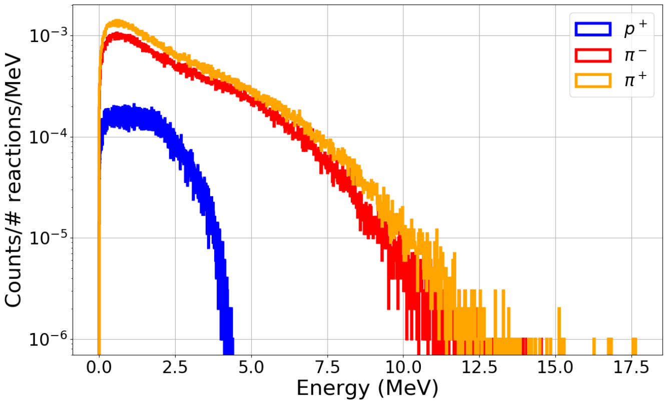

Fig. 9. Yield of secondary Mg ions normalized to the number of interactions as a function of their kinetic energy for mono-energetic protons, negative pions and positive pions at 21 MeV.

produce a larger amount of lighter ions (from $Z < 8$), which is quite evident for alphas. On the other hand, protons release a slightly higher amount of heavier ions ($Z > 11$). This indicates that protons are more likely to just knock a proton, a neutron or an alpha particle out of the Si nucleus, whereas pions are likely to induce a higher level of fragmentation.

Such effects become even more evident when considering a primary energy of 21 MeV. At this energy, all the proton-silicon interactions seem to belong to a handful of reactions. On the other hand, for pions, basically all the reaction channels that were open at 200 MeV are still open at 21 MeV. As a result, both lighter and heavier ions are produced in similar quantities to the 200 MeV case.

For the 200 MeV case, when considering both the amount of reaction products and the relative nuclear reaction cross-section (which was about 50% higher for the pions), one can conclude that the number of reaction products produced by the same number of primary protons and pions would be, when normalized to a single proton interaction, about 5 for the protons and about 9 for the pions. As a result, the number of secondary ions generated by pions will be about twice those released by protons, yielding the factor of 2 difference observed in the SEL cross-section response at 200 MeV.

At 21 MeV, the positive and negative pions have rather similar average amounts of reaction products. However, when combined with the respective nuclear reaction cross-sections, the negative pions would yield twice as many secondary ions as the positive pions. This is reflected in the simulated positive pion SEL cross-section, which is about half that of negative pions at 21 MeV.

Note that the combination of the average number of reaction products and the nuclear reaction cross-section alone is not enough to describe the enhanced pion cross-section at 21 MeV with respect to that of protons. Hence, analysing other properties of the secondary ions, such as their kinetic energy, LET and range may help shed light on this difference.

C. Pion absorption impact on secondary ion kinetic energy

In spite of their common hadronic nature, pions interact differently with heavy nuclei than protons. One of the main mechanisms in pion-silicon interactions, no matter the charge of the pion, is the pion absorption. This results in the emission of a few additional secondary particles. The main peculiarity of these secondary particles is that, even at low primary energy of the incident pion, they may be emitted with quite high kinetic energy.

One example of the consequences of the pion absorption on the kinetic energy of secondary particles is shown in Fig. 8. The yield of secondary protons emitted by proton-silicon and pion-silicon interactions as a function of their energy is shown for a primary particle energy of 21 MeV. Note that the protons emitted have a hard limit in the energy which corresponds to the energy of the primary. On the other hand, the secondary protons emitted by pion-silicon interactions have a continuous distribution in energy up to about 140 MeV. This behavior is known from past experimental measurements [33]. Basically, when absorbed, a pion can excite the nucleus to the point that highly exothermic reactions are triggered, releasing secondary particles with high kinetic content.

Fig. 9 reports the yield of magnesium ions released by proton-silicon and pion-silicon interactions as a function of their energy for a primary particle energy of 21 MeV. The same behavior observed for protons occurs for ions of any

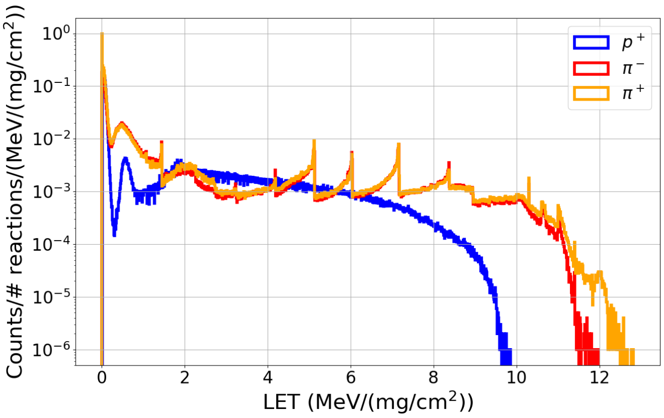

Fig. 10. Yield of secondary ions normalized to the number of interactions as a function of their LET for mono-energetic protons, negative pions and positive pions at 21 MeV.

atomic number. However, the kinetic energy transferred to ions of growing atomic mass is lower. For magnesium, pions can provide up to 13 MeV of kinetic energy, whereas protons can only provide up to 4 MeV.

As shown, thanks to this absorption mechanism, pions are capable of emitting a spectra of secondary ions which are more than twice as energetic as those emitted by protons.

D. LET and range of secondary ions

Fig. 10 shows the yield of secondary ions as a function of their LET upon generation normalized to the number of interactions for protons, negative pions and positive pions at 21 MeV. When considering LET, the atomic number of the ion is disregarded assuming that all ions of similar LET will behave similarly.

No big differences are seen between negative pions and positive pions. On the other hand, the proton LET distribution is much different as it is missing the discrete peaks. This is due to the lack of secondary ions with intermediate and low Z ($<$ 12). On the other hand, magnesium, aluminum and silicon ions are produced in a rather wide range of energies that lead to a quite smooth LET distribution.

Although having quite distinct shapes, proton and pion LET distributions do not seem to indicate that the SEL cross-section for protons would be that much lower than those of charged pions. In particular, when considering that these distributions have to be multiplied by the nuclear reaction cross-section to represent the full picture.

The range of secondary ions is an important parameter. For instance, it was shown that the range distribution of secondary ions can explain the angular dependency of proton and neutron SEL cross-sections in SRAMs [3].

Fig. 11 reports the yield of secondary ions as a function of their range normalized to the number of reactions for protons, negative pions and positive pions at 21 MeV. Note that the plot does not include all secondary ions. Ions with LET upon generation below 2.4 MeV/(mg/cm^2) have been filtered out since this is the heavy ion LET threshold of the Brilliance SRAM.

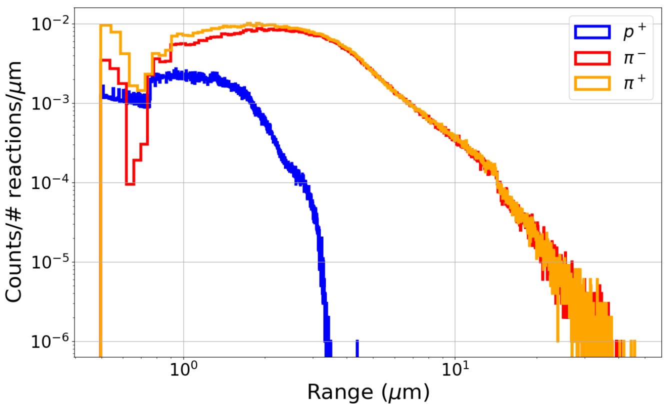

Fig. 11. Yield of secondary ions normalized to the number of interactions as a function of their range for mono-energetic protons, negative pions and positive pions at 21 MeV.

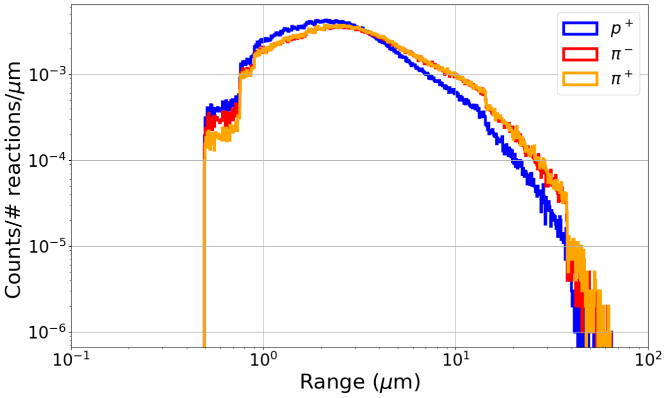

Fig. 12. Yield of secondary ions normalized to the number of interactions as a function of their range for mono-energetic protons, negative pions and positive pions at 200 MeV.

With the imposed filtering based on the ion LET threshold, all secondary ions have range above 500 nm for both proton and pion distributions.

The range distributions are very different for proton and pion secondary ions. All secondary ions from proton-siicon interactions and a sufficiently high LET have ranges below 3.5 μm. On the other hand, the pion-silicon interactions can release ions with range as high as 40 μm. The pion distributions are also seen to peak just above 3.5 μm, where the proton distribution fades.

Fig. 12 depicts the yield of secondary ions as a function of their range normalized to the number of reactions for protons, negative pions and positive pions at 200 MeV. At this energy protons and pions generate secondary ions with very similar range distributions. Therefore, considering that pions yield twice as many secondaries as protons at 200 MeV, it is confirmed that the nuclear reaction rate alone is enough to explain the SEL cross-section increase of a factor of 2 observed experimentally.

E. LET equivalent as key metric

The differences in range distributions at 21 MeV would not have a significant impact when considering typical SEU

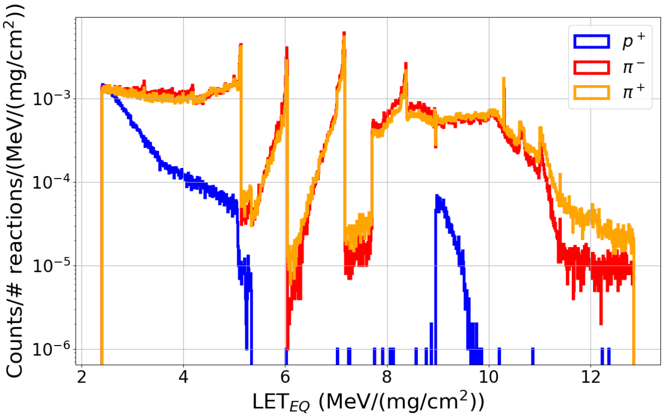

Fig. 13. Yield of secondary ions normalized to the number of interactions as a function of their LET$_{EQ}$ for mono-energetic protons, negative pions and positive pions at 21 MeV.

TABLE III
SEL CROSS-SECTIONS CALCULATED BY CONVOLUTING THE HEAVY ION WEIBULL CURVE WITH THE LET SPECTRA OF FIG. 10 AND WITH THE LET$_{EQ}$ SPECTRA OF FIG. 13. THE SEL CROSS-SECTIONS OBTAINED FROM THE MONTE-CARLO SIMULATIONS FOR PROTONS AND CHARGED PIONS ARE ALSO REPORTED. THE SEL CROSS-SECTION UNITS ARE CM^2/DEV.

Method	σ SEL protons	σ SEL negative pions	σ SEL positive pions
LET	$2.96 \cdot 10^{-7}$	$3.36 \cdot 10^{-7}$	$1.32 \cdot 10^{-7}$
LET$_{EQ}$	$9.90 \cdot 10^{-9}$	$2.27 \cdot 10^{-7}$	$8.99 \cdot 10^{-8}$
Monte-Carlo	$5.34 \cdot 10^{-9}$	$1.47 \cdot 10^{-7}$	$5.38 \cdot 10^{-8}$

sensitive volumes, as these can even have dimensions smaller than 500 nm [34]. However, they are central when it comes to converting the energy given to the secondary ion and deposited in the sensitive volume into a latch-up event. This is a characteristic of thick sensitive volumes associated with large-scale events, such as SEL. In this case, the LET of the secondary ions is not a good metric to determine the hadron response [35], [36] because most of the secondary ions will not have a range long enough to transverse a significant portion of the sensitive volume and deposit enough energy to trigger a SEL.

In such context, a different metric has to be used, that is the volume equivalent LET (LET$_{EQ}$) [35], [37]. This metric can be used to perform a new scoring of the secondary ion distributions from protons and pions when the range R of the secondary ion is shorter than the SV thickness, as indicated below:

$$\begin{cases} LET_{EQ} = \frac{E_k}{\rho t} & R \leq t \\ LET_{EQ} = LET & R > t \end{cases}$$

E$_k$ is the kinetic energy of the secondary ion upon generation, ρ is the density of the material where the energy deposition occurs (in this case silicon) and t is the thickness of the sensitive volume. Hence, this metric classifies the secondary ions depending on the properties of the sensitive volume. In accordance with the SV proposed for the Monte-Carlo (MC) simulations, the thickness is taken to be 3 μm.

Note that when an ion has a range long enough to go through the whole SV thickness and beyond, its LET$_{EQ}$ is assumed to be equal to the LET upon generation.

Fig. 13 reports the yield of secondary ions as a function of LET$_{EQ}$ normalized to the number of interactions for protons and pions at 21 MeV. As done for the range, the plot reports only the secondary ions having a LET$_{EQ}$ above 2.4 MeV/(mg/cm^2).

The pion distributions in terms of LET$_{EQ}$ have preserved somewhat the shape that was shown in the LET-upon-generation distributions in Fig. 10. Indeed, there are still particles having LET as high as 12 MeV/(mg/cm^2), though in lower abundance. The biggest difference is the deeper lowering on the left side of each peak, which shows that secondary ions generated with LET in defect of that at the peak are often associated with a range shorter than the SV thickness.

The differences between the proton LET and LET$_{EQ}$ distributions are much more evident. The previous continuous distribution is now replaced by a first continuous distribution fading at an LET$_{EQ}$ just above 5 MeV/(mg/cm^2) and a secondary peak at LET$_{EQ}$ of 9-10 MeV/(mg/cm^2). The latter represents the residual amount of magnesium, aluminum and silicon ions having a long enough range.

The LET$_{EQ}$ distributions represent a more faithful picture of what is happening inside the SV. As a cross-check, the heavy ion Weibull curve, that is used in the MC IRPP method to calculate the cross-section response, can be convoluted along with the spectra reported in Fig. 13 and multiplied by the respective nuclear reaction rates to get a SEL cross-section.

Table III reports the SEL cross-sections determined with this method for the LET distributions and for the LET$_{EQ}$ distributions for the three primary particles as well as the SEL cross-sections obtained from the MC simulations. When convoluting with the pure LET spectra, the proton SEL cross-section is predicted to be as high as that of negative pions. However, when using the LET$_{EQ}$ spectra, both the proton and the pion SEL cross-sections are much closer to those calculated through a full transport Monte-Carlo analysis.

The residual differences between the LET$_{EQ}$ spectra and the MC simulations is due to the fact that the angular distribution of the emitted secondary ions is neglected in the LET$_{EQ}$ calculation. Hence, secondary ions may have, within the SV, ionization tracks longer or shorter than the SV thickness.

In addition, the LET$_{EQ}$ calculation takes all ions as emitted at the top surface of the SV, whereas in the MC simulations the events generating secondary ions can occur at any point inside or outside the SV and the relative distance to the SV edge can play a role on whether an ion will deposit sufficient energy to trigger a SEL or not.

V. RADIATION HARDNESS ASSURANCE IMPLICATIONS

The CHARM facility [38] is taken as a study case for the RHA considerations given its wide representativeness of the various mixed-field radiation environments at CERN. The fluxes used for the computations have been calculated by means of FLUKA simulations of the facility [13]. Table IV reports the hadronic abundance in percentage of all hadrons generated in mixed-fields. The pion contribution to the total

TABLE IV

HADRONIC ABUNDANCE OF HADRONS FOR SOME TEST POSITIONS INSIDE CHARM [13]. ALL CHARGED PIONS ARE GROUPED TOGETHER. PROTONS, NEUTRONS AND KAONS FLUXES ARE INTEGRATED ABOVE 20 MEV, PION FLUXES ABOVE 1 MEV.

Position	Pions	Protons	Neutrons	Kaons
R5	15.9%	13.8%	69.8%	0.6%
R10	22.8%	17.3%	58.8%	1.1%
R13	37.1%	20.2%	42.8%	0.0%

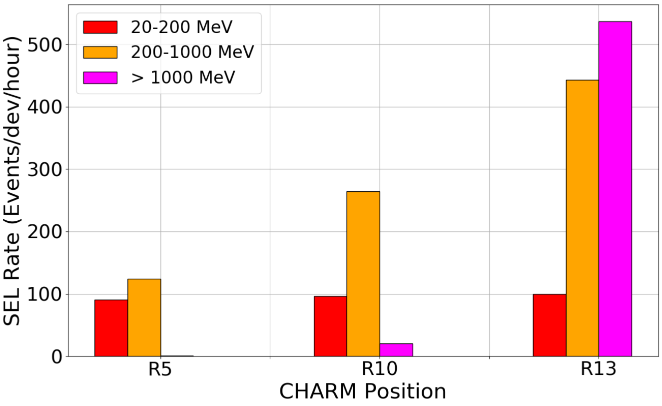

Fig. 14. SEL rates from pions from three energy ranges and three CHARM positions.

flux can be as low as 16% for the R5 test position in the CHARM facility and as high as 37% for the R13 position.

Fig. 14 depicts the pion SEL rate contributions for various CHARM position by subdividing their contributions into three energy ranges: 20-200 MeV, 200-1000 MeV and $>$ 1 GeV. As the plot shows, contributions to the total pion SEL rate may vary widely depending on the position. Typically, the 200-1000 MeV pion fluxes provide a higher contribution than the 20-200 MeV pion fluxes to the total SEL rate by up to a factor of 4. Pion fluxes with energy $>$ 1 GeV are an important contributor only for position R13.

The HEH approximation in mixed-field for the calculation of the SEL rate is based on the assumption that all particles have the same exact response no matter their nature and energy. In addition, that response would be equal to a step function starting at 20 MeV and with the proton cross-section at 200 MeV as step value. The actual SEL response in mixed-field can more precisely be calculated by convolution of each particle spectrum with the respective SEL cross-section as a function of energy. For this purpose, the numerical SEL cross-sections shown in Fig. 4 are used since they allow covering a wider range of energies than the experimental cross-sections.

Fig. 15 shows the contribution of each particle to the total SEL rate (positive and negative pion contributions are shown together) for three CHARM characteristic test positions representative of the low-Earth orbit trapped proton (R5), accelerator- and atmospheric-like (R10) and accelerator highly energetic (R13) environments, respectively.

For all the three environments, the pion contribution to the total SEL rate is underestimated when using the HEH approximation by factors of 1.6 to 2, depending on the pion abundance. For protons and neutrons, the HEH approximation provides either a fair or a conservative estimation. For the total SEL rate, while underestimating the pion contribution, the HEH approximation provides a fair estimation for R5 and R10, being the ratios between the actual-fluxes SEL rate and that delivered by the HEH approximation equal to 0.87 and 1.07, respectively. For the R13 position, the underestimation from the HEH approximation is stronger, since this ratio is 1.43.

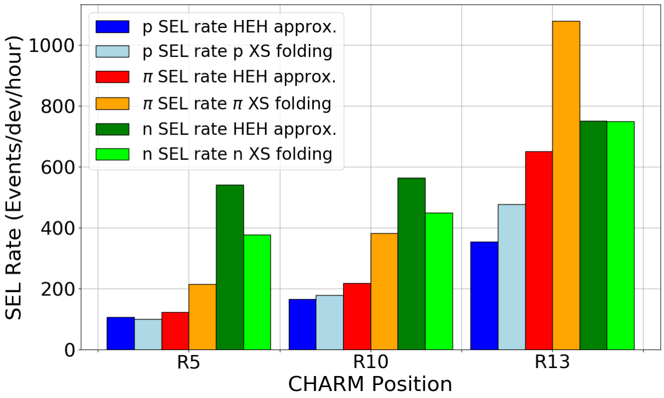

Fig. 15. SEL rate comparison between the HEH approximation approach and the full particle folding approach (XS = cross-section). Data are reported by CHARM position and further subdivided for protons (blue), pions (red) and neutrons (green)

Following these results, the HEH approximation still provides valuable estimations of the device SEL response in mixed-field in most of the application cases. Hence, characterizing the SEL cross-section out of the single 200 MeV proton data-point remains a valuable qualification scheme for accelerator applications. At the same time, the SEL rate predicted by experimental testing at CHARM and determined through the HEH approximation for other environments will be a fair representation of that obtained by proton testing.

For the only exception (R13), which concerns a small amount of accelerator equipment, the underestimation obtained by the single 200 MeV proton testing can be accounted for by assuming a margin of less than 50% on the predicted rate obtained through the HEH approximation.

VI. CONCLUSIONS

A pion SEL cross-section enhancement was experimentally observed on two SRAMs for the whole energy range under test. The enhancement was confirmed through Monte-Carlo simulations of the sensitive volume energy deposition responses based on an IRPP model.

Differently from SEU, the pion SEL cross-section was found to be higher than those of protons and neutrons for a wider range of energies. For the high-energy region ($>$ 100 MeV) it was shown that the factor of 2 higher pion cross-section is due to the higher probability of pion interaction with silicon nuclei, i.e., to the nuclear reaction cross-section. At such energies, proton-silicon and pion-silicon reactions and their secondary products do not differ that much.

At lower energies (< 100 MeV) and, in particular, for the 21-MeV case, it was shown that the nuclear reaction cross-section alone cannot explain the observed enhancement, as it would lead to a similar SEL cross-section for protons and pions. Secondary products were studied in terms of their main characteristics, such as kinetic energy, LET and range. However, it was only when the sensitive volume dimensions were added to the context and the LET_{EQ} was introduced that the higher pion SEL cross-section could be explained. The observed differences can be related to the higher energy provided to secondary products by the pion absorption mechanism, which occurs for both positive and negative pions.

Finally, the HEH approximation for mixed-fields was tested against the pion SEL cross-section enhancement. The data for representative accelerator environments showed that the effect of the pion enhancement becomes significant only when pions are in larger amount. Even in those rare cases, a small margin on the SEL cross-section measured with 200 MeV protons can be enough to account for the inaccuracy introduced by neglecting the pion cross-section enhancement.

References

[1] N.A. Dodds et al., "Effectiveness of SEL hardening strategies and the latchup domino effect," IEEE Trans. Nucl. Sci., vol. 59, no. 6, pp. 2642-2650, December 2012.

[2] R. Harboe-Sorensen et al., "The technology demonstration module onboard PROBA-II," IEEE Trans. Nucl. Sci., vol. 58, no. 3, pp. 1001-1007, June 2011.

[3] J.R. Schwank et al., "Effects of angle of incidence on proton and neutron-induced single-event latchup," IEEE Trans. Nucl. Sci., vol. 53, no. 6, pp. 3122-3131, December 2006.

[4] R. Secondo et al., "Analysis of SEL on commercial SRAM memories and mixed-field characterization of a latchup detection circuit for LEO space applications," IEEE Trans. Nucl. Sci., vol. 64, no. 8, pp. 2107-2114, August 2017.

[5] A. Coronetti et al., "The pion single event effect resonance and its impact in an accelerator environment," IEEE Trans. Nucl. Sci., vol. 67, no. 7, pp. 1606-1613, July 2020.

[6] H.H.K. Tang, "Nuclear physics of cosmic ray interaction with semiconductor materials: particle-induced soft errors from a physicist's perspective," IBM J. Res. Develop., vol. 40, no. 1, pp. 91-108, January 1996.

[7] G.J. Hofman et al., "Light-hadron induced SER and scaling relations for 16- and 64-Mb DRAMS," IEEE Trans. Nucl. Sci., vol. 47, no. 2, pp. 403-407, April 2000.

[8] S. Duzellier, D. Falguere, M. Tverskoy, E. Ivanov, R. Dufayel, and M.-C. Calvet, "SEU induced by pions in memories from different generations," IEEE Trans. Nucl. Sci., vol. 48, no. 6, pp. 1960-1965, December 2001.

[9] R. Garcia Alia et al., "SEL cross section energy dependence impact on the high energy accelerator failure rate," IEEE Trans. Nucl. Sci., vol. 61. no. 6, pp. 2936-2944, December 2014.

[10] R. Garcia Alia et al., "SEL hardness assurance in a mixed radiation field," IEEE Trans. Nucl. Sci., vol. 62, no. 6, pp. 2555-2562, December 2015.

[11] J.R. Schwank et al., "Effects of particle energy on proton-induced single-event latchup," IEEE Trans. Nucl. Sci., vol. 52, no. 6, pp. 2622-2629, December 2005.

[12] R. Garcia Alia et al, "Energy dependence of tungsten-dominated SEL cross sections," IEEE Trans. Nucl. Sci., vol. 61, no. 5, pp. 2718-2725, October 2014.

[13] A. Infantino, "FLUKA monte carlo modelling of the CHARM facility's test area: update of the radiation field assessment," CERN-ACC-NOTE-2017-0059, November 2017.

[14] K. Roed et al., "Method for measuring mixed field radiation levels relevant for SEEs at the LHC," IEEE Trans. Nucl. Sci., vol. 59, no. 4, pp. 1040-1047, August 2012.

[15] G. Spiezia et al., "A new RadMon version for the LHC and its injection lines," IEEE Trans. Nucl. Sci., vol. 61, no. 6, pp. 3424-3431, December 2014

[16] S. Danzeca et al., "Qualification and characterization of SRAM memories used as radiation sensors in the LHC," IEEE Trans. Nucl. Sci., vol. 61, no. 6, pp. 3458-3465, December 2014.

[17] W. Hajdas et al., "High energy electron radiation exposure facility at PSI," Journal of Applied Mathematics and Physics, vol. 2, pp. 910-917, August 2014.

[18] E.R. van der Graaf, R.W. Ostendorf, M.J. van Goethem, H.H. Kiewiet, M.A. Hofstee, and S. Brandenburg, "AGORFIRM, the AGOR facility for irradiations of material," RADECS proceedings, pp. 451-454, 2009.

[19] W. Hajdas, F. Burri, C. Eggel, R. Harboe-Sorensen, and R. de Marino, "Radiation effects testing facilities in PSI during implementation of the PROSCAN project," IEEE Radiation Effects Data Workshop, pp. 160-164, 2002.

[20] E.L. Petersen, J.C. Pickel, J.H. Adams, and E.C. Smith, "Rate prediciton for single event effects," IEEE Trans. Nucl. Sci., vol. 39, no. 6, pp. 1577-1599, December 1992.

[21] N.A. Dodds et al., "SEL-sensitive area mapping and the effects of reflection and diffraction from metal lines on laser SEE testing," IEEE Trans. Nucl. Sci., vol. 60, no. 4, pp. 2550-2558, August 2013.

[22] P. Wang et al., "Analysis of TPA pulsed-laser-induced single-event latchup sensitive-area," IEEE Trans. Nucl. Sci., vol. 65, no. 1, pp. 502-509, January 2018.

[23] E. Faraud et al., "Investigation on the SEL sensitive depth of an SRAM using linear and two-photon absorption laser testing," IEEE Trans. Nucl. Sci., vol. 58, no. 6, pp. 2637-2643, December 2011.

[24] A.J. Burnell, A.M. Chugg, R. Harboe-Sorensen, "Laser SEL sensitivity mapping of SRAM cells," IEEE Trans. Nucl. Sci., vol. 57, no. 4, pp. 1973-1977, August 2010.

[25] V. Pouget, P. Fouillat, D. Lewis, H. Lapuyade, F. Darracq, and A. Touboul, "Laser cross section measurement for the evaluation of single-even effects in integrated circuits," Microelectron. Reliab., vol. 40, no. 8, pp. 1371-1375, August 2000.

[26] Y.-T. Yu, J.-W. Han, G.-Q. Feng, M.-H. Cai, and R. Chen, "Correction of single-event latchup rate prediction using pulsed laser mapping test," IEEE Trans. Nucl. Sci., vol. 62, no. 2, pp. 565-, April 2015.

[27] P. Wang et al., "Sensitive-volume model of single-event latchup for a 180-nm SRAM test structure," IEEE Trans. Nucl. Sci., vol. 67, no. 9, pp. 2015-2020, September 2020.

[28] L. Artola et al., "Analysis of angular dependence of single-event latchup sensitivity for heavy-ion irradiations of 0.18-μm CMOS technology," IEEE Trans. Nucl. Sci., vol. 62, no. 6, pp. 2539-2546, December 2015.

[29] G. Battistoni et al., "Overview of the FLUKA code," Annals of Nuclear Energy, vol. 82, pp. 10-18, August 2015.

[30] T.T. Bohlen et al., "The FLUKA Code: Developments and Challenges for High Energy and Medical Applications," Nuclear Data Sheets, vol. 120, pp. 211-214, June 2014.

[31] A. Fassò, A. Ferrari, J. Ranft, and P.R. Sala, "FLUKA: performances and applications in the intermediate energy range," Proc. 1st AEN/NEA Specialists' Meeting on Shielding Aspects of Accelerators, Targets and Irradiation Facilities (SATIF), Arlington, TX, April 28-29, 1994. OECD Documents, pp. 287-304, 1995.

[32] A. Fassò, A. Ferrari, J. Ranft, and P.R. Sala, "An update about FLUKA," Proc. 2nd Workshop on Simulating Accelerator Radiation Environments, CERN, Geneva, Switzerland, October 9-11, 1185. CERN Report TIS-RP/97-05, pp. 158-170, 1997.

[33] R.D. McKeown et al., "Inclusive reactions of pions on nuclei," Phys. Rev. C, vol. 24, no. 1, pp. 211-220, July 1981.

[34] A. Coronetti et al., "Assessment of proton direct ionization for the radiation hardness assurance of deep sub-micron SRAMs used in space applications," submitted for publication.

[35] R.L. Ladbury, J.-M. Lauenstein, and K.P. Hayes, "Use of proton SEE data as a proxy for bounding heavy-ion SEE susceptibility," IEEE Trans. Nucl. Sci., vol. 62, no. 6, pp. 2505-2510, December 2015.

[36] R.L. Ladbury and J.-M. Lauenstein, "Evaluating constraints on heavy-ion SEE susceptibility imposed by proton SEE testing and other mixed environments," IEEE Trans. Nucl. Sci., vol. 64, no.1, pp. 301-308, January 2017.

[37] R. García Alía et al., "Simplified SEE sensitivity screening for COTS components in space," IEEE Trans. Nucl. Sci., vol. 64, no. 2, pp. 882-890, February 2017.

[38] J. Mekki et al., "CHARM: a mixed field facility at CERN for radiation test in ground, atmospheric, space and accelerator representative environments,"IEEE Trans. Nucl. Sci., vol. 63, no. 4, pp. 2106-2114, August 2016.